On parametric spectral estimation for induction machine faults detection in stationary and nonstationary environments

El Houssin El Bouchikhi

THÈSE/ UNIVERSITÉ DE BRETAGNE OCCIDENTALE
sous le sceau de l'Univesité européene de Bretagne

pour obtenir le titre de
DOCTEUR DE l'UNIVERSITÉ DE BRETAGNE OCCIDENTALE
Mention : Science pour l'Ingénieur
École Doctorale SICMA

Présentée par

Elhoussin ELBOUCHIKHI

Préparée au sein de l'EA 4325 LBMS

On parametric spectral estimation for induction machine faults detection in stationary and non-stationary environments

This project has received financial support from
Brest Métropole Océane

Thèse soutenue le 25 novembre 2013
devant le jury composé de :

Jose Alfonso ANTONINO-DAVIU
Professeur, Universitat Politecnica de Valencia, Espagne / examinateur

François AUGER
Professeur, Université de Nantes / rapporteur

Adel BELOUCHRANI
Professeur, Ecole Nationale Polytechnique, Algérie / examinateur

Gilles BUREL
Professeur, Université de Bretagne Occidentale / examinateur

Pascal MAUSSION
Professeur, Université de Toulouse INPT / rapporteur

Abdellatif MIRAOUI
Professeur, UTBM & Université de Marrakech Cadi Ayyad / président

Vincent CHOQUEUSE
Maître de Conférences, Université de Bretagne Occidentale / co-encadrant

Mohamed BENBOUZID
Professeur, Université de Bretagne Occidentale / directeur de thèse

Jean Frédéric CHARPENTIER
Maître de Conférences, Ecole Navale / invité

Abstract

In this thesis, a signal processing-based approach for induction machine faults detection through stator currents has been proposed. A parametric spectral estimation approach has been adopted to extract sensitive index to induction machine faults. The proposed approach can perform induction machine condition monitoring in stationary and non-stationary environment. Moreover, it allows to propose a reliable diagnosis scheme for electrical and mechanical faults that may occur in induction machines. Moreover, A Matlab-Simulink®-based tool for faulty induction machines has been developed to generate faults database and therefore to allow the performance of the proposed approach assessment. The coupled magnetic circuits approach combined with the arbitrary reference frames theory has been used for induction machines modeling.

The proposed technique has been validated using experiments on conventional induction machine test bed for bearing faults detection and diagnosis. The obtained results were satisfactory and very promising.

Acknowledgements

This work has been carried out at the Laboratoire Brestois de Mécanique et des Systèmes (EA 4325 LBMS) at the University of Brest. The financial support provided by Brest Métropole Océane (BMO) is greatfully acknowledged.

I am grateful to my thesis supervisor, **Prof. Mohamed Benbouzid** for help, inspiration, encouragement and guidance throughout the work. I am deeply indebted to my co-supervisor **Dr. Vincent Choqueuse** for his valuable comments, discussions, encouragement and timely guidance along this thesis. I express my thanks to **Dr. Jean-Frédéric Charpentier** for his time, efforts and advices especially during the first year of this project and for reviewing this manuscript.

I would like to thank the pre-examiners **Prof. François AUGER** from the University of Nantes, France and **Prof. Pascal MAUSSION** from the Polytechnique Institute of Toulouse ENSEEIHT, France, for their valuable comments and corrections. I am also grateful to my PhD thesis defense commitee members: **Prof. Jose Alfonso ANTONINO-DAVIU** from the University Polytechnique of Valencia, Spain, **Prof. Adel BELOUCHRANI** from the National Polytechnic School of Algiers, Algeria, **Prof. Gilles BUREL** from the University of Western Brittany, Brest, France, **Prof. Abdellatif MIRAOUI** from the UTBM, Belfort, France & Université de Marrakech Cadi Ayyad, Morocco, and **Dr. Jean Frédéric CHARPENTIER** from the French Naval Academy, Brest, France.

I also wish to thank all my friends and the colleagues at the IUT of Brest; their encouragement and support have been very important to me.

For their support, love, and understanding during the past three years, I am deeply indebted to my family.

List of Publications

Some of the results in this thesis have been published or are in reviewing process for possible publications in international journals.

– **INTERNATIONAL JOURNAL PAPERS**

1. **E. Elbouchikhi**, V. Choqueuse and M.E.H. Benbouzid, "Induction machine faults detection using stator current parametric spectral estimation," Mechanical Systems and Signal Processing, Published, 2014.

2. V. Choqueuse, A. Belouchrani, **E. Elbouchikhi** and M.E.H. Benbouzid, "Estimation of amplitude, phase and unbalance parameters in three-phase systems: analytical solutions, efficient implementation and performance analysis," IEEE Transactions on Signal Processing, Published, 2014.
3. **E. Elbouchikhi**, V. Choqueuse and M.E.H. Benbouzid, "Current frequency spectral subtraction and its contribution to induction machines' bearings condition monitoring," IEEE Transactions on Energy Conversion, vol. 28, no. 1, pp. 135-144, March 2013.
4. **E. Elbouchikhi**, V. Choqueuse, M.E.H. Benbouzid et J.F. Charpentier, "Etude comparative des techniques de traitement du signal non stationnaires dédiées au diagnostic des génératrices asynchrones dans les éliennes offshores et les hydroliennes," European Journal of Electrical Engineering, Vol. 16, no. 5-6, Décembre 2013.

5. M. Becherif, **E. Elbouchikhi** and M.E.H. Benbouzid, "On Impedance Spectroscopy Contribution to Failure Diagnosis in Wind Turbine

Generators," International Journal on Energy Conversion (IRECON), Vol. 1, no. 3, May 2013.

6. **E. Elbouchikhi**, V. Choqueuse and M.E.H. Benbouzid, "Induction Machine Bearing Faults Detection based on a Multi-Dimensional MUSIC Algorithm and a Maximum Likelihood Estimation," IEEE Transactions on Power Electronics (Submitted).

7. **E. Elbouchikhi**, V. Choqueuse, Y. Amirat and M.E.H. Benbouzid, "Stator Current Demodulation for Bearing Faults Diagnosis in Induction Machines: a Comprehensive Study," IEEE Transactions on Energy Conversion (Submitted).

– **INTERNATIONAL CONFERENCE PAPERS**

1. **E. Elbouchikhi**, V. Choqueuse, M.E.H. Benbouzid and J. A. Antonino-Daviu, "Stator current demodulation for induction machine rotor faults diagnosis," in Proceedings of the IEEE ICGE'14 (International Conference on Green Energy), Sfax (Tunisia), March 2014.
2. **E. Elbouchikhi**, V. Choqueuse, M.E.H. Benbouzid "Non-stationary spectral estimation for wind turbine induction generator faults detection," in Proceedings of the IEEE IECON'13 (International Conference of the IEEE Industrial Electronics Society), Vienna (Austria), November 2013.

3. **E. Elbouchikhi**, V. Choqueuse, M.E.H. Benbouzid "A Parametric Spectral Estimator for Faults Detection in Induction Machines," in Proceedings of the IEEE IECON'13 (International Conference of the IEEE Industrial Electronics Society), Vienna (Austria), November 2013.

4. **E. Elbouchikhi**, V. Choqueuse, M.E.H. Benbouzid "Induction machine fault detection enhancement using a stator current high

resolution spectrum," in Procedings of the IEEE IECON'12 (International Conference of the IEEE Industrial Electronics Society), Montréal (Canada), October 2012.

5. **E. Elbouchikhi**, V. Choqueuse, M.E.H. Benbouzid and J.F. Charpentier, "Induction machine bearing failures detection using stator current frequency spectral subtraction," in Proceedings of the IEEE ISIE'12 (International Conference of the IEEE Industrial Electronics Society), Hangzhou (China), May 2012.

6. **E. Elbouchikhi**, V. Choqueuse, M.E.H. Benbouzid, J.F. Charpentier and G. Barakat, "A comparative study of time-frequency representations for fault detection in wind turbine," in Proceedings of the IEEE IECON'11 (International Conference of the IEEE Industrial Electronics Society), Melbourne (Australia), November 2011.

– **NATIONAL CONFERENCE PAPERS**

1. V. Choqueuse, **E. Elbouchikhi** et M.E.H. Benbouzid, "Analyse Spectrale Paramétrique dans un contexte Smart-Grid" dans les Actes du GRETSI'13, Brest, Septembre 2013.

2. **E. Elbouchikhi**, V. Choqueuse et M.E.H. Benbouzid, "Estimation spectrale paramétrique dédiée au diagnostic de la génératrice asynchrone dans un contexte éolien," dans les Actes de JCGE'13 (Journée des Jeunes Chercheurs en Génie Électrique), Saint-Nazaire (France), Juin 2013.

3. **E. Elbouchikhi**, V. Choqueuse, M.E.H. Benbouzid et J.F. Charpentier, "Étude comparative des techniques de traitement de signal non stationnaires dédiées au diagnostic des génératrices asynchrones dans les éoliennes offshores et les hydroliennes," dans les Actes de EF'11 (Conférence Électrotechnique du Futur), Belfort (France), Décembre 2011.

"Verily, in the creation of the heavens and the earth, and in the succession of night and day, there are indeed signs for those who are endowed with insight" Quran, surate 3, verse 190.

"Il y a dans la création des cieux et de la terre et dans le succession de la nuit et du jour, des signes pour ceux qui sont doués d'intelligence" Coran, sourate 3, verset 190.

Table of Contents

List of Figures

LIST OF FIGURES

List of Tables

Glossary

AI	Artificial intelligence
AIC	Akaike information Criterion
AM/FM	Amplitude modulation/Frequency modulation
ANN	Artificial neural networks
$ARMA$	Autoregressive moving average
BIC	Bayesian information criterion
CRB	Cramér–Rao bound
$CRLB$	Cramér–Rao lower bounds
CT	Concordia transform
CWT	Continuous wavelet transform
DFT	Discrete Fourier transform
EMD	Empirical mode decomposition
ESA	Energy separation algorithm
$ESPRIT$	Estimation of signal parameters via rotational invariance techniques
EVD	Eigenvalues decomposition
FFT	Fast Fourier transform
GIC	Generalized information criterion
HHT	Hilbert-Huang transform
HT	Hilbert transform
IA	Instantaneous amplitude
IF	Instantaneous frequency
IMF	Intrinsic mode function
$MCMFT$	Maximum covariance method for frequency tracking
$MCSA$	Motor current signature analysis
$MDMUSIC$	Multidimensional Multiple signal classification
MDL	Minimum description length
MLE	Maximum likelihood estimation
MMF	Magnetomotive force
$MUSIC$	Multiple signal classification
MVU	Minimum variance unbiased estimator
$O \ \& \ M$	operation and maintenance
PCA	Principal component analysis
PM	Phase modulation
$PMSM$	Permanent magnet synchronous machine
$PWVD$	Pseudo Wigner-Ville distribution
SNR	Signal to noise ratio
$STFT$	Short time Fourier transform
SVM	Support vector machine
TEO	Teager energy operator
WTG	Wind turbine generator
WVD	Wigner-Ville distribution
$ZAMD$	Zhao-Atlas-Marks distribution
$ZFFT$	Zoom fast Fourier transform
$\mathfrak{STFT}$	Short-Time Fourier Transform
BF	Ball fault
DWT	Discrete Wavelet Transform
IRF	Inner raceway fault
MFS	Machinery Fault Simulator
ORF	Outer raceway fault
PSD	Power Spectral Density

$[.]^{-1}$	Matrix inverse
$[.]^{H}$	Matrix conjugate transpose
$[.]^{T}$	Matrix transpose
$[\mathbf{I}]$	Current vector
$[\mathbf{I}_r]$	Rotor current vector
$[\mathbf{I}_s]$	Stator current vector
$[\mathbf{L}]$	Global inductance matrix
$[\mathbf{L}_{rr}]$	Rotor windings self and mutual inductances
$[\mathbf{L}_{ss}]$	Stator windings self and mutual inductances
$[\mathbf{M}_{rs}]$	Mutual inductances between rotor windings and stator ones
$[\mathbf{M}_{sr}]$	Mutual inductances between stator windings and rotor ones
$[\mathbf{R}]$	Global resistance matrix
$[\mathbf{R}_r]$	Cage resistances matrix
$[\mathbf{R}_s]$	Diagonal matrix of stator phases resistances
$[\mathbf{V}]$	Voltage vector
$[\mathbf{V}_s]$	Stator voltage vector
$\frac{d}{d\theta_m}[.]$	The derivative with respect to the angular position
$\frac{d}{dt}[.]$	The derivative with respect to time
J	Rotating masses inertia
Γ_C	Load torque
Ω_r	Rotor mechanical speed
θ_m	Rotor angular position
f	Viscous friction coefficient
f_r	Shaft rotation frequency
Ω	Set of parameters to be estimated
$\mathcal{J}(\Omega)$	Exact cost function
$\mathcal{J}_a(\Omega)$	Approximate cost function
$\mathcal{J}_m(\Omega)$	MD MUSIC cost function
f_{bd}	Bearing ball fault frequency
f_{bng}	Bearing fault characteristic frequency
f_{brb}	Broken rotor bars fault characteristic frequency
f_c	Bearing cage fault frequency
f_d	Fault characteristic frequency
f_{id}	Bearing inner race fault frequency
f_{od}	Bearing outer race fault frequency
D_r	Bearing pitch diameter
α	Contact angle
d_r	Roller diameter
n_r	Roller number
F_s	Sampling frequency
I_n	Nominal current
L	Length of the magnetic circuit
L	Model order
L_b	Rotor bar leakage inductance
L_e	End ring leakage inductance
M	Signal subvectors length
N	Number of samples
N_r	Number of rotor bars or rotor slots
N_s	Number of stator slots
P_n	Nominal power
R_{av}	Average radius of the air-gap
R_b	Bar resistance
R_e	End ring resistance
R_s	Stator phase resistance
V_n	Supply voltage
Ω_n	Nominal speed
$\angle(.)$	Phase

$\omega[.]$	Time window
σ^2	Noise variance
τ	Delay
$\mathbf{G}$	Eigenvectors spanning the noise subspace
$\mathbf{I}_N$	$N \times N$ identity matrix
$\mathbf{R}$	Covariance matrix
$\mathbf{S}$	Eigenvectors spanning the signal subspace
e	Air-gap thickness
f_s	Supply frequency
p	Number of pole pairs
s	Per-unit slip

Introduction

Diagnosis and condition monitoring are effective means to improve electrical machines reliability and performance and reduce operating and maintenance costs. They are one of the important issues that face the deployment of some far-offshore wind and marine current turbines. In fact, the availability and the reliability of such offshore systems decrease significantly when they are located offshore. Even if the efficiency and energy management of renewable technologies have been continuously improved and an important technological advances have been noted, the reliability of such systems needs to be improved to increase the overall performance.

Most existing technologies for electrical machines condition monitoring such as vibration monitoring, torque monitoring, temperature monitoring, and oil/debris monitoring require additional sensors and specific data acquisition devices to be implemented. The use of such technologies increases cost, size, and hardware complexity of the whole system. Moreover, most of these condition monitoring systems are difficult to access during electrical machines operation. To address these limitations, it is desirable to develop a non-invasive, a lower-cost, and a reliable technology that fully exploit the benefits of electrical machines condition monitoring.

In the last decades, many studies have demonstrated the interest of using the stator current to monitor the electrical machines with emphasis on induction machine monitoring. In particular, many previous works have proposed to use advanced signal processing techniques as a medium for fault detection in induction machine. In stationary context, techniques based on power spectral density (PSD) estimators have been used and their performance demonstrated for induction machine fault detection and diagnosis. These techniques include non-parametric and semi-parametric methods. Non-parametric methods include the conventional periodogram and it extensions. The semi-parametric methods also known as high resolution techniques, can be divided into two sub-classes: the linear prediction methods and subspace class. The linear prediction

class contains several algorithms like the Prony and Pisarenko methods. The subspace class includes the MUSIC and ESPRIT approaches. However, these techniques performance depends on the system operating conditions. Moreover, the computation of fault related frequencies requires the knowledge of operating condition of the electrical machine or some dimensions (bearing dimensions, for instance). Besides, these techniques do not allow to distinguish several faults since most of them have similar fault related frequencies. In addition to spectral estimation techniques, other authors have also investigated the use of demodulation techniques such as the synchronous demodulator (SD), the Concordia transform (CT), the Hilbert transform (HT), and the Principal Component Analysis (PCA) for stator current instantaneous frequency and instantaneous amplitude extraction and afterwards highlighting the faults signature. However, these techniques are more suited for mono-component signals whereas the stator currents are mainly multi-component signals. In non-stationary environment such as transient and variable speed conditions where the supply voltage and the stator current have a time-varying frequency content, more sophisticated techniques have been proposed. For instance, time-frequency and time-scale techniques such as the spectrogram, Wigner-Ville distribution, scalogram and Hilbert-Huang transform have been used for condition monitoring. However, these techniques suffer from several drawbacks such as low frequency resolution for the spectrogram, introduction of artefacts for the quadratic time-frequency distributions, etc.

As a complement to the aforementioned techniques, several authors have proposed the use of intelligent artificial techniques as faults decision systems. These techniques include Support Vector Machines (SVM), Artificial Neural Networks (ANN), fuzzy logic, and genetic algorithms. The main advantage of such techniques is their ability to automatically distinguish faulty cases from healthy case for different operating conditions and various faults severity. However, most of these techniques require a learning stage and fine tuning.

In this Ph.D. thesis, we focus on the induction machine condition monitoring especially in non-stationary environments such as in wind turbine application. The main objective is to propose a reliable, efficient, and accurate faults detection algorithms. More precisely, we investigate the use of parametric spectral estimation techniques based on statistical estimation for stator currents processing. As opposed to classical spectral estimation techniques, the proposed technique exploits the particular structure

of faults signature in order to define adequate fault detection procedure. Furthermore, the proposed approach allows to simply extract a fault severity indicator in stationary and non-stationary environments.

The contribution of this thesis is threefold:

- The induction machine faults detection and diagnosis is embedded in the parametric estimation framework.
- The effectiveness of the proposed approach is analyzed on simulated and experimental data for several faults and various operating conditions.
- The proposed method, the non-parametric and semi-parametric techniques are compared for induction machine faults diagnosis.

This thesis is organized as follows:

Chapter I reviews induction machine main failures, their occurrence frequency, and failing components. It also reports on condition monitoring techniques used in industrial applications. Three-phase currents monitoring approaches presented in some relevant works that have been carried out earlier are discussed and some limitations highlighted. The emphasis is made on stator current spectral estimation, demodulation techniques and time-frequency analysis techniques.

Chapter II presents the proposed parametric spectral estimation techniques used for stator current processing and fault severity estimation in stationary operating conditions. Then, the proposed techniques are extended to non-stationary signals in order to perform fault detection in induction machine in non-stationary environment (generator application in wind turbines, for instance). Finally, a diagnosis scheme is presented and evaluated on synthetic signals.

Chapter II presents the simulation results on stator currents issued from a coupled magnetic circuits approach-based simulation tool developed on Matlab® of an induction machine. The main results are presented along with a focus on non-stationary operating conditions of the induction machine.

Chapter IV presents the experimental validation of the proposed approaches on a conventional induction machine. Several faults are studied and the performance of the proposed approaches are highlighted and some issues discussed.

Chapter V concludes this manuscript and gives some prospects for further investigations.

Chapter VI gives a French resume of the manuscript.

Chapter

1

Faults Diagnosis in Induction Machine: State of the Art Review

Contents

1.1 Introduction

In the field of energy production and many other industrial applications, the electrical drives are subject to various failures, possibly combined. These faults include:

– Failure of power supply devices;
– Failure of electrical machine (broken bars, short-circuits, demagnetization for PMSM, etc.);
– Failure of mechanical load (wear or breakage of all or part of the bearings, shafts, gears, etc.);
– Failure of control devices;
– Failure of cables, connections, protective devices,etc.

The challenge then is to detect the failures at an early stage in order to prevent breakdowns. In particular, stator current-based condition monitoring is an extensively investigated field for cost and maintenance savings.

This chapter presents a state of art of failures that can occur in induction machine, their origins, and their consequences. It also reports on condition monitoring techniques applied in industrial applications. Moreover, attempts are made to highlight induction machine faults effects over the stator current. Emphasis is made on condition monitoring techniques based on stator current processing which is already measured on the drive system for other purposes such as control and protection.

1.2 Induction Machine Faults

Nowadays, induction machines are widely used in industrial applications. In fact, induction machines are still the most important rotating electric machines in industry mainly because of their low price, ruggedness, efficiency and reliability. Although, the use of switching power converters has improved the performance of such machine and has extended it use to adjustable speed drives, the electrical machine lifetime has been reduced . This fact has increased the range of applications where the need of diagnostics is crucial.

1.2.1 Typical faults in induction machines

The induction machine can be subjected to various failures that can broadly be classified as follows [12]:

- Stator faults; opening or shorting of one or more of a stator phase winding;
- Broken rotor bar or cracked rotor end-rings;

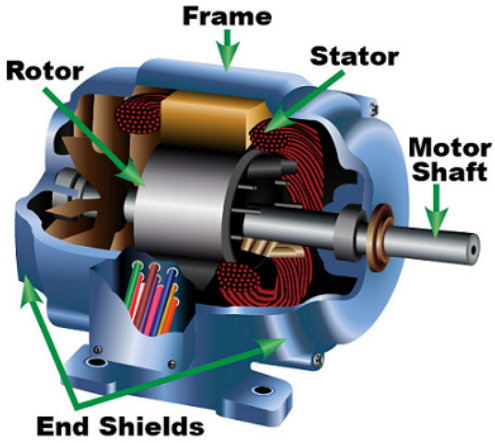

(a) components of induction machines

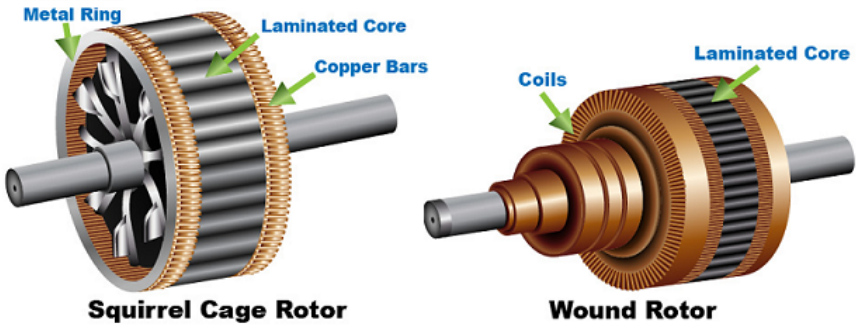

(b) Induction machine rotor

Figure 1.1: Induction machine scheme [1].

- Static and/or dynamic air-gap irregularities;
- Bent shaft and misalignment;
- Bearing and gearbox failures;
- Failure of one or more power electronic components of drive system.

These faults could be organised in two major categories which are electrical faults and mechanical faults.

Electrical faults: The electrical faults include the stator and rotor faults. Even though stator faults account for much more than rotor faults [2], rotor bars breakage have received much attention in the literature [15, 16, 17]. This interest can be explained by two main reasons: 1) the rotor faults are difficult to detect since rotor quantities are

not accessible 2) the stator electrical faults have been mitigated by recent improvements in the design and manufacture of stator windings. Two main classes of stator windings failures can be considered: asymmetry in the stator windings such as open-phase failure and short-circuit of a few turns in a phase windings. The latter fault may lead to catastrophic failure in short time if undetected [12, 13]. Concerning the rotor faults, two main failure events may occur in the case of squirrel-cage rotors. These failures include the bars and end-ring segments breakage (especially in the case of fabricated squirrel cage, in contrary to cast cage which are more rugged). The detection of such events is mandatory and constitute a key issue in order to enhance the overall performance.

Mechanical faults: Induction machine mechanical faults include bearing faults and eccentricity faults, bent shaft and misalignment. Bearing faults are due to several reasons such as vibration, internal stresses, inherent eccentricity, and bearing currents owing to power electronics. Airgap eccentricity is one of the most common mechanical failures in induction machine. It includes static eccentricity, dynamic eccentricity, and mixed eccentricity [18]. In the case of static eccentricity, the rotor geometrical center is identical with the rotational center, but it is displaced with respect to the stator geometrical center. Concerning the dynamic eccentricity, the rotor geometrical center is different from the rotational center and the rotational center is identical with the stator geometrical center. The two effects are combined for the mixed eccentricity. Eccentricity faults may be caused by several problems such as bad bearing positioning during motor assembly, worn bearing, bent rotor shaft or operation under a critical speed [19]. It causes excessive stressing of the machine and increases the bearing wear. Moreover, the radial magnetic force owing to eccentricity may expose the stator windings to harmful vibration. The second substantial effect of mechanical faults in induction machine is load torque oscillations. This fault is due to load unbalance, shaft misalignment, gearbox fault and other failures in the load part of the drive. This failure produces a periodic variation of the load torque and inertia which introduces the mechanical speed oscillations.

1.2.2 Failures occurrence frequency, origins, and consequences

The distribution of the aforementioned failures within the machine subassemblies is reported in many reliability surveys [2, 20] and are provided in Fig. 1.2. Depending on

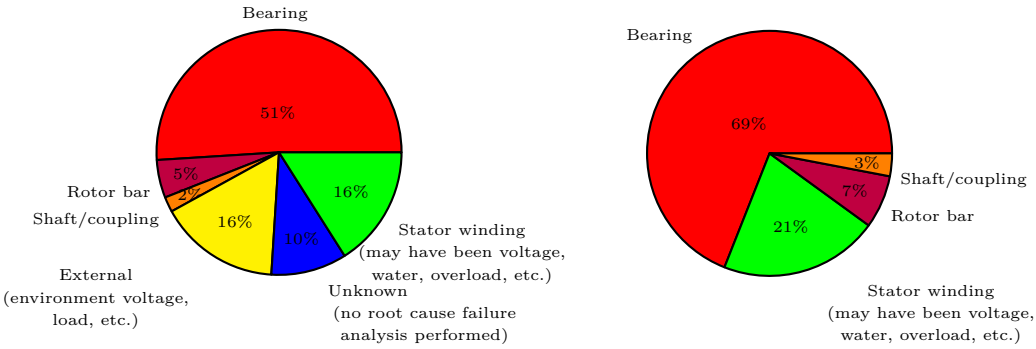

(a) Motor failures frequency.

(b) Extrapolated distribution of failure by motor components.

Figure 1.2: Distribution of known motor failures for the petroleum and chemical industries [2].

the type and size of the machine, bearing faults and stator windings faults distributions vary from 80% to 90% from large to small machines. The induction machine may be subjected to various failures that affect mainly three components : the stator, the rotor and/or the bearings (Fig. 1.2(a)). A recent paper dealing with induction machine faults distribution [2] has shown that bearings (69%), stator windings (21%), rotor (7%), and shaft/coupling (3%) are the most failing components (Fig. 1.2(b)).

The faults distribution depends on the industrial application. For instance, wind turbines are generally installed in remote sites, difficult to access, and are potentially vulnerable to very harsh environmental conditions especially for offshore farms [21]. In fact, several failures can occur on such systems which reduce the energy production and increase the overall energy cost [22, 23, 24, 25, 26]. The distribution of wind turbine faults within the systems subassemblies has been presented is several papers [3, 27] dealing with wind turbine parks reliability and availability. In Fig. 1.3, one can notice that the percentage of electrical failures is equal to the one of the mechanical faults. Moreover, it can be concluded that the gearbox, the generator and the drive train stand out as components with the longest downtime.

The failures discussed earlier are due to various causes which are associated with the design, manufacture or employment processes. Faults in the stator and bearings defects are nearly 90% of electrical machines defects. In lower power machines, the stator faults are less frequent, while high speed machines are more concerned by bearing faults and

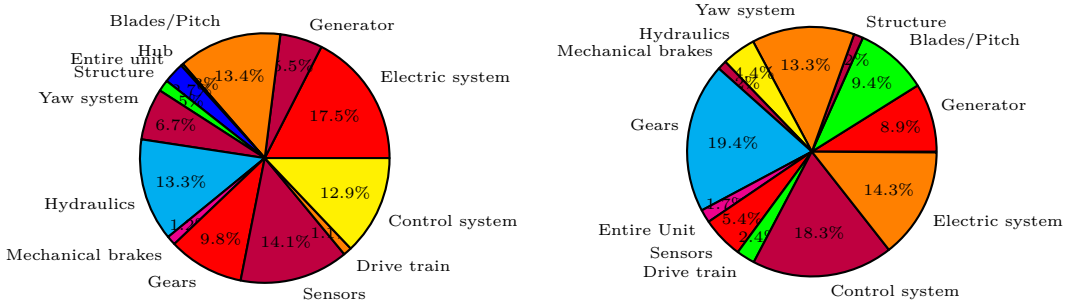

(a) Distribution of Number of failures for Swedish wind power plants between 2000 – –2004.

(b) Percentage of downtime per component in Sweden between 2000–2004.

Figure 1.3: Wind turbine failures and downtime [3].

rotor faults. It can be concluded from the previously treated items that bearings and insulation are the weak link in the electromechanical drives [28].

The origins of the electromechanical systems faults are diverse and can be summarized as follows:

- Thermal stresses: large number of consecutive starts, mechanical overload, unbalanced power supply, insulation ageing due to natural thermal stresses, poor ventilation;
- Electric origins: deterioration of insulating materials, Voltage stresses due to the use of power inverters, high power variations in inductive circuits, inhomogeneous distribution of voltage in the winding which involves heavy use of insulation and accelerated ageing;
- Mechanical causes: insulating materials or copper wear, eccentricity between the stator and the rotor, tangential and radial forces due to the presence of the magnetic field, vibration, frictional wear for bearings.
- Environmental reasons: contaminated environment (dust, humidity, air acidity, etc.), high ambient temperature.

Concerning the bearings and more specifically those used for machines fed by power inverters, their failure is mainly due to common mode voltage and current caused by capacitive and inductive coupling (high frequency stator flux created by the common

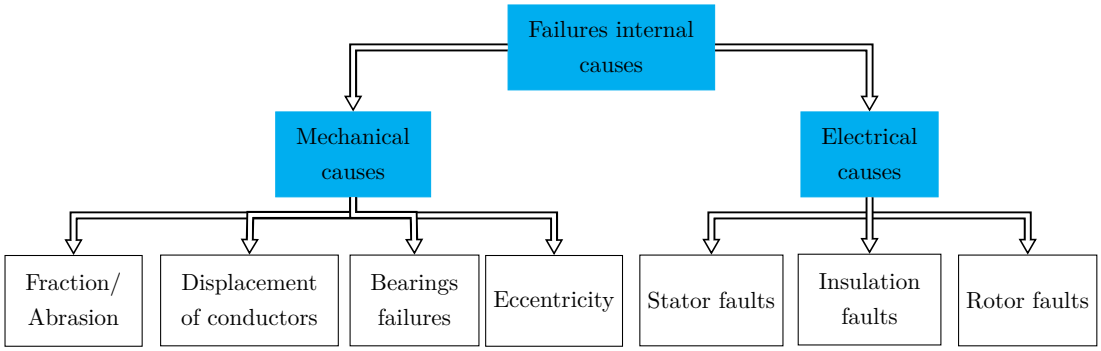

(a) Internal causes

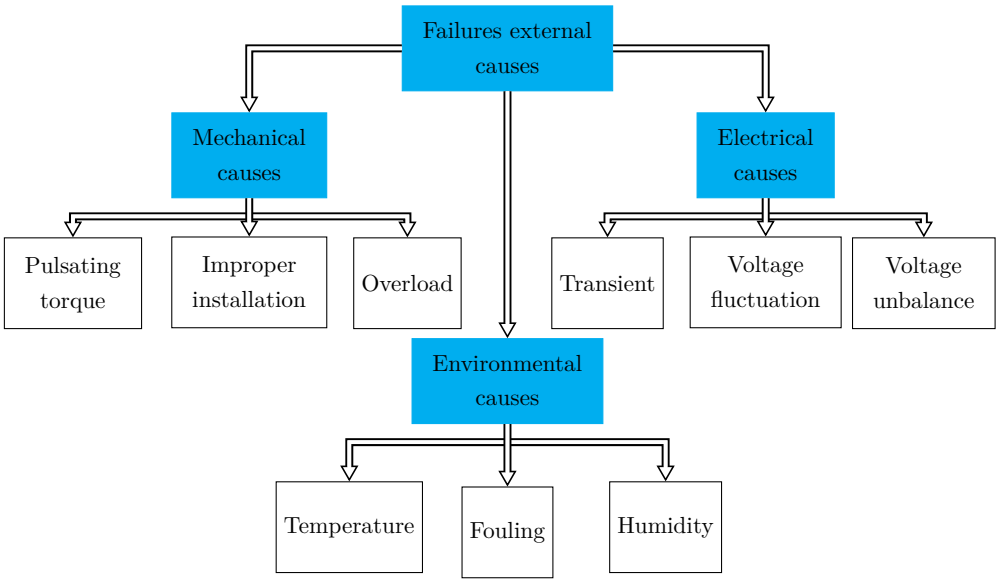

(b) External causes

Figure 1.4: Main causes of electrical machines failures [4].

mode currents flowing in the bearings causes a coupling of this flow and the circuit constituted by the rotor, the shaft, and the two bearings where current flow degrading bearings). These causes can be classified into two major categories; internal causes (Fig. 1.4(a)) and external causes (Fig. 1.4(b)).

These faults can have as consequences:

- Magnetic field distortion;
- Risk of stator damages;
- Overheating phenomena;

- Risks of electric arcs;
- Vibration effects;
- Abnormally high or destructive currents;
- Electromechanical torque oscillation;
- Noise and problem of additional torque.

The induction machine faults decrease significantly its availability and reliability. If undetected, these faults may cause catastrophic failures. To prevent these catastrophic failures, it is mandatory to define a maintenance strategy. In particular, it is suitable to develop a maintenance strategy that meets the requirements of machine availability and operational safety, at minimum cost.

1.3 Condition monitoring of induction machines

Shut-downs of plants due to unexpected breakdowns and failures are extremely costly in terms of time and money. Therefore, reducing operation and maintenance costs (O & M) is becoming a crucial motivation. Several techniques have been proposed for condition monitoring and faults detection in order to increase the reliability of such systems and therefore reduce the $O\&M$ costs. In order to achieve the condition-based maintenance, condition monitoring and faults detection strategies are required. The condition-based maintenance offers the possibility to schedule the maintenance activities. Moreover, the components may be used until their full life and defects may be detected at an early stage in order to prevent breakdowns and afterwards reduce downtime and maintenance cost. Even though such techniques require additional condition monitoring hardware and software, the overall maintenance cost is significantly decreased.

Induction machines are widely used in industrial applications such as traction, wind generation, medical equipment, and aircraft systems. Safety, reliability, efficiency and performance are major concerns that direct the research activities in the field of electrical machines. Hence, the emphasis is made on the electrical machines condition monitoring techniques with special reference to induction machines faults detection.

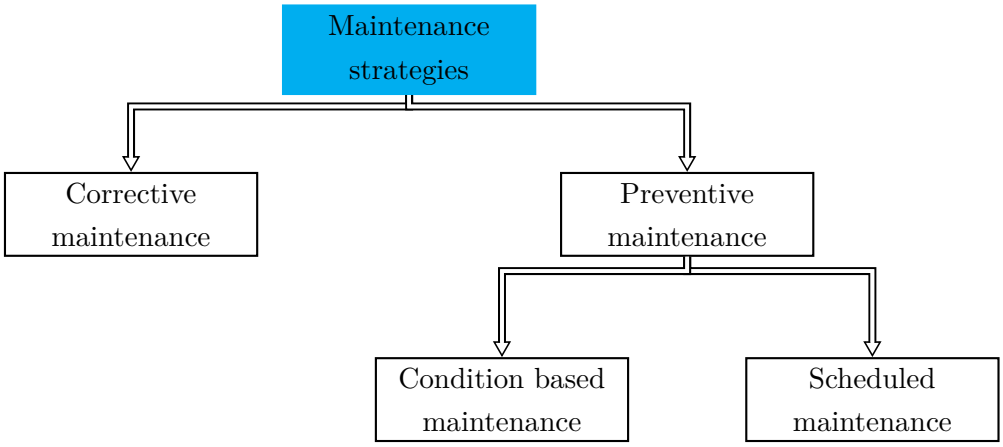

Figure 1.5: Classification of maintenance types [5].

1.3.1 Maintenance strategies

The maintenance is required for almost all types of machines in various industrial applications in order to improve the reliability and decrease operating and maintenance costs. The type of maintenance that is performed can be classified as either corrective or preventive maintenance (see Fig. 1.5). The corrective maintenance is carried out after a failure and is intended to repair the system. The corrective maintenance presents several drawbacks: risk of catastrophic failures, production loss, and reliability decrease. The preventive maintenance is intended to reduce the probability of failure and include scheduled maintenance and condition based maintenance. The scheduled maintenance is considered as cyclic maintenance strategy which is carried out at predetermined intervals, whereas the condition based maintenance tries to find the optimum time for carrying out the required maintenance actions by monitoring the current state of a specific component. The scheduled maintenance can be either clock-based or age-based maintenance. This means that components exposed to wear of fatigue are replaced regularly even if they are not at the end of their lifetime. Nevertheless, the scheduled maintenance presents a higher cost compared to corrective maintenance.

Consequently, the most interesting preventive maintenance is the condition based maintenance. The challenge concerning the condition based maintenance is to determine when the maintenance actions must be performed. This may be done by monitoring the condition of components in order to be able to plan maintenance actions

prior to failure and then minimize downtime and repair costs. This aspect is still under investigation and several methods have been proposed relying on various sensors and different measured quantities.

1.3.2 Induction machine condition monitoring and faults detection methods

Condition based maintenance of induction machine in industrial applications is based on performance and parameters monitoring. According to the sensor measurement used, most methods for induction machine monitoring could be classified into several categories: vibration monitoring, torque monitoring, temperature monitoring, oil/debris analysis, acoustic emission monitoring, optical fiber monitoring, and current/power monitoring [29, 30].

Most faults generated in the induction machine or associated components cause additional vibrations. A bearing faults, for instance, can generate a radial rotor movement and a shaft torque variation in the induction machine, and consequently vibration of the whole electromechanical drive [31, 32]. Vibration monitoring has been intensively studied in academia and widely used in industrial applications. Therefore, commercial condition monitoring and fault detection system are mostly performed based on vibration monitoring [33]. However, this technique is sophisticated and costly [34]. Moreover, the vibration sensors are mounted on the surface of the electromechanical drives and can be difficult to access during induction machine operation. These sensors are subject to failures which cause additional maintenance cost and affect the system reliability. For instance, it has been reported that sensor failures contribute to more than 14% of failures in wind turbine systems [23].

It has been demonstrated that most of faults lead to torque oscillations and rotor imbalance[35]. Hence, torque monitoring has been used to detect faults of the induction machine [31]. It has also been applied to detect generator stator windings short-circuit [36] in Wind Turbine Generator (WTG). However, the torque transducers need to be installed in the shaft to measure the electrical machine torque, which increase the cost and the complexity of the monitoring system.

Temperature measurement is generally performed for bearing faults monitoring. The IEEE standard 841 points out that the stabilized bearing temperature rise at the rated load should not exceed $45°C$ [37]. Therefore, abrupt temperature increase (for

example, the lack of lubrication) means the failure of the bearings. Much like, the temperature of gearbox oil in WTG should be in certain range during wind turbine rated operating conditions. The main drawback of temperature monitoring is that the measured temperature may be affected by multiple factors (environment temperature, stator current heating, and generator rotating speed) [38]. Oil/debris analysis is currently used for condition monitoring in industry [39]. In fact, analyzing the composition, content, size, and classification of wear particles in lubrication oil of bearings and many other components of induction machine allows to determine their health conditions. However, this method only works for high power rating electrical machines with oil lubricated bearings.

Many other methods exist such as acoustic emission monitoring [40], optical fiber monitoring, flux monitoring [41]. However, these techniques are more complicated in real-world applications and require additional sensors which increase the price/complexity of the monitoring system.

This survey of condition-based maintenance approaches highlights the need for a non-invasive, lower cost, most effective condition monitoring approach. A promising technique relies on current/power monitoring. It is based on current and/or voltage measurements that are already available for control and protection purposes. Hence, no additional sensors and acquisition devices are required. Moreover, current/voltage signals are reliable and easily accessible. It follows that current/power monitoring is of great economic interest and can be adopted by industry. Hence, several research activities have been focused on current based faults detection in electrical machines [42, 43, 44, 45]. Power measurements have also been investigated [46, 47]. However, the challenge in using current and/or voltage signals for condition monitoring is to propose signal processing techniques allowing to extract a fault detection and diagnosis criteria in stationary and non-stationary environment (variable speed drives, WTG, etc.) and intelligent diagnosis scheme able to classify faults and foresee a potential failure.

Among the various techniques presented previously, current analysis has several advantages since it is a non-invasive technique that avoids the use of extra sensors [45, 48, 49, 50]. Hence, most of the recent researches on induction machine faults detection has been directed toward electrical monitoring with emphasis on stator current supervision. In particular, the current spectrum is analyzed to extract the fre-

quency components introduced by the fault [12, 13]. In order to extract a useful information from current signals, advanced signal processing and statistical analysis are required.

The most common used techniques can be classified into two major classes: model-based and signal-based techniques [51]. The model-based methods aggregates two main approaches; theoretical analysis of the asymmetrical machine induced by fault and model development for online parameters tracking. It is used to measure the deviation between the model output and the actual machine output and then predict a potential failure signature. Model-based methods for fault detection were developed by using input and output signals and applying dynamic process models [52] as it is described by Fig. 1.6. Where, $\underline{U}$ corresponds to the inputs, $\underline{Y}$ denotes the outputs, and $\underline{N}$ is the noise. These methods are based, e.g., on parameter estimation, parity equations or state observers [6, 53]. The goal is to generate several symptoms indicating the difference between nominal and faulty status. Based on different symptoms fault diagnosis procedures are required to determine the fault by applying classification or inference methods.

The signal based model approaches (Fig. 1.7) have been also investigated. Since the induction machines are highly symmetrical electric systems because of rotating magnetic field, any kind of fault modifies their symmetrical properties. Characteristic fault frequencies therefore appear in the measured sensor signals, depending on the type of fault. Non-invasive monitoring is achieved by relying on easily measured electrical or mechanical quantities like current, voltage, flux, torque, and speed. The analysis of these signals allows to enhance the knowledge about a specific fault, its impact on intrinsic parameters of the machine, and its frequency signature. Most interestingly, this approach looks for fault-related frequencies in the measured electrical or mechanical quantities. It is performed using suitable signal conditioning and processing techniques for fault features extraction. Then, a fault decision algorithm is defined for classification purposes. Figure 1.7 describes the signal-based approach for fault detection based on stator current.

Compared to model based approaches, the signal based approaches do not require any knowledge about the machine parameters. Moreover, the fault detection procedure may be performed without any knowledge about the operating conditions of the

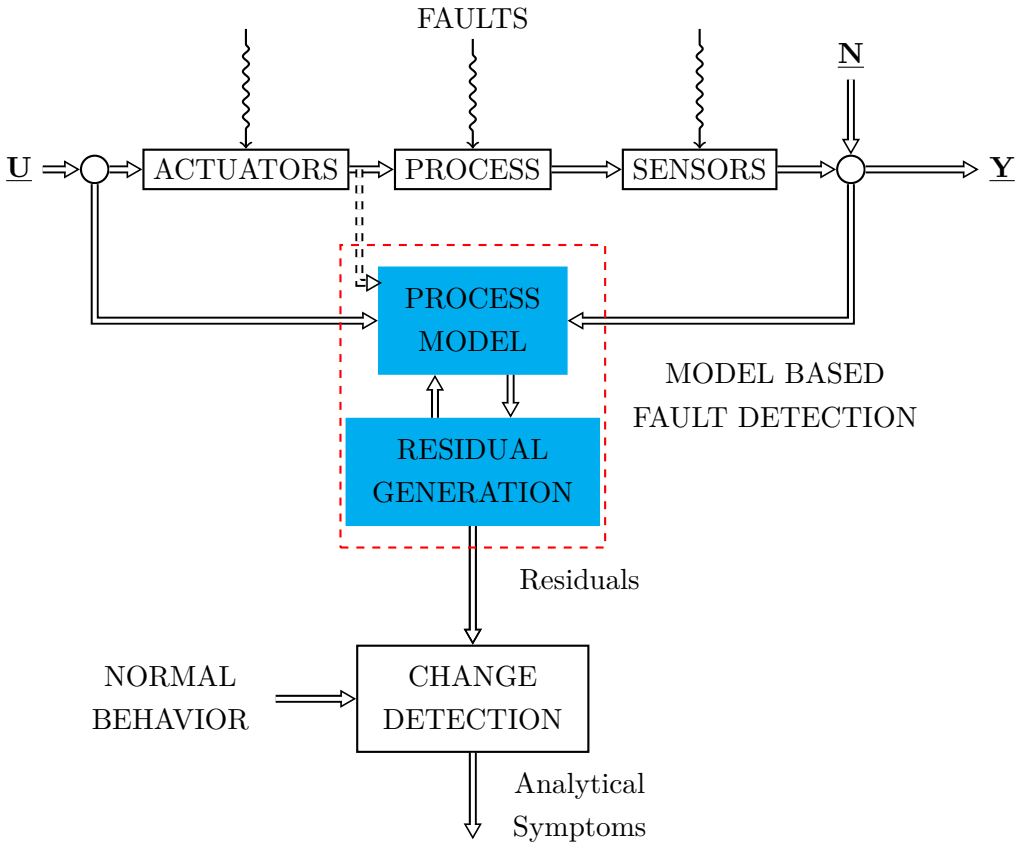

Figure 1.6: Scheme for model-based approaches for induction machine diagnosis [6].

machine. Since the stator currents are usually available and measured for other purposes related to protection and/or control, the stator current monitoring seems the most appropriate quantity to supervise. The fault detection based on stator current monitoring is known as motor current signal analysis (MCSA) [12]. For these reasons, in the following, we focus on the faults effects over the stator currents. Then, a state of the art review of the techniques used for stator current processing are presented. These approaches are used to process the output electrical currents in order to retrieve reliable diagnosis clues. Finally, The classification approaches are presented and discussed.

1.3.3 Faults effect over the stator current

The failures presented previously lead to various effects on intrinsic parameters and quantities of the electrical machine which can be classified in three major categories

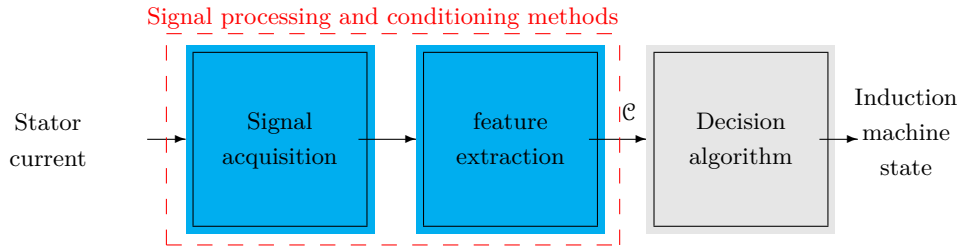

Figure 1.7: Signal-based approaches for induction machine diagnosis.

[54]:

- Faults leading to eccentricity between stator and rotor: bearing defects, shaft misalignment, centering defect;
- Failures introducing torque oscillations: mechanical load defect, bearing faults;
- Defects leading to disturbance in magnetomotive forces: stator short circuit defects, broken electrical connections in the stator, and magnets failure.

The effect of induction machine faults over the stator current has been widely investigated. Two major results could be presented:

- Introduction of additional frequencies on the current power spectral density depending on the type of fault and machine dimensions [12, 13];
- Phase and/or amplitude modulation of stator currents due to presence of specific fault [35, 54].

An induction machine is a highly symmetrical electromagnetic system. Hence, any fault in induction machines can cause a certain degree of asymmetry. For instance, Broken rotor bar induce the increase of resistance of the broken bar which leads to asymmetry of the resistance in rotor phases. Consequently, the broken bar induces asymmetry of the rotating electromagnetic field in the air gap, which introduces additional frequencies in the stator current. Most studies dealing with induction machines monitoring gives the expressions of these frequency harmonics without presenting any analytical model allowing to understand the mechanical and/or electrical faults effect on the stator current [12, 13]. In various works, numerical machine models accounting for faults have been developed allowing to understand the effect of some phenomena without presenting stator currents analytical model.

Concerning the signal-based approach for condition monitoring, several research activities have focused on faults related frequencies monitoring. In particular, stator faults detection have been widely investigated with special attention to short-circuits [55]. Effective fault detection procedure may combine the use of fault detection techniques and the monitoring of turn-to-turn insulation in order to prevent catastrophic failure. Motor current signal analysis (MCSA) has also been investigated for broken rotor bar and end-ring faults detection in induction machine [14]. Hence, diagnostic procedure has been proposed that relies on monitoring frequency components at $(1 \pm 2ks)f_s$, where s is the machine slip, f_s is the supply frequency, and $k \in \mathbb{N}$. For $k \neq 0$, these components are usually called sideband components [16, 56].

Mechanical faults detection based on stator currents have been widely investigated. Bearings defects have been typically categorized as distributed or local. Local defects cause periodic impulses in vibration signals. Amplitude and frequency of such impulses are determined by shaft rotational speed, fault location, and bearing dimensions (Fig. 1.8). The frequencies of these impulses are given by (1.1).

$$\begin{cases} f_{cd} = \frac{f_s}{2}\left(1 - \frac{d_r}{D_r}\cos(\alpha)\right) \\ f_{bd} = \frac{D_r}{d_r} f_s \left(1 - \frac{d_r^2}{D_r^2}\cos^2(\alpha)\right) \\ f_{id} = \frac{n_r f_s}{2}\left(1 - \frac{d_r}{D_r}\cos(\alpha)\right) \\ f_{od} = \frac{n_r f_s}{2d_r}\left(1 - \frac{d_r}{D_r}\cos(\alpha)\right) \end{cases} \tag{1.1}$$

where f_{cd} corresponds to fundamental cage frequency, f_{bd} is ball defect frequency, f_{id} is inner race defect frequency, and f_{od} corresponds to outer race defect frequency. f_r refers to shaft rotation frequency, n_r is the number of rollers, d_r is the roller diameter, D_r is the pitch diameter of the bearing, and α is the contact angle (Fig. 1.8).

In [57, 58], it has been demonstrated that the characteristic bearing fault frequencies in vibration can be reflected on stator currents. Since ball bearings support the rotor, any bearing defect will produce a radial motion between the rotor and the stator of the machine (air-gap eccentricity) which may lead to anomalies in the air-gap flux density. As the stator current for a given phase is linked to flux density, the stator current is affected as well by the bearing defect. The relationship between vibration frequencies and current frequencies for bearing faults can be described by (1.2).

$$f_{bng} = |f_s \pm k f_d| \tag{1.2}$$

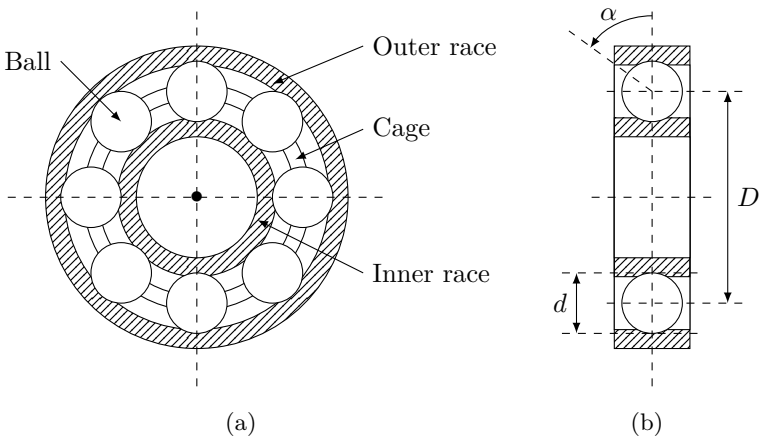

Figure 1.8: Bearing structure with main dimensions.

where f_s is the supply fundamental frequency, f_d is one of the characteristic vibration frequencies given above, and $k = 1, 2, 3, ...$

It is well established that for bearing single-point defects, the characteristic stator current fault frequencies are good fault indicators [58, 59]. In fact, by means of (1.2), it is possible to analyze the specific fault-related frequencies in order to find abnormalities in their amplitude values. There is a large number of papers dealing with the detection and diagnosis of bearing faults based on the stator current of the induction machine [59, 60, 61]. Extensive investigations have been conducted on single defects, while generalized roughness (lubrication defects, wear of bearings,etc.) is of great interest.

Eccentricity fault effect has been studied to model the fault impact on stator current [62, 63]. It has been proved, that under eccentricity faults, the stator currents contain the frequencies given by (1.3). It worth noting that when other mechanical problems exist torque oscillation characteristic frequencies may be hidden.

$$f_{ecc} = f_s \left| 1 \pm k \left(\frac{1-s}{p} \right) \right| \tag{1.3}$$

In [35, 54, 59, 64, 65], the authors have presented an analytical approach for the modeling of mechanical and bearing faults based on traditional magnetomotive force (MMF) and permeance wave approach for computation of the airgap magnetic flux density [66]. These studies have demonstrated three main results:

– A healthy induction machine already contains a great number of spectral components due to its supply voltage, rotor slotting and possible iron saturation (see Table 1.1). Where, f_r denotes the rotational frequency, f_c corresponds to fault frequency introduced by modified rotor MMF, and N_r is the number of rotor bars or rotor slots.

Table 1.1: Synopsis of stator currents frequency components under healthy conditions .

Stator current harmonics	Frequency ($l \in \mathbb{N}$)	origin
Fundamental frequency	f_s	Supply voltage
Time harmonics	$l \times f_s$	Harmonics of supply voltage PWM inverters
Rotor slot harmonics	$kN_r f_r \pm l f_s$	Modified airgap
Saturation harmonics	$f_s \pm 2k f_s$	Deformation of flux density
Torque/speed oscillation Eccentricity	$l f_s \pm f_c$ $l f_s \pm f_r$ $l f_s \pm f_r$	Modified rotor MMF Modified airgap Torque oscillation

– The mechanical faults may lead to eccentricity and load oscillation faults. The eccentricity fault is responsible of the amplitude modulation of the stator currents and the load oscillation leads to frequency modulation of the stator currents. The modulation frequency depends on the operating conditions of the machine and the fault severity. Therefore, the fault severity is proportional to modulation index.

– Depending on the defective components of the bearings, the stator currents are modulated (amplitude and/or frequency modulation) [67]. Table 1.2 gives a summary of bearing related frequencies in the stator current spectrum.

In general way, in presence of fault, the current is sinusoidally frequency or amplitude modulated. Based on this signal modeling approach, it seems that the most

Table 1.2: Summary of bearing fault-related frequencies: comparison of two studies.

Faulty bearing components	According to Schoen [58]	According to Blodt [59]	
		Eccentricity	Torque oscillations
Outer raceway	$f_s \pm kf_{od}$	$f_s \pm kf_{od}$	$f_s \pm kf_{od}$
Inner raceway	$f_s \pm kf_{id}$	$f_s \pm f_r \pm kf_{id}$	$f_s \pm kf_{id}$
Ball defect	$f_s \pm kf_{bd}$	$f_s \pm f_{cage} \pm kf_{bd}$	$f_s \pm kf_{bd}$

adapted tool to extract fault indicator is demodulation techniques. However, this modeling approach suffers from many restrictive assumptions and lack of generality since it cannot be applied for all type of faults.

The two approach seems to be different. However, we can consider reasonably that the two approaches are equivalent since both of them assume introduction of frequency components in the stator currents due to faults. Moreover, the modulation approach is more restrictive than the first one since it supposes the upper sidebands and lower sidebands have the same amplitude. Furthermore, in the case of phase modulation, the amplitude of sidebands is governed by Bessel functions [54].

A summary of induction machine stator current faults-related frequencies is presented in Table 1.3. Where p is the pole pair number, s is the per unit slip, f_s is the supply fundamental frequency, and f_x is the fault characteristic frequency. These frequencies are used to monitor the induction machines using the stator currents. When a fault occurs, the amplitude at these frequencies increases and reveal abnormal operating conditions.

Several spectral estimation approaches have been proposed for fault detection based on stator currents in stationary and non-stationary environment. These fault related signatures depend on the operating conditions of the induction machine. In fact, the fundamental frequency, the rotational speed and the fault related frequency may vary with respect to time. Then suitable techniques must be developed in order to propose reliable induction machine faults detection procedure. Hence, appropriate signal processing approaches have been proposed depending on the signal nature (mono-component signal, multi-component signal, etc.), stationarity, harmonic signals, multi-dimensional signals, etc.

Table 1.3: Induction machine faults-related frequencies on stator current PSD [12, 13, 14].

Induction machine fault	Fault related frequency	Parameters
Bearing Damage	$\|f_s \pm k f_d\|$	$k = 1, 2, 3, ...$
Broken Rotor Bars	$f_s(1 \pm 2ks)$	$k = 1, 2, 3...$
Air Gap Eccentricity	$f_s \left\|1 \pm k\left(\frac{1-s}{p}\right)\right\|$	$k = 1, 2, 3, ...$
Load oscillation	$f_s \left[1 \pm k\left(\frac{1-s}{p}\right)\right]$	$k = 1, 2, 3, ...$

1.3.4 Fault detection techniques

Depending on the modeling approach adopted, the appropriate signal processing for fault detection and diagnosis may be different. Hence, power spectral density estimation techniques and demodulation techniques have been employed for fault feature extraction. The PSD estimation techniques allow to estimate the frequency signature, while the demodulation techniques highlight the modulation presence. Afterwards, several classification techniques have been proposed for decision making. The following section focuses on the techniques used to process the output electrical currents in order to retrieve reliable diagnosis indices related to the faults. It presents a comprehensive bibliography with special reference on condition monitoring of induction machine through stator current processing. The literature on rotating electrical machines condition monitoring is abundant. Several books have been published [68, 69] as well as journal papers [12, 13, 29].

1.3.4.1 Feature extraction

Spectral estimation: It has been shown in section 1.3.3 that fault monitoring could be performed by supervising the current spectrum. In particular, it has been demonstrated that faults introduce additional spectral components in the stator current around the supply frequency [12, 13]. In steady-state conditions, techniques based

on conventional PSD estimators have been employed. These techniques can be classified into two categories: the conventional periodogram and its extensions and the high resolution techniques such as MUSIC and ESPRIT [7]. In non-stationary environment, the time-frequency/time-scale techniques have been proposed. It allows to track the fault-related frequency in the time-frequency plane. These representations allow to monitor evolution of the fault and consequently its severity.

Demodulation techniques: The demodulation techniques have also been widely investigated. These techniques include the synchronous demodulator [70], the Concordia transform [71], Hilbert transform [44, 72, 73, 74], principal component analysis [45] and other approaches [75]. Once the demodulation has been performed, demodulated signals are further processed in order to measure failure severity.

1.3.4.2 Classification approaches

In order to perform an induction machine faults detection based on stator currents monitoring, a further step is required to perform a reliable and efficient diagnosis. The artificial intelligence (AI) techniques have been proposed as useful tools to improve the diagnosis, mainly during the decision process [76, 77, 78, 79]. The AI techniques include several sophisticated approaches such as artificial neural networks [80, 81], support vector machine [82, 83], Fuzzy logic [76, 84]and many others. The genetic algorithm has been used to enhance the fault detection performance using the fuzzy logic [85].

ANN technique: Artificial neural networks (ANNs) are computational models whose design is schematically inspired by the operation of biological neurons of human brain and consists of simple arithmetical units connected in a complex architecture [79, 86]. The artificial neural networks need actual case examples used for learning which is called learning database [87]. The learning database must be sufficiently large depending on the structure and complexity of the problem studied. However, a large learning database leads to over-fitting problem and thus degrades the neural networks performance (neural network loses its ability to generalize). Indeed, there is a trade-off between generalization and over-training.

Several research papers have dealt with condition monitoring and faults diagnosis of electrical machines based on ANNs [80, 81]. The ANNs have been applied for several tasks such as pattern recognition, parameter estimation, operating condition clustering, faults classification, and incipient stage fault prediction.

SVM technique: Support vector machines (SVM) are a set of supervised learning techniques used to solve problems such as input data clustering, pattern recognition and regression analysis [87]. The SVM is based on developed statistical learning theory. Indeed, the theoretic principal of SVM comprises two steps:

1− Non-linear transform (ϕ) of input data to high dimensional space.

2− Determination of optimal hyperplane or set of hyperplanes in a high- or infinite-dimensional space allowing to linearly classify the input data in this high-dimensional space.

The SVM are able to work with large number of data and a small number of hyper-parameters. Similarly to ANNs, the SVM requires a learning stage. Various applications in academia have proven that such techniques are well suited to deal with electrical machines diagnosis [82, 83]. In [88], several statistical features have been extracted from vibration signals and used as input for SVM in order to perform a classification allowing to distinguish faulty (rolling elements faults) from healthy case for different faults severity.

Fuzzy logic: Fuzzy logic is a form of probabilistic logic; it is aimed at a formalization of modes of reasoning that is approximate rather than exact. In contrary to traditional binary sets, fuzzy logic variables may have truth value that ranges in degree from 0 to 1. Fuzzy logic is much more general than traditional combinational logic. The greater generality of fuzzy logic is needed to deal with complex problems in the realms of search, question-answering decision and control. Fuzzy logic provides a foundation for the development of new tools for dealing with natural languages and knowledge representation.

Fuzzy logic systems for diagnosis purposes are able to process linguistic variables via fuzzy if-then rules. Adaptive fuzzy logic systems use the learning capabilities of ANNs or genetic algorithms to adjust model parameters and afterwards enhance the global

system performance [89]. In [90] neural networks and fuzzy logic are combined together for the detection of stator inter-turn insulation and bearing wear faults in single-phase induction motor. Fuzzy logic for diagnosis can be applied to perform system behavior modeling, faults classification, predicting abnormal operating conditions [76, 84, 91, 92].

The main drawback of such techniques is the initial training phase which requires a large set of stator currents database for different state conditions and various conditions. This phase is critical for optimal operation and may be misleading or produce results limited to a set of systems.

The decision algorithms presented herein, are used for faults classification and severity measurement. However, the AI techniques performance depends on the feature extraction used to process the stator current (system Garbage Input, Garbage Output). For this reason, in this thesis, we focus on the feature extraction techniques in stationary and non-stationary operating conditions.

1.4 Stator current processing for induction machine faults features extraction

In the following, commonly used feature extraction techniques are presented. Specifically, we focus on the stationary techniques, the demodulation techniques, and the time-frequency/time-scale techniques.

1.4.1 Stationary techniques

As discussed earlier, in steady-state conditions, several studies have shown the interest of monitoring the spectral components in the stator current in order to perform a fault detection and diagnosis. Hence, many studies have proposed spectral estimation techniques to detect and characterize different mechanical and electrical faults.

In this section, to illustrate these techniques properties, we use a sinusoidal signal with upper sideband and lower sideband as follows

$$x[n] = A_c \cos(2\pi f_s t + \phi_c) + A_l \cos(2\pi (f_s - f_c) t + \phi_l) + A_u \cos(2\pi (f_s + f_c) t + \phi_u) + b[n] \quad (1.4)$$

where $f_s = 50\ Hz$ and $f_c = 10\ Hz$, $F_s = 1$ kHz, and $N = 1000$.

The techniques presented herein can be classified into two mean categories: the non-parametric techniques (precisely the periodogram and its extensions) and high resolution techniques.

1.4.1.1 Periodogram and its extensions

The power spectral density (PSD) $P_x(f)$ of discrete-time process is defined as the Fourier transform of its autocorrelation function [93]. The periodogram is a PSD estimator of a complex discrete-time wide sense stationary random process $x[n]$ and it is defined as follows

$$\widehat{P}_x(f) = \frac{1}{N}\left|\sum_{n=0}^{N-1} x[n]e^{\frac{-j2\pi fn}{F_s}}\right|^2 \tag{1.5}$$

where F_s is the sampling frequency and N is the number of samples. Hence, the frequency resolution is equal to the inverse of the signal acquisition length.

The periodogram is usually implemented using the FFT algorithm since it rapidly computes the Discrete Fourier transform (DFT). It should be noted that the periodogram is biased (the distance between the average of the estimates, and the single parameter being estimated is not zero) and inconsistent estimator (the variance does not decrease to zero when the data record length goes to zero) of the power spectral density [94]. This can be overcome if several realizations $x_m[n]$ of the same random process $x[n]$ are available. This is performed using Welch periodogram; the signal is split up into overlapping segments, the periodogram of each segment multiplied by a time window is computed and then averaged. Hence, the Welch periodogram is defined as:

$$\widehat{P}_w(f) = \frac{1}{L}\sum_{k=1}^{k=L} \widehat{P}_{xw}^{(k)}(f) \tag{1.6}$$

where $\widehat{P}_{xw}^{(k)}$ represents the periodogram of the windowed signal $x[n]w[n-\tau k]$, where $w[.]$ is a time window (Hanning, Hamming, etc.) and τ is a time delay.

For illustration purpose, Fig. 1.9(a) shows the periodogram and Fig. 1.9(b) depicts the Welch periodogram of the signal given by (1.4). The periodogram was computed using a signal length of 10s, a sampling frequency of 1kHz, and the Blackman window. The Welch method splits the data into eight overlapping segments, each with a 50% overlap, computes the modified periodograms of the overlapping segments, and averages

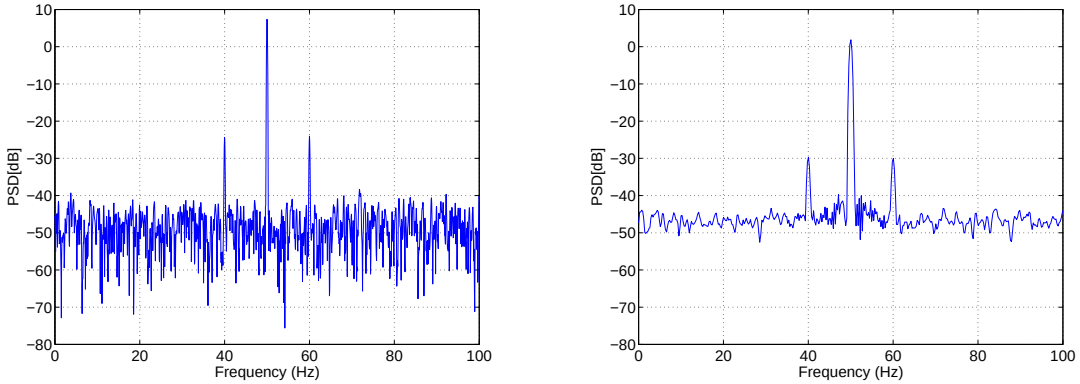

(a) Periodogram.

(b) Welch periodogram.

Figure 1.9: Periodogram and Welch periodogram of three sinusoids in noise.

the resulting periodograms to produce the the PSD estimate. Each segment is windowed with a Hamming window that is the same length as the segment. In both cases the SNR was equal to 20.

As it can be noted from these figures, the Welch periodogram enhance the performance of the estimation by decreasing the bias and the variance. Unfortunately, it decreases the spectral precision and resolution due to segmentation. In order to increase the frequency resolution, the signal acquisition time must be increased. However, the stationary signal assumption may no longer hold if the signal acquisition time is too long. The periodogram and its extensions are non-parametric methods, i.e. they do not require any a priori knowledge about the signal.

The classical periodogram have been widely applied for fault detection in induction machine as it can be seen from these state of the art review papers [12, 13]. The main drawback of this technique relies on its statistical performance and frequency resolution limitations [56]. The frequency resolution obtained by the periodogram is defined as [95]

$$\Delta f = \frac{F_s}{N} \tag{1.7}$$

where F_s is the sampling frequency and N is the number of samples.

To improve the statistical properties of the periodogram, several extensions have been employed such as the Bartlett [56] and the Welch techniques[56, 96]. Moreover, the so-called Zoom-FFT (ZFFT) technique [97, 98] has been introduced to improve

the frequency precision in a specified frequency range without increasing the computational complexity. Nevertheless, the periodogram and its extensions suffer from a low frequency resolution which is not suited especially for broken rotor bars detection [56] since the sidebands frequency and the fundamental frequency are so close and difficult to distinguish. It seems from this discussion that a lengthy signal may give good resolution, but the signal stationarity may not hold when the signal is too long.

1.4.1.2 High resolution techniques

If an *a priori* signal model is assumed, parametric methods can be employed to improve the frequency resolution. In fact, parametric methods can yield higher resolutions than non-parametric methods in cases when the signal length is short. This is due to their ability to resolve spectral lines separated in frequency by less than $\frac{1}{N}$ cycles per sampling interval, which is the resolution limit for the classical periodogram-based methods [95]. These techniques are generally called high-resolution methods and include two sub-classes: the linear prediction methods and the subspace techniques.

The linear prediction class contains several algorithms like the Prony, Yule-Walker, and autoregressive-moving-average (ARMA) methods [95]. These methods use a different approach to spectral estimation; instead of trying to estimate the PSD directly from the data, they model the data as the output of a linear system driven by white noise, and then attempt to estimate the parameters of that linear system. They are based on the estimation of a linear time invariant system from a measurement data corrupted by additive noise using ARMA model. In [99], the Prony method has been demonstrated for signal analysis in power electronics. It has been proven that when using both high-resolution methods, Prony and min-norm, the estimation accuracy in most cases is better than when using the Fourier algorithm. The use of autoregressive stator current modeling for bearing fault detection has been investigated in [100]. This method begins by filtering the stator current to remove most of the significant frequency content unrelated to bearing faults. Afterwards, the filtered stator current is used to train an autoregressive signal model. As bearing health degrades, the modelled spectrum deviates from its baseline value; the mean spectral deviation is then used as the fault index. Unfortunately, these methods are more suited for continuous PSD where the frequency content does not vary abruptly. Unfortunately, the faults signature frequency bins introduced by a specific fault (line spectra) given by table 1.3 may vary

abruptly. Consequently, these techniques are out of scope of this manuscript and then not explicitly covered in this text.

The subspace class includes the MUSIC and ESPRIT approaches [95]. These techniques are considered as parametric methods for line spectra estimation. However, as these techniques do not exploit all the information about the fault signature, we refer to them as semi-parametric techniques. The subspace approaches assume that the noise is white Gaussian noise with mean zero and variance σ^2. Moreover, it assumes that the number of frequency bins is known (it is noted P in the following). These methods relies on the decomposition of the observation space into two subspaces, the signal subspace and the noise subspace. Pisarenko have demonstrated that the signal subspace is spanned by the eigenvectors corresponding to the greatest eigenvalues of the autocorrelation matrix, and that the frequency content can be estimated by using the orthogonality between the signal and noise subspaces.

The MUSIC (MUltiple SIgnal Characterization) is based on the eigenvalues decomposition of the covariance matrix $\mathbf{R}_x$ of measurement data $\mathbf{x}[n] = [x[n], x[n+1], \ldots, x[n+M-1]]^T$ and the computation of the associated eigenvectors. The covariance matrix $\mathbf{R}_x$ and its eigenvalues decomposition (EVD) can be written as follows

$$\mathbf{R}_x = E\left\{\mathbf{x}[n]\mathbf{x}^H[n]\right\} = \mathbf{U}\mathbf{\Lambda}\mathbf{U}^H \tag{1.8}$$

where $E\{.\}$ denotes the statistical expectation, $(.)^H$ refers to Hermitian matrix transpose, $\mathbf{U}$ is formed by the M orthonormal eigenvalues of $\mathbf{R}_x$, and $\mathbf{\Lambda}$ is a diagonal matrix containing the corresponding eigenvalues λ_k listed in order of decreasing magnitude.

Let us decompose $\mathbf{U}$ as

$$\mathbf{U} = [\mathbf{S}\ \mathbf{G}] \tag{1.9}$$

where $\mathbf{S}$ is formed by the eigenvectors corresponding to the P most significant eigenvalues λ_k and $\mathbf{G}$ is formed by the eigenvectors spanning the noise subspace [101]. In practice, the samples covariance matrix $\mathbf{R}_x$ is unknown and should be estimated from the available data. Since $\mathbf{x}[n]$ has length M and we have N observations of $x[n]$, we can thus construct a set of $G = N - M + 1$ different sub-vectors $\{\mathbf{x}(n)\}_{n=0}^{G-1}$. Let

$$\widehat{\mathbf{R}}_x = \frac{1}{G}\sum_{n=0}^{G-1}\mathbf{x}[n]\mathbf{x}[n]^H \tag{1.10}$$

be the estimator of the covariance matrix and $\widehat{\mathbf{U}} = [\widehat{\mathbf{S}}\ \widehat{\mathbf{G}}]$ be its corresponding eigenvectors. The MUSIC pseudo-spectrum algorithm determines frequency estimates as the locations of the P highest peaks of the cost function

$$\mathcal{J}(f) = \frac{1}{\left\|\mathbf{a}^H(f)\widehat{\mathbf{G}}\right\|_F^2} \tag{1.11}$$

where $\|.\|_F$ denotes the Frobenius norm and the column vector $\mathbf{a}(f)$ is given by

$$\mathbf{a}(f)^H = [1, e^{\frac{j2\pi f}{F_s}}, e^{\frac{2j2\pi f}{F_s}}, \ldots, e^{\frac{(M-1)j2\pi f}{F_s}}] \tag{1.12}$$

This function is called pseudo-spectrum since it indicates the presence of sinusoidal components in the studied signal, but it is not a true PSD (it does not give the amplitude of these frequency bins). Figure 1.10(a) gives the pseudo-spectrum of the signal used for illustration in this section using MUSIC. However, although the performance advantages of MUSIC are substantial, they are obtained at a cost in computation (searching over parameter space) and storage. Moreover, its performance depends on the covariance matrix estimator and the SNR.

To reduce computational cost of the spectral estimation, ESPRIT (Estimation of Signal Parameters via Rotational Invariance Techniques) has been proposed. In fact, this technique relies on an matrix eigenvalues computation, which allows to extract directly the frequency content, rather than leading to optimization problem like the MUSIC procedure.

ESPRIT estimates the frequencies as $-\angle(\widehat{\nu}_k)$, where $\{\widehat{\nu}_k\} = [\psi_1, \psi_2, \ldots, \psi_P]$ are the eigenvalues of the matrix $\mathbf{\Phi}$ [102]

$$\widehat{\mathbf{\Phi}} = (\widehat{\boldsymbol{S}}_1^H \widehat{\boldsymbol{S}}_1)^{-1} \widehat{\boldsymbol{S}}_1^H \widehat{\boldsymbol{S}}_2 \tag{1.13}$$

where, $\widehat{\boldsymbol{S}}_1$ and $\widehat{\boldsymbol{S}}_2$ are estimated from the available signal samples as follows

$$\begin{array}{l} \widehat{\boldsymbol{S}}_1 = [I_{M-1}\ \ 0]\widehat{\boldsymbol{S}} \\ \widehat{\boldsymbol{S}}_2 = [0\ \ I_{M-1}]\widehat{\boldsymbol{S}} \end{array} \tag{1.14}$$

where, $\widehat{\boldsymbol{S}}$ is the estimate of eigenvectors corresponding to the signal subspace $\boldsymbol{S}$. Finally, the frequency estimates $\widehat{f_i}$ for $1 < i < P$ are calculated as

$$\widehat{f_i} = \frac{\angle(\psi_i)}{2\pi} \tag{1.15}$$

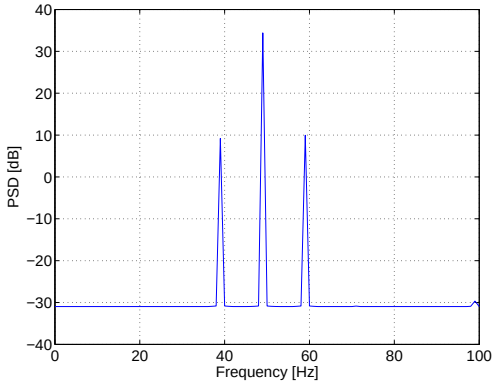

(a) Pseudospectrum via MUSIC .

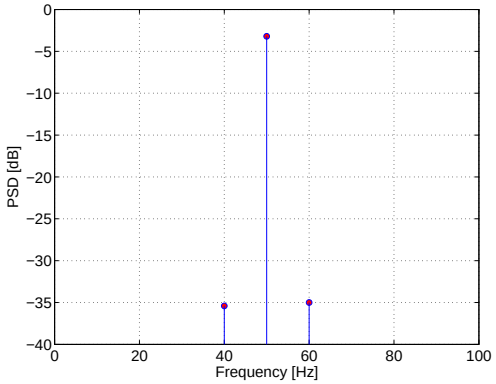

(b) Spectrum via ESPRIT.

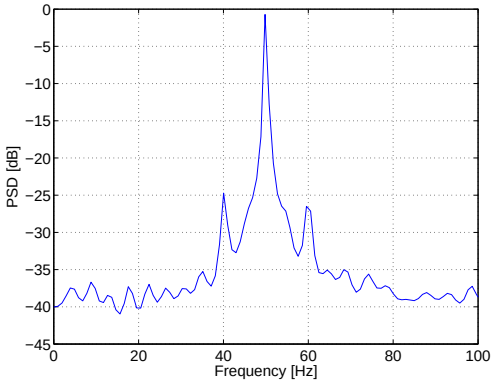

(c) Spectrum via Prony.

Figure 1.10: High resolution techniques for spectrum estimation of three sinusoids in noise.

where $\angle(.)$ corresponds to the phase. Figure 1.10(b) gives the PSD estimation based on ESPRIT. Since the ESPRIT procedure gives only the frequency content location, least squares have been used for frequency bins amplitude estimation [93].

The MUSIC and ESPRIT algorithms require the knowledge of frequency signal dimension order (number of sinusoids in noise). If it is unknown, the information theoretic criteria [103] such as Akaike Information Criterion (AIC) or Minimum Description Length (MDL) can be used.

The Prony method is based on a procedure for determining the coefficients of a linear combination of exponential functions from uniformly spaced samples. For the theoretical considerations one can refer to [94, 95]. Figure 1.10(c) gives the PSD estimation

based on the Prony method. It can be observed that the Prony method performance are equivalent to those of the MUISC and ESPRIT.

Applications for induction machine faults diagnosis are available in [30, 104, 105, 106]. In [106], the MUSIC and ESPRIT algorithm and a zooming method were combined to reduce the computational cost of the spectral estimator. The ESPRIT has been combined with Hilbert transform for broken rotor bars fault detection in [107, 108]. However, the performance of such techniques decrease significantly if the noise level increases. Moreover, these techniques estimate the frequency locations, but does not allow to measure their amplitude which is mandatory for induction machine fault detection algorithm and fault severity measurement.

1.4.2 Demodulation techniques

It has been shown in section 1.3.3 that many types of failures may lead to stator-currents phase or amplitude modulation with modulation index directly related to failure severity [35, 67, 109, 110]. Therefore, a straightforward technique to process the stator currents is to use the demodulation techniques. Demodulation techniques can be classified into two major categories; the mono-dimensional and multi-dimensional techniques. The former requires à 1-D signal , while the latter requires a 3-D signal in order to compute the IA and IF. The mono-dimensional techniques include the synchronous demodulator,the Teager energy operator, and Hilbert transform. The multi-dimensional methods include the Concordia transform and Principal Component Analysis.

Let us denote $\mathbf{x}[n] = [x_1[n], x_2[n](t), x_3[n]]^T$ the 3×1 vector which contains the stator currents. Most demodulation techniques rely on the estimation of the analytical signal of the real-valued signal. If $x[n] = a[n]\cos[\Phi[n]]$ is a real-valued signal, the corresponding analytic signal is given by

$$z[n] = a[n]e^{j\Phi[n]} \tag{1.16}$$

Once the analytic signal is computed, the instantaneous amplitude $a[n]$ and the instantaneous frequency $f[n]$ can simply be estimated as

$$\widehat{a}[n] = |z[n]| \tag{1.17}$$

$$\widehat{f}[n] = \frac{1}{2\pi}(\angle(z[n+1]) - \angle(z[n])) \times F_s \tag{1.18}$$

where F_s is the sampling rate and where $|.|$ and $\angle(.)$ is the modulus and the argument of complex-valued signal $z[n]$, respectively.

For illustration purposes, we propose to apply the studied methods on sinusoidally amplitude and frequency modulated signals described as follows

$$x_1[n] = (1 + \alpha\cos(2\pi f_c n + \phi_1)) \times \cos(2\pi f_s n + \beta\cos(2\pi f_c n + \phi_2) + \phi) \tag{1.19}$$

where, the frequencies f_c, f_s are set to 10 Hz and 50 Hz respectively.

In this section, we consider a three-phase system. In the presence of a fault, all three line currents $x_1[n]$, $x_2[n]$, and $x_3[n]$ are simultaneously modulated, and the currents can be expressed as follows

$$\begin{aligned} x_1[n] &= \alpha_1 a[n]\cos(\Phi[n]) \\ x_2[n] &= \alpha_2 a[n]\cos(\Phi[n] - \frac{2\pi}{3}) \\ x_3[n] &= \alpha_3 a[n]\cos(\Phi[n] - \frac{4\pi}{3}) \end{aligned} \tag{1.20}$$

where $a[n]$ and $\Phi[n]$ are the instantaneous amplitude and the instantaneous phase respectively.

In the following the mono-dimensional techniques are described first. In this case, a single phase stator current is used and it is noted $x[n] = x_1[n]$. Afterwards, a multi-dimensional approaches are presented and properties highlighted for the three-phase stator currents given by (1.20).

1.4.2.1 Synchronous demodulator

The synchronous demodulator is a well known as AM and PM signals demodulator. In the case of the synchronous demodulator, let's consider the following assumptions [7]:

– $\mathcal{H}_1$: $\Phi[n] = 2\pi f_0 n + \varphi[n]$
– $\mathcal{H}_2$: The carrier frequency f_0 is supposed known.

The synchronous demodulator principle is illustrated by Fig. 1.11. Mathematically speaking, the synchronous demodulator is given by

$$x_1^s[n] = 2 \times h[n] * x[n] \cos(2\pi f_0 n/F_e) \quad (1.21)$$

$$x_2^s[n] = -2 \times h[n] * x[n] \sin(2\pi f_0 n/F_e) \quad (1.22)$$

where the symbol " $*$ " denotes the convolution operator and $h[n]$ is a low-pass filter whose frequency response is given by

$$\mathcal{H}(f) = \begin{cases} 1 & \text{if } f \leq f_0 \\ 0 & \text{if } f > f_0 \end{cases} \quad (1.23)$$

Under a proper filtering, it can be shown when $a[n]$ and $\phi[n]$ do not vary too fast that [111] (see APPENDIX C)

$$x_1^s[n] = a[n] \cos(\varphi[n]) \quad (1.24)$$

$$x_2^s[n] = a[n] \sin(\varphi[n]) \quad (1.25)$$

Therefore the discrete time analytical signal is given by

$$z^s[n] = x_1^s[n] + j x_2^s[n] \quad (1.26)$$

$$= a[n] e^{j\varphi[n]} \quad (1.27)$$

For illustration purposes, the instantaneous amplitude and instantaneous frequency of the signal in (1.19) is given by Fig. 1.12. The filter used in this simulation is the

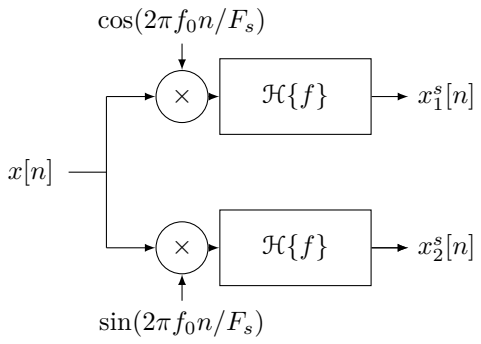

Figure 1.11: Synchronuous Demodulator.

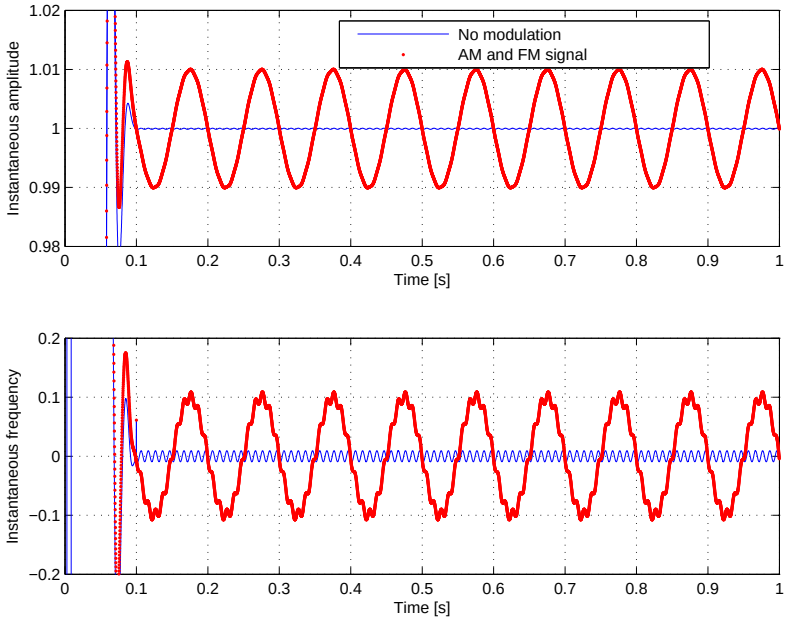

Figure 1.12: Instantaneous amplitude and frequency based on synchronous demodulator.

infinite impulse response (IIR) filter with cut-off frequency equal to 100 Hz. One of the drawbacks is the filtering stage tuning and a long time before convergence as it can be seen in Fig. 1.12. Moreover, the filtering stage may lead to additional oscillations in the estimated instantaneous amplitude or instantaneous phase as it can be seen from Fig .1.12.

The synchronous demodulator has been used for multistage gearbox diagnosis using amplitude demodulation of the current waveform in [70].

1.4.2.2 Hilbert transform

The Hilbert transform (HT) is a popular technique in signal processing for the estimation of the analytical signal. For a discrete signal $x[n]$, the discrete formulation of the Hilbert transform is given by [112]

$$x^h[n] = x[n] * h[n], \tag{1.28}$$

where

$$h[n] = \begin{cases} 0 & \text{for n even,} \\ \frac{2}{\pi n} & \text{for n odd.} \end{cases} \tag{1.29}$$

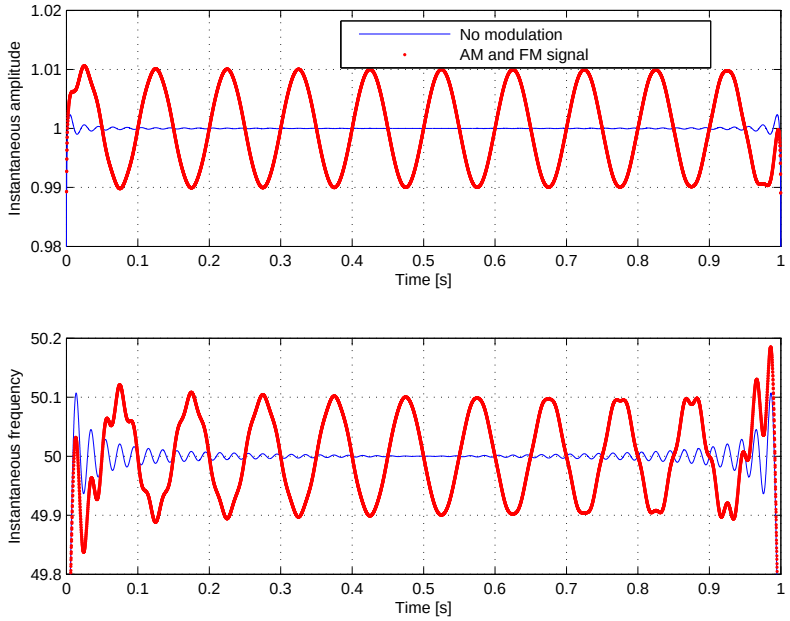

Figure 1.13: Instantaneous amplitude and frequency based on Hilbert transform.

The HT is widely used in modulation theory [113]. The Bedrosian theorem dealing with Hilbert transform of two real functions product, has shown that the uniqueness of the instantaneous frequency and the instantaneous amplitude is satisfied only if the spectra of the instantaneous frequency and the sinus of the instantaneous phase are disjoint [114]. When $\Phi[n]$ and $a[n]$ do not vary too fast, the analytical signal $z^{(h)}[n]$ associated with $x[n]$ is defined as [115]

$$z^{(h)}[n] = x[n] + jx^h[n] = a[n]e^{\Phi[n]} \tag{1.30}$$

The Hilbert transform can be computed for a real valued N-point discrete time signal efficiently using the FFT algorithm [116]. Once the analytical signal is computed, the IF and IA are extracted based on (1.18). Figure 1.13 gives the IA and IF for the signal described by (1.19). This figure illustrates one of the most disadvantages of HT which is the border effect. Moreover, the Hilbert transform is very sensitive to noise. The Hilbert transform has been employed for MCSA to detect eccentricity and bar breakages in transient conditions in [117, 118]. In [72] the Hilbert transform has been used to process the stator current in PMSM to diagnose demagnetization.

1.4.2.3 Teager energy operator

The Teager energy operator (TEO) allows tracking the instantaneous frequency (IF) and the instantaneous amplitude (IA) of a modulated signal without computing the analytical signal [119]. The discrete-time TEO is given by [120]

$$\Psi(x[n]) = x^2[n] - x[n+1]x[n-1] \tag{1.31}$$

It can be noticed that the TEO is local operator which allows to capture the energy fluctuations with good time resolution (requires only three samples (x[n-1], x[n], and x[n+1])). In [120], the authors have presented an estimator of the IA and the IF of a signal based on the TEO, which is called Energy Separation Algorithm (ESA):

$$a[n] \approx \sqrt{\frac{\Psi[x[n]]}{1-\left(1-\frac{\Psi[x[n]-x[n-1]]}{2\Psi[x[n]]}\right)^2}} \tag{1.32}$$

$$f[n] \approx \frac{1}{2\pi}\arccos\left(1-\frac{\Psi\left[x[n]-x[n-1]\right]}{2\Psi[x[n]]}\right) \tag{1.33}$$

The estimation of the instantaneous frequency and instantaneous amplitude of the proposed signal in (1.19) based on TEO is displayed in Fig. 1.14. It can be observed that the TEO tracks correctly the IF and IA of the modulated signals.

The ESA exhibits interesting property since it is less computationally demanding. Moreover, it has better time resolution than other demodulation techniques. The main drawback of this operator is its sensitivity to noise or to model mismatch. Moreover, it assumes that the estimated IF does not vary too fast or too greatly compared to carrier frequency. The ESA has been used for bearing faults detection based on the vibration signals in [121]. In [122], the Teager-Kaiser energy operator have been investigated for faults detection in induction machine with broken rotor bars, mixed eccentricity, and single-point bearing faults based on the stator current.

1.4.2.4 Concordia transform approach

Concordia transform (CT) is a multidimensional linear transform which allows to extract a two orthogonal components from a three-phase stator currents. In the case

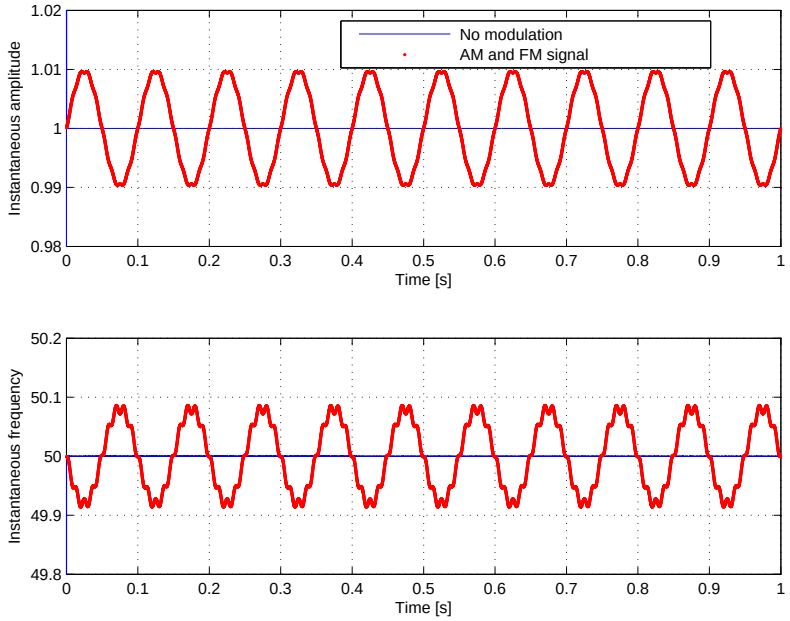

Figure 1.14: Instantaneous amplitude and frequency based on TEO.

of CT , let's assume a balanced system. Let's denote $\mathbf{x}^c[n] = [x_1^c[n], x_2^c[n]]^T$ the two Concordia components. The CT can be expressed into a matrix form as [45, 123, 124]

$$\mathbf{x}^c[n] = \begin{bmatrix} x_1^c[n] \\ x_2^c[n] \end{bmatrix} = \sqrt{\frac{2}{3}} \begin{bmatrix} \frac{\sqrt{2}}{\sqrt{3}} & -\frac{1}{\sqrt{6}} & -\frac{1}{\sqrt{6}} \\ 0 & \frac{1}{\sqrt{2}} & -\frac{1}{\sqrt{2}} \end{bmatrix} \mathbf{x}[n] \tag{1.34}$$

It can be demonstrated that the analytic signal $z^c[n]$ is given by [125]

$$z^c[n] = x_1^c[n] + jx_2^c[n] = a[n]e^{j\Phi[n]} \tag{1.35}$$

Figure 1.15 gives the results of the demodulation based on CT using the modulated signal in (1.19). It can be observed from this figure that the IA and IF are estimated correctly. The main drawback of CT is the fact that it is based on the assumption of balanced system. This assumption is rarely verified in three phase systems especially in the case of abnormal operating conditions.

The CT performance has been compared with HT for three phase machine stator current time-frequency monitoring in [71]. In [107], the CT was combined with ESPRIT to improve its performance for detecting rotor fault in induction machine at low slip.

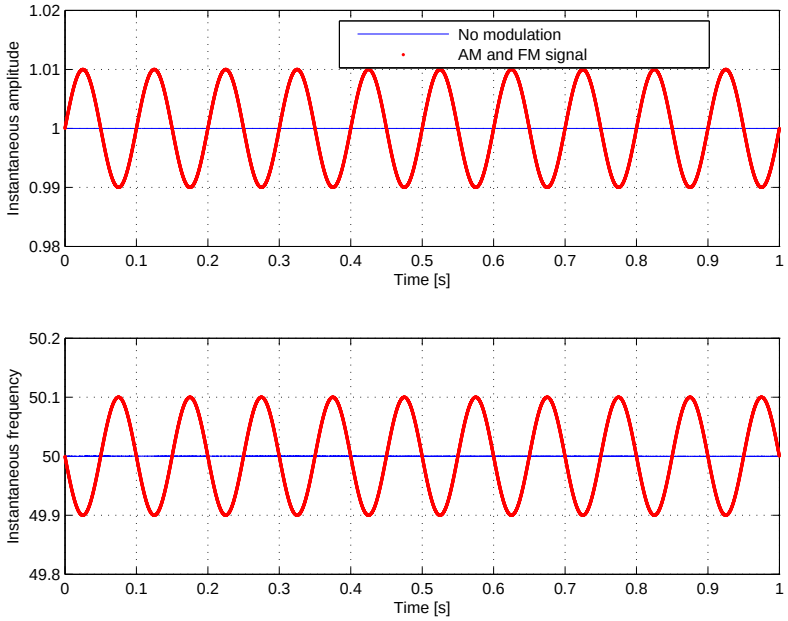

Figure 1.15: Instantaneous amplitude and frequency based on CT.

1.4.2.5 Principal component analysis approach

Principal component analysis (PCA) is a statistical tool that transforms a number of correlated signals into a small number of principal components (in-phase and quadrature components). The two principal components of $\mathbf{x}[n]$, denoted $\mathbf{x}^p[n] = [x_1^p[n], x_2^p[n]]^T$ are given by

$$\mathbf{x}^p[n] = \begin{bmatrix} x_1^p[n] \\ x_2^p[n] \end{bmatrix} = \beta \Lambda^{\frac{-1}{2}} \mathbf{S}^T \mathbf{x}[n] \tag{1.36}$$

where β is a scaling term given by

$$\beta = \sqrt{\frac{trace[\mathbf{R}_x]}{3}} \tag{1.37}$$

and where the covariance matrix $\mathbf{R}_x$ of $\mathbf{x}[n]$ is defined as

$$\mathbf{R}_x = E[\mathbf{x}[n]\mathbf{x}^T[n]] = \mathbf{U}\Lambda\mathbf{U}^T \tag{1.38}$$

with Λ and $\mathbf{U} = [\mathbf{SG}]$ are matrices containing the eigenvalues and eigenvectors of $\mathbf{R}_x$, respectively.

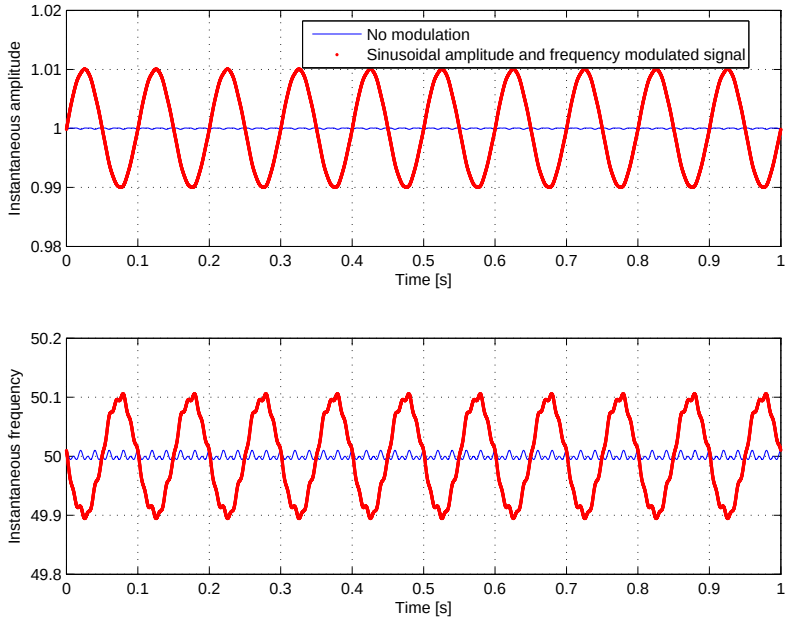

Figure 1.16: Instantaneous amplitude and frequency based on PCA.

Under the assumptions that $\Phi[n]$ is uniformly distributed in $[0;\ 2\pi]$ and that $a[n]$ and $\Phi[n]$ are independent, it can be demonstrated that the analytic signal $z^p[n]$ can be estimated up to a phase indetermination as [45]

$$z^p[n] = x_1^p[n] + jx_2^p[n] = a[n]e^{j\Phi[n]}e^{-j\theta}. \tag{1.39}$$

where θ is an unknown phase.

Once the analytic signal $z^p[n]$ is derived, the IA and IF can be computed with (1.18). Figure 1.16 gives the simulation results for the signal described in (1.19). As opposed to Concordia transform, the PCA-based demodulation is less restrictive since it holds whatever the balance assumption which is interesting for fault detection in electrical machine.

The PCA has been used for bearing faults detection in induction machine and compared with CT in [45]. In [126], the PCA has been employed for the three-phase stator currents preprocessing in order to detect turn faults in the stator winding or broken bars within the induction machine. The severity of the fault is reported according to the relationship between the eigenvectors and eigenvalues of the 3D stator currents referential. In [127], the stator current has been processed to extract alpha-beta us-

ing Park/Concordia approach as well as PCA for principal components computation. These components are then used as input for an unsupervised neural network for on-line stator faults diagnostic of induction machine.

1.4.3 Non-stationary techniques

The spectral estimation techniques presented earlier are badly suited for wind turbines and many other applications where the environment is predominantly non-stationary due to transient or variable speed conditions. In non-stationary conditions, fault detection is usually performed by using non-stationary approaches, such as time-frequency or time-scale representations [128]. These approaches include the Short-Time Fourier Transform (STFT), the Continuous Wavelet Transform (CWT), the Wigner-Ville and other quadratic distributions, and the Hilbert-Huang Transform (HHT). For the sake of clarity, we restrict the presentation here to the discrete-time mathematical formulation. For further details and continuous-time equations, the reader could refer to [128].

For illustration purposes, we use the following signal model [129]

$$x[n] = A_l \cos(2\pi p[n]) + A_c \cos(4\pi p[n]) + A_u \cos(6\pi p[u]) \tag{1.40}$$

where $p[n] = \rho \cos(2\pi f n)$, with $\rho = \frac{50}{40\pi f}$ and $f = 0.04$. For these simulations, we set $A_c = 0.7$ and $A_u = A_l = 0.5$.

All the representations, except the last one, have been implemented using the Time-Frequency Toolbox for Matlab [130]. The HHT has been implemented using the G. Rilling's subroutines for Matlab [131].

1.4.3.1 Spectrogram

The Short-Time Fourier Transform (STFT) is based on the assumption that the signal is quasi-stationary over a short time. It is obtained by computing the Fourier transform for consecutive time-frames. It is composed of three steps: first, the signal is divided into time segments, then a time window $h[.]$ is applied to reduce side-lobe effects and finally, the spectrum of each windowed time frame is computed via the Fourier transform. This procedure, called the STFT, leads to a 3-D representation which displays the frequency content over time. Let's consider discrete signals of period

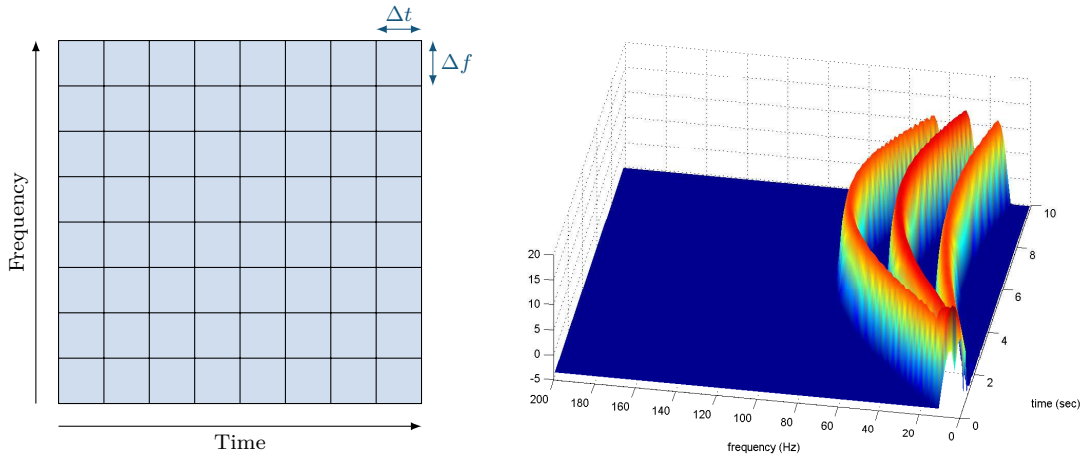

(a) Mono-resolution approach (STFT).

(b) Spectrogram of sinusoidal FM signals with smoothing window of length $N = 128$ samples.

Figure 1.17: Spectrogram and its resolution.

N. The window $h[n]$ is chosen to be a symmetric discrete signal of period N with norm $\|h\| = 1$. Mathematically, the discrete Short-Time Fourier Transform can be expressed as [132]

$$S_x[m,l] = \sum_{n=0}^{N-1} x[n]h[n-m]\exp\left(\frac{-j2\pi ln}{N}\right) \tag{1.41}$$

For each $0 \leq m \leq N$, $S_x[m,l]$ is calculated for $0 \leq l \leq N$ with N fast Fourier transform (FFT) procedures of size N. The STFT is a linear transform i.e. $S_{x+y}[m,l] = S_x[m,l] + S_y[m,l]$. The spectrogram is defined as the squared absolute value of the STFT i.e.,$|S_x[m,l]|^2$.

Classical choices for $h[n]$ is the rectangular, Hanning, Hamming or Gaussian window. The length of the window $h[n]$ determines the time and frequency resolution of the representation. This resolution is kept constant over the time-frequency plane that's why STFT is called a mono-resolution technique (Figs. 1.17(a) and 1.17(b)). As it can be shown from Fig. 1.18, a short window leads to a representation which is fine in time but coarse in the the frequency domain. Conversely, a long window leads to a representation which is coarse in time but fine in the frequency domain. This trade-off is formalized by the Heisenberg-Gabor uncertainty space[128].

The STFT has been investigated for broken bars and bearing faults in [133]. Faults

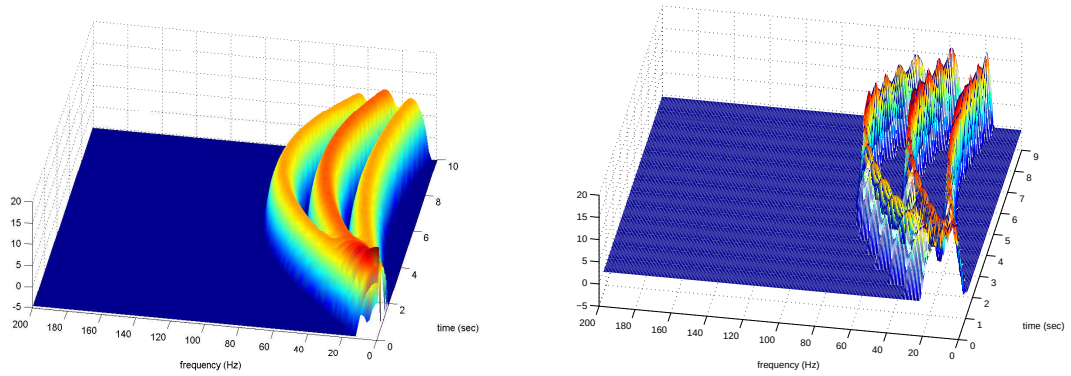

(a) $N = 64$ samples (b) $N = 512$ samples

Figure 1.18: Spectrogram of sinusoidal FM signals with smoothing window of different length N.

features have been extracted from the spectrogram. The method presented is based on a training approach in which all the distinct normal operating modes of the motor are learned before the actual testing starts. Detection of Rotor Faults in Brushless DC Motors have been performed using fault frequencies estimation based on STFT in [134]. In [47], the STFT performance has been compared with discrete wavelet transform (DWT) for broken rotor bars and shorted turns with increasing load torque. In [31], the STFT of electromagnetic torque estimation of driving induction machine has been used as a mean of mechanical torsional stresses monitoring.

1.4.3.2 Scalogram

The discrete wavelet transform (DWT) is obtained by breaking up the signal into shifted and scaled versions of a mother wavelet. Mathematically, the discrete wavelet transform can be expressed as [132]

$$T_x[n, a^l] = \sum_{m=0}^{N-1} x[m]\xi_l^*[m-n] \tag{1.42}$$

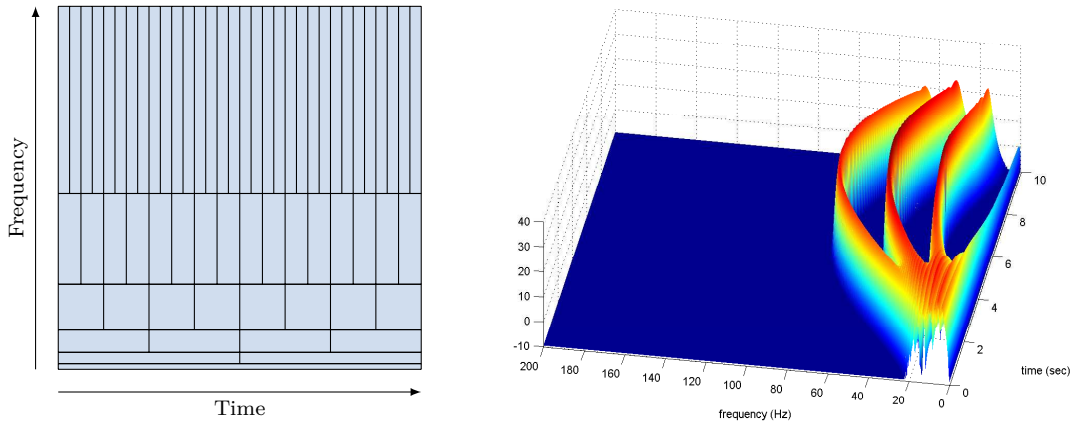

(a) Multi-resolution approach (DWT).

(b) Scalogram.

Figure 1.19: Scalogram of sinusoidal FM signals with smoothing window of different length N.

where $(.)^*$ denotes the complex conjugate, a^l is the scale, and $\xi_l[n]$ is the mother wavelet. A discrete wavelet scaled by a^l is defined by

$$\xi_l[n] = \frac{1}{\sqrt{a^l}}\xi\left(\frac{n}{a^l}\right) \tag{1.43}$$

The DWT is a linear transform i.e. $T_{x+y}[n, a^l] = T_x[n, a^l] + T_y[n, a^l]$. The scalogram is defined as squared absolute value of the DWT i.e., $\left|T_x[n, a^l]\right|^2$.

A classical choice for $\xi_l[n]$ is the Mexican-Hat, Morlet or Daubechies wavelets. Rigorously speaking, the DWT leads to a time-scale representation since it displays the signal time-evolution at different scales. However, there is a direct link between scale and frequency. Indeed, if the central frequency of the mother wavelet $\xi(t)$ is f_0, the scale a^l focuses on the frequency content at $f = f_0/a^l$. As opposed to the STFT, the DWT is a multi-resolution technique which favours the time-resolution at high-frequencies and the frequency-resolution at low-frequencies (Fig. 1.19(a)). Unfortunately, the wavelet transform is also limited by the Heisenberg-Gabor principle. Indeed, as it can be noticed from Fig. 1.19(b), the time resolution of the representation is not sufficient to distinguish the three components for $0 \leq t \leq 2$.

The Continuous wavelet transform (CWT) has been widely investigated for electrical machines monitoring based on the stator current. Detection of Dynamic Eccentricity

in brushless direct current (BLDC) motors functioning under dynamic operating conditions have been performed in [135]. In [33], the CWT-based adaptive filter has been used to track the energy in the prescribed time-varying fault-related frequency bands in the power signal in order to perform a cost-effective diagnosis for wind turbines application. The analysis of current transient in induction machine has been employed in [136] using the CWT and B-splines for broken rotor bars fault detection.

1.4.3.3 Wigner-Ville and other quadratic distributions

As opposed to the previous techniques, which focus on the decomposition of the signal itself, the Wigner-Ville distribution (WVD) focuses on the decomposition of the signal energy in the time-frequency plane.

Mathematically, the WVD of discrete signal $x[n]$ can be expressed as [132]

$$W_{x,x}[n,k] = \sum_{p=-N}^{N-1} x\left[n+\frac{p}{2}\right] x^*\left[n-\frac{p}{2}\right] \exp\left(\frac{-j2\pi kp}{N}\right) \tag{1.44}$$

The time-frequency resolution of WVD is not constrained by the Heisenberg Gabor inequality. However, the WVD is non-linear since $W_{(x+y),(x+y)}[n,k] \neq W_{x,x}[n,k] + W_{y,y}[n,k]$. This non-linearity is responsible for the introduction of interference terms (Fig.1.20(a)). These interference terms can make the time-frequency representation difficult to interpret and may lead to misleading interpretations. To reduce interference terms, the analytic signal is usually employed instead of the signal itself. Furthermore, several authors have proposed extensions of the WVD for interference reduction at the expense of reduced resolution. These extensions have been unified by the Cohen's class of time-frequency distributions[137]. The Cohen's class includes many commonly used time-frequency distributions such as the Pseudo Wigner-Ville (Fig. 1.20(b)), the Choi-Williams (Fig. 1.21(a)) and the Zhao-Atlas-Marks (Fig. 1.21(b)) Distributions [138]. It can be observed from Fig. 1.20(a) that the Wigner-Ville distribution exhibits good time and frequency resolution, but it introduces some artefacts in the signal time-frequency representation. In order to remove these cross-terms, a smoothed version of the Wigner-Ville distribution has been proposed. Figure 1.20(b) gives the Smoothed Pseudo Wigner-Ville distribution of sinusoidal FM signals with Hanning smoothing window. It can be seen that the cross-terms disappear, but the time and frequency resolution decrease. Many other distributions have been proposed in order to remove

the artefacts while keeping a high resolution as it is illustrated by Figs. 1.21(a) and 1.21(b).

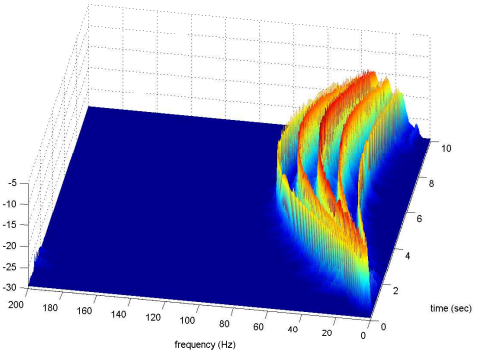

(a) Wigner-Ville distribution of sinusoidal FM signals.

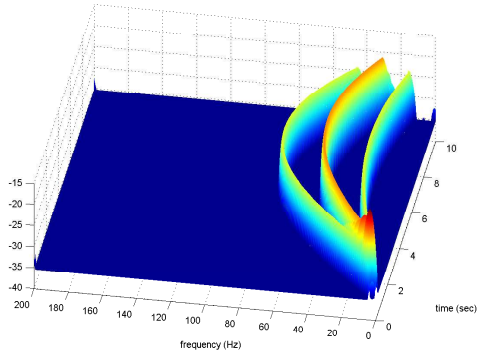

(b) Smoothed Pseudo Wigner-Ville distribution of sinusoidal FM signals with Hanning smoothing window.

Figure 1.20: Time-frequency representation of sinusoidal FM signals using WVD.

In [35, 64, 67], the authors have proposed the WVD and its extensions in order to perform a time-frequency representation which allows to distinguish load oscillation from eccentricity fault in variable speed induction motors. In [129], the Zhao-Atlas-Marks distribution has been used to enhance non-stationary fault diagnostics in electric motors. The decision step was performed by using adaptive threshold on RMS of eccentricity fault related frequency. In [134], the broken rotor bars fault in Brushless DC motors operating under non-stationary conditions has been investigated using the WVD. The short-circuit detection in permanent magnet synchronous motor (PMSM) have been performed using WVD in [139] in the case of steady-state conditions and speed transients.

1.4.3.4 Hilbert-Huang Transform

The Hilbert-Huang Transform (HTT) is the extension of the Hilbert transform for multi-component signals. This technique is composed of 2 steps: i) first, the signal is decomposed into a sum of amplitude- and frequency- modulated mono-component sine waves using an Empirical Mode Decomposition, and then ii) the instantaneous amplitude and frequency are extracted using a demodulation technique (see section 1.4.2)

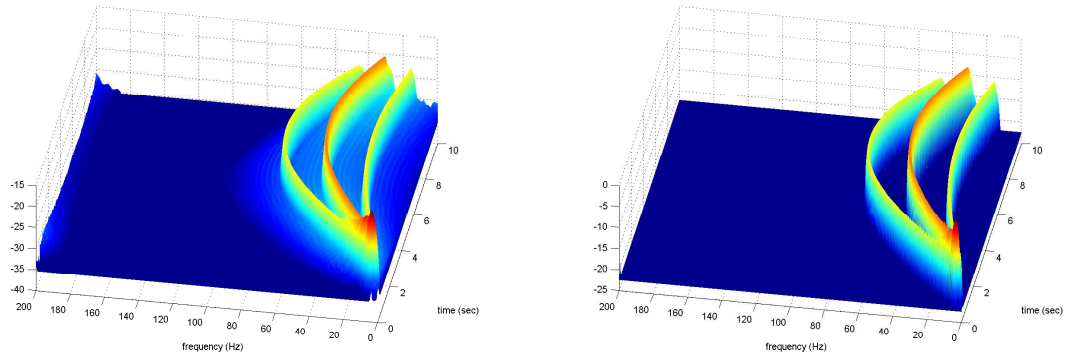

(a) Choi Williams WV of sinusoidal FM signals.

(b) ZAM WV distribution of sinusoidal FM signals with Hanning smoothing window.

Figure 1.21: Time-frequency representation of sinusoidal FM signals using different Kernels.

usually the Hilbert transform. Finally the time-frequency representation is obtained by displaying the time evolution of the instantaneous amplitude and frequency for each sine wave.

- **Empirical mode decomposition:** The Empirical Mode Decomposition (EMD) has been originally proposed by Huang [74]. As opposed to the previous techniques, the EMD is essentially defined by an algorithm and does not admit an analytical definition [131]. The algorithm is described by the following steps [74]:

  - Identification of all extrema of $x[n]$
  - Interpolation between minima (resp. maxima) ending up with some envelope $e_{min}[n]$ (resp. $e_{max}[n]$).
  - Computation of the mean:

$$m[n] = \frac{e_{min}[n] + e_{max}[n]}{2} \tag{1.45}$$

  - Extraction of the detail:

$$d[n] = x[n] - m[n] \tag{1.46}$$

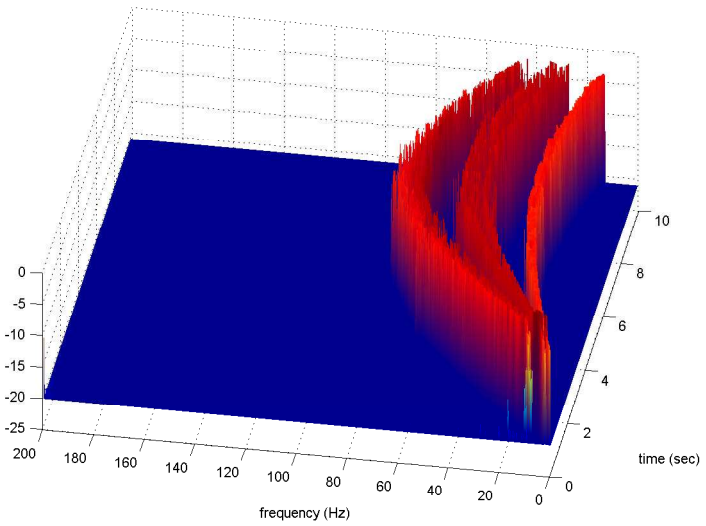

Figure 1.22: EMD-based time-frequency representation of sinusoidal FM signals.

- Iteration on the residual $m[n]$.

In practice, this algorithm has to be refined by a *shifting process* until $d[n]$ can be considered as zero-mean. After this procedure, the detail $d[n]$ corresponds to an amplitude- and frequency- modulated (AM/FM) sine wave called Intrinsic Mode Function (IMF). By iterating the algorithm on the residual $m[n]$, the EMD extracts several IMFs until a stopping criterion is reached.

- **Instantaneous amplitude (IA) and frequency (IF) extraction:**
  The IA and IF of each IMF can be extracted using a demodulation techniques. To achieve this task, a popular technique is based on the Hilbert transform. In this case the transformation is called, the HHT. It must be stressed that other demodulation techniques presented in section 1.4.2 can be used in order to compute the IA an IF from the IMFs. For example, while using the Teager Energy operator, the transformation is called Teager-Huang Transform.

Finally, the time-frequency representation is obtained by displaying the evolution of IA and IF for each IMF in the time-frequency plane. In order to illustrate the performance of the HHT, Fig. 1.22 gives the time-frequency representation of the signal described in (1.40).

The Empirical Mode Decomposition has been used in [139] to extract IMFs for the actual signal and associated with WVD for PMSM fault detection. The HHT has been applied to the stator startup current to diagnose the presence of rotor asymmetries in induction machines in [140]. The HHT is used to extract the evolution during the startup transient of the left sideband harmonic (LSH) caused by the asymmetry, which constitutes a reliable evidence of the presence of the fault. Moreover, the performance of HHT has been compared with discrete wavelet transform (DWT). It has been shown that the HHT gives satisfactory results. The demagnetization fault in PMSM is analyzed by means of decomposition of stator currents obtained at different speeds using HHT in [72].

1.4.3.5 Time-domain analysis & frequency tracking

In addition to the aforementioned techniques, a time domain analysis can be a powerful tool for three-phase induction machine faults detection and diagnosis in non-stationary environment [141]. Some researchers detect faults in induction machines by analysing the starting current transient [142]. Several techniques were presented in the literature in order to perform accurate tracking of frequencies for induction machine monitoring in non-stationary conditions such as maximum covariance method for frequency tracking (MCMFT) which is based on the computation of the covariance between the stator current signal and reference tones in the time domain [143]. It allows to track the fundamental frequency and the slip of the machine and then compute a diagnostic index without spectrum analysis. In [133], adaptive statistical time-frequency Method has been investigated for broken rotor bars and bearing faults detection. The time-frequency spectrum is analyzed statistically to distinguish a fault conditions from normal operating conditions.

1.5 Conclusion

This chapter has reviewed the state of the art of induction machine fault detection and diagnosis through a stator currents processing. Attempts have been made to highlight current trends (high resolution techniques, time-frequency / time-scale approaches, artificial intelligence techniques, etc.).

The above review emphasizes the compromise between frequency accuracy, frequency resolution, statistical performances and computational cost of analysis techniques for fault detection in induction machine. Furthermore, these previous techniques are general and do not exploit the particular structure of the stator current frequency components given in the existing works dealing with induction machine failures diagnosis. Moreover, additional post-processing algorithms are required to determine the fault-related frequencies and to extract a fault detection criterion. In fact, once the frequency spectrum is obtained and stored, empirical algorithms are used in order to reveal frequency signatures in the spectrum within various frequency ranges depending on the problem to be diagnosed. If predicted frequency patterns are present in the spectrum, a positive diagnosis is returned.

In addition to that, an accurate choice of signal processing techniques for fault detection for several induction machine operating conditions is a key issue. In fact, in transient or in variable speed and/or load, a short data acquisition time is required and reliable and efficient technique must be chosen in order to compute an index directly related to the fault severity or to stating its occurrence. However, despite of the rich literature, the choice of a particular representation is not an easy task since several criteria must be taken into account.

Based on the above discussed aspects, it is obvious that there is a need to propose signal processing techniques able to extract directly faults criteria, methods allowing to classify faults and recognize failed components. Next chapter reports on parametric spectral estimation techniques able to exploit the fault signatures given in the literature and allowing to extract relevant fault criterion.

1. FAULTS DIAGNOSIS IN INDUCTION MACHINE: STATE OF THE ART REVIEW

Chapter

2

Stator Currents Parametric Spectral Estimation for Fault Detection in Induction Machines

Contents

2.1 Introduction

This chapter introduces the proposed signal processing approaches for induction machine faults detection and diagnosis. The signals correspond to measured physical quantities, already available on the drive system for protection and control purposes, which are the electrical signals e.g. terminal voltages and more precisely the stator currents. As it was described in the previous chapter, the considered mechanical and/or electrical faults often leads to additional periodic phenomena (additional faults related frequency components or rise of existing ones in the signal spectrum). Spectral analysis is therefore, the most suited approach for condition monitoring and faults detection.

Current spectrum analysis is a proven technique for fault diagnosis in electrical machines. It is an obvious approach used in most existing works dealing with condition monitoring of electrical machines and particularly the induction machine. Current spectral estimation is usually performed using classical techniques (see section 1.4.1). However, these techniques have several drawbacks since their frequency resolution is limited and additional post-processing algorithms are required to extract a relevant fault detection criterion. To overcome these limitations, high resolution techniques have been presented such as MUSIC and ESPRIT which allow to estimate the power spectral density without proposing reliable fault indicator.

In this chapter, we present a new parametric spectral estimator that fully exploits the faults sensitive frequencies given in the literature. This approach does not rely on frequency analysis but uses the knowledge of the temporal signal model in (2.4) to estimate its parameters. The idea behind this approach is the use of the a priori knowledge about the signal structure in order to enhance the fault detection performance. The proposed technique is based on the maximum likelihood estimation and leads to an asymptotically optimal estimators [93]. In fact, it performance is optimal for large enough data records. Specifically, it is approximately a Minimum Variance Unbiased

(MVU) estimator due to its approximate efficiency. The stator currents measurements are used in order to identify the model parameters. The sidebands amplitude estimator conveys directly the information about fault severity. Indeed, based on this approach, a fault criterion is derived for detecting several fault types.

The parameter estimation approach is interesting with regard to the use of the discrete-time signals. In general, the power spectral density estimation techniques discussed in the previous chapter are theoretically studied using continuous-time signals (except for the MUSIC and ESPRIT algorithms). Concerning parametric spectral estimation, the theoretical background is based on discrete-time signals and with finite number of signals which means that the theory is more adapted to practical implementation on real time condition monitoring systems with digital signals.

The outline of the chapter is the following: First, the basic concepts of parametric spectral estimation is presented including the MLE and the MD MUSIC of signal frequency content and faults related frequency amplitudes estimation. These approaches are used in order to extract fault detection criterion. Then, a fault detection scheme is presented. Afterwards, these approaches are extended to non-stationary signals. Finally, the last part of this chapter deals with the application of the proposed approaches on synthetic signals.

2.2 Stator currents model under fault

The following section proposes a signal model which takes into account the fault characteristic frequencies given in Table 1.3. These additional components may already exist on the line currents spectrum in the healthy case due to problem at the manufacturing stage. This stator current model takes into account the effect of induction machine fault on the fundamental stator current component but not its effect over higher frequency current harmonics. Since the fundamental frequency exhibits the highest amplitude of all current components, the fault effects will also be strongest in the baseband around the fundamental. Consequently, the fault detection schemes presented in this chapter will mainly be carried out by analysis of the stator current fundamental. The problem is formulated in a general way before addressing the specific case of eccentricity faults, broken rotor bars, and bearing defects.

2.2.1 Study hypotheses

The stator current signal model presented herein, is based on the following assumptions:

- $\mathcal{H}_1$: The received signal is modelled as a sum of $2L+1$ sine waves embedded in noise. Where, $2L$ corresponds to the number of the sidebands introduced by the fault (whose amplitudes rise when a fault occur).
- $\mathcal{H}_2$: The noise is a white Gaussian noise with zero-mean and variance σ^2. This choice is motivated by:
  - The central limit theorem which states that, given certain conditions, the sum of a sufficiently large number of independent and identically random variables are approximately Gaussian distributed [144, 145].
  - The Gaussian noise assumption leads to minimize the worst-case asymptotic Cramér–Rao bound (CRB) [146, 147].
  - The MVU estimator is equivalent to mean least square estimator when the noise is white Gaussian [148].
- $\mathcal{H}_3$: The signal frequency content obeys to the particular structures given by Table 1.3.
- $\mathcal{H}_4$: The phases of the sinusoids are independent and uniformly distributed on the interval $[-\pi, \pi[$.

In practice, we must note that $\mathcal{H}_1$ requires the knowledge of L. In the present chapter, we also propose a technique to estimate L based on the stator current samples $x[n]$. Concerning the assumption $\mathcal{H}_2$, it is not particularly restrictive since the noise can be whitened by an appropriate choice of the sampling frequency [7]. Moreover, if the noise process is not white and has unknown spectral shape, then accurate frequency estimates can still be found if we estimate the sinusoids using the non-linear least squares (NLS) [7, Chapter 4, Introduction].

2.2.2 Induction machine stator current modeling

Under the assumption $\mathcal{H}_1$-$\mathcal{H}_3$, the stator-current samples $x[n]$ can be expressed as

$$x[n] = \sum_{k=-L}^{L} a_k \cos\left(2\pi f_k(\Omega) \times \left(\frac{n}{F_s}\right) + \phi_k\right) + b[n] \tag{2.1}$$

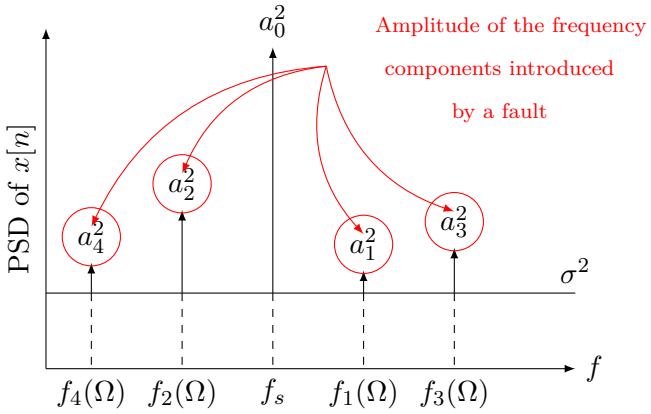

Figure 2.1: Theoretical PSD for $L = 2$.

where $b[n]$ corresponds to the noise sample. Symbols $f_k(\Omega)$, a_k and ϕ_k correspond to the frequency, the amplitude and the phase of the k^{th} frequency component, respectively. Symbol F_s corresponds to the sampling rate. The set Ω is a set of parameters to be estimated in order to reveal the presence of fault. For example, in the case of broken rotor bars, the fault related frequency f_{brb} is given by

$$f_{brb} = f_s\,(1 \pm 2ks)\,; \qquad\qquad k = 1, 2, 3, ... \tag{2.2}$$

and the corresponding parameters to be estimated are $\Omega = \{f_s, s\}$. In the general way, the faults signature studied within this manuscript are given by

$$f_d = f_s \pm k f_c,\ \ k = 0, 1, \cdots, L. \tag{2.3}$$

where f_s is the electrical supply frequency, f_c corresponds to the fault characteristic frequency, $2 \times L$ is the sidebands number and $\Omega = \{f_s, f_c\}$.

The PSD is defined as the Discrete Time Fourier Transform of the covariance function of $x[n]$ [7]. Under the assumption $\mathcal{H}_2$ and that the initial phases ϕ_k, are independent random variables uniformly distributed on $[-\pi\ \pi]$, the theoretical PSD of $x[n]$ is given by Fig. 2.1. In practice, the PSD is unknown, and must be estimated from N samples. Using a matrix notation, $x[n]$ $(n = 0, \cdots, N-1)$ can be expressed as follows (see Appendix A):

$$\mathbf{x} = \mathbf{A}(\Omega)\mathbf{v} + \mathbf{b} \tag{2.4}$$

where:

- $\mathbf{x} = [x[0], \cdots, x[N-1]]^T$ is a $N \times 1$ column vector containing the stator current samples,
- $\mathbf{b} = [b[0], \cdots, b[N-1]]^T$ is a $N \times 1$ column vector containing the noise samples,
- $\mathbf{v}$ is a $2(2L+1) \times 1$ column vector containing the amplitudes and phases of the characteristic fault frequencies. This vector is given by

$$\mathbf{v} = [a_{-L}\cos(\phi_{-L}) \dots a_L \cos(\phi_L), \quad -a_{-L}\sin(\phi_{-L}) \dots - a_L \sin(\phi_L)]^T \tag{2.5}$$

- $\mathbf{A}(\Omega)$ is a $N \times 2(2L+1)$ matrix whose elements are given by

$$\mathbf{A}(\Omega) = [\mathbf{z}_{-L} \dots \mathbf{z}_L, \mathbf{y}_{-L} \dots \mathbf{y}_L] \tag{2.6}$$

where

$$\begin{aligned} \mathbf{z}_k &= \left[1 \ \cos\left(2\pi f_k(\Omega) \times \frac{1}{F_s}\right) \dots \cos\left(2\pi f_k(\Omega) \times \frac{N-1}{F_s}\right)\right]^T \\ \mathbf{y}_k &= \left[0 \ \sin\left(2\pi f_k(\Omega) \times \frac{1}{F_s}\right) \dots \sin\left(2\pi f_k(\Omega) \times \frac{N-1}{F_s}\right)\right]^T \end{aligned} \tag{2.7}$$

The matrix $\mathbf{A}(\Omega)$ has rank $2 \times L + 1$.

Non-parametric estimators estimate the PSD from the stator current samples $\mathbf{x}$ without using any a priori knowledge about the signal. Departing from this approach, we propose a parametric estimator that exploits the signal model in (2.4). In this context, the computation of the current spectrum from stator current samples $\mathbf{x}$ is treated as a statistical estimation problem.

2.3 Maximum likelihood based approach

The following section presents the Maximum Likelihood Estimators for model parameters estimation. Furthermore, a model order estimator is presented based on information theoretic rules. Finally, the MLE is used in order to estimate the PSD of a synthetic signal.

2.3.1 Stator current model parameters estimation

2.3.1.1 Exact estimators

For a fixed set of data and underlying statistical model, the maximum likelihood method selects the set of values of the model parameters that maximizes the likelihood function. Intuitively, this maximizes the agreement of the selected model with the observed data, and for discrete random variables it indeed maximizes the probability of the observed data under the resulting distribution. The MLE is used in order to estimate $\mathbf{v}$ and $f_k(\Omega)$ of the signal model given by (2.4). The ML estimates of Ω and $\mathbf{v}$ are obtained by maximizing the probability density function (pdf) with respect to the unknown parameters. Mathematically, they are given by

$$\{\widehat{\mathbf{v}}, \widehat{\Omega}\} = \arg\max_{\mathbf{v},\Omega} \log(p(\mathbf{x}; \mathbf{v}, \Omega)) \tag{2.8}$$

where $p(\mathbf{x}; \mathbf{v}, \Omega)$ is the probability density function (pdf) of $\mathbf{x}$ which is given by

$$p(\mathbf{x}; \mathbf{v}, \Omega) = \frac{1}{\left(2\pi\sigma^2\right)^{\frac{N}{2}}} \times \exp\left[-\frac{1}{2\sigma^2}\left(\mathbf{x} - \mathbf{A}(\Omega)\mathbf{v}\right)^T\left(\mathbf{x} - \mathbf{A}(\Omega)\mathbf{v}\right)\right] \tag{2.9}$$

where $(.)^T$ denotes the matrix transpose and assume that the assumption $\mathcal{H}_2$ holds , i.e. $b[n] \sim \mathcal{N}(0, \sigma^2)$. For the sake of illustration, the one-dimensional Gaussian density function is given by Fig. 2.2.

The maximization in (2.8) is equivalent to the minimization of the following cost function [93]:

$$\mathcal{L}(\mathbf{x}; \mathbf{v}, \Omega) = \left(\mathbf{x} - \mathbf{A}(\Omega)\mathbf{v}\right)^T\left(\mathbf{x} - \mathbf{A}(\Omega)\mathbf{v}\right) \tag{2.10}$$

Differentiating $\mathcal{L}(\mathbf{x}; \mathbf{v}, \Omega)$ with respect to $\mathbf{v}$ and setting the derivative equal to 0 leads to the ML estimate of $\mathbf{v}$ [1]. By expanding the cost function, we obtain :

$$\begin{aligned}
\mathcal{L}(\mathbf{x}; \mathbf{v}, \Omega) &= \left(\mathbf{x} - \mathbf{A}(\Omega)\mathbf{v}\right)^T\left(\mathbf{x} - \mathbf{A}(\Omega)\mathbf{v}\right) \\
&= \left(\mathbf{x}^T - \mathbf{v}^T\mathbf{A}^T(\Omega)\right)\left(\mathbf{x} - \mathbf{A}(\Omega)\mathbf{v}\right) \\
&= \mathbf{x}^T\mathbf{x} - \mathbf{v}^T\mathbf{A}^T(\Omega)\mathbf{x} - \mathbf{x}^T\mathbf{A}(\Omega)\mathbf{v} + \mathbf{v}^T\mathbf{A}^T(\Omega)\mathbf{A}(\Omega)\mathbf{v}
\end{aligned} \tag{2.11}$$

[1]The proposed technique is also valid when the noise distribution is unknown. In this context, the minimization of 2.10 leads to the Least Squares Estimator of $\mathbf{v}$ and Ω.

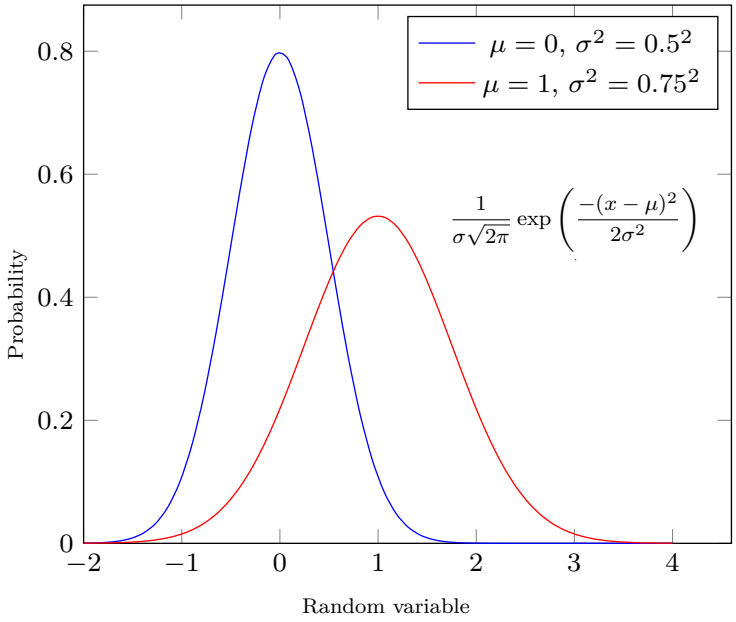

Figure 2.2: 1-D probability density function of a Gaussian distribution $N(\mu, \sigma^2)$.

The derivative of $\mathcal{L}(\mathbf{x}; \mathbf{v}, \Omega)$ with respect to $\mathbf{v}$ is equal to (see reference [149]):

$$\begin{aligned}\frac{\partial \mathcal{L}(\mathbf{x}; \mathbf{v}, \Omega)}{\partial \mathbf{v}} &= 0 - \mathbf{A}^T(\Omega)\mathbf{x} - \mathbf{A}^T(\Omega)\mathbf{x} + \left(\mathbf{A}^T(\Omega)\mathbf{A}(\Omega) + (\mathbf{A}^T(\Omega)\mathbf{A}(\Omega))^T\right)\mathbf{v} \\ &= -2\mathbf{A}^T(\Omega)\mathbf{x} + 2\mathbf{A}^T(\Omega)\mathbf{A}(\Omega)\mathbf{v} \end{aligned} \tag{2.12}$$

Setting the above derivative to 0, we obtain the ML estimator of $\mathbf{v}$, which is denoted $\widehat{\mathbf{v}}$ i.e.

$$\left.\frac{\partial \mathcal{L}(\mathbf{x}; \mathbf{v}, \Omega)}{\partial \mathbf{v}}\right|_{\mathbf{v}=\widehat{\mathbf{v}}} = 0 \Rightarrow \mathbf{x} = \mathbf{A}(f_c)\widehat{\mathbf{v}} \tag{2.13}$$

Finally, we obtain the following MLE of $\mathbf{v}$:

$$\widehat{\mathbf{v}} = \mathbf{A}^{\dagger}(\Omega)\mathbf{x} \tag{2.14}$$

where $\mathbf{A}^{\dagger}(\Omega)$ is the pseudo-inverse of $\mathbf{A}(\Omega)$ i.e.

$$\mathbf{A}^{\dagger}(\Omega) = \left(\mathbf{A}^T(\Omega)\mathbf{A}(\Omega)\right)^{-1}\mathbf{A}^T(\Omega) \tag{2.15}$$

and where $(.)^{-1}$ corresponds to the matrix inverse. It must be stressed that the MLE of $\mathbf{v}$ depends on the unknown parameters Ω which must be estimated.

The ML estimate of $f_k(\Omega)$ is obtained by minimizing $\mathcal{L}(\mathbf{x};\widehat{\mathbf{v}},\Omega)$ with respect to Ω. By replacing $\mathbf{v}$ by $\widehat{\mathbf{v}}$ in (2.10), we obtain:

$$\begin{aligned}\mathcal{L}(\mathbf{x};\widehat{\mathbf{v}},\Omega) &= (\mathbf{x}-\mathbf{A}(\Omega)\widehat{\mathbf{v}})^T(\mathbf{x}-\mathbf{A}(\Omega)\widehat{\mathbf{v}}) \\ &= \left(\mathbf{x}-\mathbf{A}(\Omega)\mathbf{A}^\dagger(\Omega)\mathbf{x}\right)^T\left(\mathbf{x}-\mathbf{A}(\Omega)\mathbf{A}^\dagger(\Omega)\mathbf{x}\right) \\ &= \mathbf{x}^T\left(\mathbf{I}_N-\mathbf{A}(\Omega)\mathbf{A}^\dagger(\Omega)\right)\mathbf{x} \end{aligned} \tag{2.16}$$

where the last equality has been obtained by using (2.15). Neglecting the terms that do not depend on Ω, it can be shown that the ML estimate of Ω is given by

$$\{\widehat{\Omega}\} = \arg\max_{\Omega} \mathcal{J}(\Omega) \tag{2.17}$$

where:

$$\mathcal{J}(\Omega) = \mathbf{x}^T\mathbf{A}(\Omega)\mathbf{A}^\dagger(\Omega)\mathbf{x} \tag{2.18}$$

Once the estimation of the set Ω is performed, the fault related frequency can be computed based on the expressions given in Table 1.3. Finally, the PSD estimate of the stator current is composed of two steps: a) the estimates of Ω and consequently $f_k(\Omega)$ are obtained from (2.17), and b) the vector $\mathbf{v}$ containing the amplitude and the phase of the fault characteristic frequencies is estimated by replacing Ω with its estimates in (2.14). Because of its statistical properties, the MLE remains the most accurate method for PSD estimation even in those cases where the noise is colored [95]. In particular, this estimator overcomes the frequency resolution limitation of the periodogram. Furthermore, as opposed to other techniques, the proposed approaches are aimed specifically at dealing with the use of the faults characteristic frequencies to improve the accuracy of the PSD estimation.

The MLE is an alternative to the Minimum Variance Unbiased (MVU) estimator which does not always exist. A benchmark against which we can compare the performance of any unbiased estimator are Cramer-Rao lower bounds (CRLB). The CRLB provides an inferior bound for any unbiased estimator variance. The MLE variance approaches asymptotically these bounds [148]. Moreover, owing to the signal model proposed, the optimization problem has been reduced from $2 \times L + 1$ dimensional problem to 2 dimensional problem.

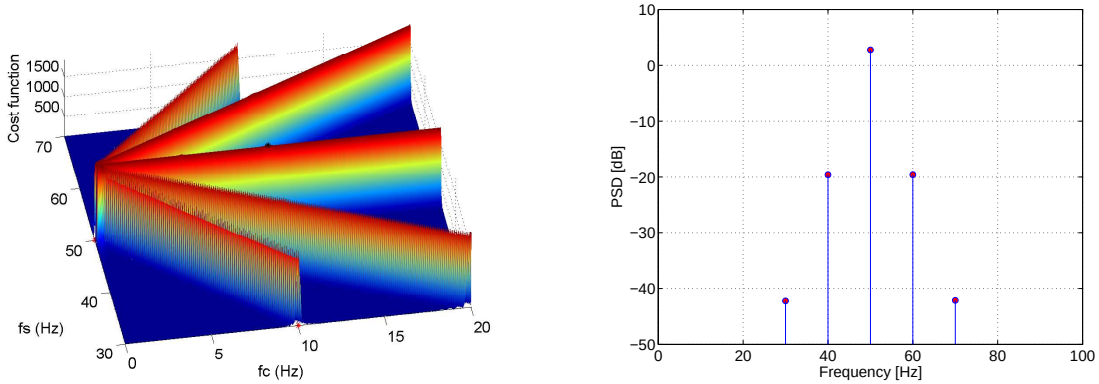

(a) Exact cost function $\mathcal{J}(\Omega)$.

(b) PSD estimation.

Figure 2.3: Cost function and ML based-PSD estimation ($f_s = 50$Hz, $f_c = 10$Hz and $L = 2$).

About the implementation, the main difficulty relies on the optimization problem in (2.17). As the maximum can not be found analytically, numerical methods should be used to estimate Ω and afterwards $f_k(\Omega)$. In our context, the cost function is only composed of two parameters, which implies a maximization in a 2-D space. Furthermore, the search space is relatively limited since the variation range of the fundamental frequency is approximately known. For these reasons, we propose to perform the maximization of (2.17) with a grid-search algorithm in the following illustrations. This algorithm evaluates the cost function at the vertices of a rectangular grid, and chooses the vertex with the highest value. Figure 2.3 illustrates the cost function for a synthetic signal with $f_k(\Omega) = f_s \pm kf_c$, $f_s = 50$ Hz, $f_c = 10$ Hz, $L = 2$, and $SNR = 50$ dB. We can observe that the maximum is reached at the true values of the fundamental frequency and fault related frequency. It should be noted that the maximization step could be computationally demanding since it requires the construction and the inversion of a large matrix for each vertex of the grid.

2.3.1.2 Approximate estimators

The computational complexity of the PSD estimator can be reduced when the number of samples, N, is sufficiently large. It must be stressed that an approximate MLE can be obtained if $f_k(\Omega)/F_s$ is not close to 0 and 1/2. By using the following

limit (see, e.g.,[148]).

$$\lim_{N\to\infty} \frac{2}{N}\left(\mathbf{A}^T(\Omega)\mathbf{A}(\Omega)\right) = \mathbf{I}_N \tag{2.19}$$

where $\mathbf{I}_N$ corresponds to the $N \times N$ identity matrix, the cost function can be approximated as

$$\begin{aligned}\mathcal{J}_a(\Omega) &= \lim_{N\to\infty} \mathcal{J}(\Omega) \\ &= \frac{2}{N}\mathbf{x}^T\mathbf{A}(\Omega)\mathbf{A}^T(\Omega)\mathbf{x} \\ &= \frac{2}{N}\left\|\mathbf{A}^T(\Omega)\mathbf{x}\right\|_F^2 \end{aligned} \tag{2.20}$$

where $\|.\|$ corresponds to the Frobenius norm. By using the structure of $\mathbf{A}(\Omega)$ we obtain

$$\begin{aligned}\mathcal{J}_a(\Omega) &= \frac{2}{N}\sum_{k=-L}^{L}\left(\sum_{n=0}^{N-1} x[n]\cos\left(2\pi f_k(\Omega)\times\frac{n}{F_s}\right)\right)^2 + \frac{2}{N}\sum_{k=-L}^{L}\left(\sum_{n=0}^{N-1} x[n]\sin\left(2\pi f_k(\Omega)\times\frac{n}{F_s}\right)\right)^2 \\ &= 2\sum_{k=-L}^{L}\left|\frac{1}{\sqrt{N}}\sum_{n=0}^{N-1} x[n]e^{-2j\pi\left(\frac{f_k(\Omega)}{F_s}\right)n}\right|^2 \end{aligned} \tag{2.21}$$

where the last equality comes from the fact that $x[n] \in \mathbb{R}$. The last equation can be expressed according to the Discrete Fourier Transform (DFT) of $x[n]$. Indeed,

$$\mathcal{J}_a(\Omega) = 2\sum_{k=-L}^{L}\left|DFT_x\left[f_k(\Omega)/F_s\right]\right|^2 = 2\sum_{k=-L}^{L}\widehat{P}_x\left(f_k(\Omega)/F_s\right) \tag{2.22}$$

where $\widehat{P}_x(.)$ is the periodogram defined in (1.6) and $DFT_x[f]$ is the DFT computed at frequency f i.e. (see [148])

$$DFT_x[f] = \frac{1}{\sqrt{N}}\sum_{n=0}^{N-1} x[n]e^{-2j\pi fn} \tag{2.23}$$

This cost function can be computed using the periodogram of the samples data given by equation (1.6).

Finally the approximate ML estimate of Ω is simply obtained by replacing $\mathcal{J}(\Omega)$ with $\mathcal{J}_a(\Omega)$ in (2.17).

Similarly, the approximate ML estimator of the vector $\mathbf{v}$ is then computed using (2.24).

$$\widehat{\mathbf{v}} \;=\; \frac{2}{N}\mathbf{A}^T(\Omega)\mathbf{x} \tag{2.24}$$

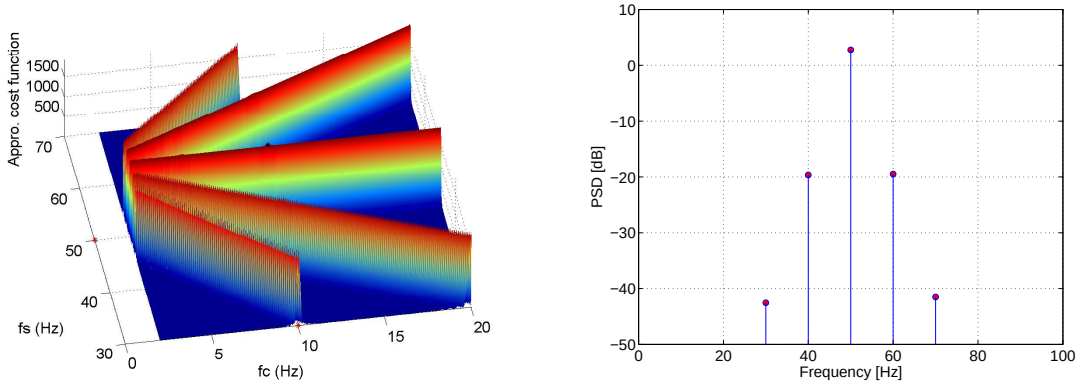

(a) Approximate cost function $\jmath_a(\Omega)$.

(b) PSD estimation.

Figure 2.4: Approximate cost function $\jmath_a(\Omega)$ and signal PSD ($f_s = 50$Hz, $f_c = 10$Hz and $L = 2$)).

Equations (2.21) and (2.24) show that the approximate cost function is reduced to a sum of DFT bins. This makes the approximate approach attractive for the following reasons: a) Most DSP-boards include functions for DFT computation b) the DFT can be efficiently computed using the FFT. However, it should be stressed that the accuracy of the approximation highly depends on the signal length N. In particular, the approximation in (2.19) is no longer valid for short data length. In this case, the DFT of the stator current signal exhibits sidelobes which affect the frequency resolution. The sidelobes can mask components close in frequency and then lead to false interpretations. Moreover, the sidelobes could be interpreted as fault characteristic frequency and then lead to false alarm.

The approximated method is then limited by the DFT algorithm resolution: the parameters are estimated correctly as long as the observed signal length N is large enough compared to the inverse of the smallest frequency difference between two neighbouring poles of the signal equivalent to two neighbouring frequency f_{k_2} and f_{k_1} i.e. (2.25).

$$N \gg \frac{1}{\min_{k_1 \neq k_2} |f_{k_2} - f_{k_1}|} \times F_s \tag{2.25}$$

One can notice that the exact cost function in Fig. 2.3 and its approximation in Fig. 2.4 have roughly the same shape and differ only in low frequencies due to frequency resolution and windowing. Indeed, these two shapes differs when the signal

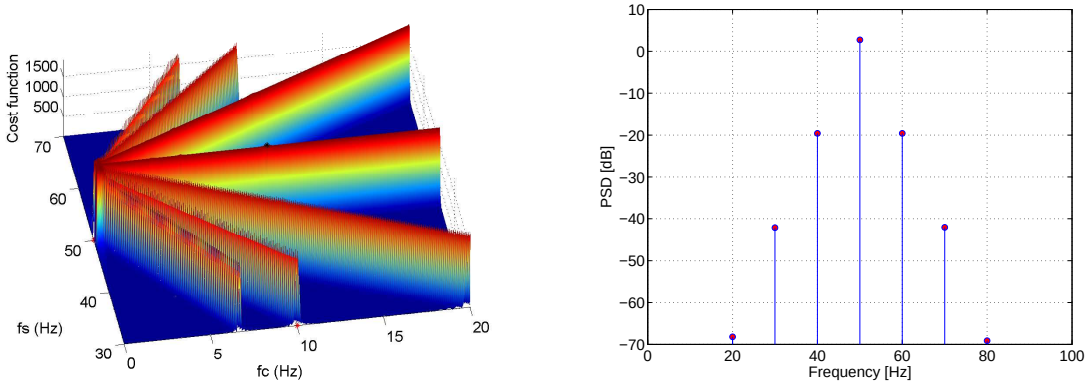

(a) Exact cost function.

(b) Exact PSD estimation.

Figure 2.5: Exact cost function $\mathcal{J}(\Omega)$ and signal PSD ($f_s = 50$Hz, $f_c = 10$Hz and $L = 2$)) for a wrong value of model order.

model contains closely spaced frequencies. For closely spaced frequencies, the resolution limitation of the DFT leads to wrong results. In particular, the approximate cost function exhibits a spurious peak located at $f_c = 0$Hz. When using the approximate approach, spurious peaks must be removed to obtain accurate estimate of f_c. This can be done by excluding small values of f_c from the grid search (see Fig. 2.4). Despite this drawback, the approximate approach is quite attractive since it leads to a drastic computational reduction. For example, the evaluation of the approximate cost function in Fig. 2.4 on a HP ProBook PC at 2.2GHz, using Matlab-Simulink® requires only 4.2s, while the evaluation of the exact one in Fig. 2.3 requires 26.7s.

2.3.2 Order estimation

The exact maximum likelihood estimators and their approximates presented above assume the knowledge of the number of sidebands which is not the case in the fault detection applications. Besides, an efficient implementation of the MLE requires the knowledge of L. This problem is known as the model order estimation. It must be emphasized that the sidebands number $(2 \times L)$ estimation is of great interest since it contributes to inform us about the fault existence. Moreover, if the order is not estimated (chosen) correctly, the fault characteristic frequency or the fundamental frequency may erroneously be estimated as it is illustrated in Figs. 2.5 and 2.6.

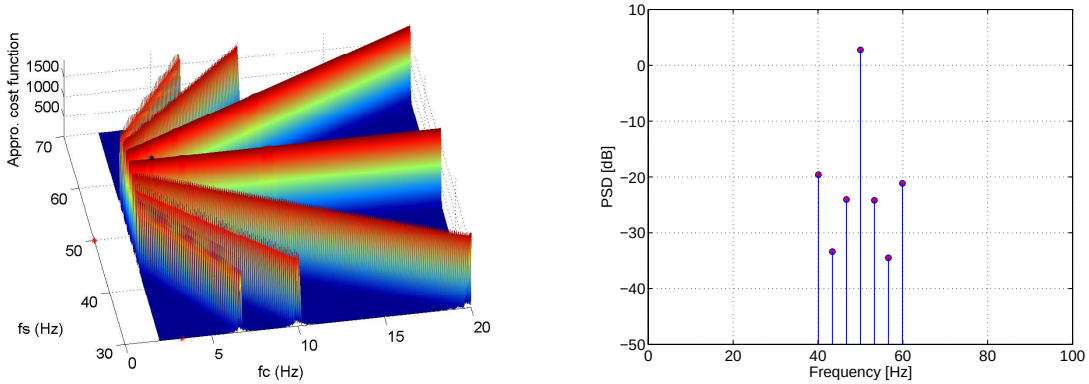

(a) Approximate cost function.

(b) Approximate PSD estimation.

Figure 2.6: Approximate cost function $\mathcal{J}_a(\Omega)$ and signal PSD ($f_s = 50$Hz, $f_c = 10$Hz and $L = 2$)) for a wrong value of model order.

The parametric methods studied require not only the estimation of a vector of real-valued parameters but also the selection of the number of sinusoidal components for the specification of a data model.

In this manuscript, we propose to combine the MLE with an order-dependent penalty term based on the information criteria rules. The information theoretic criteria rules such as Minimum description length principle (MDL), Akaike information criterion (AIC), Bayesian information criterion (BIC) and Generalized information criterion (GIC) are often used to estimate the model order [103, 150]. Hence, the estimation of L can be performed by maximizing the penalized ML estimate of Ω [103] as follows

$$\{\widehat{\Omega}, \widehat{L}\} = \arg\min_{\Omega, L}(-2\log p(\mathbf{x}, \widehat{\mathbf{v}}, \widehat{\sigma}^2, \Omega, L) + c(g, N)) \tag{2.26}$$

where $c(g, N)$ is a penalty function which depends on the number of free parameters g and the number of data samples N. Several penalty functions have been proposed in the literature [103]. In the following, we focus on the MDL principle since it minimizes the complexity of the model and maximizes the fitness [151]. Under the assumption that the number of the components is equal to $2L + 1$, the number of free parameters g is given by $g = 4L + 5$. Therefore, the MDL penalty function is given by

$$c(g, N) = g\log(N) \tag{2.27}$$

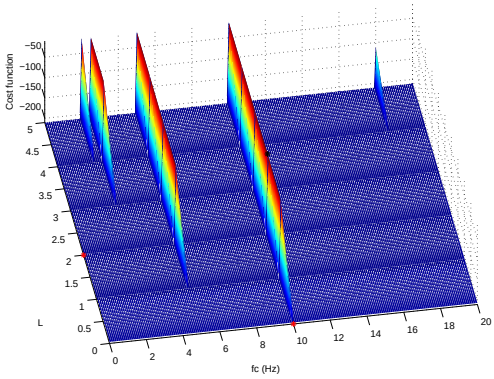

(a) Exact cost function for model order estimation in (2.28).

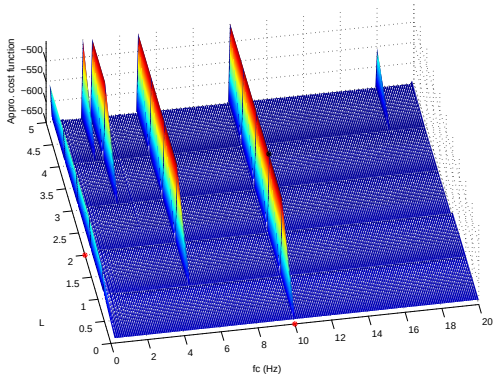

(b) Approximate cost function for model order estimation in (2.29).

Figure 2.7: Exact and approximate PSD ($f_s = 50$Hz, $f_c = 10$Hz and $L = 2$)).

As the exponential function is a monotonic increasing function, a straightforward computation leads to the following cost function:

$$\{\widehat{\Omega}, \widehat{L}\} = \arg\max_{\Omega, L} - \Big(\mathbf{x}^T\mathbf{x} - \mathcal{J}(\Omega)\Big) \times \exp\left(\frac{g\log(N)}{N}\right) \tag{2.28}$$

Similarly to the exact approach, the approximate approach can be extended in order to estimate the model order L as follows

$$\{\widehat{\Omega}, \widehat{L}\} = \arg\max_{\Omega, L} - \Big(\mathbf{x}^T\mathbf{x} - \mathcal{J}_a(\Omega)\Big) \times \exp\left(\frac{g\log(N)}{N}\right) \tag{2.29}$$

For grid connected induction machines, the fundamental frequency can be assumed to be known. Consequently, the optimization problem in (2.28) reduces to 2-D problem. Figure 2.7 illustrates the maximization step for a synthetic signal with $f_k(\Omega) = f_s \pm k f_c$, where $f_s = 50$Hz, $f_c = 10$Hz, $L = 2$, and SNR=50 dB. The acquisition time and the sampling frequency are equal to 1 s and $F_s = 1$kHz, respectively. The grid search algorithm evaluates the cost function for f_c ranging from 0Hz to 40Hz with a step size of 0.01Hz and L varying from 0 to 5. By looking at Figs. 2.7(a) and 2.7(b), it can be observed that the cost function is maximized for the true values of f_c i.e. 10Hz and $L = 2$.

Theoretically speaking, the estimation of L is of great interest since it allows to determine whatever the induction machine is operating correctly or under faulty condition. In fact, when $L = 0$, the sidebands responsible of the fault does not exist and

the machine is operating correctly. In contrary, if $L \neq 0$ the machine is faulty and the sidebands amplitude must be computed in order to measure the fault severity. Fig. 2.8 depicts the simulation results for a signal without sidebands (no fault). It is obvious from this figure that the exact method is more appropriate to discriminate the faulty from healthy case by estimating the model order L. In fact, the exact method estimates the model order correctly $L = 0$ when the approximate method based on the discrete Fourier transform overestimate the number of sidebands ($L = 1$). This is due to sidelobes in the Fourier transform introduced by windowing. Indeed, when the spectrum of sinusoidal or narrowband signals is estimated, it is often advantageous to multiply the data with a window function. The use of no particular analysis window is equivalent to the use of a rectangular window of data record length. These sidelobes can be interpreted as fault characteristic frequency and lead to false interpretations. It must be emphasized here that the use of particular window function (Triangular, Hamming, Hanning, Blackman, etc.) can reduce the sidelobe amplitudes but increases the width of the mainlobe which may lead to false alarm too. Hence, a tradeoff exists between the sidelobes amplitudes and the bandwidth of the mainlobe. In our case, it is preferable, in the case of approximate approach to compute the fault detection criteria and set a threshold beyond which the fault exists and the operator must be informed. From Figs. 2.8(b) and 2.8(d), it is clear that even if the model order is estimated erroneously, the PSD is correctly estimated and the sidebands amplitudes correspond to sidelobes amplitudes in the DFT.

2.4 Multidimensional MUSIC

In this section, we describe a customized version of MUSIC for spectrum estimation dedicated to faults detection in induction machines. Indeed, we develop a Multidimensional MUSIC (MD MUSIC) for frequency components estimation. The application of the MD MUSIC requires the computation of the analytical signal $\mathbf{z}[n]$ from the real signal $\mathbf{x}[n]$. The usual may to compute the analytical signal is the Hilbert transform [112]. Then, the MLE for amplitudes estimation is used to estimate the fault severity. Finally, we present a fault detection scheme.

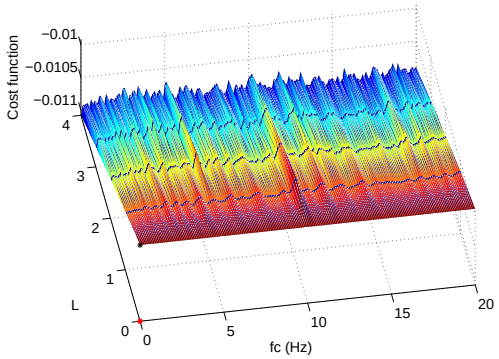

(a) Exact cost function for model order estimation in (2.28).

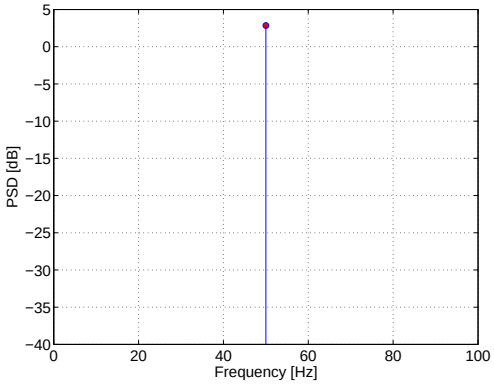

(b) PSD estimation for exact method.

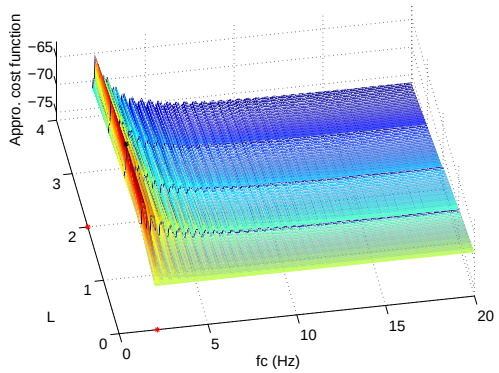

(c) Approximate cost function for model order estimation in (2.29).

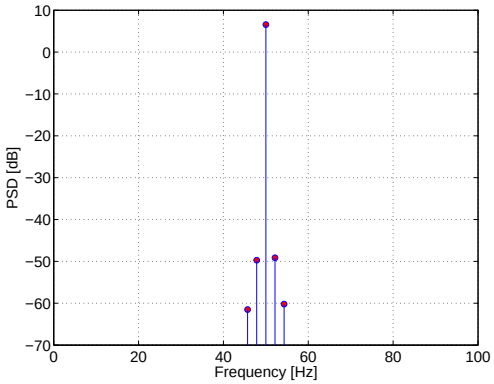

(d) PSD estimation for approximate method.

Figure 2.8: Exact and approximate MLE cost function and related PSD estimation without sidebands.

2.4.1 Parameters estimation

Let's construct the $M \times 1$ column sub-vectors, $\mathbf{x}[n]$, which contains M consecutive samples of the observed signal of length N as given by figure 2.9. It must be stressed that, for $\mathbf{A}(\Omega)$ to be full rank, the sub-vectors length M must be greater than $2 \times L + 1$ and the fault characteristic frequency should be a non zero. Moreover, the mathematical considerations are based on [101].

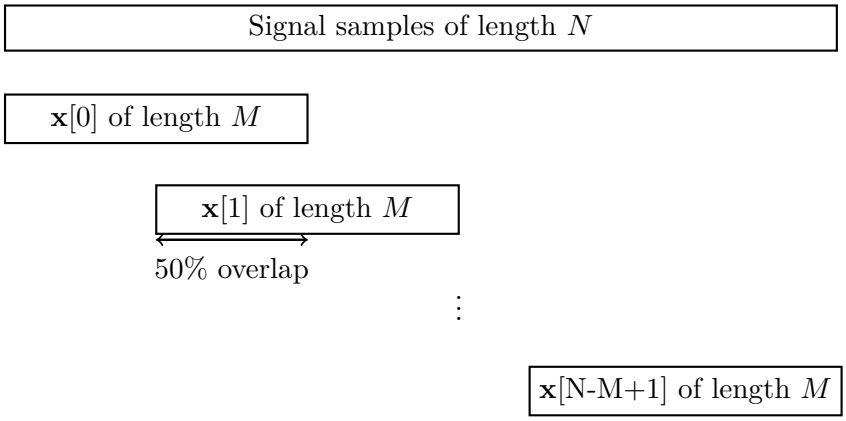

Figure 2.9: Signal segmentation.

Using the signal model in (2.4), we propose to estimate the model parameters, namely f_s, f_c and the amplitudes a_l, from $x[n](n = 0, \cdots, N-1)$, where N corresponds to the signal length.

2.4.1.1 Frequency Estimation

Assuming that $\mathcal{H}_4$ Holds, the covariance matrix of the analytical signal $\mathbf{z}[n]$, computed from the real signal $\mathbf{x}[n]$ is given by

$$\begin{aligned}\mathbf{R} =& E\{\mathbf{z}[n]\mathbf{z}^H[n]\} && (2.30)\\ =& E\Big\{(\mathbf{A}(\Omega)\mathbf{v}[n] + \mathbf{b}[n]) \times (\mathbf{A}(\Omega)\mathbf{v}[n] + \mathbf{b}[n])^H\Big\} && (2.31)\\ =& \mathbf{A}(\Omega)\ \mathbf{P}\ \mathbf{A}(\Omega)^H + \sigma^2\ \mathbf{I}_M && (2.32)\end{aligned}$$

where E{.} denotes the statistical expectation, $(.)^H$ refers to the Hermitian matrix transpose, $\mathbf{I}_M$ is the $M \times M$ identity matrix and

$$\mathbf{P} = E\{\mathbf{v}[n]\mathbf{v}^H[n]\}. \tag{2.33}$$

The covariance matrix eigenvalues decomposition can be written as follows

$$\mathbf{R} = \mathbf{U}\Lambda\mathbf{U}^H \tag{2.34}$$

where Λ is a diagonal matrix containing the eigenvalues $\lambda_1 \geq \cdots \geq \lambda_M$ of $\mathbf{R}$ and $\mathbf{U}$ is a unitary matrix containing the associated eigenvectors. Under the assumption $\mathcal{H}_1$

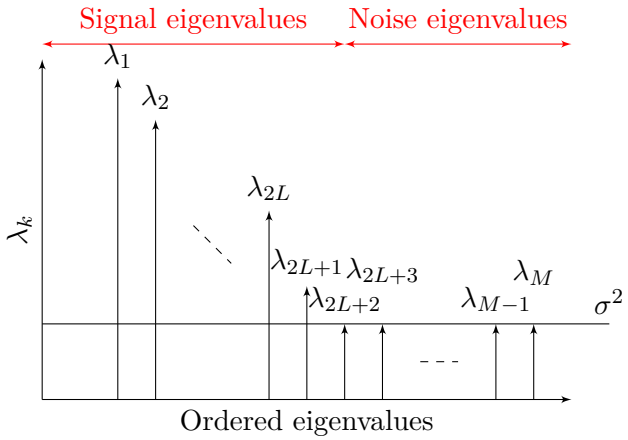

Figure 2.10: Covariance matrix eigenvalues decomposition [7].

and the fact that $\mathbf{P}$ is non-singular, the diagonal matrix Λ can be decomposed as

$$\Lambda = \begin{bmatrix} \boldsymbol{\lambda} & \mathbf{0} \\ \mathbf{0} & \sigma^2 \mathbf{I}_{M-2L-1} \end{bmatrix} \tag{2.35}$$

where $\boldsymbol{\lambda}$ is a diagonal matrix containing the $2 \times L + 1$ greatest eigenvalues of Λ. The remaining $M - 2 \times L + 1$ noise eigenvalues are theoretically equal to σ^2. Figure 2.10 shows an ordered eigenvalues distribution model for a simulated signal composed of $2 \times L + 1$ sine waves embedded in a white noise.

Let us decompose $\mathbf{U}$ as

$$\mathbf{U} = [\mathbf{S}\ \mathbf{G}] \tag{2.36}$$

where:

- $\mathbf{S}$ is a $M \times (2L + 1)$ matrix formed from the eigenvectors associated with the $2 \times L + 1$ greatest eigenvalues,
- $\mathbf{G}$ is a $M \times (M - 2L - 1)$ matrix formed from the eigenvectors associated with the $M - (2 \times L + 1)$ least significant ones.

Using (2.32), it can be shown that:

$$\mathbf{RG} = \mathbf{A}(\Omega)\ \mathbf{P}\ \mathbf{A}(\Omega)^H \mathbf{G} + \sigma^2\ \mathbf{G} \tag{2.37}$$

As $\mathbf{U}$ is a unitary matrix ($\mathbf{U}^H\mathbf{U} = \mathbf{I}_M$), $\mathbf{S}^H\mathbf{G} = \mathbf{0}$ and $\mathbf{G}^H\mathbf{G} = \mathbf{I}_{M-(2\times L+1)}$. Then, using (2.34) and (2.35) leads to

$$\mathbf{RG} = \mathbf{U}\Lambda\mathbf{U}^H\mathbf{G} \tag{2.38}$$

$$= [\mathbf{S}\ \mathbf{G}] \begin{bmatrix} \boldsymbol{\lambda} & \mathbf{0} \\ \mathbf{0} & \sigma^2\mathbf{I}_{M-2L-1} \end{bmatrix} \begin{bmatrix} \mathbf{S}^H \\ \mathbf{G}^H \end{bmatrix} \mathbf{G} \tag{2.39}$$

$$= [\mathbf{S}\ \mathbf{G}] \begin{bmatrix} \boldsymbol{\lambda} & \mathbf{0} \\ \mathbf{0} & \sigma^2\mathbf{I}_{M-2L-1} \end{bmatrix} \begin{bmatrix} \mathbf{0} \\ \mathbf{I}_{M-(2\times L+1)} \end{bmatrix} \tag{2.40}$$

$$= [\mathbf{S}\ \mathbf{G}] \begin{bmatrix} \mathbf{0} \\ \sigma^2\mathbf{I}_{M-(2\times L+1)} \end{bmatrix} \tag{2.41}$$

$$= \sigma^2\mathbf{G}. \tag{2.42}$$

Substituting (2.42) in (2.37), we obtain the following result

$$\mathbf{A}(\Omega)\ \mathbf{P}\ \mathbf{A}(\Omega)^H\mathbf{G} = \mathbf{0} \tag{2.43}$$

which readily implies

$$\mathbf{A}(\Omega)^H\mathbf{G} = \mathbf{0}. \tag{2.44}$$

In practice, $\mathbf{R}$ is unknown, but it can be estimated from the available data samples $\mathbf{z}[n]$ as

$$\widehat{\mathbf{R}} = \frac{1}{N-M+1}\sum_{n=0}^{N-M}\mathbf{z}[n]\mathbf{z}[n]^H \tag{2.45}$$

Let $\widehat{\mathbf{U}} = [\widehat{\mathbf{U}}_s\ \widehat{\mathbf{G}}]$ be its corresponding eigenvectors, the set Ω can be found as follows

$$\{\widehat{\Omega}\} = \arg\max_{\Omega} \jmath_m(\Omega) \tag{2.46}$$

where

$$\jmath_m(\Omega) = \frac{1}{\left\|\mathbf{A}(\Omega)^H\widehat{\mathbf{G}}\right\|_F^2} \tag{2.47}$$

and where $\|.\|_F^2$ denotes the Frobenius norm. If $\widehat{\mathbf{G}} = \mathbf{G}$, (2.44) and (2.47) show that the cost function $\jmath(\Omega)$ tends to infinity for $\widehat{\Omega} = \Omega$. In practice, as $\widehat{\mathbf{G}} \approx \mathbf{G}$, $\jmath_m(\Omega)$ has a finite value. Figure 2.11 displays the cost function for a synthetic signal with $f_s = 50$Hz, $f_c = 10$Hz, $L = 2$ and $SNR = 50\ dB$ and the corresponding PSD estimation. One can note that the cost function exhibits a well-defined peak at $f_s = 50$Hz and $f_c = 10$Hz.

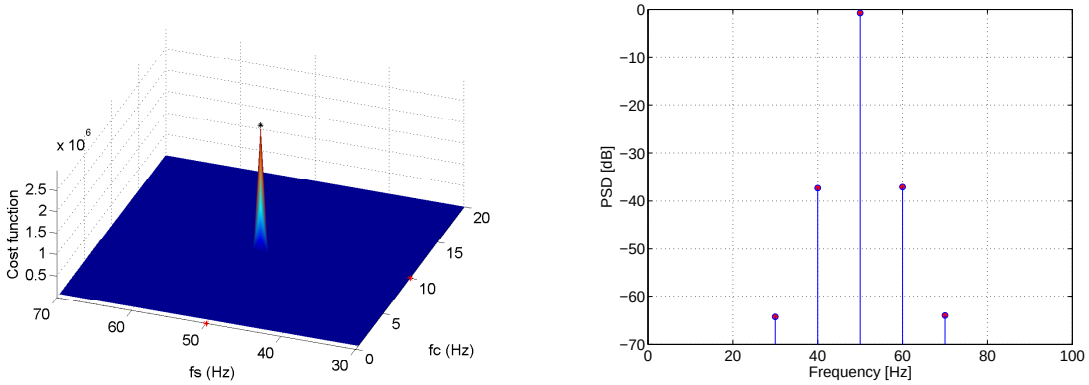

(a) Cost function $\mathcal{J}_m(\Omega)$.

(b) PSD estimation.

Figure 2.11: Multidimensional MUSIC for the estimation of f_s and f_c.

Concerning the implementation, the proposed approach leads to $2D$ optimization problem while the classical MUSIC described in (2.47) tracks $2L+1$ peaks in $1D$ cost function.

The amplitudes of the frequency components convey the information about the fault severity. These amplitudes are contained in the vector $\mathbf{v}[n]$. Given the fundamental frequency and the fault related frequency, the frequencies amplitude can be computed using the maximum likelihood estimator (MLE) of $\mathbf{v}[n]$. This estimator is denoted $\widehat{\mathbf{v}}[n]$ and given by

$$\widehat{\mathbf{v}} = \left(\sum_{n=0}^{G-1} \mathbf{A}(\Omega)^H \mathbf{A}(\Omega) \right)^{-1} \times \sum_{n=0}^{G-1} \mathbf{A}(\Omega)^H \mathbf{x}[n] \tag{2.48}$$

where G is the number of the sub-vectors which is equal to $G = N - M + 1$.

Figure 2.11 shows the cost $\mathcal{J}_m(\Omega)$ and the PSD estimation based on MD MUSIC. Figure 2.11(a) gives the MD MUSIC cost function. I can be observed that this cost function exhibits a distinct peak at the true values of f_s and f_c. Figure 2.11(b) shows the PSD of synthetic signal. The amplitudes have been computed using the structure of $\mathbf{v}[n]$ given by (2.5). Similarly to the MLE, the MD MUSIC allows to estimate the PSD and then to show the presence of sidebands.

2.4.2 Order estimation for MD MUSIC

It must be noted that the optimization of the cost function and the computation of the signal PSD require the knowledge of the number of sinusoids in noise. In fact, the proposed approach requires a priori knowledge about the number of sidebands L for the evaluation of the cost function. More specifically, this approach may lead to a wrong identification of the noise subspace in (2.36), and this, in turn, leads to the spurious estimates reported in [152]. The estimated noise subspace and signal subspace orthogonality holds only when the estimated frequencies are equal to the true frequencies value and the model order L is appropriately chosen. Herein, we extend the MD MUSIC estimation algorithm for jointly estimating both the fundamental frequency, the fault characteristic frequency and the model order. In fact, if the number of sidebands is unknown, the cost function can be modified to take into account the estimation of L. By following the same approach as in [153], it can be shown that the fundamental frequency, the fault characteristic frequency, and the number of sidebands L can be estimated as follows.

$$\left\{\widehat{\Omega}, \widehat{L}\right\} = \arg \max_{\Omega} \max_{L} \jmath_{mj}(\Omega, L) \tag{2.49}$$

where, the three-dimensional cost function $\jmath_{mj}$, depending on Ω and L, is given by

$$\jmath_{mj}(\Omega, L) = \frac{(2L+1)M(M-2L-1)}{\left\|\mathbf{A}(\Omega)^H \widehat{\mathbf{G}}\right\|_F^2}. \tag{2.50}$$

For a grid connected induction machine, the supply frequency f_s can be assumed to be known. Thus, exploiting this assumption, the cost function reduces to a two-dimensional one and the optimization problem can be solved using a two-dimensional grid search. Figure 2.12 displays the proposed cost function for estimating the number of sidebands L, assuming that the fundamental frequency f_s is known. The synthetic signal is the same as the one of Fig. 2.3 ($L = 2$, $f_c = 10$Hz). This figure shows that the proposed method correctly estimates L and f_c.

2.4.3 Efficient implementation of MD MUSIC

The MD MUSIC may be computationally expensive. This computational cost is due to the computation of the eigenvalue decomposition (EVD) of the covariance matrix in

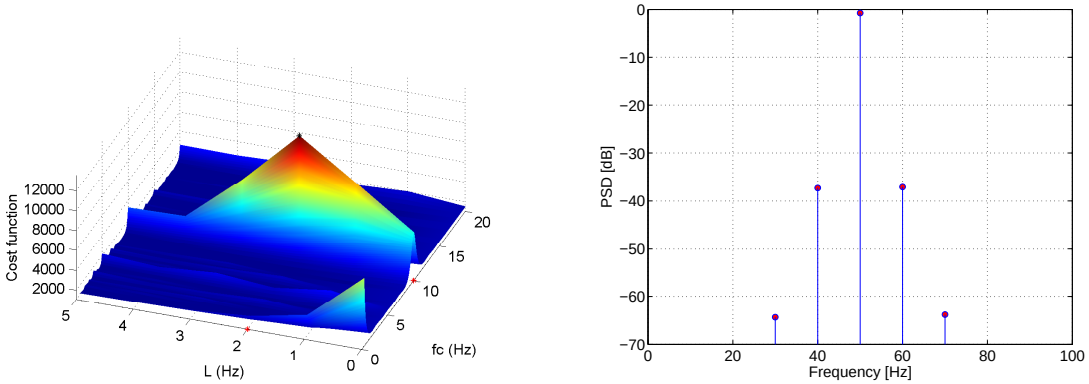

(a) Cost function $\jmath_{mj}(\Omega)$.

(b) PSD estimation.

Figure 2.12: Multidimensional MUSIC cost function for the estimation of L and f_c.

(2.45) and the $3-D$ optimization problem in (2.49). In the following, we will show how this algorithm can be implemented efficiently [153]. Let us define the Fourier matrix $\mathbf{F} \in \mathbb{C}^{F\times F}$, with $F \gg N$, as

$$\mathbf{F} = \begin{bmatrix} 1 & 1 & 1 & \dots & 1 \\ 1 & z^1 & z^2 & \dots & z^{(F-1)} \\ \vdots & \vdots & \vdots & \vdots & \\ 1 & z^{F-1} & z^{2(F-1)} & \dots & z^{(F-1)(F-1)} \end{bmatrix} \tag{2.51}$$

where $z = e^{-j2\pi/F}$. Next, let's define a matrix $\mathbf{D} \in \mathbb{R}^{F\times M}$ containing the squared absolute values of the inverse $FFTs$ of the zero-padded eigenvectors in $\mathbf{U}$ given by (2.34) as

$$[\mathbf{D}]_{lm} = \left| \left[\mathbf{F}^H \begin{bmatrix} \mathbf{U} \\ 0 \end{bmatrix} \right]_{lm} \right|^2 \tag{2.52}$$

with $[\mathbf{D}]_{lm}$ being the $(l,m)^{th}$ element of $\mathbf{D}$. For a candidate of fundamental frequency $2\pi(f_s/F)$, the fault related frequency $2\pi(f_c/F)$, and model order L, the Frobenius norm in (2.50) can be calculated as follows

$$\left\| \mathbf{A}(\Omega)^H \widehat{\mathbf{G}} \right\|_F^2 = \sum_{m=2\times L+2}^{M} \sum_{l=1}^{2\times L+1} [\mathbf{D}]_{(f_k(\Omega)l+1)m} \tag{2.53}$$

Thus, the complexity of calculating the cost function given by (2.49) for different f_s, f_c, and L can be significantly reduced by calculating the inverse FFT of all eigenvectors

once for each given data set. We note that some of the eigenvectors, corresponding to the largest eigenvalues, can be excluded from definition of (2.52), since there is a lower bound on L. Finally, a sufficiently accurate results at a reasonable computational complexity using the FFT-based method is obtained by maximizing the following cost function:

$$\mathcal{J}_c(\Omega, L) = \frac{(2L+1)M(M-2L-1)}{\sum_{m=L+1}^{M}\sum_{l=1}^{L}[\mathbf{D}]_{(f_k(\Omega)l+1)m}}. \tag{2.54}$$

Similarly to the approximate MLE, the relation above gives the relationship between the MUSIC and the Fourier transform which can be implemented efficiently using the FFT algorithm. This method gives a coarse estimator of the fundamental frequency, the fault related frequency, and the model order L. This efficient implementation is more appropriate for faults parameters tracking especially for fast varying parameters. If very accurate estimates are desired, a refined estimate can be found using the original cost function associated with adapted optimization procedure.

2.5 Fault detection scheme

When dealing with fault detection in induction machines, we want to be able to decide between healthy operating conditions and faulty ones. Therefore, the problem is equivalent to a binary hypothesis test.

In this section, we propose a fault detection criterion based on the amplitude of the fault characteristic frequencies. The decision will be based on the value of this criterion.

2.5.1 Fault detection criterion

In order to successfully perform fault detection, a fault criterion is needed to measure the machine state. As the information about the fault severity is carried out by a_k ($k \neq 0$), we propose to compute the sum of the squares of the (normalized) amplitude of the fault characteristic frequencies. The proposed criterion is expressed mathematically as

$$\mathcal{C} = \sum_{k=-L, k\neq 0}^{L} \left(\frac{a_k^2}{a_0^2}\right) \tag{2.55}$$

This criterion is inspired from the total harmonic distortion (THD) of a signal which is a measurement of the harmonic distortion present and is defined as the ratio of the sum of the powers of all harmonic components to the power of the fundamental frequency [154].

The proposed criterion in (2.55) exhibits the two following desirable properties:

Property 1 *For healthy machines, the criterion is equal to 0 i.e.*

$$\mathcal{C} = 0 \tag{2.56}$$

Property 2 *The proposed criterion is invariant to scale. Indeed, let us denote $\mathcal{C}_x$ the fault criterion relative to the stator current $x[n]$. It can be easily demonstrated that the fault criterion $\mathcal{C}_{\alpha x}$, relative to the signal $\alpha x[n]$ ($\alpha > 0$), is equal to:*

$$\mathcal{C}_{\alpha x} = \mathcal{C}_x \tag{2.57}$$

The proposed criterion in (2.55) depends on the amplitudes a_k ($k = -L, \cdots, L$). However, using the structure of $\mathbf{v}$ in (2.5), it can be shown that $\mathcal{C}$ can be obtained directly from $\mathbf{v}$ without computing a_k. By using (2.5), we obtain:

$$\begin{aligned} \mathbf{v}^T\mathbf{v} &= \sum_{k=-L}^{L} a_k^2 \cos^2(\phi_k) + \sum_{k=-L}^{L} a_k^2 \sin^2(\phi_k) \\ &= \sum_{k=-L}^{L} a_k^2 \end{aligned} \tag{2.58}$$

Introducing the $(4L+2) \times (4L+2)$ matrix $\mathbf{M}$ given by

$$\mathbf{M} = \begin{bmatrix} \mathbf{E}_{L+1,L+1} & \mathbf{0} \\ \mathbf{0} & \mathbf{E}_{L+1,L+1} \end{bmatrix} \tag{2.59}$$

where $\mathbf{E}_{u,v}$ is the $(2L+1) \times (2L+1)$ elementary matrix which is 1 in the u^{th} row and v^{th} column and is zero elsewhere, we also get:

$$\begin{aligned} \mathbf{v}^T\mathbf{M}\mathbf{v} &= [0 \cdots 0 \; a_0 \cos(\phi_0) \; 0 \cdots 0 - a_0 \sin(\phi_0) 0 \cdots 0]\mathbf{v} \\ &= a_0^2 \cos^2(\phi_0) + a_0^2 \sin^2(\phi_0) \\ &= a_0^2 \end{aligned} \tag{2.60}$$

The two equations in (2.58) and (2.60) lead to the following result:

$$\frac{\mathbf{v}^T\mathbf{v}}{\mathbf{v}^T\mathbf{M}\mathbf{v}} - 1 = \left(\sum_{k=-L}^{L} \frac{a_k^2}{a_0^2}\right) - \frac{a_0^2}{a_0^2} \tag{2.61}$$

$$= \sum_{k=-L,k\neq 0}^{L} \left(\frac{a_k^2}{a_0^2}\right) = \mathcal{C} \tag{2.62}$$

Finally, the fault criterion in (2.55) can be expressed under the following matrix form as

$$\mathcal{C} = \frac{\mathbf{v}^T\mathbf{v}}{\mathbf{v}^T\mathbf{M}\mathbf{v}} - 1 \tag{2.63}$$

In practice, one should note that $\mathbf{v}$ is unknown and must be replaced by its estimate $\widehat{\mathbf{v}}$ in (2.63) to compute $\mathcal{C}$.

2.5.2 MLE based implementation

Following the preceding considerations, a fault detection algorithm based on the MLE spectral analysis is presented first. The fault detection approach is summarized in **Algorithm** 1. First the stator current is acquired and its PSD is estimated by estimating the fundamental frequency and the characteristic fault frequency and corresponding amplitudes. The number of sidebands L informs about the existence of a fault. Once the fault is present, the algorithm allows to estimate its severity through the criterion presented earlier in (2.55).

The approximate method based fault detection scheme is slightly different from the exact algorithm described in (1). The estimation of the model order in the case of approximate method can not inform about existence of fault since it estimates erroneously the sidebands number in the case of healthy machine. Consequently, it is mandatory to compute the proposed criterion and then set a threshold based fault detection decision scheme in order to discriminate healthy operating condition and from faulty one. **Algorithm** 2 describes the approximate algorithm.

The MLE-based fault detection scheme is summed up in Fig. 2.13. This algorithm can be implemented for real-time monitoring of an induction machine. Compared to other PSD-based monitoring technique (Periodogram, MUSIC, ESPRIT), the proposed approach is quite attractive since the vector $\mathbf{v}$ directly conveys information about the characteristic frequencies. The algorithms presented above allow to extract automatically the fault related frequencies and to compute a fault detection criteria without

Algorithm 1 Exact MLE estimation-based fault severity criteria.

Require: N -data samples $\mathbf{x}[n]$**.**

1: Compute the MLE exact cost function in (2.28) for f_s and f_c estimation,

2: Optimization procedure in order to find $\widehat{\Omega}$ and $\widehat{L}$,

if $\widehat{L} = 0$ **then**
$fault = 0$
$\mathcal{C} = 0$
else
$fault = 1$
Estimate $\widehat{\mathbf{v}}$ with (2.14)
Compute fault detection criterion $\mathcal{C}$ using (2.63)
end if

3: **Return** $\widehat{\Omega}$, $\widehat{L}$, $fault$, $\widehat{\mathbf{v}}$ and $\mathcal{C}$.

Algorithm 2 Approximate MLE estimation-based fault severity criteria.

Require: N -data samples $\mathbf{x}[n]$**.**

1: Compute the approximate cost function in (2.29),

2: Optimization procedure in order to find $\widehat{\Omega}$ and $\widehat{L}$,

3: Estimate $\widehat{\mathbf{v}}$ with (2.24)),

4: Compute the fault detection criterion $\mathcal{C}$ using (2.63),

5: Threshold based decision procedure ($\mathcal{S}$ is the threshold),

if $\mathcal{C} < \mathcal{S}$ **then**
$fault = 0$
else
$fault = 1$
end if

6: **Return** $\widehat{\Omega}$, $\widehat{L}$, $fault$, $\widehat{\mathbf{v}}$ and $\mathcal{C}$.

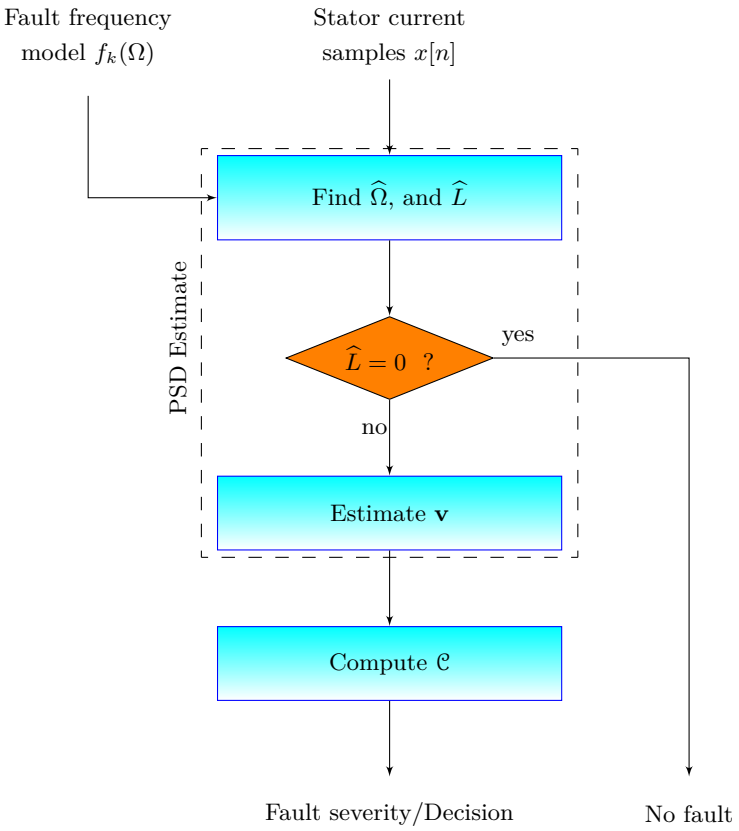

Figure 2.13: Fault detection scheme proposed.

need to an expert to interpret the current spectrum. The MLE-based fault detection does not require any further post-processing to determine fault indicator. In fact, if predicted frequency patterns are present in the MLE-based PSD, a fault exist and the criterion is computed in order to determine its severity.

The optimization may be performed, for example, using the grid search, the genetic algorithms, the neural networks, etc. This issue is discussed in the the section 2.7.1.

2.5.3 MD MUSIC based implementation

The MD MUSIC is an alternative to the proposed MLE method. Similarly to the MLE methods, the MD MUSIC is based on the 3-D optimization problem. It estimates the three parameters required to state on the health operating condition of the induction machine. Once the characteristic fault frequency is estimated, the MLE of $\mathbf{v}$ is used

to estimate the fault detection criterion. The MD MUSIC technique is described by **Algorithm** 3.

Algorithm 3 MD MUSIC estimation-based failure severity criteria.

Require: N -data samples $\mathbf{x}[n]$**.**

1: Compute the covariance matrix using (2.45).

2: Compute the MD MUSIC cost function in (2.49) or (2.54),

3: Optimization procedure in order to find $\widehat{\Omega}$ and $\widehat{L}$,

if $\widehat{L} = 0$ **then**
$fault = 0$
$\mathcal{C} = 0$
else
$fault = 1$
Estimate $\widehat{\mathbf{v}}$ with (2.48)
Compute fault detection criterion $\mathcal{C}$ using (2.63)
end if

4: **Return** $\widehat{\Omega}$, $\widehat{L}$, $fault$, $\widehat{\mathbf{v}}$ and $\mathcal{C}$.

2.6 Non-stationary parametric spectral estimation techniques

The parametric estimation methods and the classical spectral estimation are well suited for signals with stationary frequency content, i.e. frequencies that dot not vary with respect to time. However, most industrial applications are equipped with variable speed drives. Moreover, in the case of generator application, the environment may be non-stationary. Hence, the supply voltage and the stator current can contain time-varying frequencies.

A suitable signal processing technique would be able to track the fault characteristic frequency and the corresponding criterion over time. As it has been discussed in Chapter 1, this can be realized using time-frequency approaches or time-scale techniques. In the following sections, the extension of the parametric methods to the non-stationary signals is performed. The fault detection algorithm uses a recursive maximum likelihood

estimator to track the time-varying fault characteristic frequency and the related energy. The MD MUSIC is also extended in order to take into account the non-stationary signals.

The performance of the proposed approaches has been demonstrated using synthetic signals. These signals correspond to the model proposed for modeling the stator currents under fault condition and allow to highlight some interesting proprieties of the proposed approaches.

2.6.1 Mathematical formulation

In this section, we consider a stator current signal model composed of $2 \times L + 1$ sinusoids. The signal is assumed to be corrupted by an additive white noise. At time n=0,1,2,3... the observed stator current vector $\mathbf{x}(n) \in \mathbb{R}^m$, defined as $\mathbf{x}(n) = \Big[x(n)...x(n+M-1)^T\Big]$, is modeled as

$$\mathbf{x}(n) = \mathbf{A}(\Omega(n))\mathbf{v}(n) + \mathbf{b}(n) \tag{2.64}$$

where:

- $\mathbf{b}(n) = [b[n], \cdots, b[n+M-1]]^T$ is a $M \times 1$ column vector containing the noise samples,
- $\mathbf{v}(n)$ is a $2(2L+1) \times 1$ column vector containing the amplitudes and phases of the characteristic fault frequencies. This vector is given by

$$\mathbf{v}(n) = [a_{-L}\cos(\phi_{-L}) \dots a_L \cos(\phi_L), -a_{-L}\sin(\phi_{-L}) \dots - a_L \sin(\phi_L)]^T \tag{2.65}$$

- $\mathbf{A}(\Omega(n))$ is a $N \times 2(2L+1)$ matrix given by

$$\mathbf{A}(\Omega(n)) = [\mathbf{z}_{-L}(n) \dots \mathbf{z}_L(n), \mathbf{y}_{-L}(n) \dots \mathbf{y}_L(n)] \tag{2.66}$$

where:

$$\mathbf{z}_k(n) = \begin{bmatrix} 1 \\ \cos\left(2\pi f_k(\Omega(n)) \times \frac{1}{F_s}\right) \\ \vdots \\ \cos\left(2\pi f_k(\Omega(n)) \times \frac{M-1}{F_s}\right) \end{bmatrix} \qquad \mathbf{y}_k(n) = \begin{bmatrix} 0 \\ \sin\left(2\pi f_k(\Omega(n)) \times \frac{1}{F_s}\right) \\ \vdots \\ \sin\left(2\pi f_k(\Omega(n)) \times \frac{M-1}{F_s}\right) \end{bmatrix} \tag{2.67}$$

Since $\mathbf{x}[n]$ has length M and we have N observations of $x[n]$, we can thus construct a set of $G = N - M + 1$ different sub-vectors $\{\mathbf{x}[n]\}_{n=0}^{G-1}$. There is some inherent tradeoffs in choices of N and M and thereby G [155].

– $\Omega(n)$ is a set of parameters to be estimated depending on the fault.

The problem is then, to estimate the fundamental frequency, the fault characteristic frequency and their amplitudes for fault characterization at each time n. The computation of the current spectrum from stator current samples $\mathbf{x}(n)$ is treated as a statistical estimation problem. The observation noise $\mathbf{b}(n)$ is assumed to be zero-mean white Gaussian distributed with variance σ^2.

2.6.2 Non-stationary MLE

In this section, we present a maximum likelihood (ML) based fault characteristic frequency estimation and model order estimation in non-stationary context. Then, we explore a fault criterion estimation for decision making.

2.6.2.1 Estimate of $\Omega(n)$

The algorithm operates on a signal sub-vectors at times n. Although the approach of splitting the signal into sub-vectors is inherently suboptimal since it ignores inter-vector dependencies, it is required in order to estimate signal and noise covariance matrices. For multiple observation vectors, the ML estimate of $\Omega(n)$ can be shown to be the maximum of the following cost function [155]

$$\mathcal{J}(\Omega(n)) = -Tr\{\mathbf{A}(\Omega(n))\mathbf{A}^{\dagger}(\Omega(n))\mathbf{R}(n)\} \tag{2.68}$$

with

– $\mathbf{A}^{\dagger}(\Omega(n))$ is the pseudo-inverse of $\mathbf{A}(\Omega(n))$ i.e.

$$\mathbf{A}^{\dagger}(\Omega(n)) = \left(\mathbf{A}^{T}(\Omega(n))\mathbf{A}(\Omega(n))\right)^{-1}\mathbf{A}^{T}(\Omega(n)) \tag{2.69}$$

where $(.)^{-1}$ corresponds to the matrix inverse and $Tr(.)$ denotes the matrix trace.

– The covariance matrix $\mathbf{R}$(n) of the observed signal is given by (2.32).

The proposed methodology relies on this covariance matrix. In practice, the covariance matrix is unknown and must be replaced by its estimate, the sample covariance matrix. The sample covariance matrix is defined as

$$\widehat{\mathbf{R}}[n] = \frac{1}{G}\sum_{n=0}^{G-1}\mathbf{x}[n]\mathbf{x}^{H}[n] \tag{2.70}$$

Finally, $\Omega(n)$ can be estimated from this cost function as

$$\{\widehat{\Omega}(n)\} = \arg\max_{\Omega} \mathcal{J}(\Omega(n)) \tag{2.71}$$

This estimator is capable of handling non-stationary signals since the covariance matrix is estimated by dividing the signal into time segments and then, the covariance matrix is estimated with 50% overlap between segments.

2.6.2.2 Estimation of L

The estimation of L allows to distinguish the faulty machine from the healthy one. In this section, we propose the use of the same approach as in section 2.3.2 that is the MDL principle [103] for L estimation in order to enhance fault detection and afterwards accuracy while estimating the fault severity.

$$\{\widehat{\Omega}(n), \widehat{L}(n)\} = \arg\max_{\Omega,L} \; -Tr\{\Big(I_M - \mathbf{A}(\Omega(n))\mathbf{A}^{\dagger}(\Omega(n))\Big)\,\mathbf{R}(n)\} \times \exp\left(\frac{c(g,M)}{M}\right) \tag{2.72}$$

where $c\,(g, M) = g\log(M)$ is the criterion information rule, and $g = 4L + 5$ is the number of free parameters. Furthermore, I_M is the identity matrix of size M.

The cost function in (2.72) is given by Fig. 2.14 for a time segment of the signal $\mathbf{x}(n)$ when a fault exists. The model order is equal to 1. It can be seen that it allows to determine the supply frequency as well as the fault characteristic frequency.

The fault detection approach is similar to the algorithm described in **Algorithm** 1. This algorithm can be implemented for real-time monitoring of an induction machine. The non-stationary MLE is used for fault severity tracking in non-stationary environment. The fault detection scheme for fault indicator tracking is given by Fig. 2.15

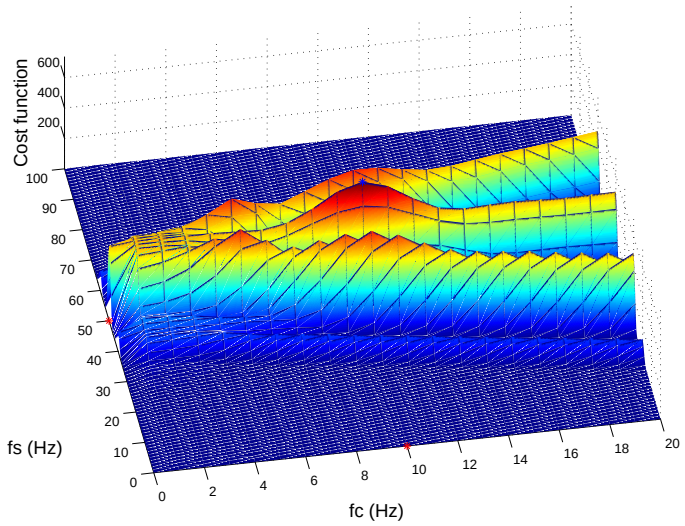

Figure 2.14: Cost function for f_c and f_s estimation (case where fault exists and $L(n) = 1$).

2.6.3 Non-stationary MD MUSIC

This section deals with the extension of the MD MUSIC on section 2.4 to the case of non-stationary signals. The covariance matrix is estimated adaptively and allows tracking the fault related frequency and fundamental frequency in the time-frequency plane. Moreover, the proposed non-stationary MD MUSIC allows tracking the fault severity.

2.6.3.1 Covariance matrix update

The implementation of the MD MUSIC-based technique has been based on batch estimation of eigenvectors of an estimate of signal covariance matrix, making them unsuitable for adaptive processing that is needed for tracking non-stationary signal parameters. In fact, the MD MUSIC described earlier is adequate when we have all the measurements. More often, we obtain new measurements and want to update our estimates. In this case, the matrix $\mathbf{A}(\Omega)$ must be augmented. We would have to recompute the estimate $\widehat{\Omega}$ and $\widehat{L}$ according to (2.50) for every new measurement. This update can become computationally expensive as the number of measurements becomes large.

This section shows how to compute the MD MUSIC estimates for non-stationary signals. More specifically, suppose we have an estimate $\widehat{\Omega}(n)$, $\widehat{L}$ after n measurements,

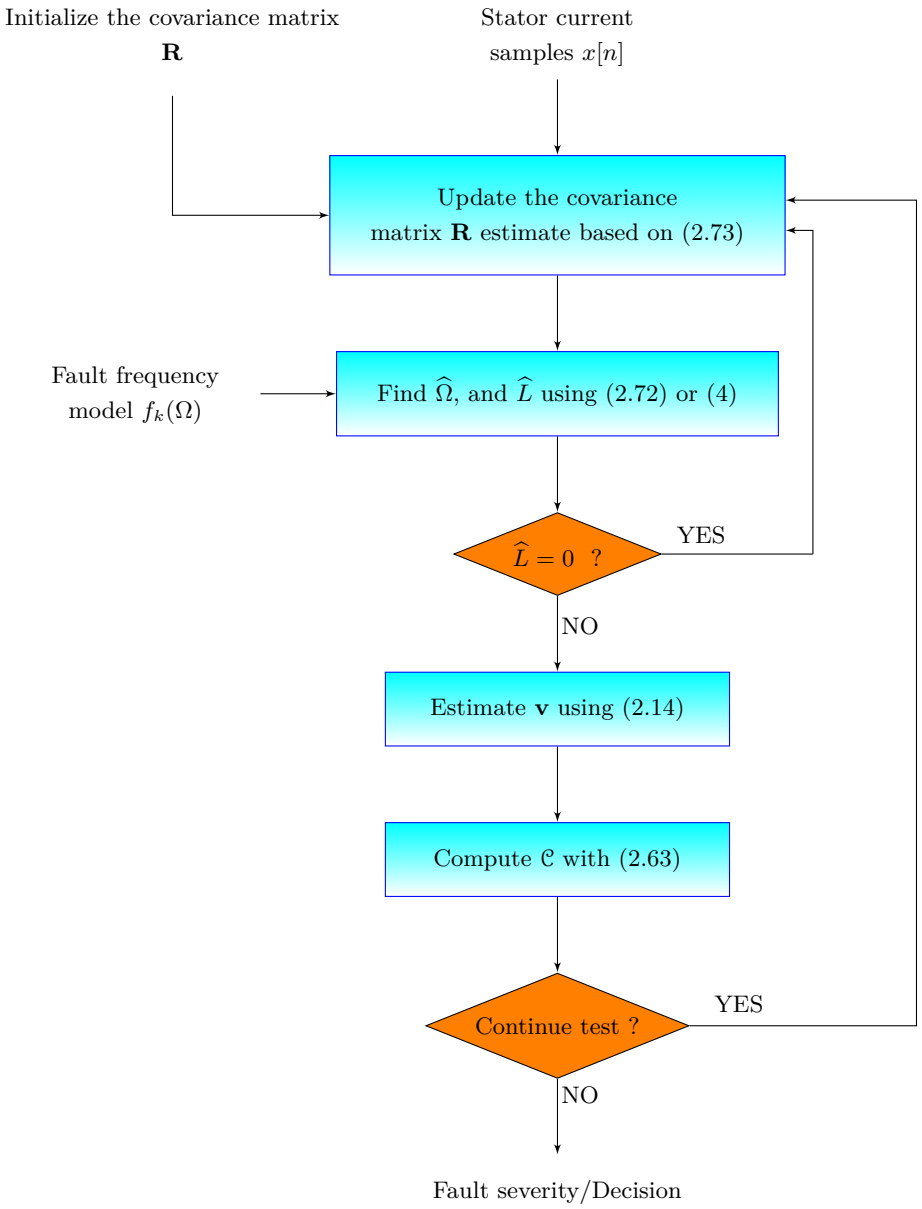

Figure 2.15: Flowchart of the proposed fault detection scheme for non-stationary operating conditions.

and obtain a new measurement $\mathbf{x}[n+1]$. We demonstrate how to update the estimate with reduced computational cost.

The proposed multidimensional MUSIC relies on the covariance matrix estimation.

Hence, it must be estimated from the observed signal. To do this in a manner that facilitates adaptivity, we employ the following estimates based on an exponential forgetting factor $0 < \lambda < 1$:

$$\mathbf{R}(n) = \lambda \mathbf{R}(n-1) + \mathbf{x}(n)\mathbf{x}^T(n) \tag{2.73}$$

The forgetting factor controls the trade-off between estimation accuracy and parameters tracking performance of the proposed algorithm. Once the covariance matrix is estimated, the frequency content and the model order L may be estimated as described in (2.50).

2.6.3.2 Non-stationary MD MUSIC for fault frequency tracking

The algorithm for recursive MD MUSIC-based fault detection technique is summarized in **Algorithm** 4.

Note that this method allows to track the fundamental frequency and the characteristic frequency. However, even though the estimation of covariance matrix is done adaptively, the computational complexity is still high.

2.7 Simulation results

2.7.1 Numerical optimization

The algorithms described earlier require a 3-D cost function maximization. Unfortunately, the maximum of these cost functions cannot be found analytically. Furthermore, the cost function derivative is not easier to compute analytically which consequently means that the Newton-based methods for fitness function optimization implementation is far from being trivial. Moreover, the cost functions are highly multimodal. Hence, numerical optimization techniques adapted to multimodal functions with various local minima and maxima are required.

Since the search space is relatively limited, a fixed grid search has first been implemented. This algorithm is based on the evaluation the cost function at the vertices of a rectangular grid, and chooses the vertex with the highest value. It should be noted that the maximization step could be computationally demanding since it requires the construction and the inversion of a large matrix for each vertex of the grid. This method

Algorithm 4 Non-stationary MD MUSIC-based fault severity criteria tracking.

Require: N -data samples $\mathbf{x}[n]$.

1: Initialize the estimator.,

(a) Estimate covariance matrix

$$\widehat{\mathbf{R}}_0 = \frac{1}{N-M+1}\sum_{n=0}^{N-M}\mathbf{x}[n]\mathbf{x}[n]^H$$

(b) Estimate $\widehat{\Omega}_0$ and $\widehat{L}_0$ by maximizing the following cost function

$$\mathcal{J}_c(\Omega, L) = \frac{(2L+1)M(M-2L-1)}{\left\|\mathbf{A}(\Omega))^H\widehat{\mathbf{G}}\right\|_F^2}.$$

2: Iterate the following two steps,

(a) Obtain new M measurements, assuming that it is given by the equation in (2.64)

(b) Update the estimates $\widehat{\Omega}(n)$, $\widehat{L}(n)$ sequentially as follows

- Updating the covariance matrix as in (2.73)
- Maximizing the cost function giving by

$$\mathcal{J}_c(\Omega, L) = \frac{(2L+1)M(M-2L-1)}{\left\|\mathbf{A}(\Omega)^H\widehat{\mathbf{G}}\right\|_F^2}.$$

if $\widehat{L}(n) = 0$ **then**
  $fault = 0$
  $\mathcal{C}(n) = 0$
else
  $fault = 1$
  Estimate $\widehat{\mathbf{v}}$ with (2.14)
  Compute fault detection criterion $\mathcal{C}$ using (2.63)
end if

3: **Return** $\widehat{\Omega}(n)$, $\widehat{L}(n)$, $fault$, $\widehat{\mathbf{v}}(n)$ and $\mathcal{C}(n)$.

has the advantage of delivering the global maximum in the search space with respect to the chosen grid. However, its computation is time-intensive and the discretization of the search space may lead to inaccurate results.

There exist several methods, how to find some suitable solution such as hill climbing, tabu search, simulated annealing and genetic algorithm. The solution found by these methods are often considered as good solution, because it is not often possible to prove what is the real optimum.

A fast class of optimization algorithms are the evolutionary algorithms. They imitate mechanisms inspired by biological evolution, such as reproduction, mutation, recombination, and selection. Candidate solutions to the optimization problem play the role of individuals in a population, and the fitness function determines the environment within which the solutions exist. Evolutionary algorithm techniques include evolutionary programming, evolution strategies, and genetic algorithms (GA) [156, 157].The latter have been chosen for our application.

Genetic algorithms are inspired by Darwin's theory about evolution [156]. Algorithm is started with a set of solutions represented by chromosomes and called population. Solutions from one population are evolved to a new population with the motivation of heading toward better solutions. The solutions selected to form the new generation are chosen according to their fitness (the fitness is usually the value of the cost function in the optimization problem being solved). In fact, the more fit individuals are stochastically selected from the current parents. Then, each individual is modified using genetic operators such as reproduction, crossover, and mutation to form a new generation. The new generation of candidate solutions is then used in the next iteration of the algorithm. This is repeated until some condition (for example maximum number of generations has been produced or improvement of the best solution) is satisfied.

The general principle of the genetic algorithm is displayed in Fig. 2.16. It illustrates the basic steps involved in using the GA and describes the different genetic operators used to evolve the population candidates.

2.7.2 Stationary fault detection approach

This section studies the proposed algorithms on synthetic signals corresponding to the model described in (2.1). Tests with simulated signals are carried out in order to

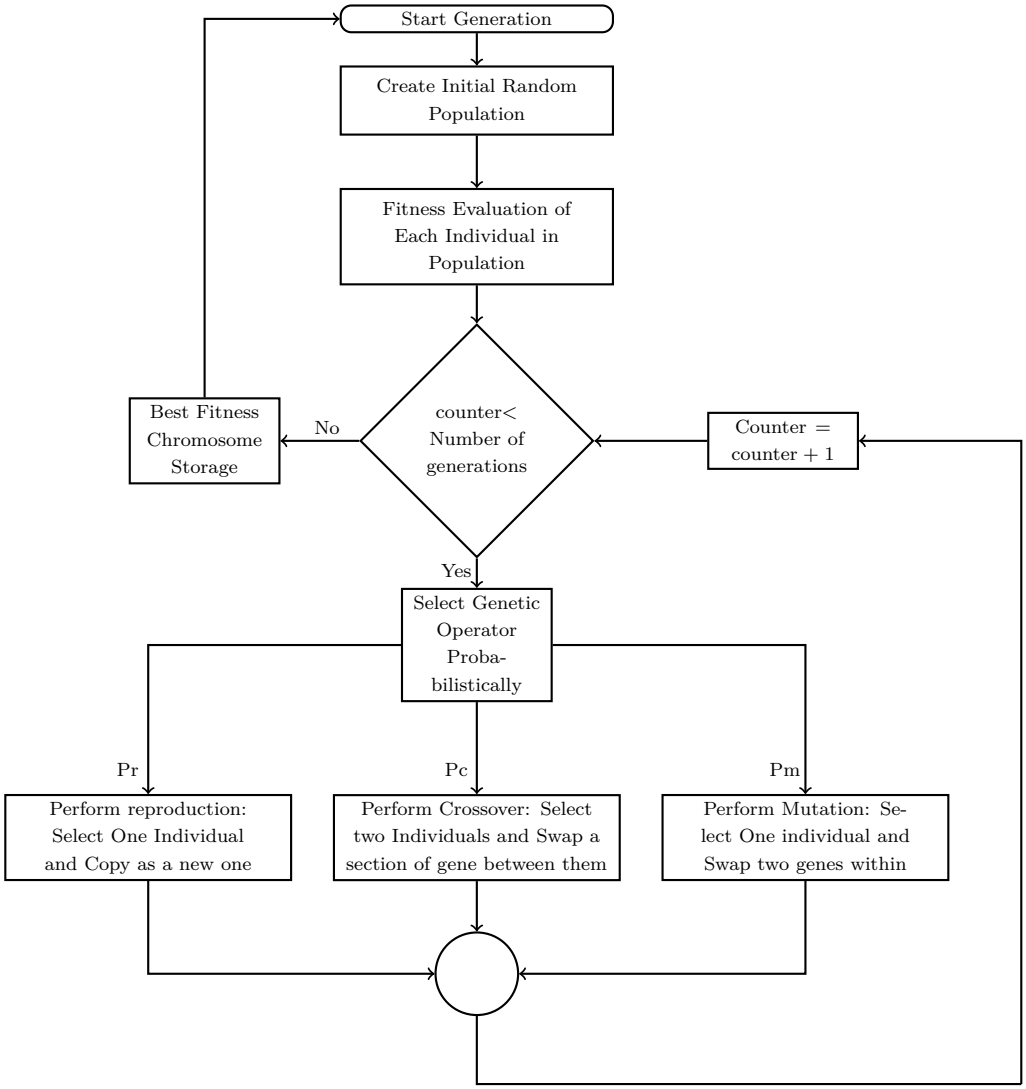

Figure 2.16: Scheme of the genetic algorithm optimization procedure [8, 9].

verify the efficiency of the proposed approaches.

2.7.2.1 Fixed model order

The proposed approaches are demonstrated on the model signal described in section 2.2. The synthetic signal used is similar to the one presented in section 1.4.1. The proposed approaches have been operated on 1 s signal segments. For each segment the model order, the fundamental frequency and the characteristic frequency are constants. From a segment to another, the sidebands frequency and amplitude vary linearly with

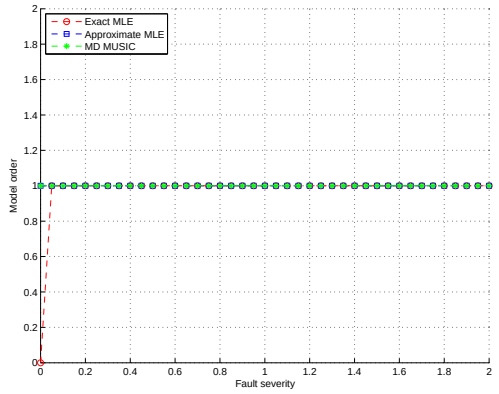

(a) Model order.

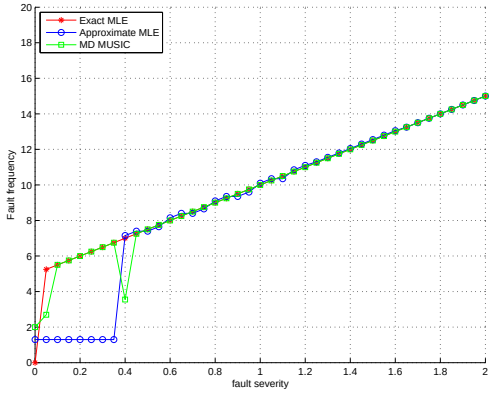

(b) Fault frequency.

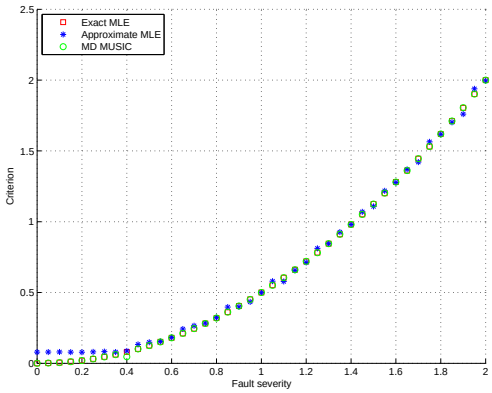

(c) Fault detection criterion.

Figure 2.17: Proposed approaches on synthetic signal: L, f_c, and criterion $\mathcal{C}(n)$ estimation for fault severity increasing.

respect to time. The sampling frequency is equal to 1kHz. Figure. 2.17 gives the simulation results for a fixed model order $L = 1$, $SNR = 50$dB, and a fault severity measured using the proposed criterion.

It can be concluded from these figures that the exact MLE and MD MUSIC algorithms track correctly the fault frequency and model order. Even though the MD MUSIC may estimate erroneously the fault related frequency probably due to convergence problems of the optimization algorithm, the fault detection criterion is estimated correctly. However, the approximate MLE does not estimate correctly the fault related frequency for lower fault severity. This is due to sidelobes in the Fourier transform (due to windowing) which are interpreted by the algorithm as fault related components. De-

spite of this limitations, the approximate MLE gives results similar to the exact MLE and MD MUSIC when the fault severity is high but overestimate the fault severity when the fault severity is low or non-existent.

2.7.2.2 Time-varying model order

In order to test the proposed approaches for model order estimation, a synthetic signal corresponding to the model depicted in Fig. 2.1 with time-varying model order has been used. The proposed approaches have been operated on 1 s signal segments. For each segment, the fundamental frequency is constant. From a segment to another, the sidebands frequency and amplitude vary linearly with respect to time. Moreover, the model order is also varying. The sampling frequency is equal to 1kHz.

Figure 2.18 gives the simulation results for estimating the model order L, f_c, and criterion $\mathcal{C}$.

It is clear from these results that the MLE-based approach tracks correctly the signal parameters. In fact, when the fault is absent, the model order and the corresponding criterion are zero. As the fault appears and the severity increases, the criterion estimated increases as well. Hence, it can be assumed that this approach may perform well for fault detection in induction machine on simulated and experimental stator currents data issued from actual process.

The model order estimation based on the approximate MLE is underestimated. However, according to the results shown in Fig. 2.18(c) the proposed fault detection criterion approximate MLE based estimator is similar to the once given by the MLE and the MD MUSIC. Thus, the approximate MLE gives results equivalent to those given by the exact MLE when the signal length is sufficiently large (the assumption made in order to extract the approximate MLE must hold).

Concerning the MD MUSIC, it is obvious from Fig. 2.18 that the model order is not reliable for fault detection. It is mandatory to estimate the fault criterion in order to get an idea about the health state of the machine. In fact, the performance of the MD MUSIC depends on the covariance matrix estimation.

To summarize, we can assume that the studied approaches exhibit the existence of the fault and allow to track its severity over the time. However, the MLE and the MD MUSIC are more suited when the fault severity is low.

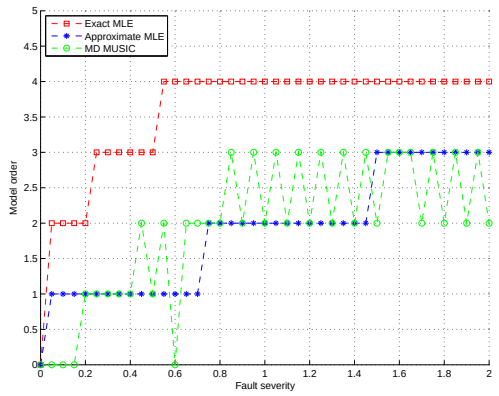

(a) Model order increasing.

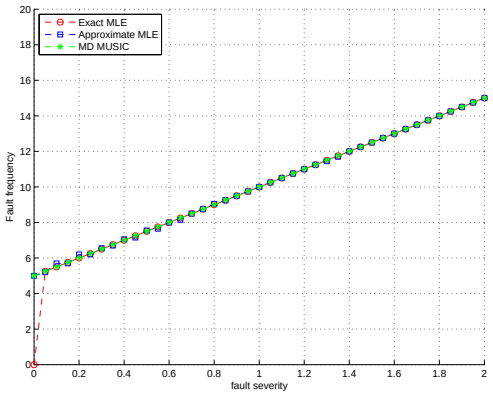

(b) Fault frequency varying in time.

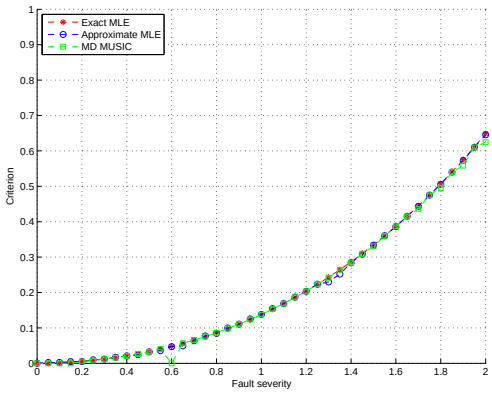

(c) Fault detection criterion.

Figure 2.18: MLE-based L, f_c, and criterion $\mathcal{C}(n)$ for fault severity increasing.

2.7.3 Non-stationary techniques analysis

The following sections study the fault signatures analysis with the previously discussed fault frequency tracking methods. In fact, the MLE, the approximate MLE and the MD MUSIC are used in order to track the fault related frequency and consequently measure fault severity. These techniques are demonstrated on non-stationary numerical signals with time-varying fault characteristic frequency and fault severity.

2.7.3.1 Non-stationary MLE analysis

Synthetic signals $\mathbf{x}(n)$ were simulated by using the signal whose PSD is depicted in Fig. 2.1. The signal parameters are the same as the ones given in section 1.4.3. The set

$\Omega = \{f_s(n), f_c(n), L(n)\}$ constitute the parameters to be estimated. The sinusoidally frequency modulated signal given by (1.40, chapter 1) is used to demonstrate the interest of the MLE for fundamental frequency and fault characteristic frequency tracking whatever the model order.

Figure 2.19 shows the simulation results. It can be observed from Figs. 2.19(b), 2.19(c), and 2.19(d) that the non-stationary MLE performs well since it allows to estimate the number of sidebands, the fundamental frequency variations, and sidebands frequency variations. The spectrogram of the same signal is given by Fig.2.19(a). This figure shows that the spectrogram does not allow to distinguish clearly the fundamental frequency and the fault related frequency. In fact, using the same time window length, the non-stationary MLE gives more interesting results than the spectrogram. In order to improve the spectrogram performance the window length must be increased (see section 1.4.3.1). For the proposed non-stationary MLE, Figs. 2.19(c) and 2.19(d) show the estimated fault frequency and fundamental frequency. It is clear, from these figures that as compared to the spectrogram, the proposed method is more reliable since it is accurate and gives directly the frequencies values at each time n.

Next, the proposed fault detection method is used in order to reveal the presence of incipient faults. We propose to apply the proposed approach on signal with no fault until $2s$, then the fault occurs with a severity increasing until $10s$. The fundamental frequency and the fault related frequency are supposed to vary linearly with respect to time in order to emulate transient signals. The signal model used for these simulations is the one given in the previous chapter in equation (1.40). The simulations results are depicted in Fig 2.20. Figure 2.20(a) gives the spectrogram of the signal. It can be seen from this figure that the signal is highly non-stationary. In fact, the fundamental frequency, the fault related frequency, and the model order vary continuously with respect to time. Figures 2.20(b), 2.20(c), and 2.20(d) give, respectively, the model order estimation, the fundamental frequency variations, and the sidebands frequency variations with respect to time. It is of great interest to estimate the sidebands number correctly in order to estimate the fault frequency and the fundamental frequency accurately. Otherwise, the cost function given by (2.72) exhibits spurious estimates which may lead to erroneously estimate of the signal parameters, and leading to false conclusions.

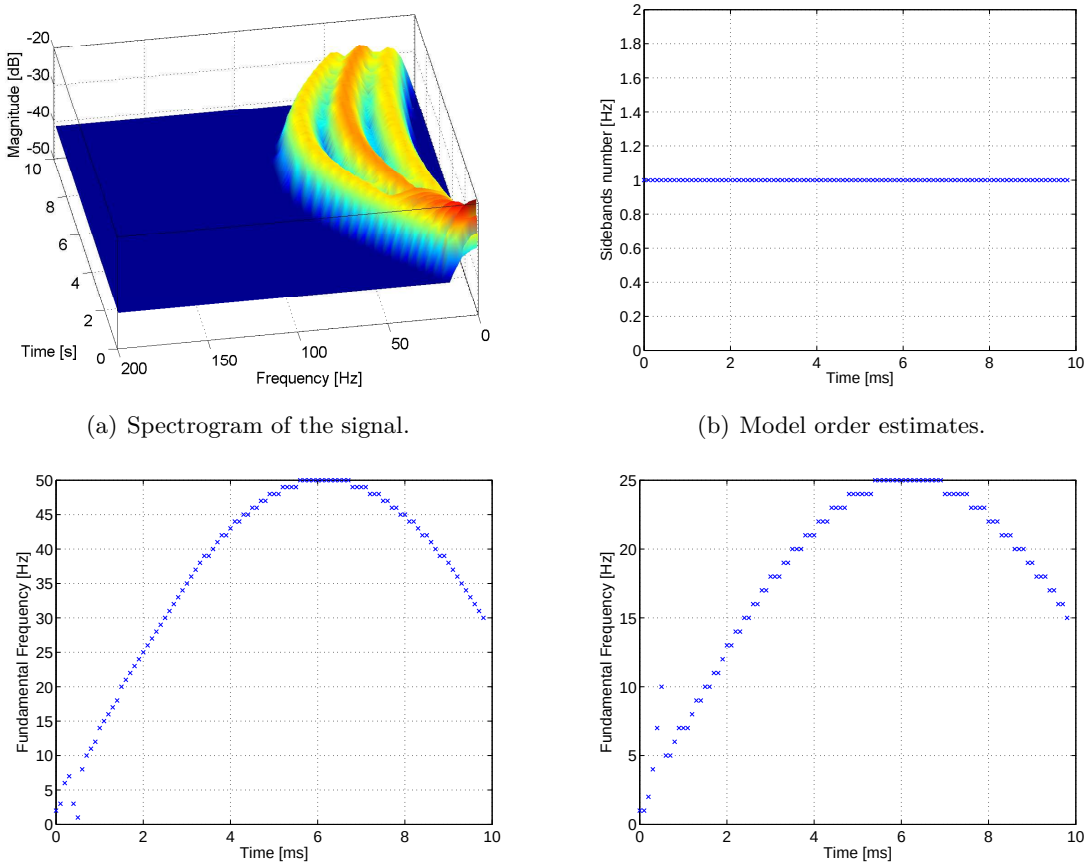

(a) Spectrogram of the signal.

(b) Model order estimates.

(c) Fundamental frequency estimates.

(d) Fault related frequency estimates.

Figure 2.19: Non-stationary MLE-based L, f_s, and f_c estimates.

It can be deduced that the proposed method allows tracking the fault related frequency and the number of sidebands. Unlike the spectrogram, the proposed approach is more accurate since it allows to estimate directly the fault related frequency and the fundamental frequency for each signal frame. Moreover, the proposed approach allows to extract directly a fault indicator revealing the presence of a fault and measuring its severity. Fig. 2.21 gives the criterion evolution for the simulation given in Fig. 2.20. This figure allows to corroborate the efficiency of the proposed method. In fact, the proposed method is interesting for fault detection since it allows to determine the presence of fault and gives an indicator of its severity even if the operating conditions are varying with time.

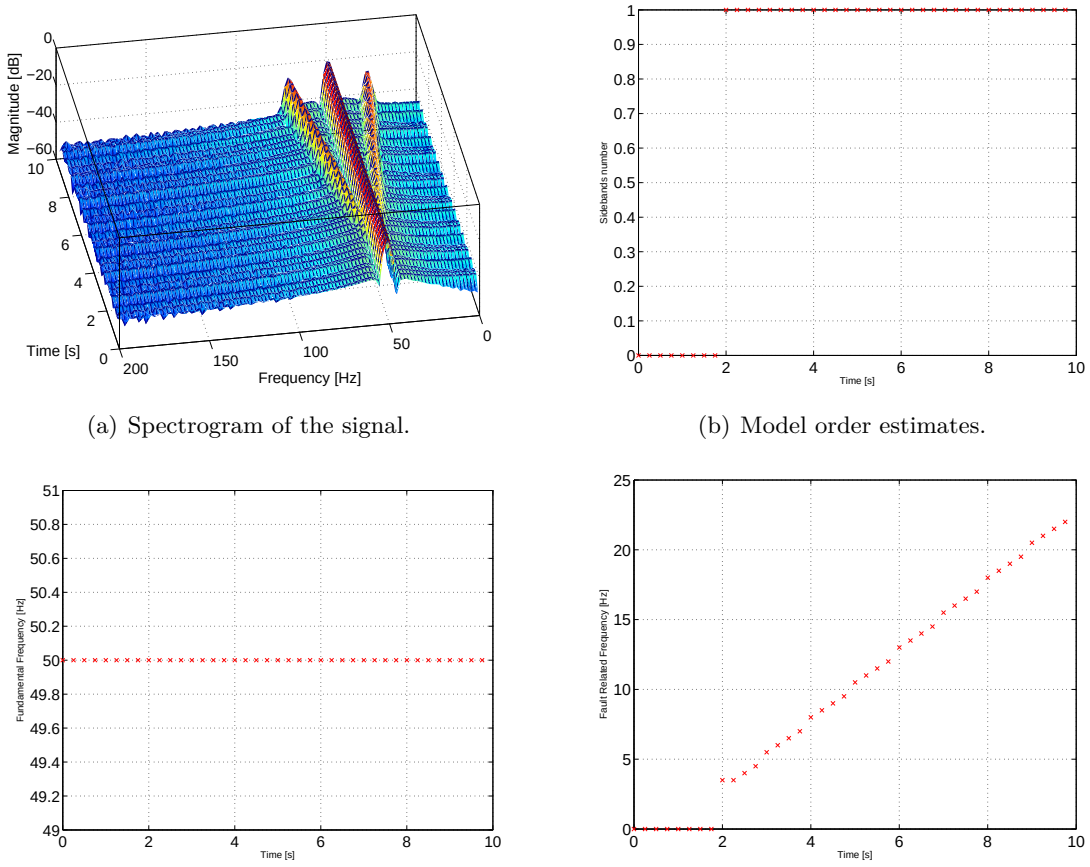

(a) Spectrogram of the signal.

(b) Model order estimates.

(c) Fundamental frequency estimates.

(d) Fault related frequency estimates.

Figure 2.20: Non-stationary MLE-based L, f_s, and f_c estimates.

2.7.3.2 Non-stationary MD MUSIC analysis

The non-stationary MD MUSIC is demonstrated herein, for fundamental frequency and fault related frequency tracking on synthetic signals. First, the signal given by (1.40, chapter 1) is used for the illustration. Figure 2.22 gives the simulation results.

The same conclusions as in the case of the non-stationary MLE can be drawn from this figures. It is interesting to note that when the proposed model does not hold or the model order is erroneously estimated, the cost function does not exhibit a distinct peak which may lead to false estimator of the fault characteristic frequency. However, the fault detection indicator proposed for fault severity measurement is always computed correctly when the fundamental frequency estimate is correct.

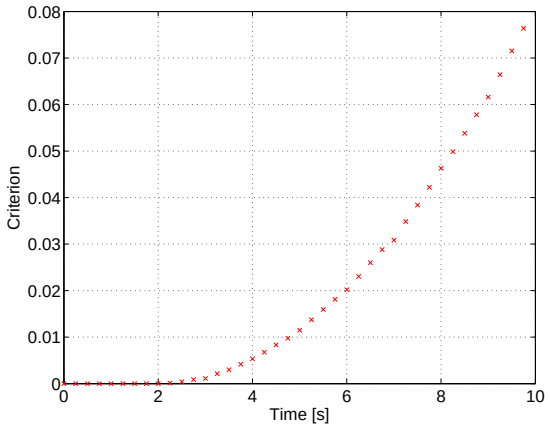

Figure 2.21: Fault detection criterion.

Similarly, we consider the case of MD MUSIC for fault severity tracking. In these simulations results on synthetic signals corresponding to the model described in (1.40), we demonstrate the usefulness of the proposed method in analysing signals with varying fault related frequency and fault severity tracking.

The spectrogram of the signal is shown in Fig. 2.23(a). This figure allows to visualize both the fundamental frequency and the fault related frequency. It permits to highlight the presence of the sidebands and the visualize its frequency evolution over the time. Unfortunately, it is not obvious to identify the amplitude of these sidebands and consequently determine the fault severity accurately. Consequently, the fault severity tracking is far from being easy using the spectrogram. Figures 2.23(b), 2.23(c), and 2.23(d) show the simulation results. These figures give the number of sidebands, the fault characteristic frequency, and fundamental frequency estimates, respectively.

As it can be seen, the model order, the fault related frequency is erroneously estimated when there is a model mismatch (no fault implies no sidebands). In fact, from 0 to $2s$ sidebands do not exist but the model order is estimated equal to 1 which leads to a wrong estimate of the fault related frequency. Despite this drawback, Fig. 2.24 shows that the fault detection criterion is estimated correctly.

It is interesting to note that the method proposed allows tracking the fault related frequency, the number of sidebands. Both examples given herein, clearly demonstrate the usefulness of the proposed estimator to non-stationary signals analysis. Moreover, the fault indicator is directly computed using sidebands amplitudes MLE-based esti-

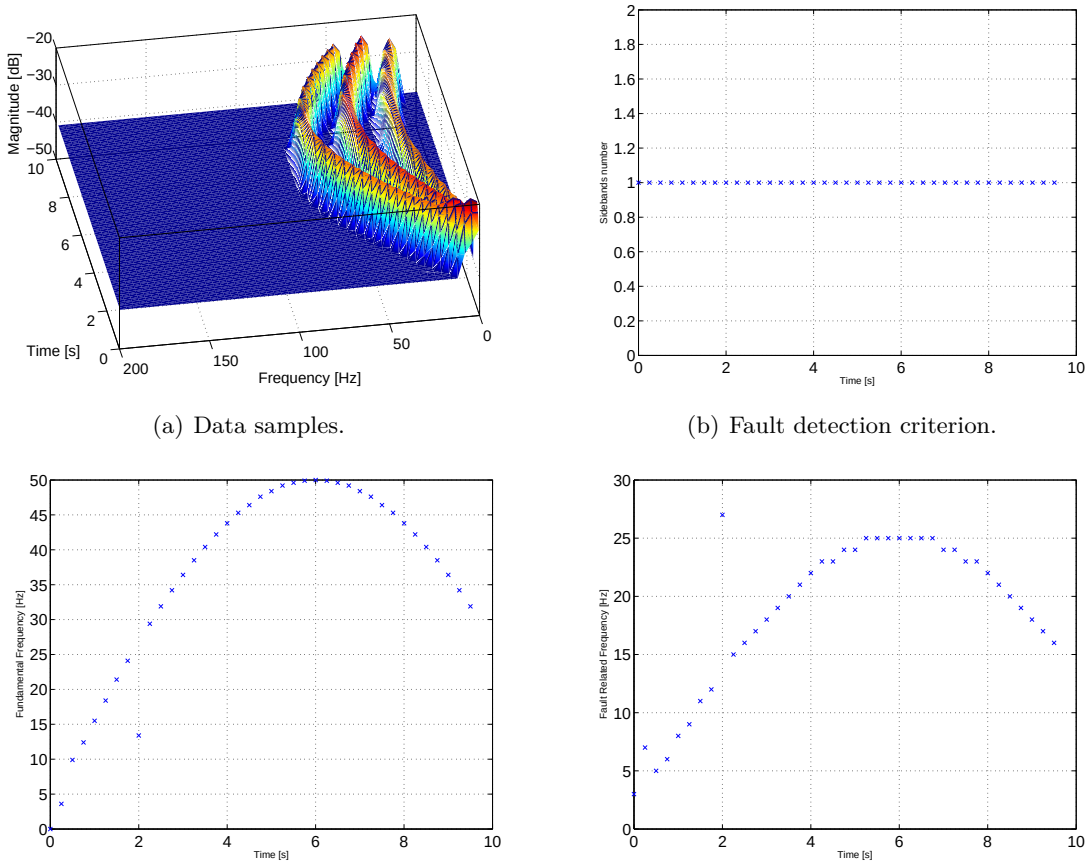

(a) Data samples.

(b) Fault detection criterion.

(c) Fault detection criterion.

(d) Fault frequency.

Figure 2.22: Non-stationary MUSIC-based L, f_s, and f_c estimates.

mates. Hence, the method can be useful in faults detection and diagnosis in induction machine for stationary and non-stationary operating conditions.

2.8 Conclusion

This chapter has described a new parametric spectral estimation methods that will be further used for fault detection in induction machines through a stator current monitoring. A stator current model has been proposed in order to develop more reliable methods for faults detection in induction machines. Then, three fault detection approaches have been proposed based on this signal model. A parametric spectral estimation approaches based on MLE, approximate MLE, and a technique based on

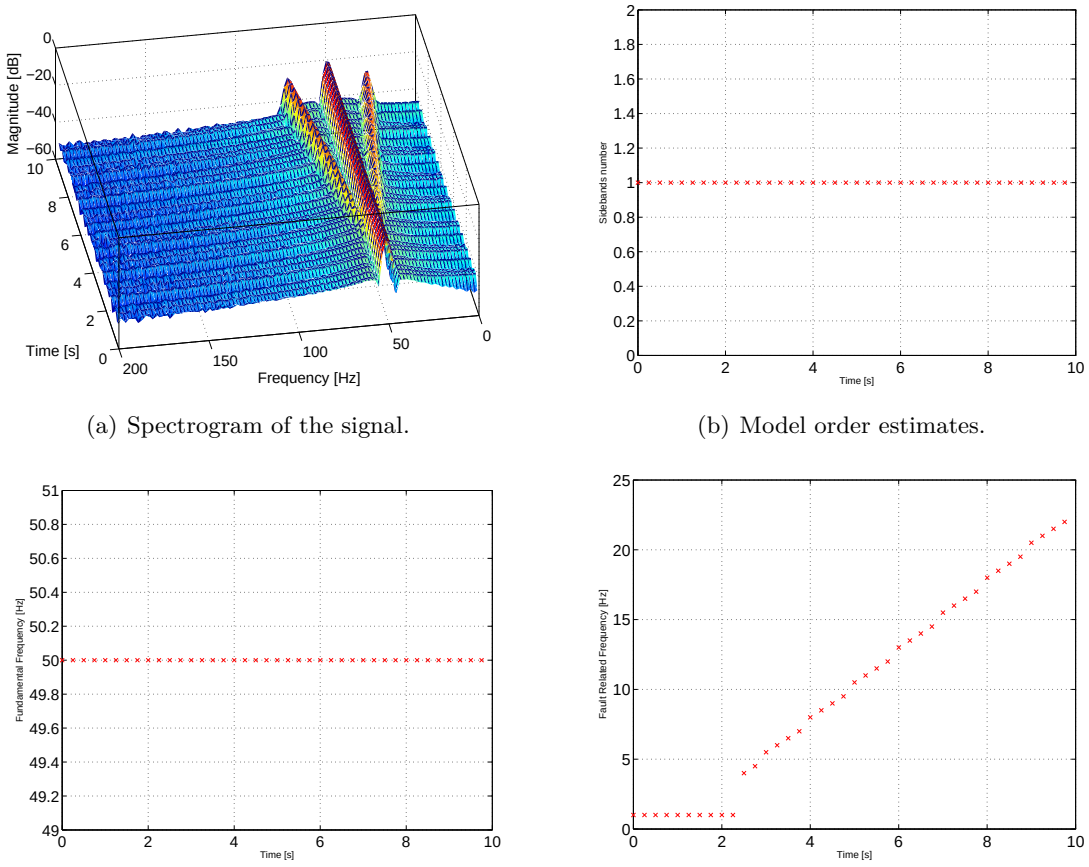

(a) Spectrogram of the signal.

(b) Model order estimates.

(c) Fundamental frequency estimates

(d) Fault related frequency estimates

Figure 2.23: Non-stationary MLE-based L, f_s, and f_c estimates.

subspace decomposition, called MD MUSIC were developed for stationary and non-stationary signal processing. Finally, a fault detection criterion has been presented based on the amplitude of the sidebands introduced by the fault on the signal PSD. This criterion allows to measure the fault severity.

Afterwards, the proposed signal processing tools for fault detection in induction machine have been demonstrated on numerical signals. The MLE has been demonstrated via simulations for various scenarios. Similarly, the MD MUSIC has been used for stationary and non-stationary parameters tracking. The two methods have been used on simulated data in order to prove their effectiveness for fault detection even when some signal parameters are time-varying.

The proposed methods are demonstrated to be suitable to estimate the PSD pa-

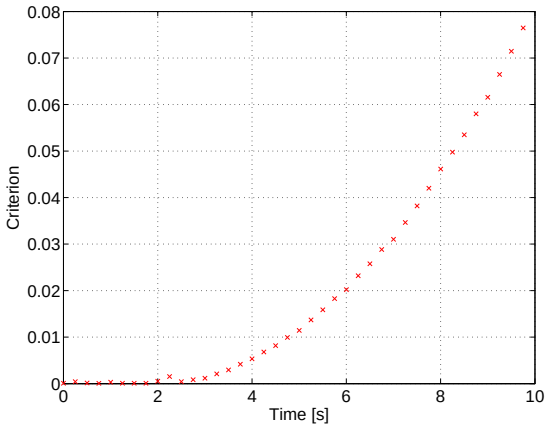

Figure 2.24: Fault detection criterion estimates.

rameters from the signal samples even for a low sidebands amplitude (except for approximate MLE where the sidelobes effects introduces some artefacts which may lead to false alarms) and more easy to implement while computing faults indicator.

Chapter

3

Simulation Validation on Stator Currents Issued from a Coupled Magnetic Circuits Modeling Approach

Contents

3.1 Introduction

This chapter deals with a global method enabling the simulation of the induction machine under stator and/or rotor faults. This approach is based on the coupled magnetic circuit theory. The coupled magnetic circuits approach combined with the arbitrary reference frames theory is the theoretical groundwork for modeling induction

machines [158]. An induction machine is considered as a highly symmetrical electromagnetic system. Any fault will therefore induce a certain degree of asymmetry [159]. In this context, a Matlab-Simulink®-based tool of faulty induction machines has been developed to generate a fault database. This simulation tool has been developed in collaboration with French Naval Academy [160]. This tool allows testing different stator current-based fault detection techniques proposed in chapter 2.

First of all, the three-phase induction machine modeling is treated. The dealt with approach is based on the induction machine analytical models. Inductances are calculated from the actual geometry and winding layout of the machine. The resolution of the system of differential equations describing the behavior of induction machine is described. The healthy case is presented first, then the faulty case is exposed with special emphasis on broken rotor bars, and eccentricity faults. Afterwards, the proposed methods for faults detection and diagnosis are tested on stator currents and results are analyzed for several faults and for stationary and non-stationary operating conditions.

The outline of the chapter is the following: First, some basic concepts of machine modeling based on magnetic circuits approach and windings functions theory are reviewed including the inductances computation, the analytical model and the system of differential equations resolution method. Then, some simulation results are presented and discussed. Finally, the effectiveness of the proposed methods for fault detection is demonstrated on stator currents for eccentricity, and broken rotor bars faults detection. Moreover, the usefulness of these methods is proved for several operating conditions.

3.2 Induction machine modeling

Although the induction machine is known as robust, reliable, and cost effective electrical machine, it is subjected to several faults. These faults may lead to failures and result in an unscheduled shut-down leading to loss of production and subsequently loss of revenue. Consequently, it is mandatory to develop a reliable and efficient induction machine dynamic models to characterize these faults and understand their effect over intrinsic parameters. Simple and fast models such as space vector models may not be very accurate for monitoring purposes whereas detailed models, e.g. based on finite elements or permanence network methods are too computationally expensive.

To overcome these limitations, the coupled magnetic circuits approach has been chosen. This method serves the trade-off between the modeling complexity and accuracy. The system of differential equations describing the induction machine in presence of faults is presented. The machine inductances may be calculated by means of the flux or the magnetic energy stored in the air-gap. In this chapter, we focus on the use of flux and the winding functions method to perform the computation of machine self and mutual inductances. The developed model allows emulating several mechanical and electrical faults.

3.2.1 Coupled magnetic circuits approach

For most faults, the harmonic contents of the stator current can be calculated satisfactory using linear models of the machine such as the coupled magnetic circuit method associated with winding function theory[11, 161]. This approach is based on the analytical equations of the induction machine. All parameters are calculated from the actual geometry and winding layout of the machines rather than from transformed or equivalent variables. Let us consider a three phase squirrel cage induction machine with the following assumptions:

$\mathcal{H}_1$: Three identical stator windings with axes of symmetry such that even harmonics of the resulting spatial winding distribution are zero,

$\mathcal{H}_2$: Infinite iron permeability and non conductive magnetic circuit,

$\mathcal{H}_3$: Uniform airgap,

$\mathcal{H}_4$: Negligible saturation,

$\mathcal{H}_5$: Insulated rotor bars (no inter-bars currents),

$\mathcal{H}_6$: Eddy current, friction, windage losses are neglected,

$\mathcal{H}_7$: No air-gap leakage flux and the flux is considered to be radial.

Under these assumptions, the representation of an induction machine with a cage rotor is fundamentally the same as one with a phase wound rotor, where it is assumed that the cage rotor can be replaced by a set of mutually coupled loops as shown by Fig. 3.1. It consists in replacing the N_r bars squirrel cage by an equivalent circuit containing $N_r + 1$ magnetically coupled meshes. The current of each rotor cage mesh is considered

3. SIMULATION VALIDATION ON STATOR CURRENTS ISSUED FROM A COUPLED MAGNETIC CIRCUITS MODELING APPROACH

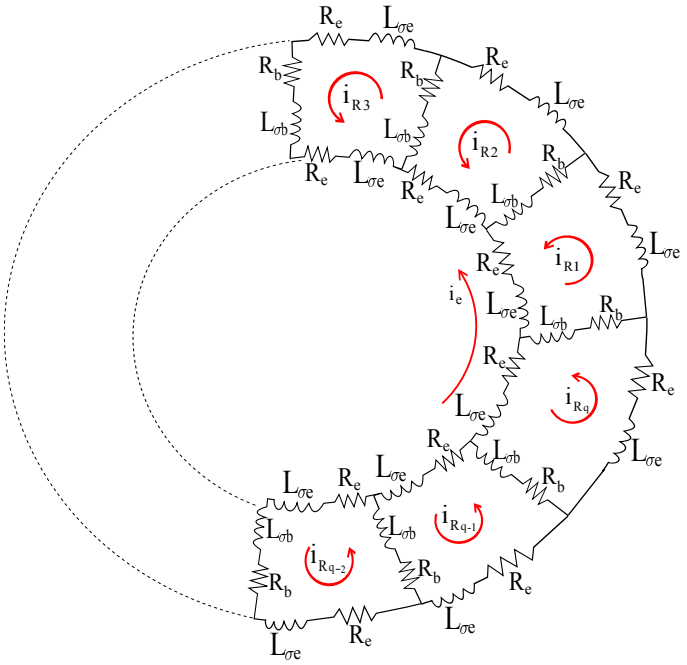

Figure 3.1: Equivalent circuit of a cage rotor showing rotor loop and circulating end-ring current [10].

as independent variable. The electrical equation of the rotor loop $j(0 < j < N_r)$ is given by [158, 162]

$$R_e i_{rj} + R_{bj} i_{bj} + R_e(i_{bj} - i_e) - R_{b(j-1)} i_{b(j-1)} + \frac{d\Phi_{rj}}{dt} = 0 \tag{3.1}$$

where Φ_{rj} is the j^{th} rotor loop flux, i_{rj} is the current crossing the loop j, i_e is the end ring current, and i_{bj} is the current crossing the bar j of the rotor cage. This current is given by

$$i_{bj} = i_{rj} - i_{r(j+1)} \tag{3.2}$$

The system of differential equations describing the behavior of induction machine with 3 stator phases and N_r rotor bars can be written in vector matrix form as follows (3.3) [10]

$$\begin{cases} \frac{d}{dt}\mathbf{I} = -\mathbf{L}^{-1}\left(\mathbf{R} + \Omega_r \frac{d}{d\theta_m}\mathbf{L}\right)\mathbf{I} + \mathbf{L}^{-1}\mathbf{V} \\ \frac{d}{dt}\Omega_r = \frac{1}{2J}\mathbf{I}^T\left(\frac{d}{d\theta_m}\mathbf{L}\right)\mathbf{I} - \frac{f}{J}\Omega_r - \frac{1}{J}\Gamma_C \\ \frac{d}{dt}\theta_m = \Omega_r \end{cases} \tag{3.3}$$

where,

– J, f, and Γ_c represent the rotating masses inertia, the viscous friction coefficient, and load torque respectively.

– $\frac{d}{dt}[.]$ and $\frac{d}{d\theta_m}[.]$ are the derivatives with respect to time to the angular position respectively.

– Ω_r and θ_m are the rotor mechanical speed and the rotor angular position respectively.

– $\mathbf{V}$ is the voltage vector, which is given by

$$\mathbf{V} = \begin{bmatrix} \mathbf{V}_s & \mathbf{V}_r \end{bmatrix}^T \Leftrightarrow \begin{cases} \mathbf{V}_s = [v_{s1} \quad v_{s2} \quad v_{s3}] \\ \mathbf{V}_r = [0 \quad 0 \quad 0 \quad \dots \quad 0]_{1\times(N_r+1)} \end{cases} \tag{3.4}$$

where N_r is the number of rotor bars.

– $\mathbf{I}$ is the current vector, which is defined as

$$\mathbf{I} = \begin{bmatrix} \mathbf{I}_s & \mathbf{I}_r \end{bmatrix}^T \Leftrightarrow \begin{cases} \mathbf{I}_s = [i_{s1} \quad i_{s2} \quad i_{s3}] \\ \mathbf{I}_r = [i_{r1} \quad i_{r2} \quad i_{r3} \quad \dots \quad i_{rN_r} \quad i_e] \end{cases} \tag{3.5}$$

– $\mathbf{R}$ is the global resistance matrix given by

$$\mathbf{R} = \begin{bmatrix} \mathbf{R}_s & \mathbf{0}_{3\times(n+1)} \\ \mathbf{0}_{(n+1)\times 3} & \mathbf{R}_r \end{bmatrix} \tag{3.6}$$

where $\mathbf{R}_s$ is the stator resistance matrix, which is given by

$$\mathbf{R}_s = \begin{bmatrix} R_{s1} & 0 & 0 \\ 0 & R_{s2} & 0 \\ 0 & 0 & R_{s3} \end{bmatrix} \tag{3.7}$$

where $R_{s1} = R_{s2} = R_{s3}$ are the resistances of a stator phase winding.

The $(N_r+1)\times(N_r+1)$ symmetric matrix $\mathbf{R}_r$ corresponds to rotor cage resistances and is expressed as follows

$$\mathbf{R}_r = \begin{bmatrix} R_{rr} & -R_b & 0 & \dots & 0 & -R_b & -R_e \\ -R_b & R_{rr} & -R_b & \dots & 0 & 0 & -R_e \\ \vdots & \vdots & \vdots & \dots & \vdots & \vdots & \vdots \\ \vdots & \vdots & \vdots & \dots & \vdots & \vdots & \vdots \\ 0 & 0 & 0 & \dots & R_{rr} & -R_b & -R_e \\ -R_b & 0 & 0 & \dots & -R_b & -R_{rr} & -R_e \\ -R_e & -R_e & -R_e & \dots & -R_e & -R_e & N_r R_e \end{bmatrix} \tag{3.8}$$

where $R_{rr} = 2(R_e + R_b)$, R_e is the end ring resistance and R_b is the rotor bar resistance.

The global matrix inductance can be presented by

$$\mathbf{L} = \begin{bmatrix} \mathbf{L}_{ss} & \mathbf{M}_{sr} \\ \mathbf{M}_{rs} & \mathbf{L}_{rr} \end{bmatrix} \tag{3.9}$$

The stator inductance matrix $\mathbf{L}_{ss}$ is symmetric with constant elements; its expression is given by

$$\mathbf{L}_{ss} = \begin{bmatrix} L_{s1} & M_s & M_s \\ M_s & L_{s2} & M_s \\ M_s & M_s & L_{s3} \end{bmatrix} \tag{3.10}$$

where M_s is the mutual inductance between the stator phases, and L_{s1}, L_{s2}, L_{s3} are the total inductances of the stator coil which represents the sum of the magnetizing inductance for each stator coil L_{ms} and the leakage inductance L_{sf}, i.e.,

$$L_{s1} = L_{s2} = L_{s3} = L_{ms} + L_{sf} \tag{3.11}$$

The inductance matrix of the rotor loops (Fig. 3.1) is given by

$$\mathbf{L}_{rr} = \begin{bmatrix} L_{rr} & M_{rr} - L_{\sigma b} & M_{rr} & \dots & M_{rr} & M_{rr} - L_{\sigma b} & -L_{\sigma e} \\ M_{rr} - L_{\sigma b} & L_{rr} & M_{rr} - L_{\sigma b} & \dots & M_{rr} & M_{rr} & -L_{\sigma e} \\ \vdots & \vdots & \vdots & \dots & \vdots & \vdots & \vdots \\ \vdots & \vdots & \vdots & \dots & \vdots & \vdots & \vdots \\ M_{rr} & M_{rr} & M_{rr} & \dots & L_{rr} & M_{rr} - L_{\sigma b} & -L_{\sigma e} \\ M_{rr} - L_{\sigma b} & M_{rr} & M_{rr} & \dots & M_{rr} - L_{\sigma b} & L_{rr} & -L_{\sigma e} \\ -L_{\sigma e} & -L_{\sigma e} & -L_{\sigma e} & \dots & -L_{\sigma e} & -L_{\sigma e} & N_r L_{\sigma e} \end{bmatrix} \tag{3.12}$$

where $L_{rr} = L_{mr} + 2(L_{\sigma b} + L_{\sigma e})$, L_{mr} is the magnetizing inductance for each rotor loop, $L_{\sigma b}$ is the rotor bar leakage inductance, $L_{\sigma e}$ is the rotor end ring leakage inductance and the mutual inductance between two rotor rotor loops is denoted M_{rr}.

The mutual inductance $\mathbf{M}_{sr}$ is a $3 \times N_r$ matrix consisting of mutual inductances between stator coils and rotor loops and is given by

$$\mathbf{M}_{sr} = \begin{bmatrix} M_{s1r1} & M_{s1r2} & \dots & M_{s1rN_r} \\ M_{s2r1} & M_{s2r2} & \dots & M_{s2rN_r} \\ M_{s3r1} & M_{s3r2} & \dots & M_{s3rN_r} \end{bmatrix} \tag{3.13}$$

where M_{sirj} is the mutual inductance between stator coils 'i' an rotor loops 'j'.

The electromagnetic torque is given by

$$\Gamma_e = \frac{1}{2}\mathbf{I}^T \frac{d\mathbf{L}}{d\theta_m}\mathbf{I}. \tag{3.14}$$

The computation of the matrices containing all magnetizing, leakage, and mutual inductances is the key to a successful simulation of the squirrel cage induction machine. In the following, all the relevant inductances matrices in $\mathbf{L}$ are calculated using the winding function method [18]. The expression of the inductance matrix $\mathbf{L}$ of the induction machine can be extracted from the flux or from the magnetic energy stored on the airgap.

3.2.2 Inductances calculation

The computation of all relevant inductances for the induction machine is based on the winding functions theory. Two approaches can be used in order to compute the inductances based on the airgap flux density. The first one consists of integrating the airgap flux density upon a specific winding to determine its self inductance or its mutual inductances. The second approach is based on the computation of the magnetic energy stored on the airgap. The two approaches are described, but only the flux based approach has been implemented.

3.2.2.1 Stator coil and rotor mesh winding functions

Consider a coil having n_{sp} turns in series that is placed in the stator of an induction machine with N_{es} slots. The winding function of this coil is the magneto-motive force (MMF) created in the airgap by this coil when a unit current is flowing throw it. This winding function is expressed as follows

$$F_{wc}(\theta_s) = \begin{cases} -(\frac{\theta_b}{2\pi})n_{sp} \text{ for } \theta_s \in [-\pi; \frac{-(\theta_s+\alpha_{es})}{2}[\\ \frac{n_{sp}}{\alpha_{es}}(\theta_s + \frac{1}{2}(\alpha_{es} + (1 - \frac{\alpha_{es}}{\pi})\theta_b)) \text{ for } \theta_s \in [-\frac{(\theta_b+\alpha_{es})}{2}; -\frac{(\theta_b-\alpha_{es})}{2}[\\ (1 - \frac{\theta_b}{2\pi})n_{sp} \text{ for } \theta_s \in [-\frac{(\theta_b-\alpha_{es})}{2}; 0[\end{cases} \tag{3.15}$$

Where θ_b and α_{es} denote the coil opening and the slot opening, respectively. The winding function of this coil is illustrated in Fig. 3.2

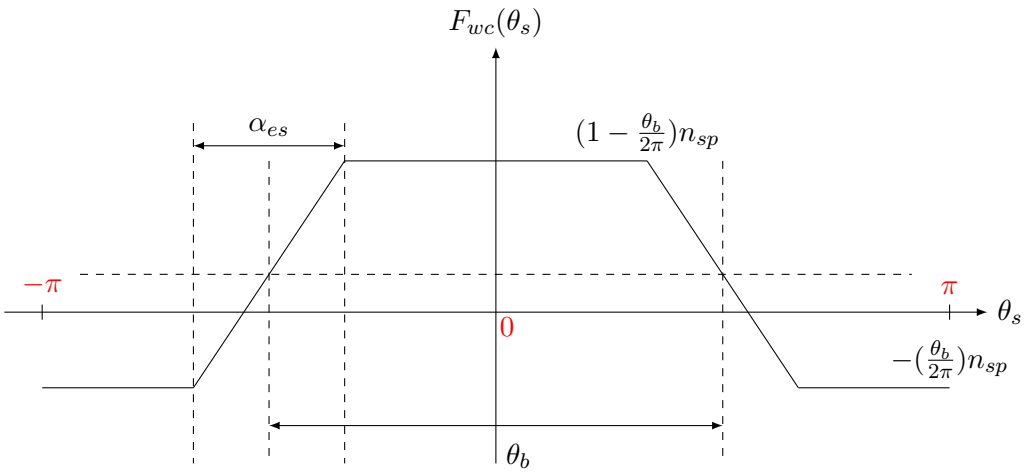

Figure 3.2: Winding function of a coil with n_{sp} turns in series [10].

The winding function of a rotor cage mesh can be deduced from the winding function of a stator coil by replacing n_{sp} by one. If the cage is healthy, the mesh opening is equal to $\frac{2\pi}{p}$. In the case of broken bars or broken end-ring, the considered mesh opening can be multiple of $\frac{2\pi}{p}$.

3.2.2.2 Flux based inductances computation

In the developed model, the calculation of inductances is performed from the flux flowing through the windings. Let's denote Φ_j the flux created by the j^{th} winding carrying a current I_j and flowing through the i^{th} winding, the mutual inductances can be expressed as follows

$$L_{ij}(\theta) = \frac{\Phi_j(\theta)}{I_j} \tag{3.16}$$

Where θ represent the angle between the rotor and the stator reference frame. Let's consider that the i^{th} winding is composed of m coils in series each of them constituted by $n_l (l = 1 \dots m)$ turns in series. The total flux is then given by

$$\Phi_j(\theta) = \sum_{l=1}^{m} n_l \iint_{S_l} B_j(\theta, \theta_s, z) dS_l \tag{3.17}$$

Symbols S_l and θ_s represent the l^{th} coil surface and the angular position of the observation point in the airgap with respect to the stator reference frame. The airgap

flux density $B_j(\theta, \theta_s, z)$ is the product of the magnetomotive force of the j^{th} winding denoted $F_j(\theta, \theta_s, z)$ with the airgap permeance $P(\theta, \theta_s, z)$, i.e.

$$B_j(\theta, \theta_s, z) = F_j(\theta, \theta_s, z)P(\theta, \theta_s, z) \tag{3.18}$$

where the airgap permanence function $P(\theta_s, \theta, z)$ is given by

$$P(\theta_s, \theta, z) = \frac{\mu_0}{e(\theta_s, \theta, z)} \tag{3.19}$$

and the the j^{th} magnetomotive force is the product of the winding function $F_{wj}(\theta, \theta_s, z)$ by the current I_j flowing through the considered winding, i.e.

$$F_j(\theta_s, \theta, z) = F_{wj}(\theta_s, \theta, z)I_j \tag{3.20}$$

The winding function $F_{wj}(\theta_s, \theta, z)$ reflects the winding distribution in the slots in terms of geometrical position, connection, and number of coil turns [18].

Combining (3.16), (3.17), and (3.18), leads to the following expressions of mutual inductance between the i^{th} and j^{th} windings:

$$L_{ij}(\theta) = \sum_{l=1}^{m} n_l \iint_{S_l} F_{wj}(\theta, \theta_s, z)P(\theta, \theta_s, z)dS_l \tag{3.21}$$

Let's denote R_{rot} the rotor radius and $\delta(\theta, \theta_s, z)$ the airgap length, then the airgap average radius is given by $r_{av} = R_{rot} + \frac{\delta(\theta,\theta_s,z)}{2}$. Consequently, dS_l is given by

$$dS_l = r_{av}(\theta, \theta_s, z)d\theta_s dz \tag{3.22}$$

Moreover, the summation over the coils of the i^{th} winding in (3.21) may be replaced by the i^{th} winding distribution function, $F_{Di}(\theta, \theta_s, z)$ describing the coils geometrical location and the coil turns number around the airgap. Finally, the expression of the mutual inductance between the i^{th} and j^{th} windings is given by

$$L_{ij}(\theta) = \int_{-L_{ax}/2}^{L_{ax}/2} \int_0^{2\pi} F_{wj}(\theta, \theta_s, z)F_{Di}(\theta, \theta_s, z)P(\theta, \theta_s, z)r_{av}(\theta, \theta_s, z)d\theta_s dz \tag{3.23}$$

where L_{ax} is the effective airgap axial length and $e(\theta, \theta_s, z)$ is the effective airgap thickness function.

Similarly, the self inductance of the i^{th} winding can be expressed as follows

$$L_{ii}(\theta) = \int_{-L_{ax}/2}^{L_{ax}/2} \int_0^{2\pi} F_{wi}(\theta, \theta_s, z)F_{Di}(\theta, \theta_s, z)P(\theta, \theta_s, z)r_{av}(\theta, \theta_s, z)d\theta_s dz \tag{3.24}$$

3.2.2.3 Magnetic energy stored in the airgap based inductances computation

The magnetic energy stored in the space by a i^{th} winding where flows a current I_i is expressed as

$$W_i = \frac{1}{2} L_{ii} I_i^2 \tag{3.25}$$

where L_{ii} is the winding self inductance.

Based on the above assumptions, the magnetic energy is only stored in the airgap, in the rotor and stator slots, and in stator winding heads and the rotor end ring. Consequently, the i^{th} winding total self inductance is a sum of the self inductance corresponding to principal flux flowing through the airgap, the leakage inductance due to leakage flux in the slots, and the leakage inductance owing to leakage flux in the winding heads. Hence, the magnetic energy stored in the induction machine airgap by the i^{th} winding expresses as follows

$$W_i = \frac{1}{2\mu_0} \iiint_{V_{air}} B_i^2(\theta, \theta_s, z) dV_{air} \tag{3.26}$$

where V_{air} is the airgap volume. Replacing $B_i(\theta, \theta_s, z)$ by its expression in (3.18) gives

$$W_i = \frac{I_i^2}{2\mu_0} \iiint_{V_{air}} F_{wi}^2(\theta, \theta_s, z) P^2(\theta, \theta_s, z) dV_{air} \tag{3.27}$$

From (3.25) and (3.27), it can be concluded that

$$L_{ii}(\theta) = \frac{1}{\mu_0} \iiint_{V_{air}} F_{wi}^2(\theta, \theta_s, z) P^2(\theta, \theta_s, z) r dr d\theta_s dz \tag{3.28}$$

The proposed model does not take into account the flux density variations along the airgap, hence

$$L_{ii}(\theta) = \frac{1}{\mu_0} \int_{-L_{ax}/2}^{L_{ax}/2} \int_{0}^{2\pi} F_{wi}^2(\theta, \theta_s, z) P^2(\theta, \theta_s, z) r_{av}(\theta, \theta_s, z) e(\theta, \theta_s, z) d\theta_s dz \tag{3.29}$$

Concerning the mutual inductances, let's consider a j^{th} winding in which flows a current I_j. The energy stored in the airgap can be expressed as follows

$$W_{ij} = \frac{1}{2} L_{ii} I_i^2 + L_{ij} I_i I_j + \frac{1}{2} L_{jj} I_j^2 \tag{3.30}$$

This magnetic energy can be expressed in terms of flux density as

$$W_{ij} = \frac{1}{2\mu_0} \iiint_{V_{air}} B_{ij}^2(\theta, \theta_s, z) dV_{air} \tag{3.31}$$

where the flux density $B_{ij}^2(\theta, \theta_s, z)$ is the sum of the flux densities created by the two windings i and j. Replacing the flux densities by their expressions, this leads to

$$\begin{aligned} W_{ij} =& \frac{I_i^2}{2\mu_0} \iiint_{V_{air}} F_{wi}^2(\theta, \theta_s, z) P^2(\theta, \theta_s, z) dV_{air} + \frac{I_j^2}{2\mu_0} \iiint_{V_{air}} F_{wj}^2(\theta, \theta_s, z) P^2(\theta, \theta_s, z) dV_{air} \\ &+ \frac{I_i I_j}{2\mu_0} \iiint_{V_{air}} F_{wi}(\theta, \theta_s, z) F_{wj}(\theta, \theta_s, z) P^2(\theta, \theta_s, z) dV_{air} \end{aligned} \tag{3.32}$$

By comparing (3.30) and (3.32) and taking into account the expression of the self inductance in (3.33), the mutual inductance L_{ij} expresses as

$$L_{ij}(\theta) = \frac{1}{\mu_0} \int_{-L_{ax}/2}^{L_{ax}/2} \int_0^{2\pi} F_{wi}(\theta, \theta_s, z) F_{wj}(\theta, \theta_s, z) P^2(\theta, \theta_s, z) r_{av}(\theta, \theta_s, z) e(\theta, \theta_s, z) d\theta_s dz \tag{3.33}$$

In the following the inductances matrices are computed by mean of the airgap flux density. Both the induction machine model in the case of healthy and faulty conditions are investigated.

3.2.3 Induction machine faults simulation

3.2.3.1 Broken rotor bars

Under healthy operating conditions, the balanced three-phase stator current system creates a fundamental clockwise rotating magnetic field in the airgap. This field induces a current in the rotor bars with a frequency proportional to rotor slip s. The rotor bars generate a clockwise filed rotating at $s\omega_s$ in the rotor referential. Under rotor faults, an anticlockwise field appears, created by the imbalance of rotor bar currents and which rotates at an angular velocity $-s\omega_s$. This velocity is associated with a negative-sequence current system.

Under rotor fault, the rotor structure given by Fig. 3.1 is modified. In fact, if a particular bar breaks, the corresponding resistance becomes infinite. Consequently,

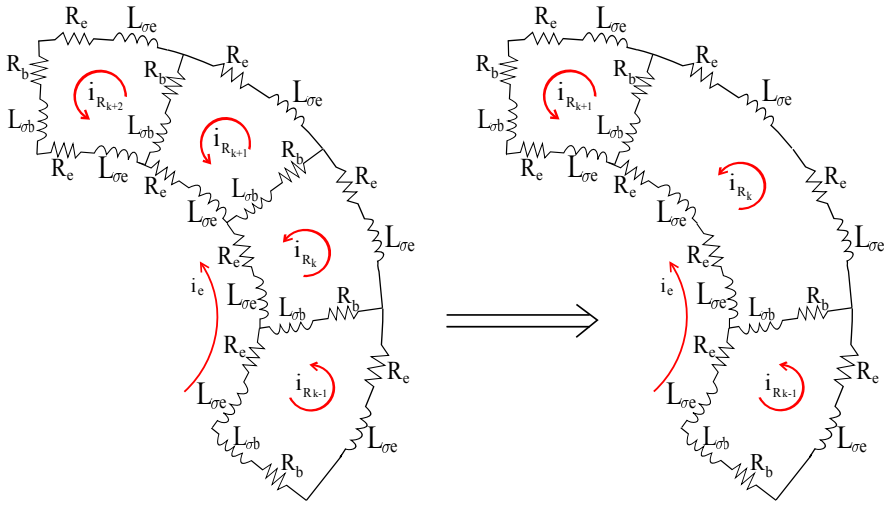

Figure 3.3: Broken rotor bar.

the corresponding loop is modified as it is illustrated in Fig. 3.3. The easier way to implement this on a mathematical model of the faulty induction machine is to consider that the resistance corresponding to the broken bar is infinite.

3.2.3.2 Static, dynamic and mixed eccentricity faults

When static eccentricity occurs in a cylindrical machine, the effective airgap function varies in a sinusoidal manner with respect to angular position θ_s in the stator frame. The effective airgap function can be expressed as follows [54]

$$e(\theta_s) = e_0 - \delta_s \cos(\theta_s - \theta_{sta}) \tag{3.34}$$

where e_0 is the regular airgap length and δ_s is the static eccentricity degree. In this case the rotor geometrical center is identical with the rotational center, but it is displaced with respect to the stator geometrical center (Fig. 3.4(a)). For static eccentricity, the minimum airgap located at θ_{sta} in the stator frame does not revolve with the rotor position.

For dynamic eccentricity the minimum airgap revolves with rotor position θ and the effective airgap function can be approximated by

$$e(\theta, \theta_s) = e_0 - \delta_d \cos(\theta_s - \theta) \tag{3.35}$$

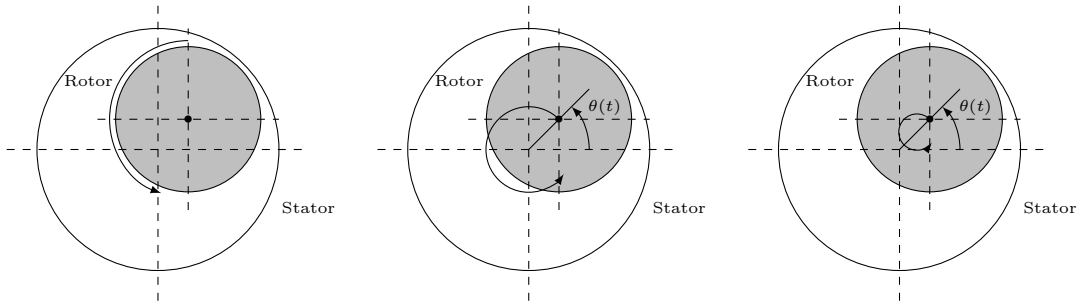

(a) Static eccentricity (b) Dynamic eccentricity (c) Mixed eccentricity

Figure 3.4: Different types of eccentricity.

where δ_d is the dynamic eccentricity degree.

In this case, the rotor geometrical center is different from the rotational center. However, the rotational center is identical with the stator geometrical center (Fig. 3.4(b)).

These types of eccentricity can also exist in the same time in the machine leading to a mixed eccentricity. For mixed eccentricity the two effects are combined which means the geometrical center, rotor rotational center and stator geometrical center are different (Fig. 3.4(c)). Hence, the the effective airgap function can be approximated by [163]

$$e(\theta, \theta_s) = e_0 - \delta_s \cos(\theta_s - \theta_{sta}) - \delta_d \cos(\theta_s - \theta) \tag{3.36}$$

The airgap variations is taken into account in the airgap permanence function and consequently in the inductances expressions.

3.3 Numerical simulation of the induction machine

In this section, we present the simulation results by considering induction machine with broken rotor bars and eccentricity faults. To solve the system of the differential equations in (3.3), the Runge-Kutta's integration method is used. The simulation is performed using Matlab® software.

The machine considered in this study is a three-phase squirrel-cage induction motor with four poles 4 kW/50 Hz, 230/400 V. The machine has 28 rotor bars and 48 stator slots. The remaining parameters of this machine are presented in Table 3.1.

Symbol	Quantity	Machine
P_n	nominal power	4 kW
f_s	supply frequency	50 Hz
V_n	supply voltage	230/400 V
I_n	nominal current	9.1 A
Ω_n	nominal speed	1425 rpm
p	number of pole pairs	2
N_r	number of rotor bars	28
N_s	number of stator slots	48
J	inertia	0.0131 kg $\cdot$ m^2
R_s	stator phase resistance	1.5 Ω
R_b	bar resistance	$69.9 \cdot 10^{-6}$ Ω
R_e	end ring resistance	$5 \cdot 10^{-6}$ Ω
L_b	rotor bar leakage inductance	$0.28 \cdot 10^{-6}$ H
L_e	end ring leakage inductance	$0.036 \cdot 10^{-6}$ H
L	length of the magnetic circuit	$148 \cdot 10^{-3}$ m
R_{av}	average radius of the air-gap	$45 \cdot 10^{-3}$ m
e	air-gap thickness	$0.28 \cdot 10^{-3}$ m

Table 3.1: Machines parameters used in simulation.

3.3.1 Healthy induction machine

The simulations have been performed firstly for a healthy induction machine. The simulation is done with 230 V sine voltage supply (star connected) and with constant load torque $\Gamma_c = 10\ N \cdot m$. Many simulation results can be exposed here but we choose the stator currents, the rotor speed and the electromagnetic torque waveforms. It must be stressed here that the developed induction machine model have been validated using 2-D Finite Difference Field calculation software (DIFIMEDI) [164] in [160]. This tool enables the validation of the induction machine model with a good accuracy. The simulation results are depicted in Fig. 3.5. These simulation results under steady-state and transient conditions demonstrate the modeling accuracy and efficiency since these waveforms correspond to the expected ones. Hence, the coupled magnetic circuits approach is an appropriate model for use in a transient and a steady-state analysis of induction machine drives.

The stator currents issued from the developed coupled magnetic circuits approach

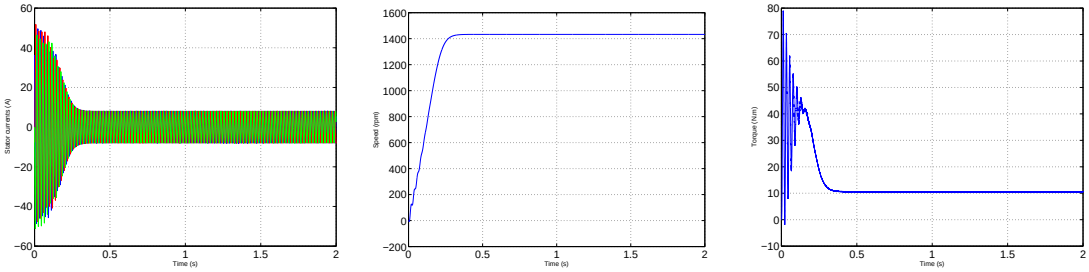

(a) Stator currents. (b) Rotor speed. (c) Electromagnetic torque.

Figure 3.5: Healthy induction machine simulation results.

Broken rotor bars	Adjacent	Non adjacent
One broken bar	10	–
Two broken bars	10 and 11	10 and 15
Three broken bars	10, 11 and 12	10, 15 and 20

Table 3.2: Broken rotor bars for the conducted simulations.

based-simulator will be processed using the algorithms proposed in chapter 2 for induction machine faults detection. Especially, the broken rotor bars and the eccentricity fault are simulated to demonstrate the effectiveness of the proposed approach for faults detection.

3.3.2 Broken rotor bars simulation

3.3.2.1 Simulation results

The broken rotor bars fault is one of the electrical asymmetries that is difficult to detect since the squirrel cage currents are not directly accessible. Hence, the broken rotor bars fault is investigated. The simulation results for broken rotor bars induction machine are given in Fig. 3.6. The faulty bar has been chosen as the tenth. When one bar is broken, the corresponding current is zero. It follows that the amplitudes of bar currents in adjacent bars increase significantly compared with the healthy case. This larger current imply extra stresses on the adjacent bars potentially propagating the fault and probably leading to more severe failure. The broken bars are given by table 3.2

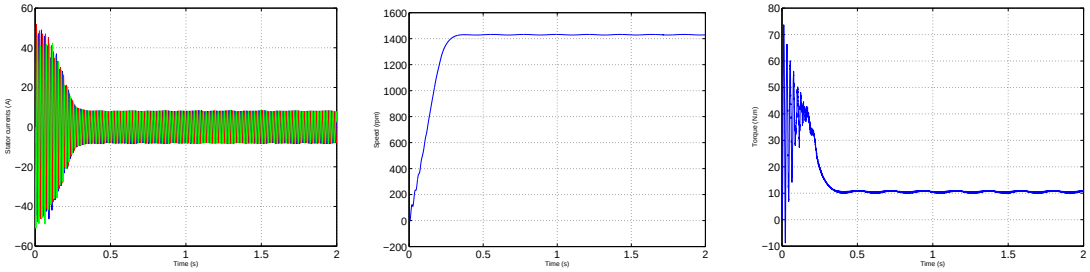

(a) Stator currents. (b) Rotor speed. (c) Electromagnetic torque.

Figure 3.6: Broken rotor bar induction machine simulation results.

Figure 3.6(c) shows the electromagnetic torque waveforms for faulty induction machine with one broken rotor bar. As compared with Fig. 3.5(c) in the case of healthy machine, this figure shows the torque ripple introduced by the fault. In fact, for broken rotor bars, the torque is clearly modulated by the $2sf_s$ related to the $(1 \pm 2s)f_s$ stator current harmonics. These oscillations increase with the number of broken rotor bars and generate speed ripple (Fig. 3.6(b)). Moreover, when the fault appears the slip increases slightly. Concerning the stator current, it appears from Fig. 3.6(a) that the stator current is slightly amplitude modulated. It is worth mentioning that the practical measurement of this modulation is not easy and consequently difficult to use in order to distinguish the faulty case from the healthy one especially for one broken bar. Hence, the proposed approaches are used in order to detect broken rotor bars fault using stator current processing under stationary and non-stationary operating conditions.

3.3.2.2 Broken rotor bars detection with the proposed techniques

Computer simulations have been performed to assess the operating features of the proposed fault detection schemes for 1, 2, and 3 broken rotor bars. The simulations have been done for adjacent and non-adjacent broken rotor bars. Figure 3.7 gives the simulation results for 100% loaded induction machine and for fault severity increasing.

It can be concluded from these figures that the proposed approaches have equivalent performance and allows to distinguish the faulty case and to measure its severity. However, concerning the approximate MLE, the fault detection criterion is non zero (due to sidelobes introduced by windowing) and then a threshold must be set in order to distinguish the faulty machine from the healthy one. It must be mentioned that

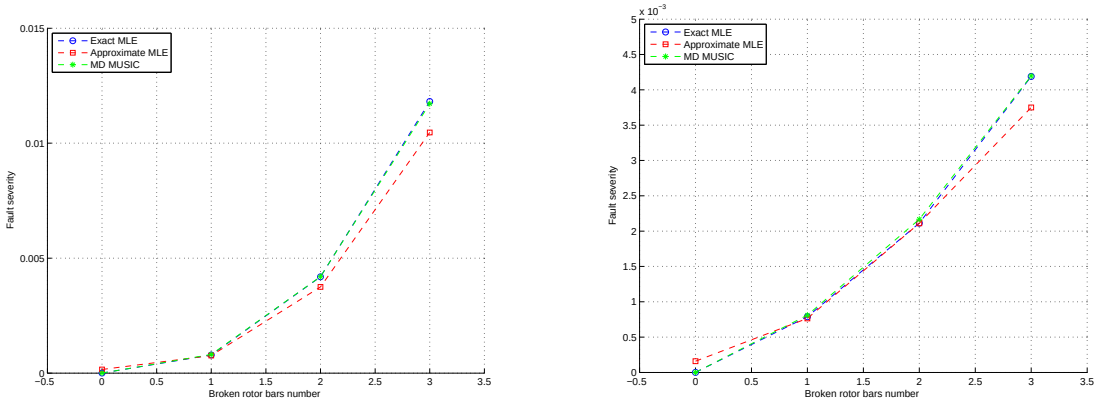

(a) Adjacent broken rotor bars detection using the proposed approaches.

(b) Non-adjacent broken rotor bars detection using the proposed approaches.

Figure 3.7: Fault detection criterion based on the three methods for broken rotor bars detection: fault severity increasing.

the fault criterion is higher when the damaged bars are adjacent than in the case of non-adjacent bars.

In order to measure the robustness of the proposed approaches to the load variations, further simulations have been performed for no load, 50% and 100% rated load. The simulation results are depicted in Fig. 3.8 for one broken rotor bar and for varying load.

It is obvious from these figures that the fault detection criterion based on the three approaches depends on the load condition. The higher is the load, the higher is the fault indicator. Moreover, the MLE and MD MUSIC have similar results while the Approximate MLE for fault detection criterion estimation is almost higher. This can be explained by sidelobes introduced due to the computation of the FFT.

In order to evaluate the performance of the proposed approaches for non-stationary environment, the induction machine model was operated as generator driven by wind turbine. The model was operated for $10s$ and the fault appears at $5s$. The simulation results; the mechanical speed, the electromagnetic torque, and the stator current are given in Fig. 3.9 for one broken rotor bar.

Further simulations have been done in order to assess the performance of the proposed non-stationary fault detection procedures. The induction generator was operated without fault until $5s$, then the one broken rotor bar fault occurs at $5s$, two broken

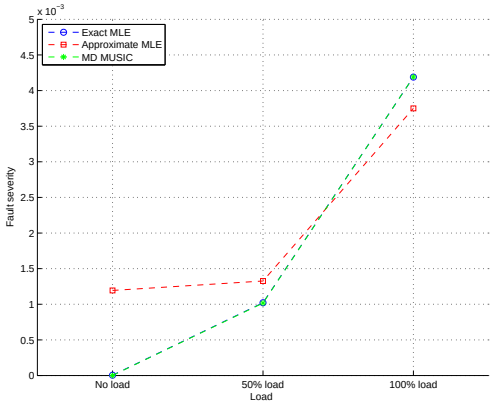

(a) Adjacent broken rotor bars detection using the proposed approaches.

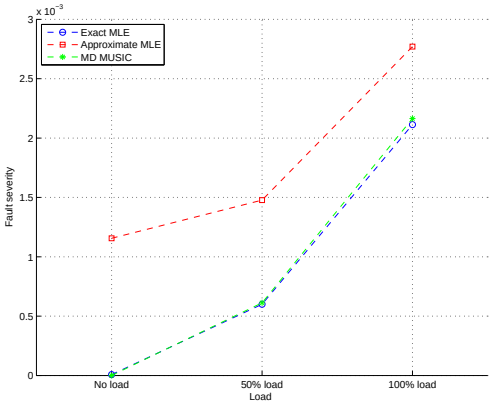

(b) Non-adjacent broken rotor bars detection using the proposed approaches.

Figure 3.8: Fault detection criterion based on the three methods for broken rotor bars detection: load increasing.

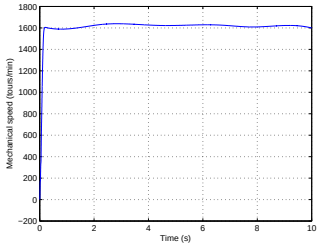

(a) Induction machine mechanical speed.

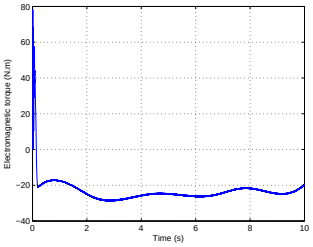

(b) Induction machine electromagnetic torque.

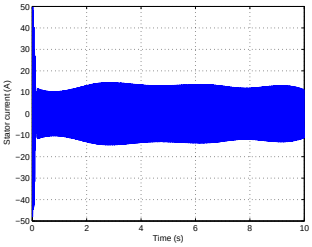

(c) Induction machine stator current.

Figure 3.9: Faulty Wind turbine based induction generator simulation signals.

rotor bars at $10s$ and three broken rotor bars at $15s$. Simulation results for broken rotor bars detection are depicted in Fig. 3.10. Figure 3.10(a) give the time-domain stator current waveform. It appears from the time-domain waveforms that the stator current is amplitude modulated due to wind turbulence. Moreover, Fig. 3.10(b) shows the corresponding spectrogram. This spectrogram exhibits the existence of sidebands introduced by the fault around the fundamental frequency which amplitude increases as the fault severity increases. It worth to notice here that the spectrogram gives acceptable results since the signal length is sufficiently high to get appropriate resolution in order to show the sidebands.

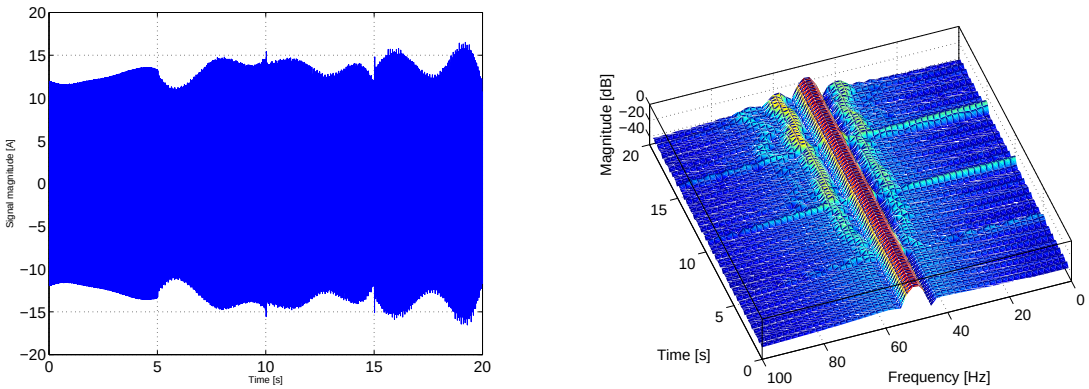

(a) Stator current waveform.

(b) Spectrogram.

Figure 3.10: Simulation results for broken rotor bars of wind driven induction generator.

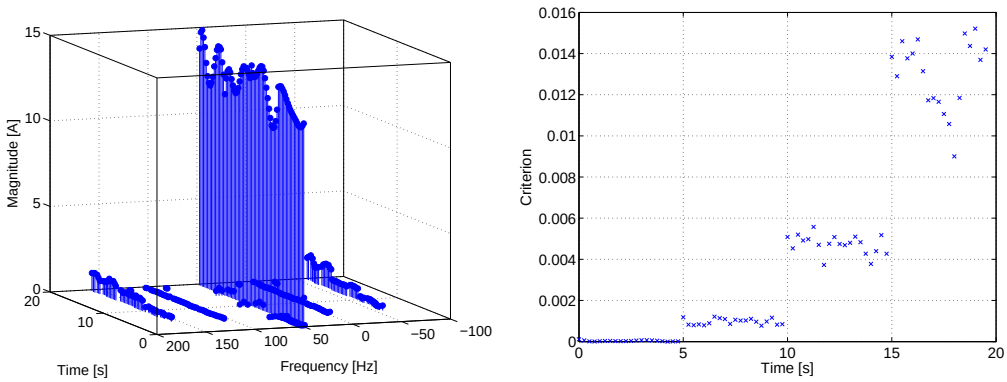

(a) Time-frequency representation-based on MLE.

(b) Fault detection criterion tracking.

Figure 3.11: Fault severity tracking using the MLE; 1, 2 and 3 bars has been broken consecutively.

The MLE and MD MUSIC have been used in order to track the fault severity over time. The approximate MLE is not investigated herein since it is based on FFT computation which suffers from low frequency resolution due to the signal segmentation. The MLE performance are depicted in Figs. 3.11(a) and 3.11(b). The former gives the time-frequency representation using non-stationary MLE, and the latter shows the fault criterion evolution.

These figures allow to conclude on the appropriateness of the non-stationary MLE for fault detection and severity measurement in induction machine in non-stationary

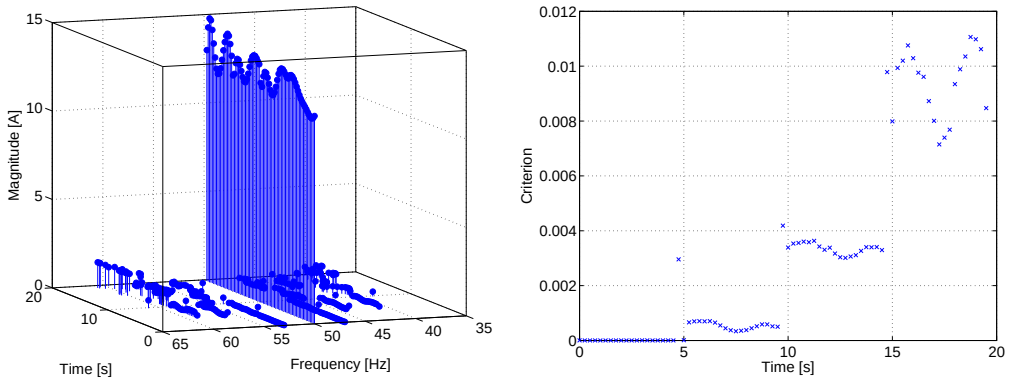

(a) Time-frequency representation-based on MD MUSIC.

(b) Fault detection criterion tracking.

Figure 3.12: Fault severity tracking using the MD MUSIC; 1, 2 and 3 bars has been broken consecutively.

environment.

The MD MUSIC simulation results are depicted in Fig. 3.12. Figure 3.12(a) shows the time-frequency representation using MD MUSIC. It can be observed that the non-stationary MD MUSIC is well suited for broken rotor bars fault characteristic parameters tracking in non-stationary environment. As it can be seen, the fault characteristic frequency varies with respect to time due to the wind variations. Furthermore, Fig.3.12(b) gives the fault detection criterion with respect to time. This criterion allows to distinguish the faulty machine from the healthy one. In addition of that, as the number of broken rotor bars increase, the fault detection criterion increase.

It can be seen from Fig.3.10 that the proposed methodology provides a reliable way to track the fault related frequency based on the stator current. Moreover, it allows to track the fault severity which gives to the operator an idea about the health state of the induction generator and associated turbine. This shows the potential of the proposed approach to detect incipient electrical asymmetry faults on a geared-drive WT generator.

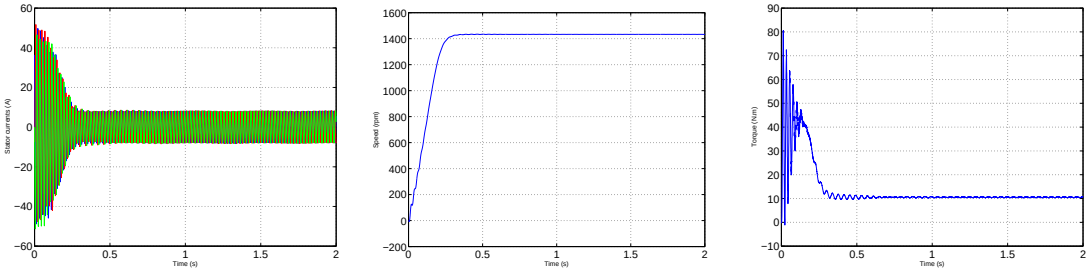

(a) Stator currents. (b) Rotor speed. (c) Electromagnetic torque.

Figure 3.13: Faulty induction machine simulation results with eccentricity fault.

3.3.3 Simulation of the eccentricity faults

3.3.3.1 Simulation results

In order to validate the proposed approaches for mechanical faults detection, the eccentricity fault have been introduced in the induction machine model. The three different types of eccentricity are considered. The induction machine was operated under full load and grid-connected. The mechanical speed, the electromagnetic torque and the stator current waveforms are given by Fig. 3.13 in the case of 10% mixed eccentricity .

Figure 3.13 gives the faulty induction machine simulation results with eccentricity fault. The stator currents are depicted in Fig. 3.13(a). This figure shows that the stator currents are slightly modulated. The rotor speed is shown in Fig. 3.13(b), while the electromagnetic torque waveform is given by Fig. 3.13(c). It can be observed that the torque ripple appears which consequently lead to speed ripple in Fig. 3.13(b). The stator currents are used in the following to demonstrate the effectiveness of the parametric spectral estimation methods for fault detection and severity measurement.

3.3.3.2 Eccentricity fault detection using the proposed approaches

The proposed approaches are used to investigate the eccentricity fault detection for several fault severities and load conditions. The simulation results for static eccentricity detection are depicted in Fig. 3.14. Figure 3.14(a) gives the fault detection criterion variation with respect to fault severity using the three proposed methods. It can be observed that the MD MUSIC and MLE have equivalent results and allows to track the

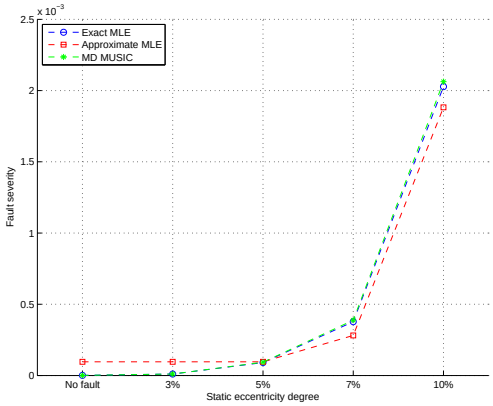

(a) Static eccentricity detection for varying eccentricity degree.

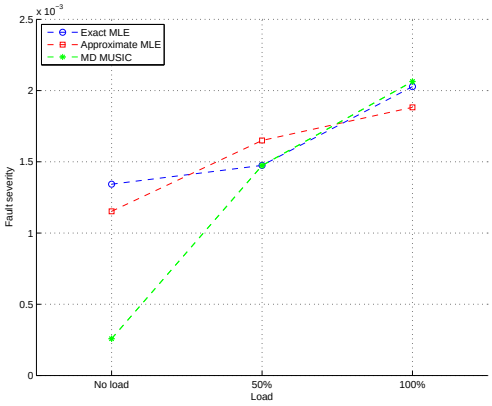

(b) Static eccentricity detection for varying load conditions.

Figure 3.14: Fault detection criterion based on the three methods for static eccentricity detection.

fault severity. In contrary, the approximate MLE is not suited for fault detection when the fault severity degree is low. This is due to FFT computation which increases the criterion value since the sidelobes in the PSD are interpreted as sidebands. Similarly to broken rotor bars, the fault detection criterion is computed for varying load conditions for 10% static eccentricity. Figure 3.14(b) shows the simulation results. It can be deduced from this figure that the fault criterion increases when the load increase.

Similarly to static eccentricity, the dynamic eccentricity is investigated using the proposed methods. Figure.3.15(a) summarizes the simulation results for varying eccentricity degree. This figure shows that the proposed fault detection criterion increases when the the fault degree increases. This means that the proposed methods allow to reveal the existence of dynamic eccentricity and measure its severity for diagnosis purpose. Moreover, simulations have been done for varying load conditions. Figure 3.15(b) gives the criterion variations with respect to load. Generally speaking, concerning the dynamic eccentricity, it can be deduced from this results that the fault detection criterion varies slightly for varying load.

Finally, the mixed eccentricity is investigated. Figure 3.16 shows the simulation results. In fact, Fig. 3.16(a) gives the fault criterion evolution when the mixed eccentricity degree increases. The same conclusions as for previously discussed eccentricities, can be drawn from this figure. Indeed, the fault criterion increases when the fault de-

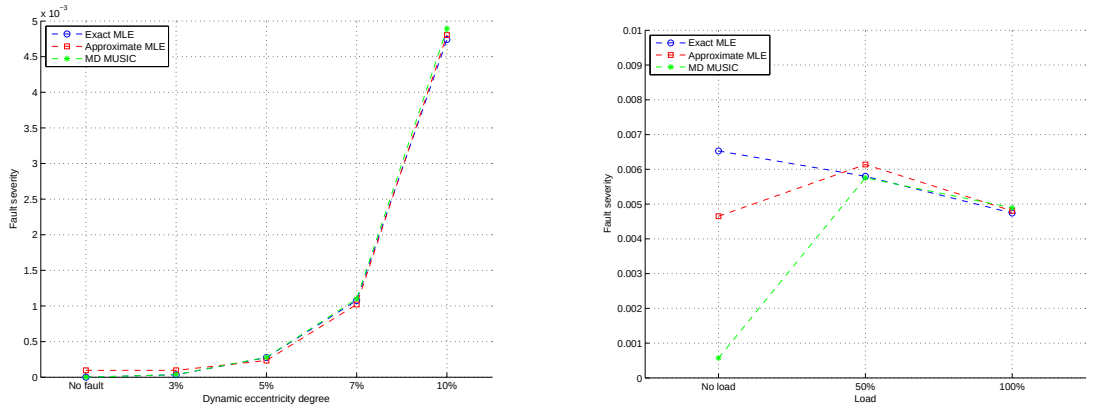

(a) Dynamic eccentricity detection for varying eccentricity degree.

(b) Dynamic eccentricity detection for varying load conditions.

Figure 3.15: Fault detection criterion based on the three methods for dynamic eccentricity detection.

gree increases. In addition of that, the MD MUSIC and MLE give similar results. However, the approximate MLE is not reliable to distinguish the faulty machine from the healthy one when the fault severity is low. Concerning the fault criterion evolution when the load varies, Fig. 3.16(b) depicts the simulation results for 10% mixed eccentricity. From this figure, it can be assumed that the fault detection criterion increases when the load increases.

Furthermore, the non-stationary approaches have been used for eccentricity fault detection. In this simulations, 5% eccentricity fault is considered until $5s$, then the severity increases to 10% air gap eccentricity. Figures 3.17, 3.18 and 3.19 give the simulation results for static, dynamic and mixed eccentricities fault detection using the proposed algorithms when the induction machine is driven by wind.

These results demonstrate the effectiveness of the proposed approach for mechanical fault detection in induction machine operated as generator. Even if the influence of wind turbulence (amplitude modulation seen in the time domain) tends to hide the fault influence on the stator current especially for incipient fault, the proposed approaches provide encouraging results and allow to measure the fault severity. As compared to other time-frequency techniques [43], the proposed approach is developed to met the requirement of fault detection which are the fault characteristic frequency tracking and fault severity measurement. However, the proposed technique is time consuming since

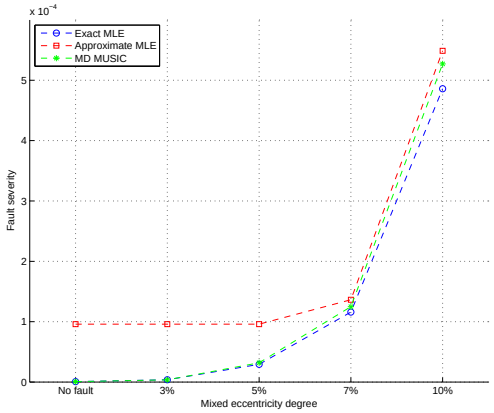

(a) Mixed eccentricity detection for varying eccentricity degree.

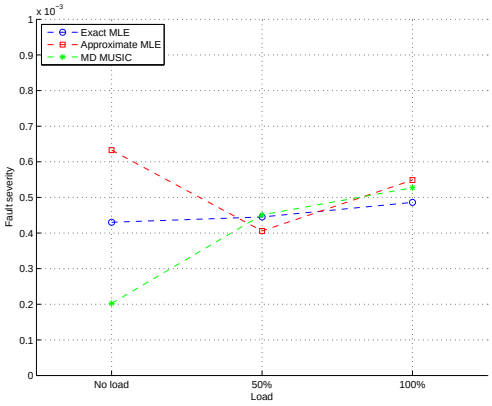

(b) Mixed eccentricity detection for varying load conditions.

Figure 3.16: Fault detection criterion based on the three methods for mixed eccentricity detection.

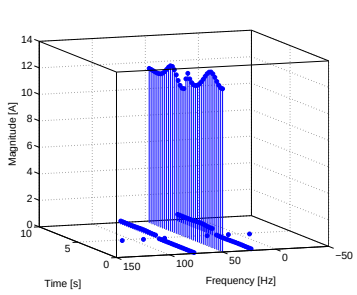

(a) Time-frequency representation.

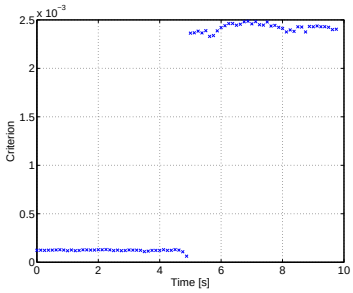

(b) Fault detection criterion tracking using MLE.

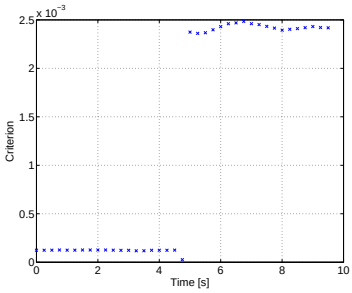

(c) Fault detection criterion tracking using MD MUSIC.

Figure 3.17: Static eccentricity fault severity tracking using the proposed approaches.

a lengthy signal is required in order to have a good estimator of the covariance matrix. Moreover, the time window length determines whether there is good frequency and/or time resolution. In fact, a short window leads to a representation which is fine in time but coarse in the frequency domain. Consequently, a long window leads to good covariance matrix estimator and therefore good frequency estimator.

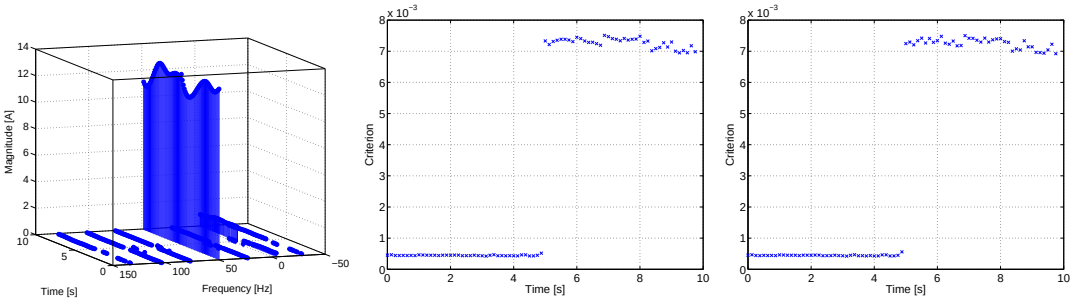

(a) Time-frequency representation. (b) Fault detection criterion tracking using MLE. (c) Fault detection criterion tracking using MD MUSIC.

Figure 3.18: Dynamic eccentricity fault severity tracking using the proposed approaches.

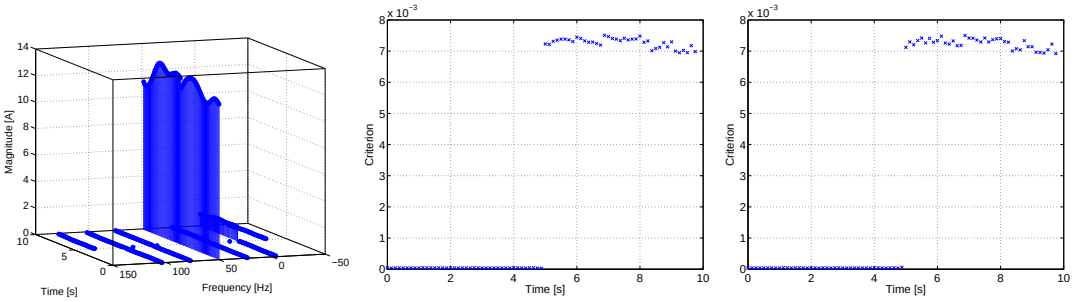

(a) Time-frequency representation. (b) Fault detection criterion tracking using MLE. (c) Fault detection criterion tracking using MD MUSIC.

Figure 3.19: Mixed eccentricity fault severity tracking using the proposed approaches.

3.4 Conclusion

In this chapter, the previously presented signal processing methods were applied to faulty stator currents with broken rotor bars and eccentricity faults. The faulty current signals have been generated through simulations. Specifically, the stator current is issued from a coupled magnetic circuits approach model of the induction machine. The proposed methods have been evaluated on their capability to detect, to track the fault over the time, and to measure its severity for fault diagnosis and decision making.

The first analysis method, the maximum likelihood estimator, has been used for faults detection based on stator currents. In fact, the maximum likelihood-based fault related frequency tracking method allows to extract features from lengthy online data but also provides a feasible condition monitoring approach applicable for stationary and

non-stationary operating conditions. This results show that the proposed approach is quite interesting to establish a simple and cost-effective condition monitoring system for induction machine monitoring in several applications.

The MD MUSIC has been shown to have equivalent performance to those of the maximum likelihood estimator. It has been shown through the simulations that the MD MUSIC provides a reliable way for real time monitoring of the induction machine. In fact, the efficient implementation of MUSIC using Fourier transform may lead to significant decrease of the computational cost with performance close to those of the Maximum Likelihood based method. This makes the MD MUSIC attractive for the following reasons: a) Most DSP-boards include functions for DFT computation, b) the DFT can be efficiently computed using the FFT.

From the achieved simulation results, it can be deduced that the proposed methods are able to detect both electrical and mechanical faults using stator current processing. The appropriateness of the proposed parametric approaches have been shown to give good results for both steady-state conditions and time-varying conditions.

In the following, further investigations are performed in order to validate the proposed approaches on power signals issued from experimental setup equipped with induction machine.

Chapter

4

Validation and Experimental Analysis

Contents

4.1 Introduction

This chapter illustrates the behavior of the proposed techniques for faults detection in induction machine with experimental signals. The machine under test is a 230/400 V, 0.75 kW, three phase induction motor with $p = 1$ and 2780 rpm rated speed. The induction machine is supplied by a synchronous generator in order to eliminate the time harmonics introduced by industrial inverters. Moreover, the current signals are not

Table 4.1: Rated Data of the Tested Induction Machine.

Quantity	Machine
nominal power	0.75 kW
supply frequency	50 Hz
supply voltage	220/380 V
nominal current	3.4/1.95 A
nominal speed	2780 rpm
number of pole pairs	p =1

influenced by current, torque or speed control. Measured signals are the line currents. Data acquisition is performed by a 24 bits acquisition card with 10 kHz sampling frequency.

Bearing failure is one of the foremost causes of breakdowns in rotating machinery, resulting in costly downtime [2]. One of the key issues in bearing diagnostic is to detect the defect at its incipient stage and alert the operator before it develops into catastrophic failure. Hence, each mentioned signal processing method is tested with experimental signals recorded from the pre-described induction machine with bearing faults.

The remaining parts of this chapter are dedicated to illustrate the limitations of the techniques discussed in chapter 1. Then, the proposed techniques in chapter 2 for faults detection in induction machines are used in order to reveal the presence of the fault and measure its severity. Finally, some perspectives for further works are presented.

4.2 Test facility description

4.2.1 Test rig

The conventional induction machine drive test rig used in order to test the proposed fault detection approaches is depicted in Fig. 4.1. The test bed mechanical part is composed of a synchronous and an induction machine. The induction machine is fed by the synchronous generator. Indeed, this will automatically eliminate supply harmonics and therefore allow focusing only on bearing faults effect on the stator current. The rated data of the used induction machine are given in Table 4.1.

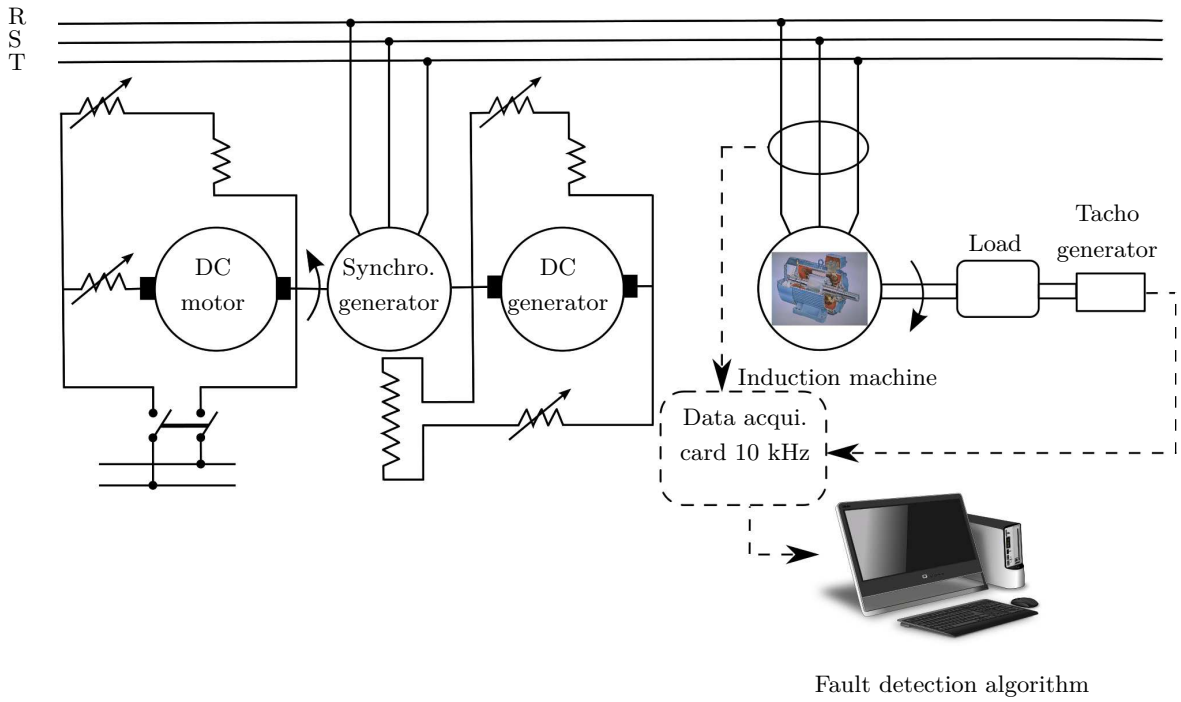

Figure 4.1: Test rig scheme [11] .

The induction machine has two 6204.2 ZR type bearings (single row and deep groove ball bearings) with the following parameters: outside diameter is 47 mm, inside diameter is 20 mm, and pitch diameter D is 31.85 mm. Bearings have 8 balls with an approximate diameter d of 12 mm and a contact angle of 0 °. Fig. 1.8 gives the bearing structure and the mean dimensions.

Bearing faults are obtained by simply drilling holes in different parts [165] as it is shown in Fig. 4.2. This figure gives artificially deteriorated bearings with outer race deterioration, inner race deterioration, cage deterioration and ball deterioration.

4.2.2 Measured quantities

The measured quantities for off-line bearing fault detection were the line-currents. These stator currents have been acquired and stored for further processing using the proposed methods on Matlab-Simulink®. For all the experiments, the stator fundamental frequency was almost equal to $f_s = 50$ Hz.

A healthy and faulty single phase stator current data collected from the experimental setup are shown in Fig. 4.3. A single phase stator current data waveform

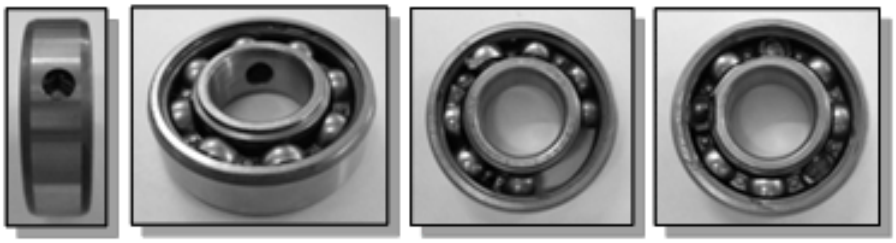

(a) (b) (c) (d)

Figure 4.2: Artificially deteriorated bearing: (a) outer race deterioration, (b) inner race deterioration, (c) cage deterioration, (d) ball deterioration.

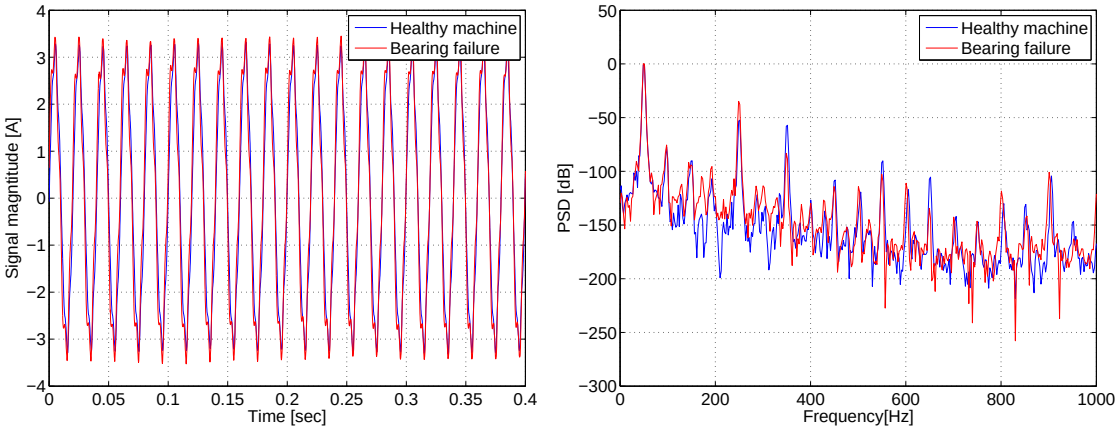

(a) Stator current waveform.

(b) Corresponding spectrum.

Figure 4.3: A healthy and faulty (Bearing cage fault) phase motor current data collected from the experimental setup.

corresponding to a healthy and faulty state of the motor under 50% load condition are given by Fig. 4.3(a). This figure shows that the stator currents are not exactly sinusoidal due to space harmonics. These space harmonics are due to the synchronous generator used to supply the induction machine. These space harmonics are visible on the stator current spectrum depicted in Fig. 4.3(b). Hence, in order to eliminate these space harmonics and since the information concerning the bearing faults is mostly contained in the low frequency content, the stator current signals were down-sampled at a 200 Hz sampling rate.

4.3 Bearing faults detection

As mentionned above, the fault studied herein is the bearing failures. This artificial fault is chosen for the validation of the fault detection methods based on the stator currents processing presented in chapter 1. Moreover, the bearing fault is used in order to prove the effectiveness of the proposed approaches in chapter 2 for fault detection in induction machine through the stator current processing. For the first experiments the signals were acquired at a 10kHz sampling frequency for $20s$ by a data acquisition card and processed using Matlab-Simulink®.

4.3.1 Stationary spectral estimation

This section presents the PSD estimation methods for bearing faults detection in induction machine. First, the periodogram and the Welch periodogram are studied. Then, the high resolution techniques are illustrated. Finally, some limitations are presented.

4.3.1.1 Periodogram and Welch periodogram

First, the classical spectral estimation techniques are used in order to analyze the stator current by assuming that signals are stationary. This provides a reference results for subsequent comparison with the advanced faults detection techniques presented in chapter 2. For the spectra visualization, the stator current and the corresponding periodogram and Welch periodogram for a healthy and a faulty machines with bearing fault are given by Fig. 4.4. The stator current and the corresponding periodogram are depicted in Figs. 4.4(a) and 4.4(b), respectively. Then, the Welch periodogram is computed using segments of length $N_w = 20000$ windowed with Hanning window. The segment overlap is equal to 50%. The obtained stator current spectra is shown in Fig. 4.4(c).

The healthy induction machine stator current PSD exhibits sidebands around the supply frequency. This phenomenon can be explained by a natural level of eccentricity or torque oscillations due to the coupling. In the case of a faulty machine, Figs. 4.4(b) and 4.4(c) show a rise of these sideband components.

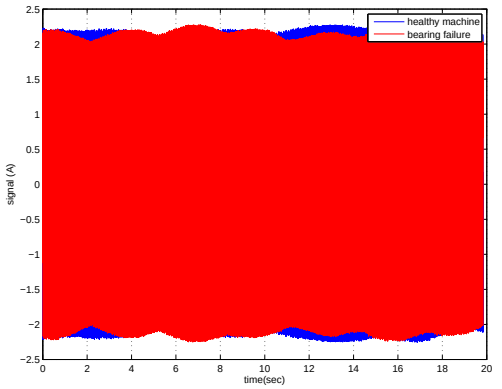

(a) Single phase stator current.

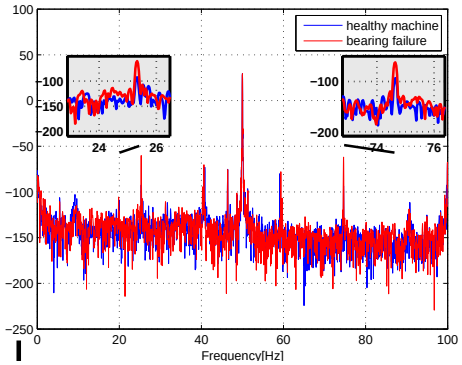

(b) The periodogram.

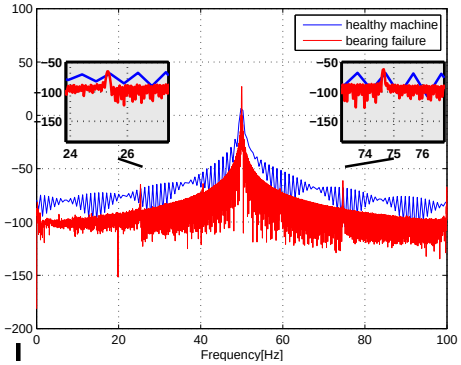

(c) The Welch periodogram.

Figure 4.4: PSD of stator current with bearing fault vs. healthy case.

4.3.1.2 MUSIC, ESPRIT and Prony methods

The high resolution spectral estimation techniques have been then used in order to estimate the stator current PSD. For MUSIC and ESPRIT, the number of sinusoids in noise has been chosen equal to 6 [166]. The covariance matrix has been computed using the forward-backward method. Regarding, the Prony method, the signal $x[n]$ is modelled as the impulse response of a filter having a system function of the form,

$$H(z) = \frac{B(z)}{A(z)} \tag{4.1}$$

where, the polynomials $B(z)$ and $A(z)$ are formed from the vectors

$$b = [b(0), b(1), ...b(p_1)] \tag{4.2}$$

$$a = [1, a(1), ...a(p_2)], \tag{4.3}$$

respectively. The parameter $p_1 = 1$ defines the number of zeros in the model and $p_2 = 128$ defines the number of poles.

The high resolution spectrum estimation simulation results are shown in Fig. 4.5. Figure 4.5(a) gives the MUSIC-based PSD estimation. It can be observed that the MUSIC algorithm exhibits the presence of sidebands responsible of the fault. However, the MUSIC algorithm does not estimate the sidebands amplitudes. Figure 4.5(b) depicts the ESPRIT-based PSD estimation. Similarly to MUSIC, the ESPRIT algorithm does not estimate the frequency components amplitude which means that it is not sufficient to measure the fault severity. In the sake of visualisation, the ESPRIT-based PSD has been drawn using the MLE for amplitudes estimation. Finally, Fig. 4.5(c) shows the Prony method for PSD estimation. This method allows to estimate the sidebands amplitude which allow to measure the fault severity (which may be done manually by an operator).

4.3.1.3 Summary on PSD estimation

It can be deduced from the results discussed above concerning the PSD estimation techniques for fault detection in stationary environment that :

- The periodogram suffers from a bad resolution for a short signal acquisition time and a bad statistic performance. The Welch periodogram enhances the statistic performances but decreases the frequency resolution. The way to get an acceptable representation is to acquire the signal during a long window time. Unfortunately, this way, the signal may be no longer stationary.
- The so called semi-parametric techniques allow to get high resolution representation but it requires some informations about the signal content (the PSD estimation based on MUSIC and ESPRIT requires the knowledge of the number of sinusoids in noise and the Prony method requires the knowledge of the polynomials order).

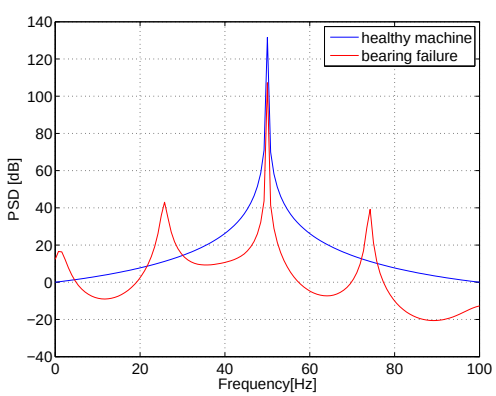

(a) MUSIC-based PSD estimation.

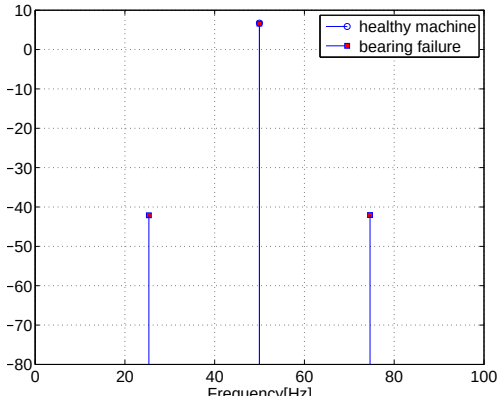

(b) ESPRIT-MLE-based PSD estimation.

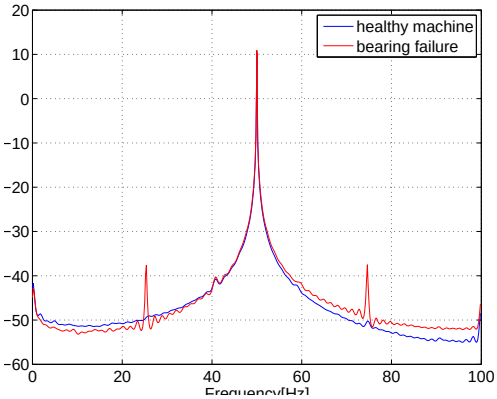

(c) Prony-based PSD estimation.

Figure 4.5: PSD of stator current with bearing fault vs. healthy case using high resolution techniques.

4.3.2 Demodulation techniques

The following subsections illustrate the demodulation techniques performance and some limitations. In fact, this section presents results obtained with the demodulation techniques presented in chapter 1. The stator current signal is a multicomponent signal due to the presence of several supply frequency harmonics. In order to obtain an approximation of a mono-component signal, the current is bandpass filtered with upper and lower cut-off frequencies equal to 80 Hz and 20 Hz and downsampled to 200 Hz. Then, the demodulation techniques are used to compute the analytical signal. Finally, the instantaneous amplitude and the instantaneous phase in the case of healthy

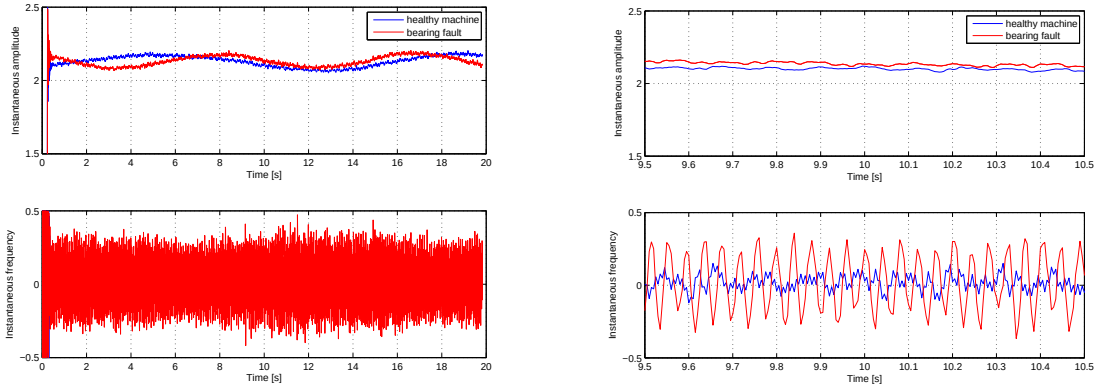

(a) Instantaneous amplitude and frequency.

(b) Zoom.

Figure 4.6: Synchronous demodulator-based demodulation.

induction machine and faulty one are computed in order to reveal the presence of the fault.

4.3.2.1 Synchronous demodulator

The instantaneous amplitude and frequency based on synchronous demodulator are given by Fig. 4.6. In this figure, one can note that the synchronous demodulator performs well and exhibits the existence of frequency modulation when a bearing fault exists. The modulation on the instantaneous amplitude can be explained by the low-pass filtering stage which introduces oscillations. These oscillations are not responsible of the fault but are a result of the filtering stage.

4.3.2.2 Concordia Transform

The Concordia transform performance is depicted in Fig. 4.7. As expected the stator current is frequency modulated when the bearing fault occurs. The CT based demodulation techniques outperform the synchronous demodulator and is easy to implement. The delay of 0.2s is not due to CT but to the preprocessing by bandpass filtering the stator current. It should be mentioned that the CT is more appropriate for balanced system. The CT may lead to incorrect results for the unbalanced case.

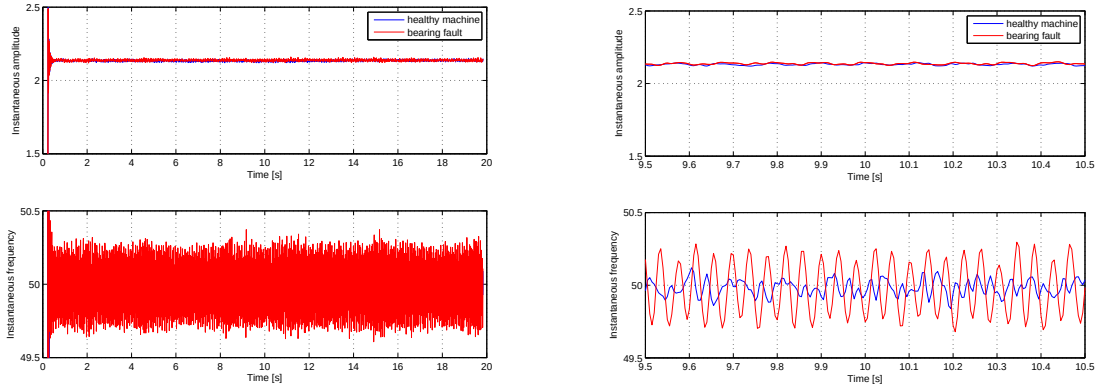

(a) Instantaneous amplitude and frequency. (b) Zoom.

Figure 4.7: Concordia Transform-based demodulation.

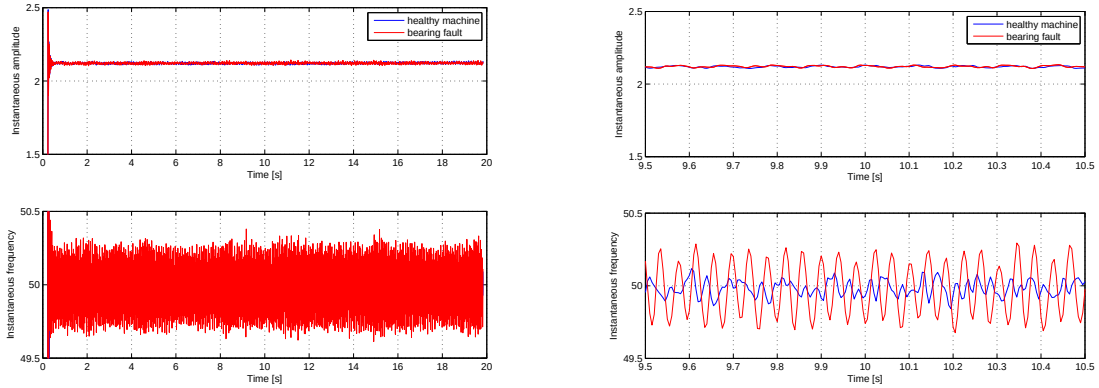

(a) Instantaneous amplitude and frequency. (b) Zoom.

Figure 4.8: Principal Component Analysis-based demodulation.

4.3.2.3 Principal Component Analysis

As opposed to CT the Principal Component Analysis leads to a better IA and IF estimation whatever the balance assumption [45]. The PCA-based demodulation results are shown in Fig. 4.8. Similar conclusions as previously can be drawn from this figure.

4.3.2.4 Hilbert transform

The Hilbert transform is well known approach for analytical signal computation. The advantage of the HT compared to CT and PSA is the fact that it requires a single

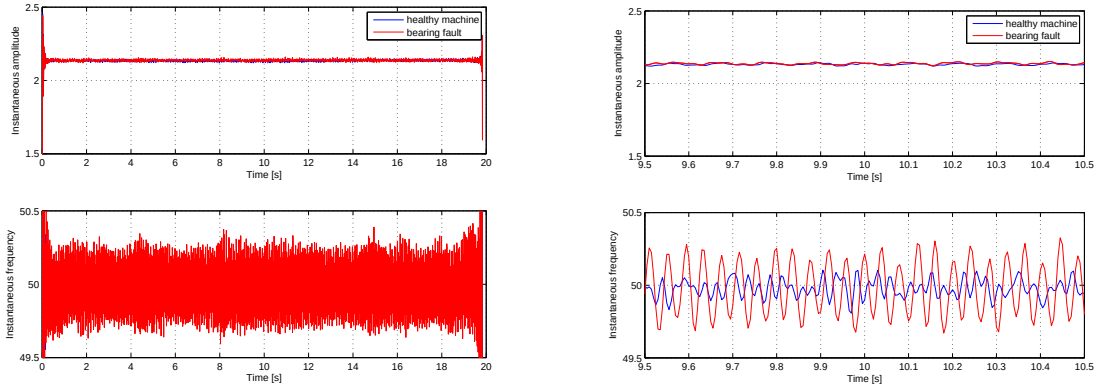

(a) Instantaneous amplitude and frequency.

(b) Zoom.

Figure 4.9: Hilbert transform-based demodulation.

phase stator current to extract the IA and the IF. The Hilbert transform simulation results are given by Fig. 4.9. From this figure, it can be deduced that the stator current is frequency modulated and the fault severity may be measured by estimating the frequency modulation index. Even if the Hilbert transform allows to reveal the frequency modulation and subsequently the presence of the fault, it suffers from border effects illustrated by Fig. 4.9(a). These border effects may lead to false conclusions on the health state of the bearing.

4.3.2.5 Teager energy operator

The Teager energy operator is a local estimator of the amplitude and frequency modulation. The instantaneous amplitude and frequency estimation based on TEO is shown by Fig. 4.10. It is clear from this figure that the TEO performs well and allows to exhibit the frequency modulation introduced by the fault.

4.3.2.6 Summary on demodulation techniques

After demodulation, the analytical signal and the corresponding instantaneous amplitude and frequency must be appropriately analyzed to assess the fault severity. Several papers have proposed to monitor the deviation of the analytical signal from a circle in the complex plane [167, 168]. This approach holds when the stator current is amplitude modulated but is not appropriate when the stator current is frequency

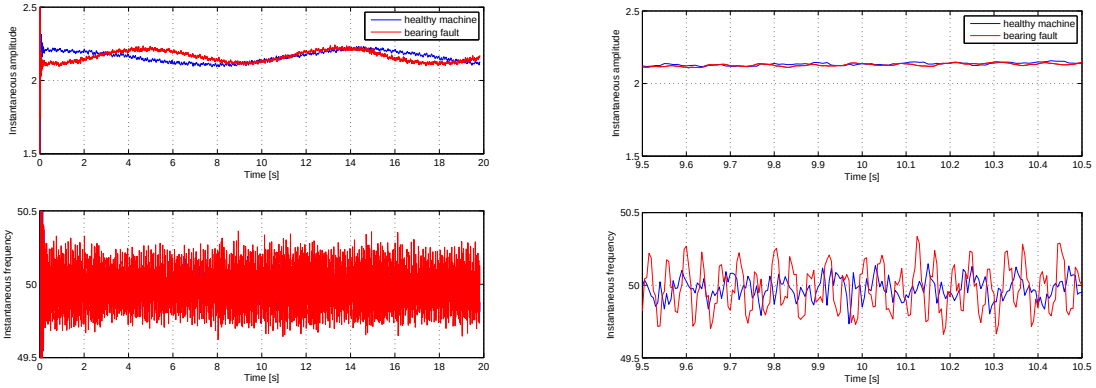

(a) Instantaneous amplitude and frequency.

(b) Zoom.

Figure 4.10: Teager energy operator-based demodulation.

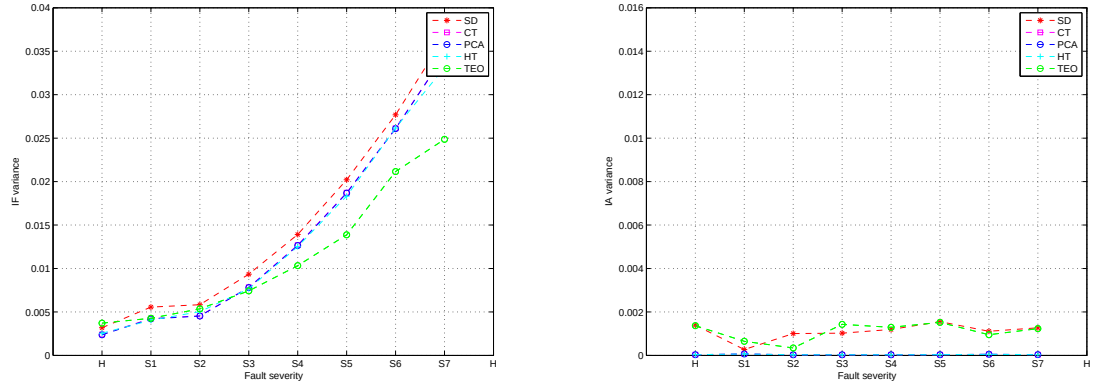

(a) Instantaneous frequency variance.

(b) Instantaneous amplitude variance.

Figure 4.11: Failure severity criteria: demodulation based on Hilbert transform.

modulated since the fault only affects the rotational speed in the complex plane. For this reason, we propose to compute the variance of the instantaneous amplitude and the instantaneous frequency. The simulation results for several faults severity are given by Fig. 4.11. As expected, the IF variance increases as the fault severity increases. The IA does not change significantly which means that the bearing fault introduces a frequency modulation not an amplitude modulation. Finally, it can be seen that the bearing fault introduces a frequency modulation in the stator current which can be highlighted by the variance of the instantaneous frequency. This result is in accordance with the theoretical study and experimental validation in [59].

4.3.3 Time-frequency/time-scale techniques

In this section, we compare several time-frequency/time-scale representations presented in chapter 1 for the detection of bearing faults. The stator-current signals have been analyzed with the following time-frequency representations:

- A Short-Time Fourier Transform with a Hamming window $h(t)$ of 256 samples length with 50% overlap,
- A Continuous Wavelet Transform with a Morlet mother wavelet $w(t)$,
- The Pseudo Wigner-Ville distribution computed from the analytical signal,
- The Hilbert-Huang transform.

All these representations, except the last one, have been implemented using the Time-Frequency Toolbox for Matlab® [130]. The HHT has been implemented using the G. Rilling's subroutines for Matlab-Simulink® [74, 131]. The following subsections compare the computational complexity and the readability of these time-frequency representations.

4.3.3.1 Representation readability and easiness of interpretation

The time-frequency/time-scale techniques have been used on a single phase stator current in order to reveal the bearing fault signature. Figures 4.12 to 4.15 display the time-frequency representations for healthy and faulty induction machines.

For each representation, we can observe a strong difference between the time-frequency representations of healthy and faulty induction machines. For the STFT (Fig. 4.12), CWT (4.13) and Pseudo WV (4.14), the faulty induction machine exhibits singular time-varying components (the sidebands amplitude changes with respect to time) at frequencies below 40Hz and above 70Hz. For the HHT (4.15), the bearing fault introduces frequency modulation of the 50Hz component.

Concerning the time-frequency resolution, figures show that the resolution of the STFT and CWT is lower than the one of the other representations. Indeed, as opposed to the Pseudo WV and HHT, the resolution of the STFT and CWT are limited by the Heisenberg-Gabor uncertainty principle. This constraint makes the STFT and CWT badly suited for analysis of signals with rapidly evolving frequency content.

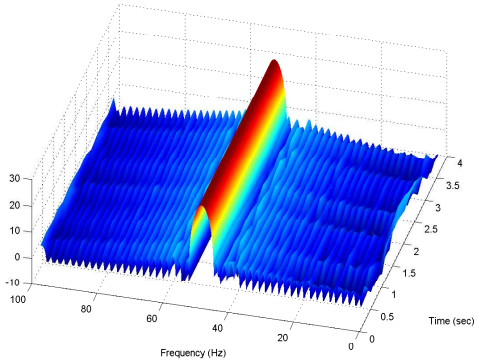

(a) Healthy Induction Machine.

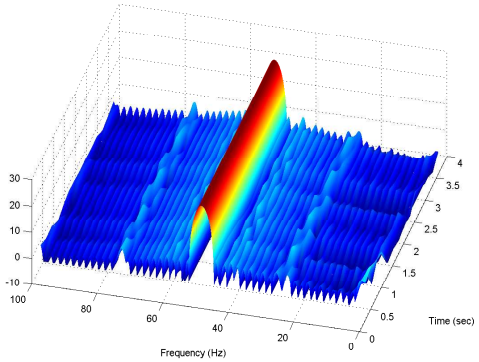

(b) Faulty Induction Machine.

Figure 4.12: Modulus of the STFT for a) healthy and b) faulty induction machine.

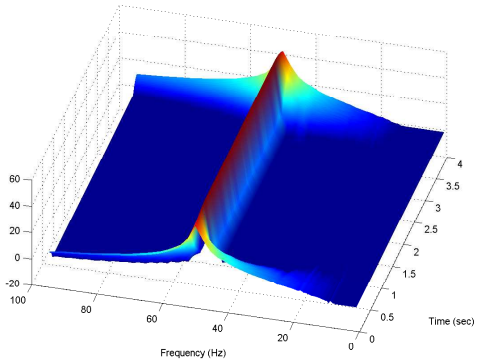

(a) Healthy Induction Machine.

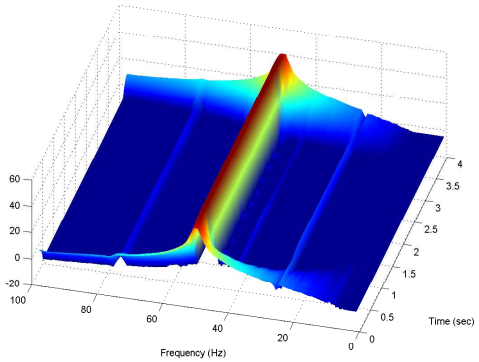

(b) Faulty Induction Machine.

Figure 4.13: Modulus of the Continuous Wavelet Transform for a) healthy and b) faulty induction machine.

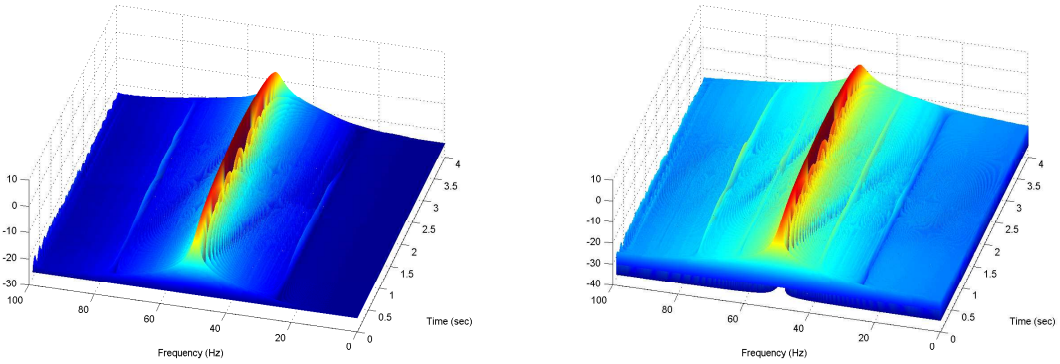

(a) Healthy Induction Machine. (b) Faulty Induction Machine.

Figure 4.14: Wigner-Ville Distribution for a) healthy and b) faulty induction machine.

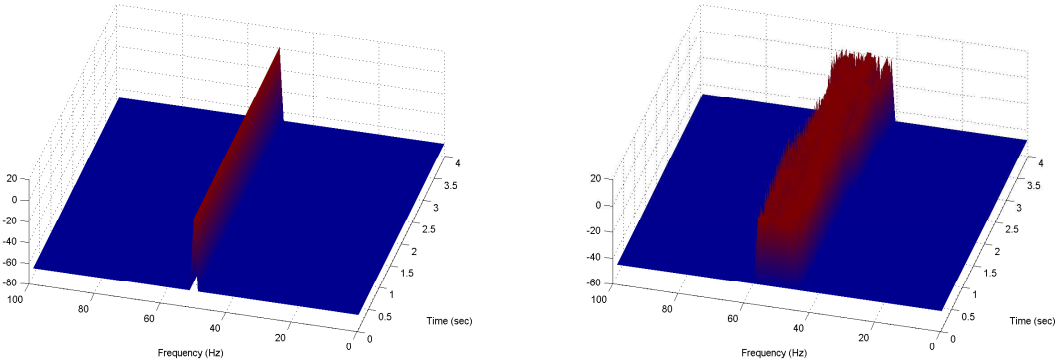

(a) Healthy Induction Machine. (b) Faulty Induction Machine.

Figure 4.15: Hilbert Huang Transform for a) healthy and b) faulty induction machine.

We can observe that the readability of the Pseudo-WV and HHT is lower than the one of the STFT and CWT. First, the Pseudo-WV exhibits interference terms which can render difficult the interpretation. Then, the HHT performance relies on the results of the EMD algorithm which means that the IMFs may not be mono-component signals. Moreover, the subsequent Hilbert may introduces some artefacts (border effect).

4.3.3.2 Computational Complexity

Matlab® programs were run offline on Elitebook PC at 2.3 GHz with 4 Go of RAM. The computational requirement of each algorithm is reported in Table 4.2.

Table 4.2: Computational Complexity.

Representation	(Average) Computational time
STFT	0.4 s
CWT	50.2 s
Pseudo WV	0.9 s
HHT	3.14 s

It can be deduced from this table that the CWT is the most computationally demanding technique as compared to the STFT, the Pseudo WV and the HHT. By comparing the computational time with the length of the recorded signal (4s), we can observe that the STFT and the Pseudo WV are the only two candidates that could be implemented in real-time under our configuration. In particular, the STFT, which has the lowest computational cost, is an attractive technique since it can be efficiently implemented using Fast Fourier Transform algorithm.

4.3.3.3 Summary of the time-frequency/time-scale representations

This section has presented a comparison of several time-frequency representations for bearing faults detection in a squirrel-cage induction machine. The Short-Time Fourier transform, the Continuous Wavelet transform, the Pseudo Wigner-Ville distribution and the Hilbert-Huang transform have been compared according to their computational complexity, time-frequency resolutions and readability. Offline simulations on experimental data have showed that each technique allows detection of the

Table 4.3: Comparison of several time-frequency representations.

Representation	Computational Cost	Resolution	Readability
STFT	++	- -	++
CWT	- -	+	++
Pseudo WV	+	+	-
HHT	-	++	+

bearing fault. For our simulations, Table 4.3 reports the advantages and disadvantages of each representation.

This table shows that the choice of a particular representation depends on the user's constraints and priorities in terms of computation complexity and easiness of interpretation. Moreover, the extraction of a fault detection criterion from these representations is far from being easier and is all the time done manually which is an handicap when it comes to the automatic implementation of fault detection procedure. In the next sections, we explore the proposed fault detection algorithms that allow to overcome some of these shortcomings, at the expense of requiring some information about the fault impact on the stator current.

4.3.4 MLE-based approach

This section investigates the appropriateness of the MLE-based approach for bearing faults detection in stationary and non-stationary operating conditions. The MLE-based approach was demonstrated first for specific bearing fault (bearing cage fault).

4.3.4.1 Fault detection results for stationary environment

In presence of bearing faults, it has been shown that the fault characteristic frequencies are given by: $f_k(\Omega) = |f_s \pm k f_c|$ $(k \in \mathbb{Z})$. The exact and the approximate MLE have been employed to investigate the existence of fault and its severity. The signal length was equal to 1s. Similarly to prior sections, the signal has been down-sampled at 200 Hz sampling rate in order to eliminate the time and space harmonics and then allowing to only focus on the fault signature on the induction machine stator current. The experimental results for different bearing fault severities are reported in Fig. 4.16

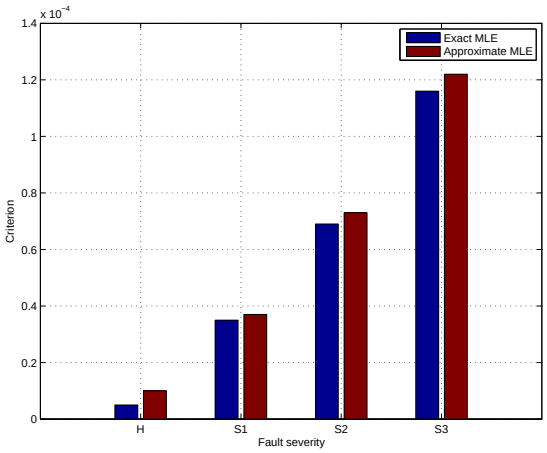

Figure 4.16: MLE and approximate MLE for bearing fault detection: values of the fault detection criterion $\mathcal{C}$ for several fault severities.

for the exact and the approximate MLE. This figure shows the proposed fault detection criterion with respect to the fault severity.

It can be seen from this figure that the fault detection criterion increases as the fault severity increases. The criterion is not equal to zero when the induction machine is operating under healthy condition. This result is entirely in accordance with the prior results found using the classical spectral estimation methods [59]. In fact, even if the machine is considered as healthy, there exist some manufacturing errors and natural shaft misalignment. Moreover, the approximate MLE results are slightly higher than those of the the exact MLE. This can be explained by the sidelobes introduced by the Fourier transform computation using the FFT algorithm step when using the approximate MLE.

By comparing the two techniques, we can note that the exact approach is more reliable than the approximated method. However, it must be emphasized that the approximate approach has practical advantages since it is based on the DFT (easiness of implementation and fast computation with FFT). The results given above confirm the effectiveness of the exact MLE-based technique over the approximate MLE-based approach.

The proposed technique may be used in order to detect several induction machine faults. Moreover, the proposed technique results may be used as an input for a fault classifier since it allows the extraction of the fault frequency signatures. Once the fault

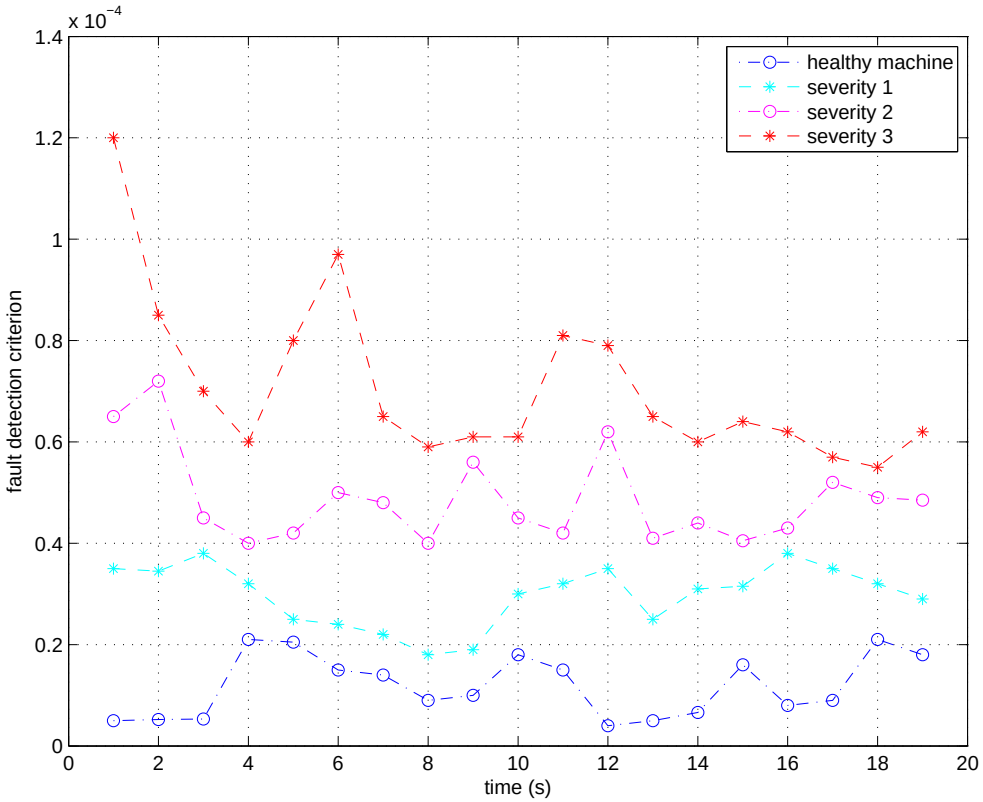

Figure 4.17: Criterion variations for bearing fault detection using the proposed Non-stationary MLE-based approach.

sensitive frequencies are extracted, the signatures given in the literature may be used to discriminate several faults. Afterwards, the proposed fault detection criterion could be used in order to measure fault severity.

4.3.4.2 Non-stationary MLE for fault detection

Figure 4.12 gives the stator current spectrogram in the case of healthy and faulty machine. It appears from this figure that the bearing fault can be detected using the stator current since the stator current spectrogram with bearing fault exhibits side-bands around the supply frequency introduced by the fault. Moreover, the sidebands amplitude changes with respect to time. For this reasons, the proposed algorithm; the non-stationary MLE is used in order to track the fault severity with respect to time. The simulation results on the experimental data are shown in Fig. 4.17.

It can be noticed from this figure that the fault detection criterion is non zero when the induction machine is operating under healthy condition. Moreover, the fault detection criterion is higher as the fault severity increases. It must be observed that the fault detection criterion is not constant with respect to time which confirms the fault severity variations with respect to time.

The experimental results for the MLE-based approach in stationary and non-stationary environment have confirmed the simulation results discussed in the previous chapter. These results have proved the effectiveness of the proposed approach for bearing faults tracking in induction machine. In the following, the MD-MUSIC is compared with the MLE-based method for bearing fault severity tracking.

4.3.5 Multidimensional MUSIC based method

This section reports on the performance of the proposed MD MUSIC for bearing fault detection on the experimental data. Experiments were performed with a supply frequency equal to $f_s = 50$ Hz. Signals are processed using the proposed MD MUSIC-based technique using Matlab-Simulink®.

4.3.5.1 Experimental results analysis in stationary operating conditions

The MD MUSIC have been tested on the same experimental data as for the MLE-based method. The MD MUSIC is used to estimate the power spectral density, then the MLE for spectral content amplitude estimation has been used in order to estimate the fault detection criteria.

The off-line experimental results are summarized on Table 4.4 for several bearing fault severities. This table gives the fundamental frequency, the fault characteristic frequency, the sidebands number and the sidebands amplitude estimation for a healthy and a faulty induction machine. Moreover, this Table presents the fault criterion variation for healthy and faulty induction machine. This table highlights the presence of the sidebands even if the induction machine is healthy since the model order is non-zero. A non-zero model order means that the healthy machine presents some asymmetries which are dues to manufacturing problems. However, these sidebands amplitude is lower than in the faulty case. The criterion computed using these amplitudes is given by figure 4.18.

Table 4.4: MD MUSIC: results for experimental healthy and faulty machines with L estimation for bearing faults detection.

State	$\widehat{f_s}$ (Hz)	$\widehat{f_c}$ (Hz)	$\widehat{L}$	$\widehat{a}_k$ (A)	$\mathcal{C}$ ($\times 10^{-5}$)
Healthy machine	49.92	24.918	2	$a_{-2} = 0.0014$ $a_{-1} = 0.0012$ $a_0 = 2.1648$ $a_1 = 0.0016$ $a_2 = 0.0032$	0.33736
Bearing fault (severity 1)	49.99	8.4020	1	$a_{-2} = 0$ $a_{-1} = 0.0081$ $a_0 = 2.1371$ $a_1 = 0.006$ $a_2 = 0$	2.2116
Bearing fault (severity 2)	50.07	24.8294	2	$a_{-2} = 0.0066$ $a_{-1} = 0.0105$ $a_0 = 1.9856$ $a_1 = 0.0069$ $a_2 = 0.0039$	5.5043
Bearing fault (severity 3)	50.05	24.8401	2	$a_{-2} = 0.0094$ $a_{-1} = 0.0110$ $a_0 = 2.0837$ $a_1 = 0.0079$ $a_2 = 0.0058$	7.037

This figure shows that the criterion increases in the case of a faulty machine. In fact, the fault detection criteria proposed based on MD MUSIC is proportional to the fault severity. Therefore, it can be assumed that this fault criterion based on the MD MUSIC and the MLE of amplitudes gives a reliable indicator of the fault existence. Moreover, its criticality can be measured correctly using the MD MUSIC. Note that

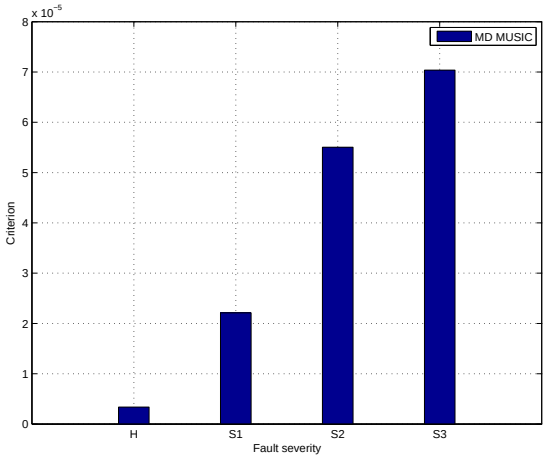

Figure 4.18: MD MUSIC for bearing fault detection: values of the fault detection criterion $\mathcal{C}$ for several fault severities.

the computed criterion is almost two times smaller than in the case of the MLE-based approach.

4.3.5.2 Non-stationary MD MUSIC-based bearing faults detection

In order to investigate the criterion variations with respect to time, experiments have been performed for 20 s signal length. The proposed approach was then applied on signal sub-vectors of 1 s length in order to demonstrate the usefulness of the proposed approach for fault severity tracking. Figure 4.19 summarizes the experimental results for several fault severities.

From this figure, it can be assumed that the proposed fault detection criterion is sensitive to the fault but varies with respect to time. Moreover, the fault detection criterion remains higher in the faulty case compared to the healthy one. These results are equivalent to those given by the non-stationary MLE-based approach.

When dealing with fault detection in electrical drives, we might want to decide between two situations: The drive is healthy or a fault is present. The decision will be based on a signal observation followed by an adequate processing in order to extract a suitable fault indicator. The indicator computation can be based on the previously described parametric or non-parametric methods. The problem is then equivalent to a binary hypothesis test [169]. An ideal detector is characterised by a probability of detection equal to 1 and probability of false alarm is equal to 0. In non-stationary

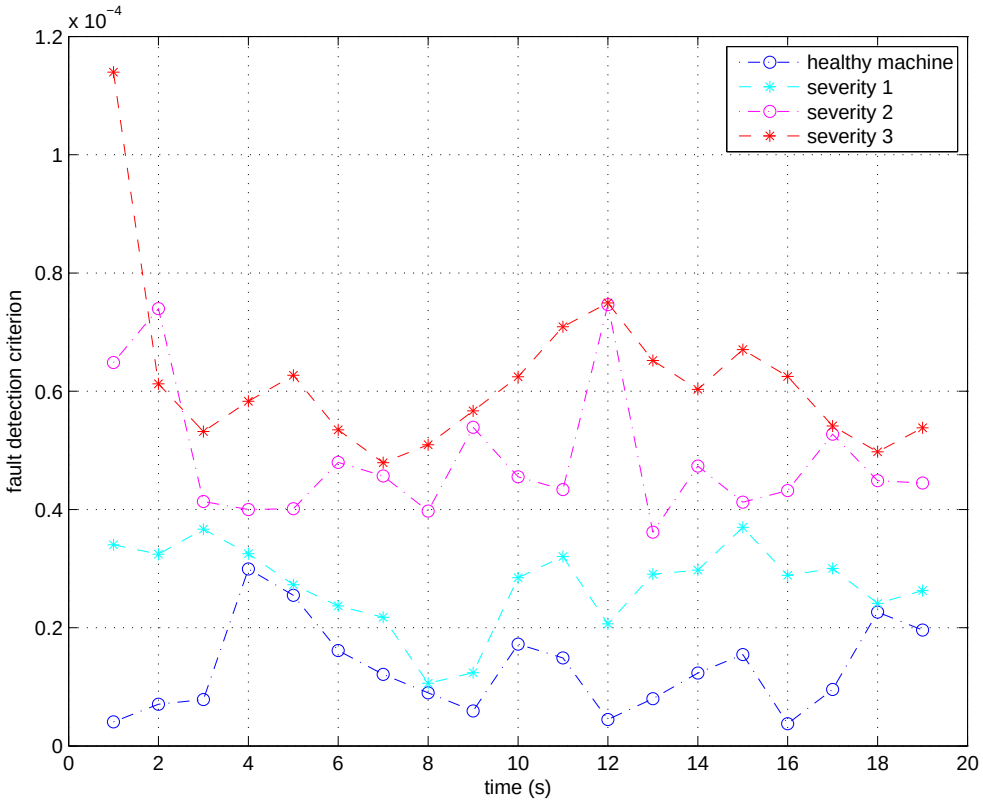

Figure 4.19: Criterion variations for bearing fault detection using the proposed MD MUSIC-based approach.

conditions and since the fault detection criterion depends on time it will be difficult to set a threshold allowing to distinguish a faulty machine from a healthy one with higher probability of detection.

4.4 Online condition monitoring

The proposed approaches for mechanical and electrical faults detection will be used in further works in order to validate the primary results presented within this chapter. An experimental study will investigate the effect of motor mechanical and electrical faults in induction machine. Machinery Fault Simulator (MFS-Magnum) with a 3-phase, 1 HP induction motor will be used for experiments. Mechanical and electrical faults such as shorted turn, broken rotor bars, mechanical imbalance, rolling element bearing faults, and rotor eccentricity can be introduced. For each case, motor voltages

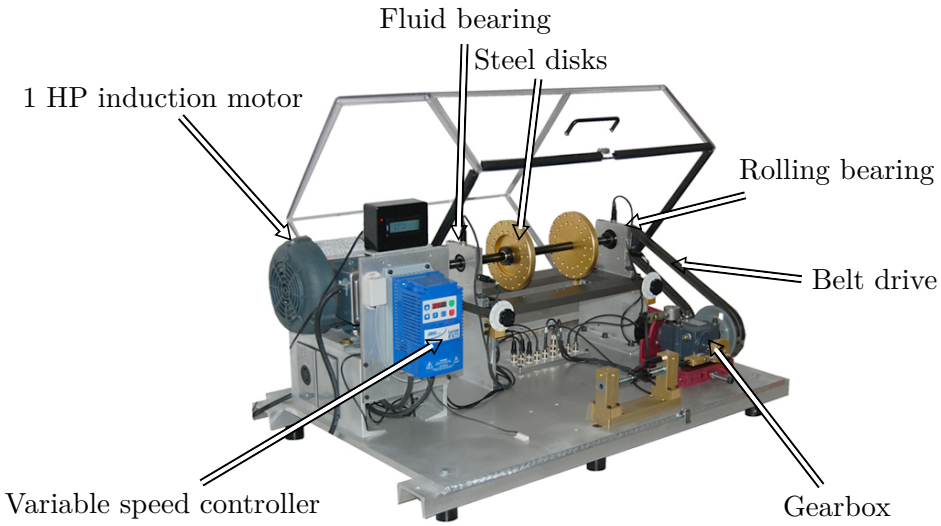

Figure 4.20: Machinery Fault Simulator.

and currents can be monitored and studied in time- and frequency-domains. The data for motor current/voltage on all three phases can then be analyzed using the proposed approaches.

4.4.1 Machinery Fault Simulator Description

Experiments will be performed on the Machinery Fault Simulator (MFS) designed by SpectraQuest Inc. [170]. MFS is a comprehensive test-bed for rotating machinery experiments and for in-depth studies of the most common machinery faults. The experimental setup is given by Fig. 4.20.

This test bed consists of an induction motor coupled to the main shaft supported by two rolling element bearings. The MFS specification are given by Table 4.5.

4.4.2 Further Investigations in Future Works

Using this test bed several faults can be emulated. Bearing faults (ORF, IRF, BF) can be introduced at the inboard bearing. Windings with a coil of the induction motor in phase can be shorted in various severity levels. Broken rotor bar experiments can be done too for three cases 1) healthy motor 2) motor with three broken bars and 3) motor with 6 broken rotor bars. Finally, the eccentricity fault can be emulated as well as torque oscillation.

Parameter	Value	Parameter	value
Induction Motor	1 HP	Rolling element bearings	MB ER-10K
Number of rotor bars	34	Number of balls	9
Number of stator slots	24	Ball Diameter [mm]	7.94
Shaft diameter [in]	0.625	Outer race Diameter [mm]	31.38
Shaft length [in]	21	Inner race Diameter [mm]	47.26
Rotor bearings span [in]	14.1	Bearing pitch Diameter [mm]	39.32

Table 4.5: Experiment parameters and specifications.

This tool allows to study the signatures of common machinery faults discussed in chapter 1. Moreover, various faults can be introduced either individually or jointly in a totally controlled environment.

Further investigations will be conducted in the next few months in order to validate the fault detection approaches presented within this manuscript. Specifically, the stator current will be processed in order to prove the effectiveness of the proposed approaches for mechanical/ electrical faults detection in induction machine.

4.5 Conclusion

This chapter has presented experimental results for stator current based monitoring of bearing faults. The used signal processing methods for stator current analysis are the MLE, the approximate MLE, and the MD MUSIC in steady-state conditions. In all cases, suitable fault indicators were automatically extracted from the stator current signal. In fact, the three approaches have been proposed and proven to be efficient for a bearing faults detection in induction machines. The model order estimation (sidebands number produced by fault and their localization) enhances the fault indicator reliability and then allows to detect incipient faults. This method could be adapted to any kind of fault assuming that the fault characteristic frequencies are known.

The advantages of these non-invasive approaches compared to other existing methods are their ability to extract information about the fault existence and then to compute criterion allowing to measure its severity. Moreover, the frequency components introduced by the fault depend on the machine operating conditions. Consequently, the

analysis allows to directly estimate the fault characteristic frequency without estimating the machine speed or slip.

These experimental tests are satisfactory and very encouraging regarding the validation of these three proposed approaches for several induction machine faults detection and for various operating conditions.

Chapter

5

Conclusions and Recommendations for Future Research

The predictive maintenance in electrical drives is of huge interest for engineers and researchers. Indeed, the predictive maintenance allows to overcome the shortcomings of traditional corrective and preventive maintenances. For instance, it is of great interest for far settled systems such as offshore wind and marine current turbines which are installed in a harsh environment and are difficult to access during operation. Condition monitoring and fault diagnosis in electrical drives and associated mechanical components are the root element of condition-based maintenance. This requires accurate and effective fault detection strategy able to detect any type of faults at an early stage and robust to load and inertia. As reported by the included references in chapter 1, a large majority of research was oriented toward induction machines fault in stationary environment (without speed or torque variations). It appears from this literature, that recent research topics have exceeded the traditional model-based methods for faults diagnosis. In fact, the focus has been made on the use of signal processing and AI techniques.

This PhD thesis has proposed statistics-based approaches for fault detection in induction machines. The proposed approaches are composed of two steps: a) the estimation of the PSD with a new parametric technique and b) the computation of a fault detection criterion in stationary and non-stationary operating conditions.

For the PSD estimation, we have proposed three techniques: the MLE, the approximate MLE and the MD MUSIC. Concerning the first approach, the PSD estimator has been computed using the maximum likelihood estimation approach. As opposed to non-parametric PSD estimators, the proposed technique exploits the fault frequency signatures in order to improve the performance of the fault detection criterion. As a result, the proposed estimator has better frequency-resolution and frequency-accuracy

than other techniques such as the periodogram. When the number of samples goes to infinity, it has also been demonstrated that the proposed PSD estimator can be efficiently implemented using the discrete Fourier transform (DFT). However, this approximate method does not perform as well as the exact method for short signals. The third approach is based on the MD MUSIC associated with the MLE for frequency bins amplitude estimation. Concerning the fault detection criterion, we have proposed a criterion based on the amplitude of the fault-related frequencies. This criterion is theoretically equal to zero for a healthy machine and increases for a faulty case.

The proposed approaches were successfully tested on simulations with eccentricity and broken rotor bars faults and experimental test rig with various bearing faults and load conditions. Simulation and experimental results have corroborated the efficiency of the exact MLE and the MD MUSIC, regardless of the fault type in contrary to the FFT-based approach. Furthermore, these results have suggested that the estimation of the model order L is very interesting since it allows to have a direct and fast first idea about the machine state.

Further works on these approaches must be conducted in order to implement classical optimization techniques such as gradient and the Newton method, etc. Moreover, from the signal processing point of view, it could be interesting to derive the Cramer-Rao bounds of the frequency parameters. These bounds could inform us about the advantages of using the faults frequency structure for PSD estimation.

Further investigations must be conducted in order to demonstrate the feasibility of the proposed techniques for transients in the case of real-time applications. Moreover, the use of these techniques must be generalized to generator operating conditions. This generalization may require more sophisticated optimization techniques for fault characterization. In addition of that, additional works are required in order to study the effects of the induction machine faults over the time- and space-harmonics of the stator current. Furthermore, the impact of these harmonics over the reliability of the proposed technique should be highlighted.

The work presented herein has dealt with induction machine faults detection, however, it will be interesting to propose techniques which allow to monitor the mechanical and electrical components : gearbox, power electronics and control devices. Furthermore, we believe that the control may have an effect over the faults impact on the magnetic quantities (flux) and afterwards the electrical signals through its corrective

effect. Hence, the forthcoming studies must highlight this impact and propose techniques allowing to monitor the induction machine operating conditions even in closed-loop control schemes.

5. CONCLUSIONS AND RECOMMENDATIONS FOR FUTURE RESEARCH

Chapter

6

Contribution à la détection et au diagnostic des défauts dans les machines asynchrones

Contents

6.1 Introduction

La surveillance et le diagnostic des éoliennes deviennent primordiaux pour diminuer les coûts de maintenance, augmenter la disponibilité des équipements et garantir la continuité de la production. Le coût de maintenance des éoliennes offshores est plus important a cause d'un environnement plus hostile et des sites d'installations difficilement accessibles. Les hydroliennes sont assujetties aux même types de défaillances que les éoliennes mais avec un degré de sévérité plus important et une possibilité d'intervention dépendante de la vitesse des courants marins ce qui engendre une diminution importante de la disponibilité. Ces contraintes justifient l'intérêt d'une surveillance en continue des hydroliennes et des éoliennes offshores.

L'objectif de ces travaux de recherche est de proposer des techniques fiables et efficaces pour détecter et caractériser les défauts des systèmes électromécaniques telles que les éoliennes et les hydroliennes de façon précoce et ainsi intervenir avant l'arrêt définitif du système.

Le moyen le plus efficace pour minimiser les coûts de maintenance et diminuer les taux de défaillances des éoliennes/ des hydroliennes et de leurs sous-systèmes est de construire des systèmes plus robustes. Par ailleurs, afin de favoriser la maintenance prédictive, l'accent doit être mis sur la conception de systèmes de surveillance en temps réel. L'objectif et l'intérêt du diagnostic et de la surveillance est d'améliorer leur disponibilité, leur fiabilité, valoriser la maintenance préventive par rapport à la

maintenance corrective et les rendre plus compétitifs par rapport à d'autres sources d'énergie, principalement le nucléaire et les énergies fossiles.

Ce chapitre relate mes travaux de recherche qui se focalisent sur les techniques de diagnostic des défaillances dont les systèmes électriques peuvent être assujetties. Ces travaux s'intéressent à la détection et le diagnostic des machines utilisées dans les applications éoliennes terrestres et offshores. Les résultats de ces recherches peuvent être généralisés aux systèmes de récupération des courants marins (hydroliennes) qui sont en phase de développement. Dans le cadre de ma thèse, nous traitons le cas de la machine asynchrone triphasé qui est largement utilisé dans l'industrie pour sa fiabilité et sa robustesse.

Mes travaux de thèse se focalisent essentiellement sur l'utilisation des grandeurs électriques, principalement des courants électriques, pour détecter les défauts d'origine mécanique et/ou électrique. Des techniques de traitement de signal avancées sont utilisées pour extraire la signature fréquentielle des défauts sur les courants statoriques. Ces signatures permettent dans un second temps de caractériser le défaut en terme de composant défaillant (à chaque composant défaillant correspond une signature fréquentielle particulière) et en terme de sévérité. La sévérité du défaut est mesurée à travers l'amplitude des composantes fréquentielles liées aux défauts des machines.

Ce chapitre décrit les principaux travaux réalisés dans le cadre de cette thèse. En effet, la section 6.2 présente un état de l'art des techniques de traitement de signal dédiées au diagnostic des machines asynchrones en se basant sur les courants statoriques. Ainsi, nous décrivons les principales techniques utilisées pour extraire la signature fréquentielle des défauts tout en mettant en évidence leurs limitations. La section 6.3 décrit les méthodes d'estimation spectrale paramétrique proposées pour la détection et la caractérisation des défauts dans la machine asynchrone. Il s'agit de formuler le problème de détection de défauts d'un point de vue statistique et de proposer ainsi une procédure de détection de défaut qui sort des sentiers battus qui consistent majoritairement à l'utilisation de techniques classiques d'estimation spectrale. Ensuite, ces techniques ont été étendues afin de prendre en considération les signaux non-stationnaires dans la section 6.4. Les méthodes proposées ont été testées en simulation en utilisant des courants statoriques issues d'un outil de simulation de la machine asynchrone basé sur les circuits électriques magnétiquement couplés dans la section 6.5, puis validée en expérimentation en utilisant une machine asynchrone conventionnelle dans la section 6.6. La section 6.7 conclue ce chapitre et présente quelques pistes pour des travaux à venir.

6.2 État de l'art des techniques existantes pour la détection des défauts de la machine asynchrone

La surveillance des systèmes électromécaniques devient primordiale pour améliorer leur fiabilité, disponibilité, sécurité et optimiser leur production. Les opérations de détection des défauts dans les moteurs et les générateurs sont habituellement réalisées en utilisant des techniques de surveillance vibratoire, mesure de température, surveillance de lubrification, surveillance du flux magnétique ou encore des courant statoriques [29, 30]. La surveillance basée sur l'acquisition des courants statoriques présente l'avantage d'être non-invasive et ne requiert pas d'instrumentation particulière [45, 48, 49, 50]. De plus, les signaux électriques sont généralement mesurés à d'autre fins, telles que le contrôle ou la protection.

6.2.1 L'impact des défauts sur le courant statorique

La machine asynchrone est assujettie à diverses défaillances qui affectent principalement trois composants: le stator, le rotor et/ou les roulements. Les travaux récents traitant des défaillances de la machine asynchrone [2] démontrent que les roulements (69%), les enroulements du stator (21%), le rotor (7%) et l'arbre moteur/couplage sont les principaux éléments défaillants dans les entraînements électriques. La plupart des travaux de recherche récents traitant de la détection des défauts dans les machines asynchrones ont été dirigés vers la surveillance électrique tout en mettant l'accent sur la surveillance basé sur le courant statorique. En particulier, le spectre du courant est analysé dans le but d'extraire les composantes fréquentielles introduites par le défaut. Le tableau 6.1 présente un résumé des effets des défauts sur le courant statorique de la machine asynchrone (signature fréquentielle).

Les signatures fréquentielles présentées dans la table.6.1 sont exploitées, dans le cadre de ce rapport, dans le but de proposer des techniques plus précises et par conséquent plus fiables pour la détection des défaillances dans les machines asynchrones. La présence d'un défaut entraîne l'augmentation de l'amplitude de ces composantes ce qui révèle l'existence d'un état anormale de fonctionnement

6.2.2 Techniques non-paramétriques

Plusieurs études ont démontrées l'intérêt de l'utilisation du contenu spectrale des courants statoriques pour la détection et la caractérisation des défauts. En particulier, il a été démontré que les défauts introduisent des composantes fréquentielles spécifiques

Table 6.1: La signature fréquentielle des défauts pour la machine asynchrone [12, 13]. Le symbole f_o correspond à la fréquence vibratoire caractéristique du défaut de roulements, qui dépend des dimensions des roulements.

État de la machine asynchrone	Signature fréquentielle	Paramètres
Défaut de roulement	$\|f_s \pm k f_o\|$	$k = 1, 2, 3, ...$
Rupture de Barres	$f_s \left[k(\frac{1-s}{p}) \pm s\right]$	$\frac{k}{p} = 1, 3, 5, 7, 11, 13...$
Excentricité	$f_s \left[1 \pm k \left(\frac{1-s}{p}\right)\right]$	$k = 1, 2, 3, ...$
Oscillation de charge	$f_s \left[1 \pm k \left(\frac{1-s}{p}\right)\right]$	$k = 1, 2, 3, ...$

autour de la fréquence fondamentale [12, 13]. Pour une machine défaillante, la localisation de ces fréquences est donnée par $f_k(\Omega)$, où f_k corresponds à la k^{eme} composantes ($k \in \mathbb{Z}$), et Ω est un ensemble de paramètres à estimer dans le but de déterminer l'état de fonctionnement de la machine asynchrone. Par exemple, dans le cas d'une rupture de barre $\Omega = \{f_s, s\}$. Ces composantes fréquentielles sont associées à des défauts d'origines mécaniques et électriques tels que les défauts d'excentricité, les défauts de roulements, les défauts de rupture de barres rotoriques, etc.

Les techniques d'estimation spectrale classique utilisées pour la détection des défauts permettent de rendre compte de l'existence d'un défaut en comparant visuellement les spectres dans le cas sain (base de données) et le cas de la machine supervisée [43]. En régime permanent, des techniques d'estimation spectrale ont été utilisées et peuvent être regroupées en deux catégories: les techniques non-paramétriques et les techniques paramétriques [7].

Les techniques non-paramétriques comprennent le périodogramme et ses extensions, qui est généralement implémenté en utilisant la FFT. Le périodogramme a été utilisé pour la détection des défauts dans [12, 13]. L'inconvénient majeur de ce dernier réside dans ses, relativement, mauvaises performances. En effet, le périodogramme est un estimateur biaisé et non-consistent de la densité spectrale de puissance. D'autres extensions du périodogramme permettent d'améliorer ses propriétés statistiques telles que le périodogramme de Bartlett [56] et le périodogramme de Welch [56, 171]. Par ailleurs, une autre technique nommée Zoom-FFT (ZFFT) [97, 98] a été introduite afin

d'améliorer la précision fréquentielle sans augmenter la complexité calculatoire en se focalisant sur des zones fréquentielles particulières. Néanmoins, le périodogramme et ses extensions souffrent d'une faible résolution fréquentielle, définie comme étant la capacité à distinguer deux composantes de fréquences rapprochées.

6.2.3 Techniques paramétriques

Des connaissances préalables sur le modèle du signal permettent l'utilisation de méthodes dites paramétriques pour améliorer la résolution fréquentielle. Ces techniques sont généralement appelées méthodes à haute résolution et comprennent deux sous-classes: les méthodes de prédiction linéaire et les techniques des sous-espaces. La classe de prédiction linéaire contient plusieurs algorithmes tels que les méthodes de Prony et de Yule-Walker. L'utilisation de ces méthodes pour la détection de défauts dans les entraînements électriques a été étudiée dans [99] et [100]. La deuxième classe comprend des approches dites méthodes des sous-espaces telles que MUSIC et ESPRIT. L'application de ces méthodes pour le diagnostic des machines asynchrones sont disponibles dans [30, 104, 105, 106]. Dans [106], l'algorithme MUSIC et une méthode de zoom ont été combinées pour réduire le coût calculatoire de l'estimateur spectral en se focalisant sur une bande fréquentielle particulière. Cependant, ces techniques sont généralement gourmandes en temps de calcul et présentent des estimateurs sous-optimaux de la PSD. De plus, leurs performances diminuent de manière significative lorsque le niveau de bruit augmente.

En plus des techniques mentionnées ci-dessus, de nombreuses procédures de détection des défauts basées sur l'analyse statistique des courants statoriques ont été proposées telles que MCMFT [143] et les méthodes temps-fréquence adaptative [133] sans présenter des critères de détection de défauts pour réaliser un diagnostic automatique .

La figure 6.1 représente un schéma récapitulatif des techniques d'analyse spectrale dédiées aux diagnostic des machines asynchrones basé sur l'acquisition des courants statoriques.

6.2.4 Techniques de démodulation

Il a été démontré que de nombreux types de défauts des machines asynchrones peuvent conduire à la modulation d'amplitude ou de phase des courants statoriques avec un indice de modulation directement liée à la sévérité des défauts [35, 67, 109, 110]. Par conséquent, la détection de ces défauts peut être réalisée en utilisant les techniques

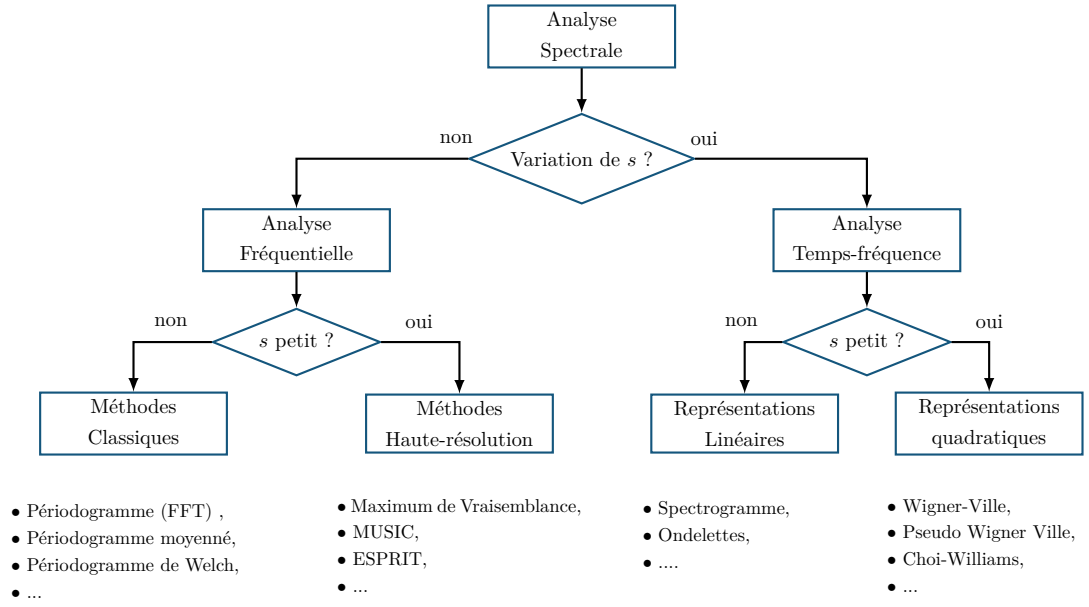

Figure 6.1: Techniques d'analyse spectrale dédiées à la détection des défauts dans les machines asynchrones.

de démodulation. Ces techniques peuvent être classés en deux grandes catégories: les techniques mono-dimensionnelles et multi-dimensionnelles. Les techniques mono-dimensionnelles comprennent le démodulateur synchrone, l'opérateur d'énergie de Teager et la transformée de Hilbert. Les méthodes multidimensionnelles comprennent la transformation de Concordia et l'analyse en composantes principales.

Dans cette section, nous considérons un système triphasé. En présence d'un défaut, les trois courants de phase $x_1[n]$, $x_2[n]$ et $x_3[n]$ sont simultanément modulés, et les courants peuvent être exprimés comme suit

$$\begin{aligned} x_1[n] &= \alpha_1 a[n] cos(\Phi[n]) \\ x_2[n]) &= \alpha_2 a[n] cos(\Phi[n] - \frac{2\pi}{3}) \\ x_3[n] &= \alpha_3 a[n] cos(\Phi[n] - \frac{4\pi}{3}) \end{aligned} \tag{6.1}$$

On note $\mathbf{x}[n] = [x_1[n], x_2[n](t), x_3[n]]^T$ les 3×1 le vecteur contenant les courants statoriques. L'objectif principal de la majorité des techniques de démodulation consiste à calculer le signal analytique à partir des signaux récupérés sur la machine asynchrone. Si $x[n]$ est un signal à valeur réelle, le signal analytique correspondant s'exprime sous

la forme

$$z[n] = a[n]e^{j\Phi[n]} \tag{6.2}$$

Une fois le signal analytique est calculé, l'amplitude instantanée $a[n]$ et la fréquence instantanée $f[n]$ peuvent être exprimées respectivement

$$a[n] = |z[n]| \tag{6.3}$$

$$f[n] = \frac{1}{2\pi}\frac{arg(z[n+1]) - arg(z[n])}{T_s} \tag{6.4}$$

Où $T_s = \frac{1}{F_s}$ est la période d'échantillonnage et $|.|$ et $arg(.)$ sont le module et l'argument du signal complexe $z[n]$, respectivement.

Dans ce qui suit les techniques mono-dimensionnelles sont décrites en premier. Dans ce cas, un seul courant de phase est utilisé et il est noté $x[n] = x_1[n]$. Ensuite, les approches multi-dimensionnelles sont présentées et leurs propriétés mises en évidence pour les courants statoriques donnés par (6.1).

6.2.4.1 Le démodulateur synchrone

Le démodulateur synchrone est connu comme un démodulateur des signaux AM/FM. Dans le cas du démodulateur synchrone, nous adoptons les hypothèses suivantes:

- $\mathcal{H}_1$: $\Phi[n] = 2\pi f_0 n + \varphi[n]$
- $\mathcal{H}_2$: La fréquence porteuse f_0 est supposée connue.

Le principe du démodulateur synchrone est illustrée par la Fig. 6.2. Mathématiquement parlant, le démodulateur synchrone est donnée par

$$x_1^s[n] = 2\mathcal{F}\left\{x[n]\cos(2\pi f_0 n/F_e)\right\} = 2 \times h[n] * x[n]\cos(2\pi f_0 n/F_e) \tag{6.5}$$

$$x_2^s[n] = -2\mathcal{F}\left\{x[n]\sin(2\pi f_0 n/F_e)\right\} = -2 \times h[n] * x[n]\sin(2\pi f_0 n/F_e) \tag{6.6}$$

où la symbole " $*$ " désigne l'opérateur de convolution. L'opérateur $\mathcal{F}\{.\}$ correspond à un filtre passe-bas. Par ailleurs, $h[n]$ est un filtre passe-bas dont la réponse fréquentielle est donnée par

$$\mathcal{H}(f) = \begin{cases} 1 & \text{if } f \leq f_0 \\ 0 & \text{if } f > f_0 \end{cases} \tag{6.7}$$

En vertu d'un filtrage approprié, il peut être démontré lorsque $a[n]$ et $\phi[n]$ ne varient pas trop vite que [111] (voir ANNEXE C)

$$x_1^s[n] = a[n]\cos(\phi[n]) \tag{6.8}$$
$$x_2^s[n] = a[n]\sin(\phi[n]) \tag{6.9}$$

Par conséquent, le signal analytique en temps discret est donnée par

$$z^s[n] = x_1^s[n] + jx_2^s[n] \tag{6.10}$$
$$= a[n]e^{j\varphi[n]} \tag{6.11}$$

Le démodulateur synchrone a été utilisé pour le diagnostic du multiplicateur à plusieurs étages par démodulation d'amplitude du courant de phase dans [70].

6.2.4.2 La transformée de Hilbert

La transformée de Hilbert (HT) est un outil largement utilisé dans le domaine du traitement de signal. Pour un signal discret $x[n]$, la transformée de Hilbert est donnée par

$$x^h[n] = x[n] * h[n], \tag{6.12}$$

où

$$h[n] = \begin{cases} 0 & \text{si n est pair,} \\ \frac{2}{\pi n} & \text{si n est impair.} \end{cases} \tag{6.13}$$

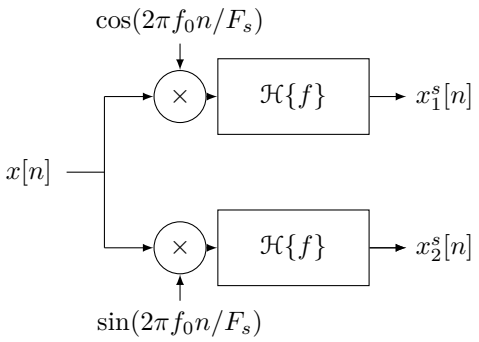

Figure 6.2: Démodulateur synchrone.

Lorsque $\Phi[n]$ et $a[n]$ ne varient pas trop vite, le signal analytique $z^h[n]$ associée à $x[n]$ est définie comme suit [115]

$$z^h[n] = x[n] + jx^h[n] = a[n]e^{\Phi[n]} \tag{6.14}$$

La transformée de Hilbert peut être calculée pour un signal réel à temps discret de taille N en utilisant efficacement l'algorithme de transformée de Fourier rapide [116].

Le théorème de Bedrosian [114], traitant de la transformée de Hilbert du produit de deux fonctions réelles, a démontré que l'unicité de la fréquence instantanée et l'amplitude instantanée n'est satisfaite que si les spectres de la fréquence instantanée et du sinus de la phase instantanée sont disjoints.

La transformée de Hilbert a été employée pour détecter l'excentricité et la rupture de barres en régime transitoire dans [117, 118]. De plus, dans [72], la transformée de Hilbert a été utilisée pour traiter le courant statorique dans la machine synchrone à aimant permanent pour diagnostiquer la démagnétisation des aimants.

6.2.4.3 L'opérateur d'énergie de Teager

Il a été démontré que l'opérateur d'énergie de Teager (OET) permet de suivre la fréquence instantanée (FI) et l'amplitude instantanée (AI) d'un signal [119], sans calculer le signal analytique. L'OET pour des signaux à temps discret est donnée par [120]

$$\Psi(x[n]) = x^2[n] - x[n+1]x[n-1] \tag{6.15}$$

On constate que l'OET est un opérateur local qui permet de capturer les fluctuations d'énergie avec une bonne résolution temporelle. Dans [120], les auteurs ont présenté un estimateur des AI et FI d'un signal vocal appelé l'algorithme de séparation d'énergie (ASE):

$$a[n] \approx \sqrt{\frac{\Psi[x[n]]}{1 - \left(1 - \frac{\Psi[x[n] - x[n-1]]}{2\Psi[x[n]]}\right)^2}} \tag{6.16}$$

$$f[n] \approx \frac{1}{2\pi}\arccos\left(1 - \frac{\Psi\left[x[n] - x[n-1]\right]}{2\Psi[x[n]]}\right) \tag{6.17}$$

L'ASE présente une propriété intéressante car il demande moins de temps de calcul et a une meilleure résolution temporelle que les techniques de démodulation classiques comme la transformée de Hilbert. Le principal inconvénient de cet opérateur est sa

sensibilité au bruit ou la non-concordance du modèle. En outre, il suppose que la FI évaluée ne varient pas trop rapidement par rapport à la fréquence porteuse. L'ASE a été utilisé pour la détection des défauts en se basant sur des signaux de vibration dans [121].

6.2.4.4 La transformée de Concordia

La transformée de Concordia (TC) est une transformée linéaire multidimensionnelle qui permet d'extraire deux composantes orthogonales à partir des courants statoriques triphasés. Dans le cas de la TC, nous supposons que les courants triphasés constituent un système équilibré. Nous désignons par $\mathbf{x}^c[n] = [x_1^c[n], x_2^c[n]]^T$ les deux composantes extraites par la transformée de Concordia. La TC peut être exprimée sous une forme de matrice comme suit

$$\mathbf{x}^c[n] = \begin{bmatrix} x_1^c[n] \\ x_2^c[n] \end{bmatrix} = \sqrt{\frac{2}{3}} \begin{bmatrix} \frac{\sqrt{2}}{\sqrt{3}} & \frac{1}{\sqrt{6}} & -\frac{1}{\sqrt{6}} \\ 0 & \frac{1}{\sqrt{2}} & -\frac{1}{\sqrt{2}} \end{bmatrix} \mathbf{x}[n] \tag{6.18}$$

Il est démontré que le signal analytique $z^c[n]$ est donnée par [125]

$$z^c[n] = x_1^c[n] + jx_2^c[n] = a[n]e^{j\Phi[n]} \tag{6.19}$$

Les performances de la TC ont été comparées avec la TH pour la détection des défauts dans la machine asynchrone dans le domaine temps-fréquence en se basant sur les courants triphasé dans [71]. Dans [107], la TC a été combinée avec ESPRIT pour améliorer ses performances de détection de défauts rotoriques dans la machine asynchrone à faible glissement.

6.2.4.5 L'analyse en composantes principales

L'analyse en composantes principales (ACP) est un outil statistique qui transforme un certain nombre de signaux corrélés en un petit nombre de composantes principales (une composante en phase et une autre en quadrature). Les deux principales composantes de $\mathbf{x}[n]$, notée $\mathbf{x}^p[n] = [x_1^p[n], x_2^p[n]]^T$ sont données par

$$\mathbf{x}^p[n] = \begin{bmatrix} x_1^p[n] \\ x_2^p[n] \end{bmatrix} = \beta \Lambda^{\frac{-1}{2}} \mathbf{U}^T \mathbf{x}[n] \tag{6.20}$$

où β est un terme donné par

$$\beta = \sqrt{\frac{trace[\mathbf{R}_x]}{3}} \tag{6.21}$$

et où la matrice de covariance $\mathbf{R}_x$ du signal $\mathbf{x}[n]$ est définie par

$$\mathbf{R}_x = E[\mathbf{x}[n]\mathbf{x}^T[n]] = \mathbf{U}\Lambda\mathbf{U}^T \tag{6.22}$$

avec λ et $\mathbf{U}$ sont des matrices contenant les valeurs propres et les vecteurs propres de $\mathbf{R}_x$, respectivement.

Sous les hypothèses que $\Phi[n]$ est répartie uniformément dans $[0;\ 2\pi]$ et $a[n]$ et $\Phi[n]$ sont indépendants, il peut être démontré que le signal analytique $z^p[n]$ peut être estimé comme

$$z^p[n] = x_1^p[n] + jx_2^p[n] = a[n]e^{j\Phi[n]}e^{-j\theta}. \tag{6.23}$$

L'ACP a été utilisée pour la détection des défauts des roulements dans la machine asynchrone et comparée avec la TC dans [45]. Dans [126], l'ACP a été utilisée pour le prétraitement des courants statoriques triphasés afin de détecter les défauts des enroulements statoriques et les ruptures de barres dans la machine asynchrone. Dans [127], le courant statorique a été traité pour en extraire les composantes alpha-bêta en utilisant la transformée de Park/Concordia ainsi que la ACP pour le calcul des composantes principales. Ces composants sont utilisés comme entrée pour un réseau de neurones non supervisé pour diagnostiquer les défauts statoriques dans la machine asynchrone.

6.2.5 Techniques temps-fréquence/temps-échelle

Si l'analyse fréquentielle de Fourier met en œuvre deux représentations conjuguées et globales, l'une de type temporelle, et l'autre de type fréquentielle, la nature est cependant riche en signaux pour lesquels l'information utile est véhiculée non seulement par les fréquences émises mais aussi par la structure temporelle même du signal [172]. Pour les besoins de l'analyse, il est possible d'associer, à un signal temporel ou fréquentiel, des représentations possédant simultanément les deux caractères temporel et fréquentiel. Ces représentations sont qualifiées de représentations temps-fréquence ou temps échelle. Ces représentations ne constituent pas un gain d'informations, mais plutôt une redistribution de l'information contenue dans le signal analysé de façon à en faciliter l'interprétation. Diverses méthodes permettent d'obtenir des représentations temps-fréquence ou temps-échelle possédant des propriétés et performances variées.

6.2.5.1 Spectrogramme

Le spectrogramme est basé sur la Transformée de Fourier à Court Terme (TFCT). La TFCT considère implicitement que l'évolution du contenu fréquentiel du signal est quasi-stationnaire sur l'étendue d'une fenêtre d'analyse. Elle divise le signal en segments courts et consécutifs, puis calcule la transformée de Fourier de chaque segment. La formulation mathématique de la TFCT est donnée par l'équation (6.24).

$$S_x(t,f) = \int_{-\infty}^{\infty} x(\tau) w^*(\tau - t) e^{-2j\pi f \tau} d\tau \tag{6.24}$$

Où $x(.)$ représente le signal temporel échantillonné, $w(.)$ est la fenêtre temporelle. Le spectrogramme est défini comme étant le carré du module de TFCT, c'est à dire $|S_x(t,f|^2$. La résolution en temps et en fréquence du spectrogramme est limitée par le principe d'incertitude de Heisenberg-Gabor qui stipule que l'on ne peut pas être infiniment précis en temps et en fréquence [173], la formulation mathématique du principe est donnée ci-dessous (6.25).

$$\Delta f . \Delta t \geq \frac{1}{4\pi} \tag{6.25}$$

Où Δf et Δt sont respectivement la résolution temporelle et la résolution fréquentielle (la dispersion d'énergie). Ces quantités sont définies par (6.26).

$$\Delta t = \sqrt{\tfrac{1}{E}\int (t - < t >)^2 |x(t)|^2 dt} \quad \Delta f = \sqrt{(\tfrac{1}{E}\int (f - < f >)^2 |X(f)|^2 df} \tag{6.26}$$

E Étant l'énergie du signal et $< t >$, $< f >$ représentent respectivement, la moyenne temporelle et fréquentielle d'énergie définies par (6.27).

$$< t >= \tfrac{1}{E}\int |x(t)|^2 dt \quad < f >= \tfrac{1}{E}\int f |X(f)|^2 df \tag{6.27}$$

Le spectrogramme est une analyse mono-résolution. Autrement dit, la résolution est la même quelque soit la fréquence et le temps. Par ailleurs, le spectrogramme ne permet pas d'être à la fois précis en temps et en fréquence.

6.2.5.2 Scalogramme

La transformée en ondelettes permet une analyse des différentes fréquences avec diverses résolutions. Cette analyse privilégie la résolution fréquentielle en basses fréquences et la résolution temporelle en hautes fréquences. La transformation en ondelettes (TO) revient à projeter le signal à analyser sur une base de fonctions déduites par décalage

temporel et dilatation/compression d'une fonction initiale réelle ou complexe appelée ondelette mère. La transformée en ondelettes continue est donnée par (6.28).

$$T_x(t,a) = \frac{1}{\sqrt{a}} \int_{-\infty}^{\infty} x(\tau)\psi^* \left(\frac{\tau - t}{a}\right) d\tau \tag{6.28}$$

Où $\psi(t)$ est l'ondelette mère qui doit être passe-bande, de moyenne nulle et a est un facteur d'échelle de la décomposition.

Le scalogramme est défini comme étant le carré du module de la TO, c'est à dire $|W(t,a)|^2$. Stricto sensu, le scalogramme est une distribution d'énergie temps-échelle [128]. En considérant que les contenus temporel et fréquentiel de l'ondelette mère sont concentrés respectivement, autour de l'instant 0 et d'une fréquence f_0 appelée fréquence centrale, la transformation en ondelettes peut être interprétée comme une représentation temps-fréquence ; la variable échelle est alors liée à la fréquence f par la relation $a = \frac{f_0}{f}$.

La résolution temps-fréquence du scalogramme obéit également au principe d'incertitude d'Heisenberg-Gabor. Toutefois, la résolution temporelle s'améliore et la résolution fréquentielle se dégrade avec la croissance de la fréquence. L'inconvénient majeur de la TO vient de l'absence de critères de choix sur l'ondelette mère à utiliser.

6.2.5.3 Distributions temps-fréquence quadratiques

Pour remédier aux inconvénients des représentations précédentes (spectrogramme, scalogramme), plusieurs distributions temps-fréquence quadratiques ont été proposées [137]. Elles permettent une meilleure résolution temps-fréquence car leur résolution n'est pas contrainte par le principe d'incertitude d'Heisenberg-Gabor. La distribution de Wigner-Ville (DWV), qui peut être interprétée comme étant la distribution de l'énergie en fonction du temps et de la fréquence, est l'une de ces distributions. La DWV est définie par l'équation (6.29).

$$W_{x,x}(t,f) = \int_{-\infty}^{\infty} x\left(t + \frac{\tau}{2}\right) x^*\left(t - \frac{\tau}{2}\right) e^{-2j\pi f\tau} d\tau \tag{6.29}$$

Cette expression peut être interprétée comme étant la transformée de Fourier du noyau $K_x(\tau,t)$ défini par (6.30).

$$K_x(\tau,t) = x(t - \frac{\tau}{2}) x^*(t - \frac{\tau}{2}) \tag{6.30}$$

La DWV donne une concentration parfaite de la fréquence instantanée en cas de modulation linéaire. Cependant, pour d'autres types de modulation, elle introduit des termes d'interférences internes dans la distribution [174]. De plus, de part sa non

linéarité, elle produit des interférences externes appelées "cross-terms" dans le cas de signaux multi-composants.

Pour limiter l'influence des "cross-terms", une solution consiste à remplacer le signal $x(t)$ par sa version analytique (c-à-d dépourvue des fréquences négatives) dans l'équation (6.29). Il est également possible de diminuer les interférences en lissant la représentation temps-fréquence. Cette technique, nommée distribution de Wigner-Ville lissée, s'obtient en remplaçant l'équation (6.29) par l'équation (6.31).

$$W_{x,x}(t,f) = \int_{-\infty}^{\infty} p(\tau) x\left(t+\frac{\tau}{2}\right) x^*\left(t-\frac{\tau}{2}\right) e^{-2j\pi f\tau} d\tau \tag{6.31}$$

Où $p(\tau)$ est une fenêtre de lissage. Cette fenêtre permet de réduire les interférences au détriment de la résolution temps-fréquence.

Les techniques mentionnées ci-dessus représentent la distribution énergétique du signal dans le plan temps-fréquence (ou temps-échelle). Elles peuvent toutes être formulées comme une convolution temps-fréquence, temps-échelle d'un noyau avec la distribution de Wigner-Ville (Classe de Cohen, Classe de Rioul-Flandrin) [137, 175].

6.2.5.4 La transformée de Hilbert-Huang et ses extensions

La transformée de Hilbert-Huang (THH) est une technique non linéaire qui permet d'extraire le contenu temps-fréquence des signaux non-stationnaires. Pour obtenir une représentation temps-fréquence, les signaux sont décomposés en une somme de signaux mono-composants modulés en amplitude et/ou en fréquence. Ensuite, la fréquence et l'amplitude instantanées sont extraites des signaux résultants en utilisant une technique de démodulation.

Pour décomposer le signal en une somme de signaux mono-composants appelés "Intrinsic Mode Function" (IMF), Huang et al. [74] ont proposé une technique empirique nommée Empirical Mode Decomposition (EMD). La transformée d'Hilbert quant à elle permet de calculer le signal analytique des IMFs. Ensuite, on déduit la fréquence instantanée et l'enveloppe complexe des IMFs.

Pour résumer, la transformée de Hilbert-Huang est effectuée en 3 étapes :

- Les IMFs sont extraites du signal original grâce à l'EMD dont l'algorithme est décrit dans [131];
- La transformée d'Hilbert est appliquée sur les IMFs ;
- L'enveloppe complexe et de la fréquence instantanée sont extraites.

En représentant conjointement l'amplitude instantanée et la fréquence instantanée en fonction du temps, il est alors possible de représenter le contenu temps-fréquence du signal. En utilisant d'autres techniques de démodulation, il est possible d'obtenir de nouvelles représentations. En particulier la transformée de Huang-Teager est une dérivée de la THH obtenue en remplaçant la démodulation basée sur la transformée de Hilbert par une démodulation basée sur l'opérateur d'énergie de Teager-Kaiser [176].

6.2.6 Limitations et perspectives

L'analyse ci-dessus met l'accent sur le compromis entre la précision fréquentielle, la résolution fréquentielle et les performances statistiques des techniques d'analyse spectrale pour la détection des défauts dans la machine asynchrone. Les techniques temps-fréquence/ temps-échelle sont généralement difficiles à calibrer et interpréter pour la détection des défauts de la machine asynchrone. De plus, les techniques de démodulation présentent certaines inconvénients liées à la difficulté à interpréter les résultats et la nécessité d'un post-traitement afin de mesurer la sévérité du défaut.

Les techniques précédentes sont général et n'exploitent pas la structure particulière du contenu fréquentiel des courants statoriques. Ces techniques mettent en évidence la présence d'un défaut (bandes latérales liées au défaut), mais elles ne permettent pas d'extraire directement des critères mesurant la sévérité des défauts. Par conséquent, d'autres algorithmes de post-traitement sont nécessaires pour déterminer les fréquences liées aux défaillances (principalement réalisés de façon manuelle) et d'extraire un critère de détection de défaut à partir de ces représentations fréquentielles. Une fois le spectre obtenu, des méthodes empiriques sont utilisées pour révéler la signature fréquentielle à partir du spectre et ainsi déterminer le type de défaut à diagnostiquer. Le principal avantage des méthodes proposées est leur capacité à extraire automatiquement la signature fréquentielle du défaut et de calculer automatiquement un indicateur de la sévérité du défaut sans avoir besoin d'un expert pour interpréter la représentation spectrale.

Dans le cadre de ce chapitre, on s'intéresse à l'étude de deux techniques d'analyse spectrale paramétrique basée sur le maximum de vraisemblance et sur le MUSIC multi-dimensionnel. Ces techniques permettent de surmonter les limitations des techniques précédemment listées. Le maximum de vraisemblance est un estimateur (EMV) asymptotiquement optimal de la PSD et atteint de manière asymptotique la borne de Cramer-Rao [148] lorsque le nombre d'échantillons ou le rapport signal bruit (SNR) tend vers l'infini. Cette technique est largement utilisé en traitement de signal pour l'estimation du spectre des signaux harmoniques [177] et non-harmoniques [178] et [179]. Malheureusement, le maximum de vraisemblance a un coût calculatoire élevé car il néces-

site l'optimisation d'une fonction de coût dans un espace de haute dimension. Dans le cas de la détection des défauts de la machine asynchrone, nous démontrons que le maximum de vraisemblance nécessite moins de ressources en terme de temps de calcul étant donné que le problème d'estimation conduit à un problème d'optimisation 2-D qui est facile à mettre en œuvre. Par ailleurs, une mise en œuvre efficace du maximum de vraisemblance nécessite la connaissance des nombres de composantes fréquentielles qui est appelé problème d'estimation de l'ordre du modèle. Afin d'estimer l'ordre du modèle, nous proposons de combiner le maximum de vraisemblance avec un terme de pénalité dépendant de l'ordre du modèle basé sur le critère MDL (minimum description length)[103]. Il faut souligner que l'estimation du nombre des bandes latérales ($2 \times L$) est d'un grand intérêt car elle contribue à nous informer sur l'existence du défaut. En outre, si l'ordre du modèle n'est pas estimé (choisi) correctement, la fréquence caractéristique du défaut peut être estimé à tort, par exemple, la moitié ou le double de la valeur réelle. Dans [180], une technique basée sur le maximum de vraisemblance a été proposée pour la détection des défauts mécaniques dans la machine asynchrone. Néanmoins, cette technique est limitée a des défauts particuliers et son extension à d'autres types de défauts est loin d'être triviale. En outre, sa mise en œuvre nécessite l'utilisation d'outil d'optimisation sophistiqué. De plus, le MUSIC multi-dimensionnel est utilisé afin d'estimer le contenu fréquentielle en présence de défaut. Ensuite le EMV des amplitudes est utilisée afin de calculer un critère de détection des défauts.

Les contributions majeures de ce travail peuvent être résumées comme suit:

- Nous proposons deux nouvelles techniques pour l'estimation d'ordre et du contenu spectrale visant à détecter les défauts d'une machine asynchrone. Cette technique est asymptotiquement optimale et est une technique haute résolution.

- Nous démontrons la pertinence des approches sur les défauts les plus communs dans la machine asynchrone. En fait, ces techniques rendent une défaillance potentielle identifiable et quantifiable.

- Nous démontrons l'efficacité des techniques sur des données simulées et en expérimentation.

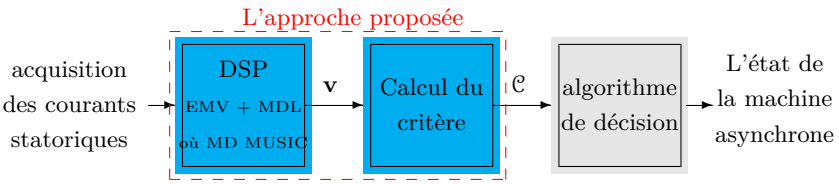

Figure 6.3: Schéma explicatif de la méthode proposée. L'acronyme DSP se réfère à la Densité Spectrale de Puissance du signal. Le symbole $\mathcal{C}$ correspond au critère de détection de défauts proposé et $\mathbf{v}$ est un vecteur contenant les estimateurs des paramètres du courant statoriques.

6.3 Estimation paramétrique dédiée à la détection des défauts dans un contexte stationnaire

L'analyse spectrale paramétrique basée sur le maximum de vraisemblance est explorée dans le cadre de cette section. En effet, nous démontrons que la détection des défauts de la machine asynchrone en analysant le courant statorique peut être réalisée d'une manière optimale en utilisant le maximum de vraisemblance associé à une méthode d'estimation de l'ordre du modèle. Cette technique d'estimation permet l'extraction d'un critère mettant en relief l'existence d'un défaut. Cet indicateur permet également de mesurer la sévérité du défaut.

6.3.1 Modèle analytique du courant statorique de la machine asynchrone

Les estimateurs non-paramétriques estiment la DSP de $\mathbf{x}[n]$ sans connaissance préalable sur le signal. Partant de ce constat, nous proposons un estimateur paramétrique qui exploite un modèle du courant statorique (6.33) en se basant sur les structures fréquentielles présentes dans la littérature. Le modèle du courant statorique présenté dans ce document est basé sur les hypothèses suivantes:

- $\mathcal{H}_1$: Le signal reçu est modélisée comme étant une somme de $2L+1$ de sinusoïdes bruitées. Où L correspond au nombre des bandes latérales liées au défaut.
- $\mathcal{H}_2$: Le bruit est un bruit gaussien, blanc de moyenne nulle et de variance σ^2.
- $\mathcal{H}_3$: Le contenu fréquentiel du signal obéit aux structures particulières données par le tableau 6.1.

En pratique, $\mathcal{H}_1$ n'est pas valide tout le temps car le courant statorique de la machine asynchrone peut contenir des harmoniques de temps et d'espace. Toutefois,

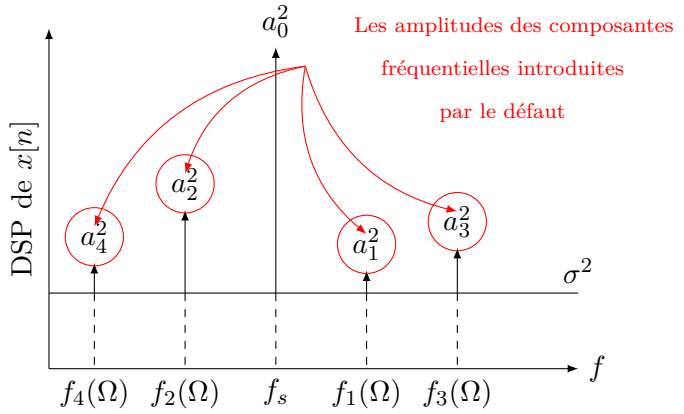

Figure 6.4: La DSP théorique pour $L = 2$ [7].

certaines de ces harmoniques peuvent être éliminés par filtrage du courant statorique afin de se concentrer sur la bande fréquentielle affectée par la présence d'un défaut. Par ailleurs, il faut noter que $\mathcal{H}_1$ nécessite la connaissance de L. Dans ce travail, nous proposons une technique permettant d'estimer L à partir du courant statorique. En ce qui concerne l'hypothèse $\mathcal{H}_2$, elle n'est pas particulièrement restrictive, puisque tout bruit peut être construit comme un bruit blanc filtré ou par un choix approprié de la fréquence d'échantillonnage [7].

Sous l'hypothèse $\mathcal{H}_1$ - $\mathcal{H}_3$, les échantillons du courant statorique $x[n]$ peuvent être exprimés comme

$$x[n] = \sum_{k=-L}^{L} a_k \cos\left(2\pi f_k(\Omega) \times \left(\frac{n}{F_s}\right) + \phi_k\right) + b[n] \tag{6.32}$$

Où $b[n]$ correspond aux échantillons du bruit blanc. Les symboles $f_k(\Omega)$, a_k et ϕ_k correspondent à la fréquence, l'amplitude et la phase de la k^{eme} composante fréquentielle, respectivement. Le symbole F_s correspond à la fréquence d'échantillonnage.

La DSP est définie comme étant la transformée de Fourier discrète de la fonction de covariance de $x[n]$ [7]. Sous l'hypothèse $\mathcal{H}_2$ et que les phases initiales ϕ_k,sont les variables aléatoires indépendantes et uniformément distribuées sur $[-\pi\ \pi]$, la DSP théorique de $x[n]$ est donnée par la Figure. 6.6 [7].

En pratique, la DSP est inconnue, et peut par conséquent être estimé à partir des N échantillons. En utilisant la notation matricielle, $x[n]$ $(n = 0, \cdots, N-1)$ peut être exprimé sous la forme

$$\mathbf{x} = \mathbf{A}(\Omega)\mathbf{v} + \mathbf{b} \tag{6.33}$$

où:

- $\mathbf{x} = [x[0], \cdots, x[N-1]]^T$ est un vecteur colonne $(N \times 1)$ contenant les échantillons du courant statorique, et où $(.)^T$ désigne le transposé d'une matrice,
- $\mathbf{b} = [b[0], \cdots, b[N-1]]^T$ est un vecteur colonne ($N \times 1$) contenant les échantillons du bruit,
- $\mathbf{v}$ est un vecteur colonne ($2(2L+1) \times 1$) contenant les amplitudes et les phases de la fréquence caractéristique du défaut. Ce vecteur est donné par

$$\mathbf{v} = [a_{-L}\cos(\phi_{-L}) \ldots a_L \cos(\phi_L), -a_{-L}\sin(\phi_{-L}) \ldots - a_L \sin(\phi_L)]^T \tag{6.34}$$

- $\mathbf{A}(\Omega)$ est une matrice de taille $N \times 2(2L+1)$

$$\mathbf{A}(\Omega) = [\mathbf{z}_{-L} \quad \ldots \quad \mathbf{z}_L \quad \mathbf{y}_{-L} \quad \ldots \quad \mathbf{y}_L] \tag{6.35}$$

où

$$\begin{aligned} \mathbf{z}_k &= \left[1 \ \cos\left(2\pi f_k(\Omega) \times \frac{1}{F_s}\right) \ldots \cos\left(2\pi f_k(\Omega) \times \frac{N-1}{F_s}\right)\right]^T \\ \mathbf{y}_k &= \left[0 \ \sin\left(2\pi f_k(\Omega) \times \frac{1}{F_s}\right) \ldots \sin\left(2\pi f_k(\Omega) \times \frac{N-1}{F_s}\right)\right]^T \end{aligned} \tag{6.36}$$

Dans ce contexte, le calcul du spectre du courant statorique des échantillons $\mathbf{x}[n]$ est traité tel un problème d'estimation statistique.

6.3.2 Estimation paramétrique de la DSP

Cette section présente une technique d'estimation paramétrique pour l'estimation de L ainsi que le spectre du signal basé sur le modèle du signal présenté précédemment (6.33). Le principe du maximum de vraisemblance est utilisé pour estimer $\mathbf{v}$ et Ω. Ensuite, un terme de pénalité est appliqué à la fonction de coût afin d'estimer l'ordre du modèle L. En outre, nous proposons une approche approchée déduite du maximum de vraisemblance basée sur la FFT qui conduit à une réduction significative de la complexité calculatoire.

6.3.2.1 Les estimateurs de v et Ω

L'estimateur du maximum de vraisemblance de $\mathbf{v}$ noté $\widehat{\mathbf{v}}$ est donné par

$$\widehat{\mathbf{v}} \quad = \quad \mathbf{A}^{\dagger}(\Omega)\mathbf{x} \tag{6.37}$$

où $\mathbf{A}^{\dagger}(\Omega)$ est la pseudo-inverse de $\mathbf{A}(\Omega)$ i.e.

$$\mathbf{A}^{\dagger}(\Omega) = \left(\mathbf{A}^{T}(\Omega)\mathbf{A}(\Omega)\right)^{-1}\mathbf{A}^{T}(\Omega) \tag{6.38}$$

et où $(.)^{-1}$ correspond à l'inverse d'une matrice.

L'estimateur du maximum de vraisemblance de Ω est donné par

$$\{\widehat{\Omega}\} = \arg\max_{\Omega} \mathcal{J}(\Omega) \tag{6.39}$$

où:

$$\mathcal{J}(\Omega) = \mathbf{x}^{T}\mathbf{A}(\Omega)\mathbf{A}^{\dagger}(\Omega)\mathbf{x} \tag{6.40}$$

6.3.2.2 L'estimateur de l'ordre du modèle L

L'estimation de L améliore les performances de l'estimateur du maximum de vraisemblance de Ω. Les critères d'informations théoriques sont utilisés pour estimer L [150]. En fait, un terme de pénalité basé sur le principe MDL (minimum description length) est appliqué à la fonction de coût initiale afin d'estimer L. Par conséquent, l'estimation de L peut être effectué en maximisant la fonction de coût pénalisée de l'estimation de Ω [103] comme suit

$$\{\widehat{\Omega}, \widehat{L}\} = \arg\max_{\Omega, L} -\left(\mathbf{x}^{T}\mathbf{x} - \mathcal{J}(\Omega)\right) \times \exp\left(\frac{c(g,N)}{N}\right) \tag{6.41}$$

Finalement, l'estimation de la DSP du courant statorique est composée de deux étapes: a) les estimations de Ω et L sont donnés par (6.41), et b) le vecteur $\mathbf{v}$ contenant l'amplitude et phase de la fréquence caractéristique du défaut est estimé en remplaçant Ω, et L par leurs estimateurs respectives dans (6.37). En raison de ses propriétés statistiques, il convient de noter que l'estimation par maximum de vraisemblance reste la méthode la plus précise pour l'estimation de la DSP, même dans les cas où le bruit est coloré [95]. En particulier, cet estimateur surmonte la limitation en terme de résolution fréquentielle du périodogramme. De plus, contrairement à d'autres techniques, l'approche proposée exploite les fréquences caractéristiques des défauts dans le but d'améliorer la précision de l'estimation de la densité spectrale de puissance.

Concernant la mise en œuvre, la principale difficulté repose sur le problème d'optimisation dans (6.41). On adopte les méthodes numériques parce que ce problème d'optimisation (estimation de Ω et L) ne peut être résolue de manière analytique. Dans notre contexte, la fonction de coût ne dépend que de trois paramètres, ce qui implique une maximisation dans un espace 3-D. L'espace de recherche est relativement limité puisque la plage

de variation de Ω et de L est connues. Par conséquent, nous proposons d'effectuer la maximisation de (6.41) en utilisant les algorithmes génétiques.

Pour une machine asynchrone connectée au réseau électrique, la fréquence fondamentale peut être supposée connue (fluctuation de $\mp 1\%$). Par conséquent le problème d'optimisation dans (6.41) peut être réduit à un problème d'optimisation 2-D.

6.3.3 Lien avec la transformée de Fourier discrète

La complexité calculatoire de l'estimateur DSP peut être réduite lorsque le nombre d'échantillons, N, tend vers l'infini. En effet, en utilisant la limite suivante (voir, e.g.,[148]).

$$\lim_{N\to\infty} \frac{2}{N}\left(\mathbf{A}^T(\Omega)\mathbf{A}(\Omega)\right) = \mathbf{I}_N \tag{6.42}$$

où $\mathbf{I}_N$ correspond à une matrice identité de taille $N \times N$, la fonction de coût s'exprime sous la forme

$$\mathcal{J}_a(\Omega) = 2\sum_{k=-L}^{L} \left|DFT_x\left[f_k(\Omega)/F_s\right]\right|^2 \tag{6.43}$$

où $DFT_x[f]$ est la TFD calculée à la fréquence f i.e. (voir [148])

$$DFT_x[f] = \frac{1}{\sqrt{N}}\sum_{n=0}^{N-1} x[n]e^{-2j\pi fn} \tag{6.44}$$

Enfin, l'estimation approchée de Ω est simplement obtenue en remplaçant $\mathcal{J}(\Omega)$ par $\mathcal{J}_a(\Omega)$ dans (6.39). Il faut souligner que l'estimateur approximatif peut être obtenu que si $f_k(\Omega)/F_s$ n'est pas proche de 0 et de 1/2.

De même, l'estimateur approché du vecteur $\mathbf{v}$ est alors calculé en utilisant (6.45).

$$\widehat{\mathbf{v}} \;=\; \frac{2}{N}\mathbf{A}^T(\Omega)\mathbf{x} \tag{6.45}$$

Cette approche approximée peut être étendue afin d'estimer l'ordre du modèle L comme suit

$$\{\widehat{\Omega}, \widehat{L}\} = \arg\max_{\Omega,L} - \left(\mathbf{x}^T\mathbf{x} - \mathcal{J}_a(\Omega)\right) \times \exp\left(\frac{c(g,N)}{N}\right) \tag{6.46}$$

Les équations (6.46) et (6.43) montrent que la fonction de coût approchée est réduite à une somme d'échantillons de la TFD. Cela rend la méthode approchée attractive pour les raisons suivantes: a) la plupart des cartes DSP comprennent des fonctions de calcul de la TFD b) la TFD peut être calculée efficacement en utilisant la FFT. Toutefois, il

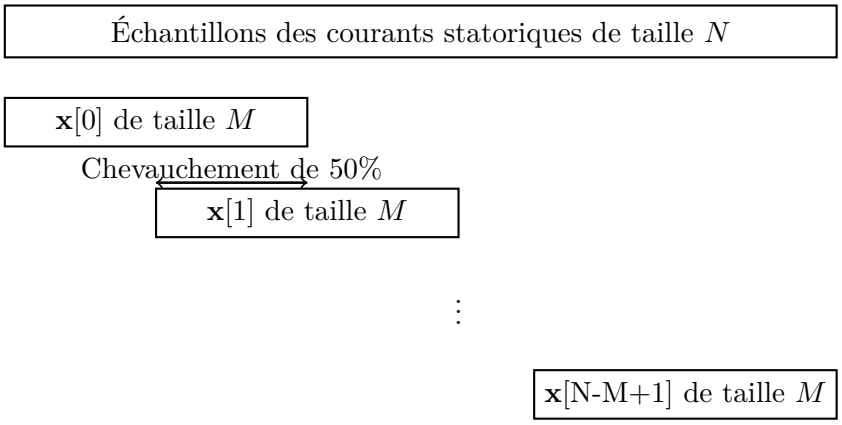

Figure 6.5: La segmentation du signal.

convient de souligner que la précision de l'approche approximée dépend fortement de la longueur du signal N. En particulier, l'approximation dans (6.42) n'est plus valable pour des signaux de courte durée. Dans ce cas, la TFD du courant statorique présente des lobes secondaires qui affectent la résolution en fréquence. Les lobes secondaires peuvent masquer des composantes fréquentielles voisines et conduire par la suite à des interprétations erronées. Par ailleurs, les lobes secondaires peuvent être interprétés comme étant les fréquences caractéristiques des défauts et amener par la suite à des fausses alarmes.

6.3.4 MUSIC multi-dimensionnel pour l'estimation de la DSP

Cette section décrit l'utilisation de MUSIC multi-dimensionnel pour la détection des défauts dans la machine asynchrone basé sur le modèle du courant statorique décrit précédemment.

6.3.4.1 Les hypothèses de l'étude

Le signal échantillonné de taille N est décomposé en segments de taille $M \times 1$ comme illustré sur la figure 6.5.

En utilisant le modèle du signal proposé dans (6.33), nous proposons d'estimer les paramètres du modèle, à savoir f_s, f_c et les amplitudes a_l à partir des échantillons du courant statorique $x[n](n = 0, \cdots, N-1)$, où N corresponds à la longueur du signal. La méthode proposée repose sur les hypothèses suivantes :

- $\mathcal{H}_1$: La matrice $\mathbf{A}(\Omega)$ est de rang $2 \times L + 1$ ce qui implique que $M > 2 \times L + 1$ et la fréquence caractéristique du défaut est différente de zéro.

– $\mathcal{H}_2$: Les phases des sinusoïdes sont indépendantes et uniformément réparties sur l'intervalle $[-\pi, \pi[$.

6.3.4.2 Estimation de la DSP

En supposant que les phases des sinusoïdes sont indépendantes et uniformément réparties sur l'intervalle $[-\pi, \pi[$, la matrice de covariance de $\mathbf{x}[n]$ est donnée par

$$\begin{aligned} \mathbf{R} =& E\{\mathbf{x}[n]\mathbf{x}^T[n]\} && (6.47)\\ =& \mathbf{A}(\Omega)\ \mathbf{P}\ \mathbf{A}(\Omega)^T + \sigma^2\ \mathbf{I}_M && (6.48) \end{aligned}$$

où E{.} désigne l'espérance mathématique, $(.)^T$ désigne la transposée, $\mathbf{I}_M$ est la matrice identité de taille $M \times M$ et où

$$\mathbf{P} = E\{\mathbf{v}[n]\mathbf{v}^T[n]\}. \tag{6.49}$$

La décomposition en valeurs propres de la matrice de covariance peut être écrite comme suit

$$\mathbf{R} = \mathbf{U}\Lambda\mathbf{U}^H \tag{6.50}$$

où Λ est une matrice diagonale contenant les valeurs propres $\lambda_1 \geq \cdots \geq \lambda_M$ de $\mathbf{R}$ et $\mathbf{U}$ est une matrice unitaire contenant les vecteurs propres associés. Sous l'hypothèse $\mathcal{H}_1$ et le faite que $\mathbf{P}$ est non singulière, la matrice diagonale Λ s'exprime sous la forme

$$\Lambda = \begin{bmatrix} \boldsymbol{\lambda} & \mathbf{0} \\ \mathbf{0} & \sigma^2\mathbf{I}_{M-2L-1} \end{bmatrix} \tag{6.51}$$

où $\boldsymbol{\lambda}$ est une matrice diagonale contenant les $2 \times L + 1$ plus grandes valeurs propres de Λ. Décomposons le vecteur $\mathbf{U}$ comme suit

$$\mathbf{U} = [\mathbf{U}_s\ \mathbf{G}] \tag{6.52}$$

où :

– $\mathbf{U}_s$ est une matrice de taille $M \times (2L+1)$ contenant les vecteurs propres associés aux $2 \times L + 1$ plus grandes valeurs propres,

– $\mathbf{G}$ est une matrice de taille $M \times (M - 2L - 1)$ constituée des $M - (2 \times L + 1)$ moins significatifs valeurs propres.

En utilisant (6.48), nous démontrons que :

$$\mathbf{RG} = \mathbf{A}(\Omega)\ \mathbf{P}\ \mathbf{A}(\Omega)^H\mathbf{G} + \sigma^2\ \mathbf{G} \tag{6.53}$$

Sachant que $\mathbf{U}$ est une matrice unitaire, ($\mathbf{U}^H\mathbf{U} = \mathbf{I}_M$) et que $\mathbf{U}_s^H\mathbf{G} = \mathbf{0}$. Par conséquent, en utilisant (6.50) et (6.51) nous trouvons

$$\begin{aligned}
\mathbf{RG} &= \mathbf{U}\Lambda\mathbf{U}^H\mathbf{G} && (6.54)\\
&= [\mathbf{U}_s\ \mathbf{G}] \begin{bmatrix} \boldsymbol{\lambda} & \mathbf{0} \\ \mathbf{0} & \sigma^2\mathbf{I}_{M-2L-1} \end{bmatrix} \begin{bmatrix} \mathbf{U}_s^H \\ \mathbf{G}^H \end{bmatrix} \mathbf{G} && (6.55)\\
&= [\mathbf{U}_s\ \mathbf{G}] \begin{bmatrix} \boldsymbol{\lambda} & \mathbf{0} \\ \mathbf{0} & \sigma^2\mathbf{I}_{M-2L-1} \end{bmatrix} \begin{bmatrix} \mathbf{0} \\ \mathbf{I}_{M-(2\times L+1)} \end{bmatrix} && (6.56)\\
&= [\mathbf{U}_s\ \mathbf{G}] \begin{bmatrix} \mathbf{0} \\ \sigma^2\mathbf{I}_{M-(2\times L+1)} \end{bmatrix} && (6.57)\\
&= \sigma^2\mathbf{G}. && (6.58)
\end{aligned}$$

En substituant (6.58) dans (6.53), on obtient le résultat suivant :

$$\mathbf{A}(\Omega)\ \mathbf{P}\ \mathbf{A}(\Omega)^H\mathbf{G} = \mathbf{0} \tag{6.59}$$

ce qui implique

$$\mathbf{A}(\Omega)^H\mathbf{G} = \mathbf{0}. \tag{6.60}$$

En pratique, $\mathbf{R}$ est inconnue mais peut être estimée en se basant sur les échantillons $\mathbf{x}[n]$ suivant l'équation (6.61).

$$\widehat{\mathbf{R}} = \frac{1}{N-M+1}\sum_{n=0}^{N-M}\mathbf{x}[n]\mathbf{x}[n]^H \tag{6.61}$$

Ainsi l'ensemble Ω est donné par

$$\{\widehat{\Omega}\} = \arg\max_{\Omega} \jmath_m(\Omega) \tag{6.62}$$

où :

$$\jmath_m(\Omega) = \frac{1}{\left\|\mathbf{A}(\Omega)^H\widehat{\mathbf{G}}\right\|_F^2} \tag{6.63}$$

et où $\|.\|_F^2$ désigne la norme de Frobenius. Concernant la mise en œuvre, l'approche proposée mène à un problème d'optimisation bidimensionnel alors que l'algorithme MUSIC classique décrit dans (2.47) traque $2L+1$ maxima dans un espace de dimension 1.

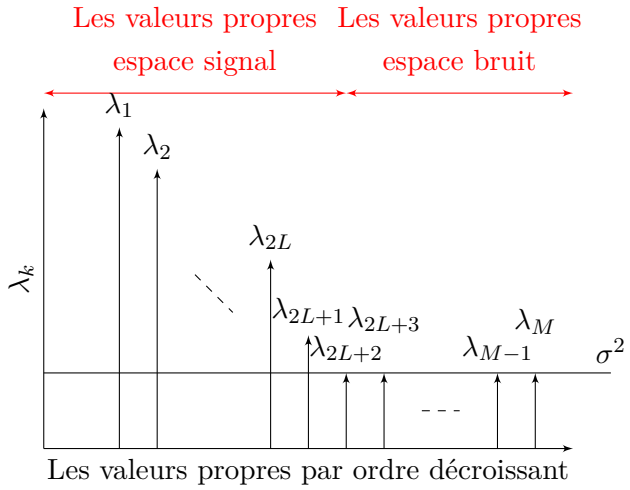

Figure 6.6: La décomposition en valeurs propres de la matrice de covariance [7].

6.3.4.3 L'estimation de l'ordre du modèle pour le MUSIC multi-dimensionnel

Nous étendons l'algorithme d'estimation MD MUSIC pour estimer conjointement la fréquence fondamentale, la fréquence caractéristique du défaut et l'ordre du modèle. L'approche proposée nécessite une connaissance a priori du nombre de bandes latérales L pour l'évaluation de la fonction de coût. En effet, cette approche peut conduire à une mauvaise identification du sous-espace bruit dans (6.52), et ce, à son tour, conduit à des estimations erronées rapportées dans [152]. L' orthogonalité du sous-espace bruit estimé et du sous-espace signal tient seulement lorsque les fréquences estimées sont égaux aux vraies valeurs et l'ordre du modèle L est choisi de manière appropriée. Par conséquent, si le nombre de bandes latérales est inconnu, la fonction de coût peut être modifiée pour tenir en compte de l'estimation de L. En effet, en suivant la même approche que dans [153], il peut être démontré que la fréquence fondamentale, la fréquence caractéristique du défaut et le nombre de bandes latérales L peuvent être estimés comme suit

$$\left\{\widehat{\Omega}, \widehat{L}\right\} = \arg \max_{\Omega} \max_{L} \jmath_{mj}(\Omega, L) \tag{6.64}$$

où :

$$\jmath_{mj}(\Omega, L) = \frac{(2L+1)M(M-2L-1)}{\left\|\mathbf{A}(\Omega)^H \widehat{\mathbf{G}}\right\|_F^2}. \tag{6.65}$$

6.3.4.4 Estimation de l'amplitude des composantes fréquentielles

Les amplitudes des composantes fréquentielles véhiculent l'information concernant la sévérité du défaut. Ces amplitudes sont contenues dans le vecteur $\mathbf{v}[n]$. Par conséquent, connaissant la fréquence fondamentale et la fréquence lié au défaut, ces amplitudes peuvent être calculées en utilisant le maximum de vraisemblance. En effet, l'estimateur MV de $\mathbf{v}[n]$, noté $\widehat{\mathbf{v}}[n]$ est donné par

$$\widehat{\mathbf{v}} = \left(\sum_{n=0}^{G-1} \mathbf{A}(\Omega)^H \mathbf{A}(\Omega) \right)^{-1} \times \sum_{n=0}^{G-1} \mathbf{A}(\Omega)^H \mathbf{x}[n] \tag{6.66}$$

où G est le nombre de sous-vecteurs défini par $G = N - M + 1$.

6.3.5 Critère de décision automatique

Nous nous intéressons au critère de détection des défauts qui émane de l'estimation des paramètres du modèle présenté précédemment. Nous démontrons qu'un critère de décision peut être déduit du vecteur $\widehat{\mathbf{v}}$ en exploitant la structure particulière du contenu fréquentiel en présence du défaut.

6.3.5.1 Le critère proposé

Un critère de défaillance est nécessaire pour mesurer la sévérité du défaut. Nous proposons d'utiliser le vecteur $\widehat{\mathbf{v}}$ pour calculer la sévérité du défaut, étant donné qu'il contient l'amplitude des fréquences caractéristiques du défaut a_k ($k \neq 0$). Le critère proposé s'exprime mathématiquement sous la forme

$$\mathcal{C} \quad = \quad \sum_{k=-L, k\neq 0}^{L} \left(\frac{a_k^2}{a_0^2} \right) \tag{6.67}$$

Ce critère présente les deux propriétés suivantes.

Property 3 *Dans le cas d'une machine saine, le critère est égale à i.e.*

$$\mathcal{C} = 0 \tag{6.68}$$

Property 4 *Le critère proposé est invariant à l'échelle. En effet, Notons $\mathcal{C}_x$ la valeur du critère liée à la valeur du courant statorique $x[n]$. Nous pouvons démontrer que la valeur du critère $\mathcal{C}_{\alpha x}$, relative au signal $\alpha x[n]$ ($\alpha > 0$), est égale à:*

$$\mathcal{C}_{\alpha x} = \mathcal{C}_x \tag{6.69}$$

Le critère proposé dans (6.67) dépend des amplitudes a_k ($k = -L, \cdots, L$). L'estimation de la DSP permet d'extraire les valeurs des amplitudes a_k à partir du vecteur $\mathbf{v}$. Cependant, en utilisant la structure de $\mathbf{v}$ dans (6.34), on peut montrer que $\mathcal{C}$ peut être directement obtenu à partir de $\mathbf{v}$ sans avoir à calculer les a_k. En effet, le critère proposé dans (6.67) peut être écrit sous la forme matricielle suivante:

$$\mathcal{C} = \frac{\mathbf{v}^T\mathbf{v}}{\mathbf{v}^T\mathbf{M}\mathbf{v}} - 1 \tag{6.70}$$

où $\mathbf{M}$ est une matrice de taille $(4L+2) \times (4L+2)$ donné par

$$\begin{bmatrix} \mathbf{E}_{L+1,L+1} & \mathbf{0} \\ \mathbf{0} & \mathbf{E}_{L+1,L+1} \end{bmatrix} \tag{6.71}$$

et où $\mathbf{E}_{u,v}$ est une matrice élémentaire de taille $(2L+1) \times (2L+1)$ dont l'unique élément non nul et égale à 1 est placé sur la u^{eme} ligne et la v^{eme} colonne. En pratique, le vecteur $\mathbf{v}$ est inconnu et doit être remplacer par son estimateur $\widehat{\mathbf{v}}$ dans (6.70) pour calculer $\mathcal{C}$.

6.3.5.2 Synthèse de l'algorithme

L'algorithme de détection de défauts proposé est résumé sur la Figure. 6.7. Cet algorithme peut être mis en place pour surveiller une machine asynchrone en temps réel. Contrairement à d'autres techniques de surveillance basées sur l'estimation de la DSP telles que le Periodogramme, MUSIC, ESPRIT, l'approche proposée est attrayante puisque le vecteur $\mathbf{v}$ transmet directement les informations sur les fréquences caractéristiques des défauts.

6.4 Estimation paramétrique adaptée à un fonctionnement dans un contexte non-stationnaire

6.4.1 Maximum de vraisemblance non-stationnaire

6.4.1.1 Estimateur MV de $\Omega(n)$

L'algorithme opère sur des sous-vecteurs du signal à des instants n. Bien que l'approche consistant à diviser le signal en sous-vecteurs est intrinsèquement sous-optimale car elle ne tient pas compte des dépendances inter-vecteurs, elle est nécessaire pour estimer la matrice de covariance du signal et du bruit. Pour de multiples obser-

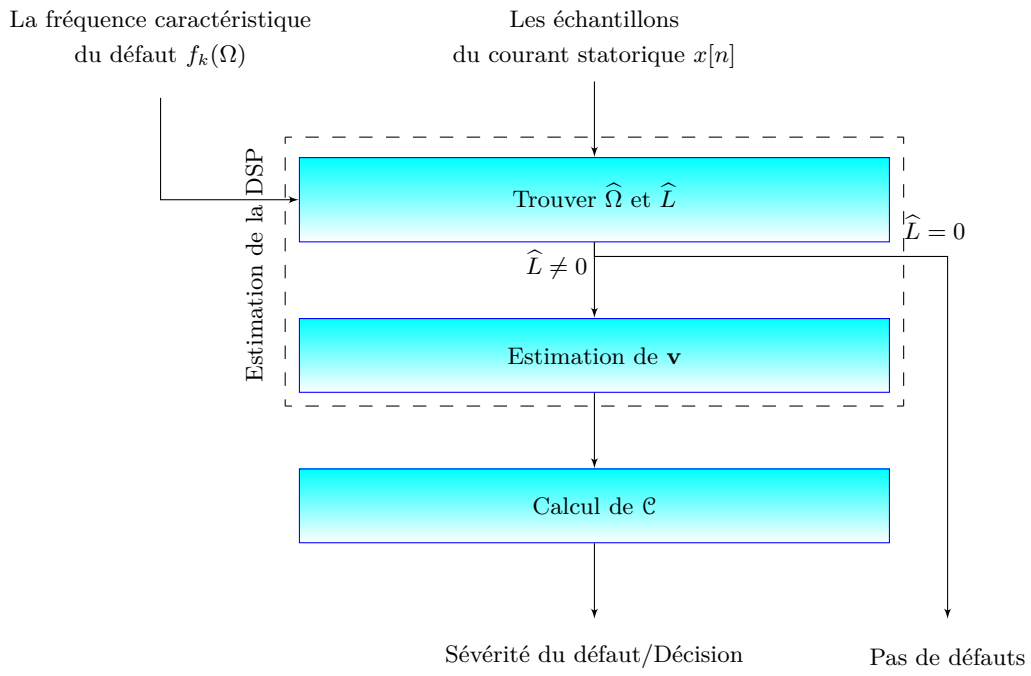

Figure 6.7: Algorithme de détection des défauts.

vation, l'estimateur MV de $\Omega(n)$ est égale au maximum de la fonction de coût suivante [155]

$$\mathcal{J}(\Omega(n)) = -Tr\{\mathbf{A}(\Omega(n))\mathbf{A}^{\dagger}(\Omega(n))\mathbf{R}(n)\} \tag{6.72}$$

où

- $\mathbf{A}^{\dagger}(\Omega(n))$ est la matrice pseudo-inverse de $\mathbf{A}(\Omega(n))$ i.e.

$$\mathbf{A}^{\dagger}(\Omega(n)) = \left(\mathbf{A}^{T}(\Omega(n))\mathbf{A}(\Omega(n))\right)^{-1}\mathbf{A}^{T}(\Omega(n)) \tag{6.73}$$

  où $(.)^{-1}$ corresponds à l'inverse d'une matrice et $Tr(.)$ désigne la trace d'une matrice.

- La matrice de covariance $\mathbf{R}$(n) du signal observé est donné par (6.48).

La méthode proposée repose sur cette matrice de covariance. En pratique, la matrice de covariance est inconnue et doit être remplacée par son estimateur, la matrice de

covariance des échantillons du signal. La matrice de covariance des échantillons du signal est définie comme suit

$$\widehat{\mathbf{R}}[n] = \frac{1}{G}\sum_{n=0}^{G-1}\mathbf{x}[n]\mathbf{x}^{H}[n] \tag{6.74}$$

Finalement, $\Omega(n)$ peut être estimé à partir de la fonction de coût suivante

$$\{\widehat{\Omega}(n)\} = \arg\max_{\Omega} \mathcal{J}(\Omega(n)) \tag{6.75}$$

Cet estimateur est capable de traiter des signaux non-stationnaires étant donné que la matrice de covariance est estimée de manière récursive en divisant le signal en segments de temps et ensuite, la matrice de covariance est estimée avec un chevauchement de 50% entre des segments.

6.4.1.2 Estimateur de l'ordre du modèle L

Dans cette section, nous proposons d'utiliser le même principe que la section 6.3.2.2 qui est le principe dont l'acronyme anglais est MDL [103] pour estimer l'ordre du modèle L afin d'améliorer la détection des défauts et par la suite la précision de la mesure de la sévérité du défaut.

$$\{\widehat{\Omega}(n), \widehat{L}(n)\} = \arg\max_{\Omega,L} \; -Tr\{\Big(I_M - \mathbf{A}(\Omega(n))\mathbf{A}^{\dagger}(\Omega(n))\Big)\,\mathbf{R}(n)\} \times \exp\left(\frac{c(g,M)}{M}\right) \tag{6.76}$$

où $c\,(g, M) = g\log(M)$ est le critère d'information théorique proposé et $g = 4L + 4$ est le nombre de paramètres libres. Par ailleurs, I_M est une matrice identité de taille M.

Pour la détection de défauts dans la machine asynchrone dans un environnement non-stationnaire, il est obligatoire d'être en mesure de suivre en temps réel le contenu fréquentiel du courant statorique. Cela peut être fait en utilisant (6.76).

6.4.1.3 Algorithme de l'estimateur MV non-stationnaire

L'algorithme de détection de défaut dans un contexte non-stationnaire est similaire à celui décrit dans la Fig. 6.7. Cet algorithme peut être mis en œuvre pour la surveillance en temps réel d'une machine asynchrone. L'estimateur MV non-stationnaire est utilisé pour le suivi de la sévérité du défaut dans un environnement non-stationnaire. L'algorithme de détection des défaut pour le suivi de l'indicateur de sévérité du défaut est décrit sur la Fig. 6.8

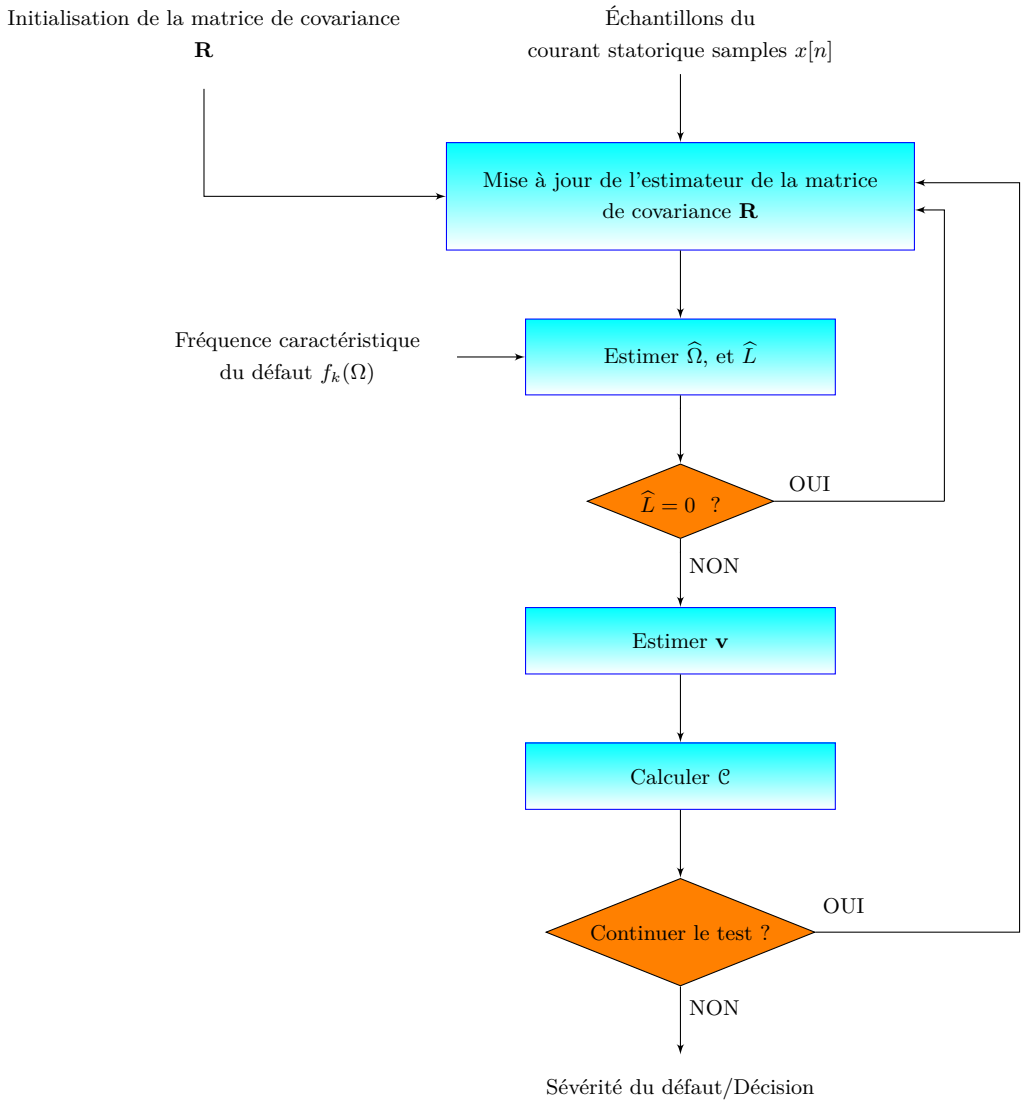

Figure 6.8: Algorithme de détection du défaut proposé pour des conditions de fonctionnement non-stationnaires.

6.4.2 MD MUSIC non-stationnaire

6.4.2.1 Mise à jour de la matrice de covariance

La mise en œuvre du MD MUSIC est basée sur l'estimation des vecteurs propres d'un estimateur de la matrice de covariance du signal. Afin que l'algorithme soit adapté à des signaux non-stationnaires, l'estimation de la matrice de covariance du signal

doit être réalisé de façon adaptative. Par conséquent, cette section présente comment calculer de manière récursive les estimateurs des paramètres du modèle du signal. Plus précisément, supposons que nous avons une estimation $\widehat{\Omega}(n)$ et $\widehat{L}$ après n mesures, et que nous obtenons une nouvelle mesure $x[n+1]$, nous démontrons comment mettre à jour l'estimation avec une complexité calculatoire réduite.

La méthode MD MUSIC proposée repose sur l'estimation de la matrice de covariance. Par conséquent, elle doit être estimée à partir du signal observé. Pour ce faire, de façon adaptative, nous utilisons l'estimateur suivant basé sur le facteur d'oubli exponentiel $0 < \lambda < 1$:

$$\mathbf{R}(n) = \lambda \mathbf{R}(n-1) + \mathbf{x}(n)\mathbf{x}^T(n) \tag{6.77}$$

Le facteur d'oubli permet de contrôler le compromis entre un bon estimateur de la matrice de covariance et le caractère adaptatif de l'algorithme. Une fois la matrice de covariance est estimée, le contenu fréquentiel et l'ordre du modèle L peuvent être estimés comme décrit dans (6.65).

6.4.2.2 MD MUSIC non-stationnaire pour le suivi des fréquences

L'algorithme MD MUSIC récursif pour la détection des défauts de la machine asynchrone est décrit dans l'**Algorithme** 5

6.5 Validation en simulation sur des signaux issus d'un modèle basé sur les circuits électrique magnétiquement couplés

6.5.1 Élément sur la modélisation d'une machine asynchrone en défaut

La modélisation de la machine asynchrone à cage d'écureuil en présence de défaillances peut être réalisée grâce à des modèles physiques basés sur les lois régissant l'électromagnétisme. Ces modèles sont divers et variés et peuvent varier en complexité et en précision selon la méthode de modélisation utilisée (méthode des circuits magnétiquement couplés, méthode des réseaux de perméances, méthode des éléments finis).

La méthode des circuits électriques magnétiquement couplés (CEMC) est une méthode analytique basée sur la décomposition des bobinages de la machine en bobines élémentaires dont les inductances propres et mutuelles sont calculées à partir de l'induction

Algorithm 5 MD MUSIC non-stationnaire pour le suivi de la criticité du défaut.

Require: N -échantillons du courant statorique $\mathbf{x}[n]$.

1: Initialiser l'estimateur,

(a) Estimer la matrice covariance

$$\widehat{\mathbf{R}}_0 = \frac{1}{N-M+1}\sum_{n=0}^{N-M}\mathbf{x}[n]\mathbf{x}[n]^H$$

(b) Estimer $\widehat{\Omega}_0$ et $\widehat{L}_0$ en maximisant la fonction objective suivante

$$\mathcal{J}_c(\Omega, L) = \frac{(2L+1)M(M-2L-1)}{\left\|\mathbf{A}(\Omega))^H\widehat{\mathbf{G}}\right\|_F^2}.$$

2: Itérer les étapes suivantes,

(a) Obtenir des nouveau mesure de taille M,

(b) Mettre à jour les estimateurs $\widehat{\Omega}(n)$ et $\widehat{L}(n)$ de manière séquentielle comme suit

- Mettre à jour la matrice de covariance en utilisant (6.77)
- Maximiser la fonction de coût suivante

$$\mathcal{J}_c(\Omega, L) = \frac{(2L+1)M(M-2L-1)}{\left\|\mathbf{A}(\Omega)^H\widehat{\mathbf{G}}\right\|_F^2}.$$

if $\widehat{L}(n) = 0$ **then**
  $fault = 0$
  $\mathcal{C}(n) = 0$
else
  $fault = 1$
  Estimer $\widehat{\mathbf{v}}$ en utilisant (6.37)
  Calculer le critère de détection de défaut $\mathcal{C}$ en utilisant (6.70)
end if

3: **Return** $\widehat{\Omega}(n)$, $\widehat{L}(n)$, $fault$, $\widehat{\mathbf{v}}(n)$ et $\mathcal{C}(n)$.

normale dans l'entrefer de la machine. Ces calculs s'appuient sur la technique des fonctions de distribution des bobinages [18]. Ces inductances peuvent être calculées par le biais du flux ou par le biais de l'énergie stockée dans l'entrefer.

Les inductances propres et mutuelles entre stator et rotor de la machine prennent une place importante dans cette méthode de modélisation car elles contiennent la signature des différents phénomènes pouvant apparaître au sein de la machine asynchrone. Une modélisation précise de ces inductances mènera à un apport d'informations supplémentaires sur les signaux tels que le courant statorique ou encore la vitesse du rotor. Par ailleurs, cette modélisation permet de prendre en compte un certain nombre de défauts d'origine électromagnétique tels que les défauts de court-circuit entre spires statoriques, les défauts de types rupture de barres rotoriques ou de portions d'anneau de court-circuit. Les défauts d'excentricité statique et dynamique peuvent également être intégrés à ce type de modélisation. La méthode CEMC est caractérisée par sa capacité à prendre en compte les détails géométriques des constituants de la machine et par un bon compromis précision/temps de calcul. Cette méthode de modélisation est basée sur un certain nombre d'hypothèses dont les principales sont les suivantes :

- Les tôles ferromagnétiques ont une perméabilité infinie.
- Le circuit magnétique est non conducteur.
- Les effets de fréquence sont négligeables.
- Les conducteurs sont parfaitement isolés du circuit magnétique.

On considère, par ailleurs, que la machine est constituée d'un stator à bobinage réparti ayant 3 phases et d'un rotor à cage ayant 30 barres.

Les équations différentielles régissant l'évolution des grandeurs électriques et mécaniques de la machine asynchrone dans l'espace des phases sont générées à partir des connaissances sur la géométrie de la machine (caractéristiques des bobinages, formes d'encoches statoriques et rotoriques, les éléments défaillants et les dimensions). Dans ce système d'équations, les matrices d'inductances propres et mutuelles nécessaires pour le calcul du modèle de la machine sont calculées en se basant sur l'énergie magnétique stockée dans l'entrefer qui est déterminée grâce à la théorie des fonctions de bobinages [161]. Cette méthode de calcul permet d'obtenir des coefficients de mutuelles symétriques quelque soit l'état de la machine, ce qui est en accord avec l'interprétation physique des inductances mutuelles. Ce modèle est utilisé pour générer les courants statoriques de la machine asynchrone en fonctionnement à vitesse variable (émulant le fonctionnement d'une éolienne ou d'une hydrolienne) dans le cas sain et le cas défaillant.

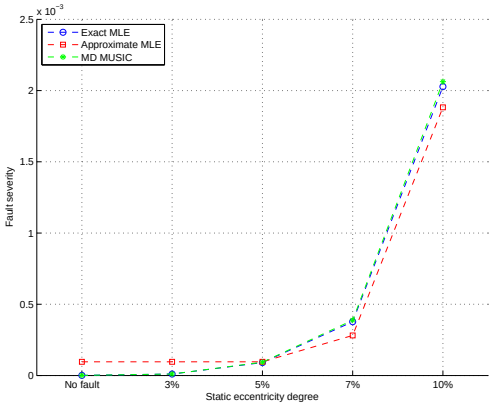

(a) La détection du défaut d'excentricité statique pour un degré de sévérité variable.

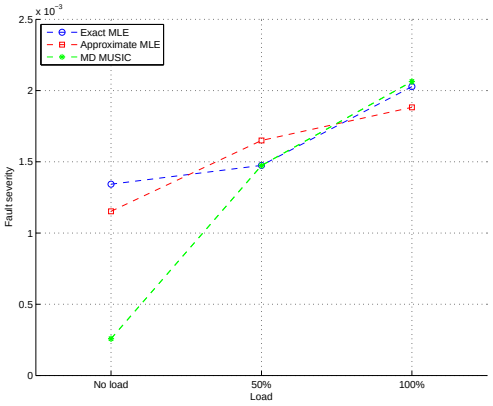

(b) La détection du défaut d'excentricité statique pour une charge variable.

Figure 6.9: Détection du défaut d'excentricité statique en se basant sur les trois techniques proposées.

6.5.2 Détection des défauts d'excentricité

Les techniques proposées sont utilisées pour la détection du défaut d'excentricité sur des signaux simulés en se basant sur le modèle de la machine asynchrone décrit dans le chapitre3. La fréquence caractéristique du défaut utilisée dans le modèle du signal est $f_k(\Omega) = f_s \pm k f_c$ où $f_c = \left(\frac{1-s}{p}\right) f_s$. Les approches proposées sont utilisées afin de détecter le défaut d'excentricité statique pour différent degré de sévérité et différentes charges. Les résultats de simulation sont données sur la Fig. 6.9. La Fig. 6.9(a) donne la variation du critère de détection en fonction de la sévérité du défaut pour les trois techniques proposées. Nous pouvons constater que le MD MUSIC et le MLE donnent des résultats similaires. En revanche, le MLE approchée n'est pas adapté pour la détection des défauts lorsque le degré de sévérité est faible. Ceci est du au calcul de la FFT qui introduit des sidelobes qui contribuent à augmenter la valeur du critère. Des simulations ont également été conduites en faisant varier la charge pour une excentricité statique de 10%. Les résultats de ces simulations sont donnés sur la Fig. 6.9(b). Nous constatons donc que le critère augmente quand la charge augmente.

L'excentricité dynamique a également été étudiée. La Fig.6.10(a) donne les résultats de simulation pour divers degrés d'excentricité. Cette figure montre que le critère de détection du défaut augmente lorsque la sévérité du défaut augmente. Cela signifie que les méthodes proposées permettent de révéler l'existence de l'excentricité dynamique et de mesurer sa gravité. En outre, des simulations on été conduites pour une charge

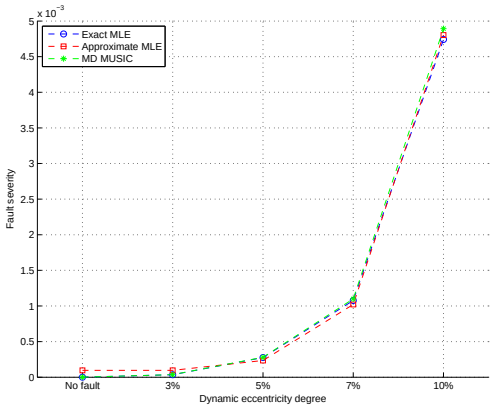

(a) La détection de l'excentricité dynamique pour un degré de sévérité variable.

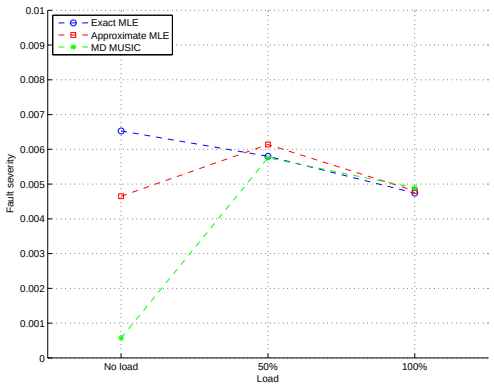

(b) La détection du défaut d'excentricité dynamique pour une charge variable.

Figure 6.10: Détection du défaut d'excentricité dynamique en se basant sur les trois techniques proposées.

variable. La Fig. 6.10(b) donne la variation du critère en fonction de la charge. Nous en déduisons que le critère de détection du défaut varie légèrement en fonction de la charge.

Finalement, l'excentricité mixte est étudiée. La Fig. 6.11 donne les résultats des simulations. En effet, la Fig. 6.11(a) donne la variation du critère en fonction de la sévérité du défaut. Les même constations que précédemment peuvent être tirées de cette figure. De plus, la variation du critère de détection en fonction de la charge a également été étudiée. La Fig. 6.11(b) donne les résultats des simulations. Cette figure montre que le critère augmente avec la charge.

En outre, les approches non-stationnaires ont été utilisés pour la détection du défaut d'excentricité. Des simulations ont été conduites avec 5% d'excentricité jusqu'à $5s$, puis le degré de sévérité augmente à 10% d'excentricité. Les Figs 6.12, 6.13 et 6.14 donnent les résultats des simulations pour l'excentricité statique, dynamique et mixte, respectivement en utilisant l'EMV et le MD MUSIC.

Ces résultats démontrent l'efficacité des approches proposées pour la détection des défauts mécaniques dans la machine asynchrone dans un contexte non-stationnaire. En effet, ces approches fournissent des résultats encourageants et permettant de mesurer la sévérité du défaut en fonction du temps. Par rapport à d'autres techniques temps-fréquence [43], les approches proposées ont été développées afin de satisfaire les exigences de la détection des défauts à savoir le suivi des fréquences caractéristiques des défauts et la mesure de leur sévérité.

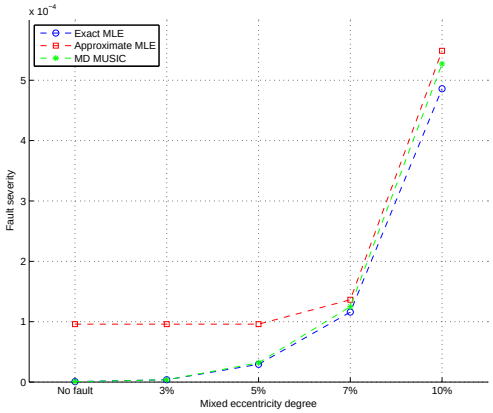

(a) La détection de l'excentricité mixte pour un degré de sévérité variable.

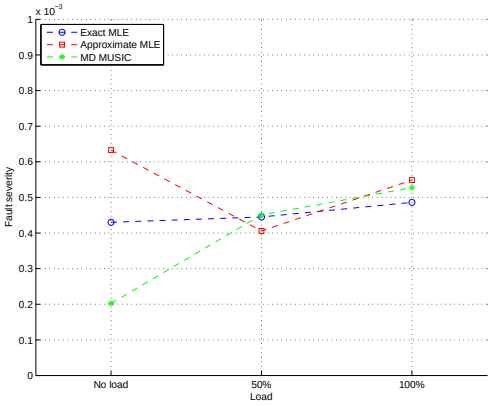

(b) La détection du défaut d'excentricité mixte pour une charge variable.

Figure 6.11: Détection du défaut d'excentricité mixte en se basant sur les trois techniques proposées.

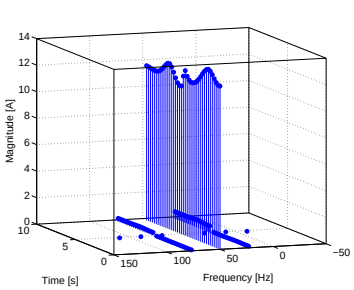

(a) Représentation temps-fréquence.

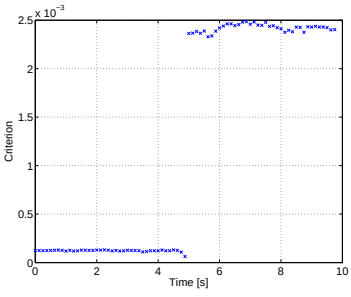

(b) Suivi de la sévérité du défaut en utilisant l'EMV.

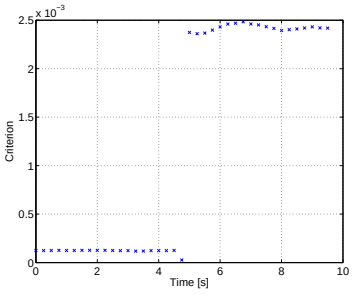

(c) Suivi de la sévérité du défaut en utilisant le MD MUSIC.

Figure 6.12: Détection de l'excentricité statique en utilisant les approches non-stationnaires proposées .

6.5.3 Détection des défauts de rupture de barres rotoriques

La rupture de barres rotoriques est l'un des défauts électriques les plus difficiles à détecter puisque les courants des barres et des anneaux de court-circuit de la cage d'écureuil ne sont pas accessibles. La fréquence caractéristique du défaut de rupture de barres est donnée par $f_k(\Omega) = f_k(f_s, s) = f_s\left[k\left(\frac{1-s}{p}\right) \pm s\right]$. Des simulations ont été effectuées en utilisant cette signature afin d'évaluer les performances des trois approches présentés dans le cadre de ce manuscrit. Les simulations ont été réalisées en cassant 1, 2 et 3 barres rotoriques. Les deux cas de barres adjacentes et non-adjacentes sont

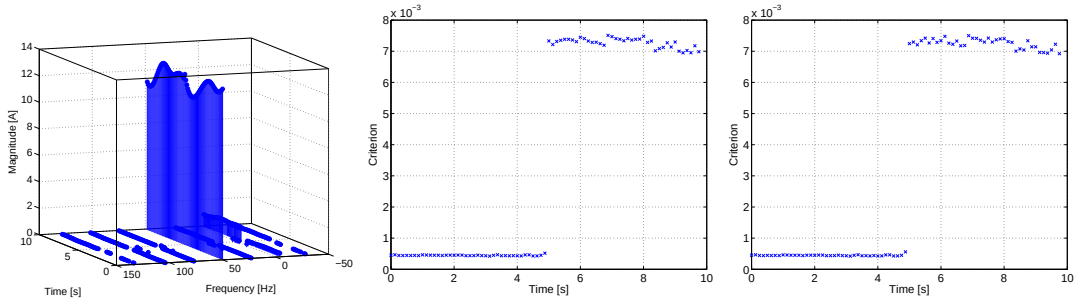

(a) Représentation temps-fréquence. (b) Suivi de la sévérité du défaut en utilisant l'EMV. (c) Suivi de la sévérité du défaut en utilisant le MD MUSIC.

Figure 6.13: Détection de l'excentricité dynamique en utilisant les approches non-stationnaires proposées.

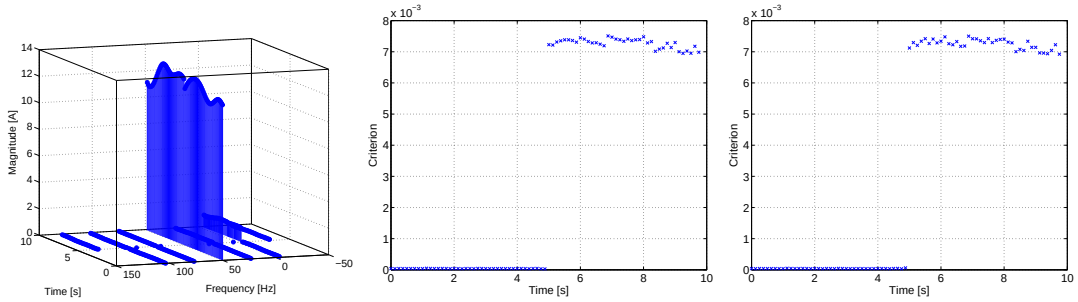

(a) Représentation temps-fréquence. (b) Suivi de la sévérité du défaut en utilisant l'EMV. (c) Suivi de la sévérité du défaut en utilisant le MD MUSIC.

Figure 6.14: Détection de l'excentricité mixte en utilisant les approches non-stationnaires proposées.

considérés.

La figure 6.15 donne les résultats des simulations pour une machine asynchrone en pleine charge. Nous déduisons de ces figures que les approches proposées donnent des résultats similaires et permettent de distinguer le cas défaillant ainsi que mesurer la sévérité du défaut. Toutefois, dans le cas du EMV approché, le critère n'est pas nul dans le cas sain ce qui nécessite de fixer un seuil à partir duquel la machine peut être considérée comme défaillante. Il est à mentionner que le critère de détection est plus élevé lorsque les barres endommagées sont adjacentes que dans le cas de barres non-adjacentes.

Des simulations supplémentaires ont été réalisées afin de mesurer la robustesse du critère de détection vis à vis de la variation de charge. Les résultats des simulations

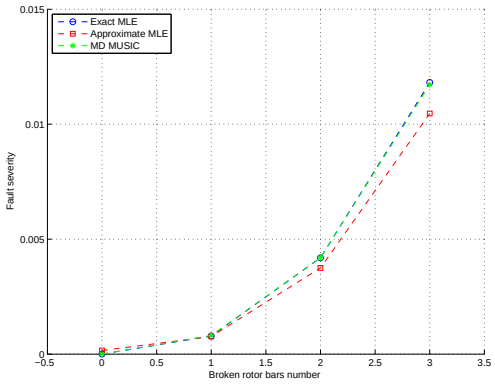

(a) Détection de rupture de barres par les approches proposées dans le cas de barres adjacentes.

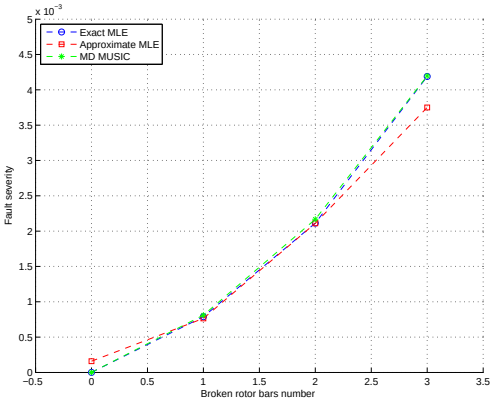

(b) Détection de rupture de barres par les approches proposées dans le cas de barres non-adjacentes.

Figure 6.15: Détection de défaut de rupture de barres par les approches proposées.

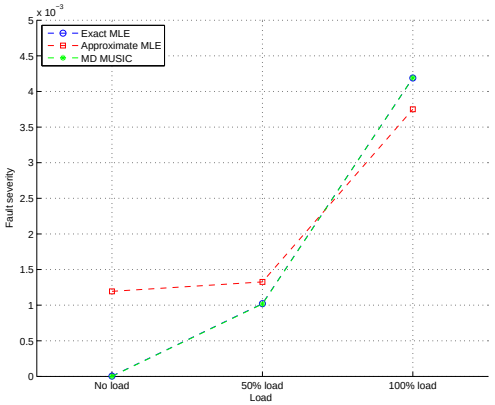

(a) Détection de rupture de barres par les approches proposées dans le cas de barres adjacentes.

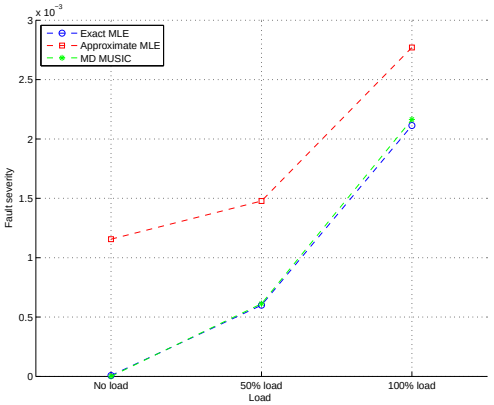

(b) Détection de rupture de barres par les approches proposées dans le cas de barres non-adjacentes.

Figure 6.16: Détection de défaut de rupture de barres par les approches proposées dans le cas de charge croissante.

pour une barre cassée et une charge croissante sont données sur la Fig. 6.16.

Il est claire à partir de ces résultats que le critère proposé dépend de la charge. En effet, celui-ci augmente avec la charge. Par ailleurs, L'EMV et le MD MUSIC donnent des résultats similaires alors que l'EMV approché donne des résultats légèrement supérieur. Ceci peut être expliqué par les sidelobes introduites par le calcul de la DFT.

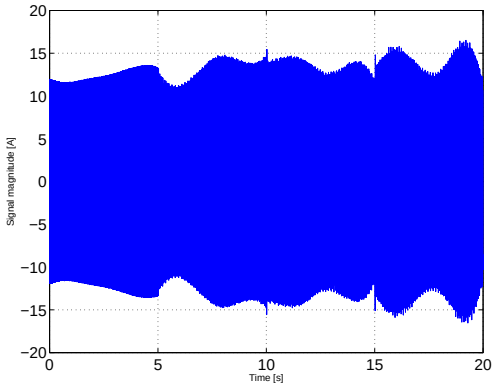

(a) Les courants statoriques.

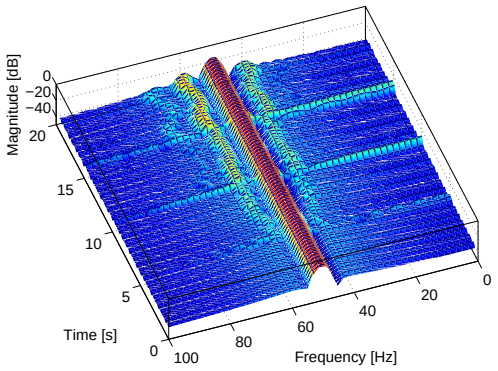

(b) Le spectrogramme.

Figure 6.17: Les résultats de simulation dans le cas d'une rupture de barres d'une machine asynchrone.

Des simulations ont été réalisées dans le cas non-stationnaire afin de tester la faisabilité des techniques proposées pour la détection du défaut de rupture de barres. Le modèle développé a été simulés pendant $20s$. Le défaut apparaît à partir de $5s$ avec une seule barre cassée, puis 2 barres à $10s$ et finalement 3 barres cassées à $15s$. Les résultats des simulations sont donnés sur la Fig. 6.17. Il apparaît à partir de ces figures que le spectrogramme permet de visualiser l'effet du défaut de rupture de barres. L'amplitude de ces bandes latérales évolue en fonction du temps et reflète le degré de sévérité du défaut. Le spectrogramme dans la figure 6.17(b) donne des résultats acceptable parce que le temps d'acquisition du signal est importante ce qui permet d'avoir une résolution meilleure.

Les approches proposées EMV et MD MUSIC ont été évaluées pour la détection de rupture de barres dans le cas non-stationnaire. Les performances de l'EMV sont données sur les Figs. 6.18(a) et 6.18(b).

Ces figures permettent d'affirmer que l'EMV non-stationnaire est fiable pour la détection du défaut de rupture de barres dans un environnement non-stationnaire. De façon similaire à l'EMV, les résultats de simulation pour la détection du défaut de rupture de barres sont données sur le Fig. 6.19 en utilisant le MD MUSIC. Nous pouvons en déduire que le MD MUSIC donne les résultats équivalentes à ceux de l'EMV.

Ces résultats permettent d'affirmer que les deux approches EMV et MD MUSIC fournissent un outil fiable pour la détection des défauts dans le cas non-stationnaire en se basant sur le traitement du courant statorique. De plus, elle permettent de fournir un indicateur sur la sévérité du défaut permettant ainsi un suivi en temps

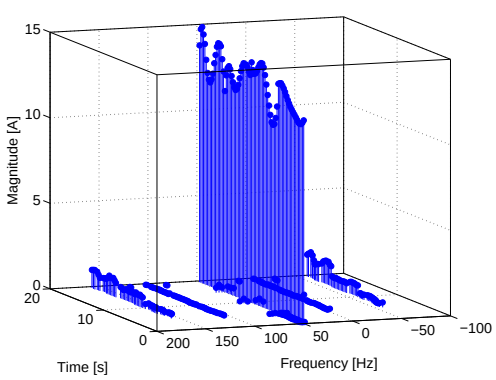

(a) Représentation temps-fréquence basée sur l'EMV.

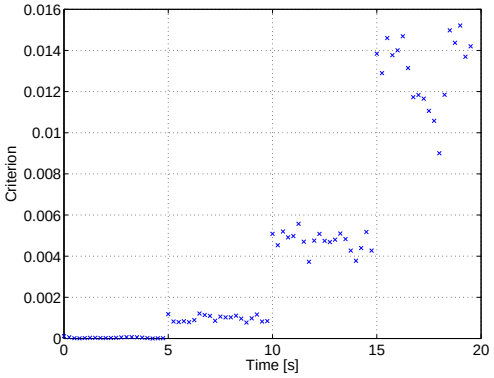

(b) Suivi de la sévérité du défaut.

Figure 6.18: Suivi de la sévérité du défaut par l'EMV; 1, 2 et 3 rupture de barres de façon consécutive.

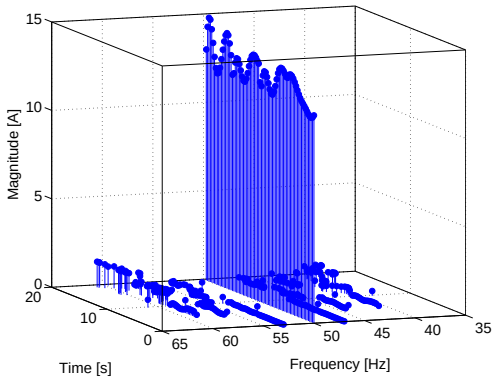

(a) Représentation temps-fréquence basée sur le MD MUSIC.

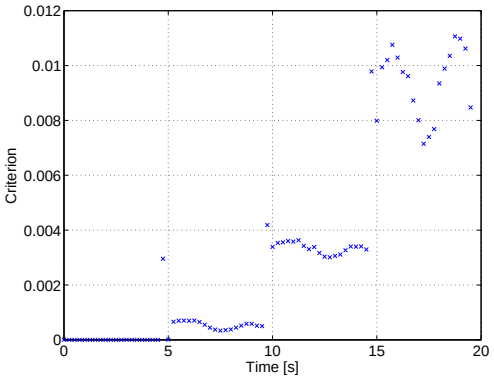

(b) Suivi de la sévérité du défaut.

Figure 6.19: Suivi de la sévérité du défaut par le MD MUSIC; 1, 2 et 3 rupture de barres de façon consécutive.

réel de l'évolution du défaut et une intervention au moment optimal afin d'éviter une défaillance catastrophique.

6.6 Validation expérimentale

Les défauts de roulement est l'une des principales causes des pannes dans les machines tournantes. Ces défauts entraînent des temps d'arrêt coûteux(Fig. 1.2(b)) [2].

L'une des questions clés quant au diagnostic des défauts de roulement est de les détecter à leur stade précoce et d'alerter l'opérateur avant qu'ils n'entraînent des défaillances sévères.

6.6.1 Banc expérimental

Un banc expérimental constitué d'une machine asynchrone conventionnelle d'une puissance de 0.75 kW est utilisé pour valider les approches paramétriques proposées pour détecter les défauts de roulements (Fig. 4.1).

La partie mécanique du banc d'essai est constitué par une machine synchrone et une machine asynchrone. La machine asynchrone est alimentée par une génératrice synchrone afin d'éliminer les harmoniques de temps et ainsi nous permettre de se focaliser sur les effets des défauts de roulement sur le courant statorique.

La machine asynchrone est équipée de deux types de roulements 6204.2 ZR (des roulements à billes à une seule rangée) avec les paramètres suivants : un diamètre extérieur de 47 mm, un diamètre intérieur de 20 mm et un pas de $D = 31.85$ mm. Le roulement est constitué par des billes d'un diamètre approximativement égale à 12 mm. L'angle de contact est égale à $0\,^{\circ}$.

Les défauts de roulements sont obtenus en réalisant des trous dans les différentes parties du roulement[165].

Les courants statoriques ont été mesurés afin de les utiliser comme médium pour la détection des défauts. La fréquence fondamentale des courants est fixe et égale à $f_s = 50$Hz. La fréquence d'échantillonnage des signaux était égale à 10kHz en utilisant une carte numérique d'acquisition. Ensuite, les signaux sont traitées sur Matlab-Simulink®. Les signaux ont été sous-échantillonnés à une fréquence d'échantillonnage égale à 200Hz car l'information relative aux défauts de roulement est principalement contenue dans les basses fréquences.

6.6.2 Détection des défauts de roulements par la méthode du EMV

En présence des défauts de roulement, il a été démontré dans [58, 67] que les fréquences caractéristiques sont données par : $f_k(\Omega) = |f_s \pm k f_c|$ ($k \in \mathbb{Z}$). L'algorithme proposée sur la Figure. 6.7 est utilisé afin d'extraire le critère de détection de défaut élaboré précédemment. Le nombre de lobes latéraux L est estimé afin de discriminer le cas sain du cas défaillant. En effet, si $L = 0$, les roulements sont sains, sinon ils sont endommagés et le critère dans (6.70) doit être estimé afin de mesurer la sévérité du défaut et par conséquent prendre une décision concernant l'état de fonctionnement de

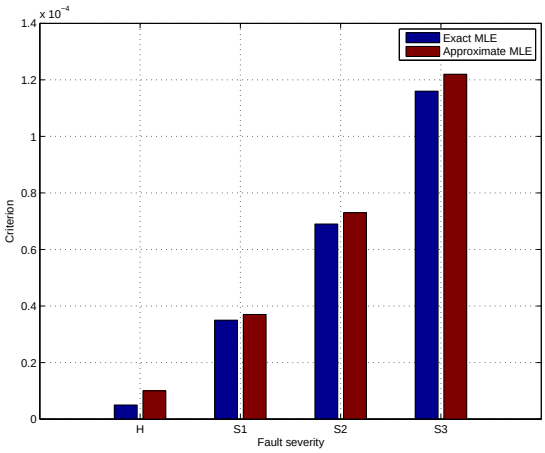

Figure 6.20: Détection des défauts de roulements en utilisant le EMV exacte et approché : critère de détection $\mathcal{C}$ en fonction de la sévérité.

la machine.

Les résultats expérimentaux pour des défauts de roulements avec des degré de sévérité différentes sont données sur la Fig. 6.20 pour l'approche EMV exacte et approchée. Cette figure montre l'évolution du critère de détection du défaut en fonction de la sévérité du défaut pour le cas exacte et approché.

On déduit à partir ce cette figure, dans un premier temps, que le critère est différent de zéro dans le sain cas pour les deux approche. Ce constat corrobore avec les résultats obtenus avec les méthodes d'estimation spectrale classique. Dans un second temps, nous pouvons constater que le critère augmente proportionnellement à la sévérité du défaut dans le cas d'une machine défaillante. Cependant, l'estimation de L n'est pas un indicateur fiable pour distinguer le cas sain du cas défaillant puisque L est différent de zéro même dans le cas sain. Par conséquent, il est indispensable de calculer le critère afin de déterminer un seuil à partir duquel la machine peut être considérée comme étant défaillante.

La comparaison entre les deux techniques permet de conclure que l'approche exacte est plus fiable (dans le sens où elle donne des résultats cohérente même dans le cas de signaux échantillonnés sur une courte durée) que la méthode approximée pour la détection des défauts dans la machine asynchrone. Néanmoins, il faut souligner que l'approche approximée présente des avantages pratiques car elle est fondée sur la TFD (facilité d'implémentation, calcul rapide basé sur la FFT). Ces résultats démontrent l'efficacité de la technique EMV pour la détection des défauts et plus particulièrement la méthode exacte qui est plus précise et plus fiable que la méthode approchée.

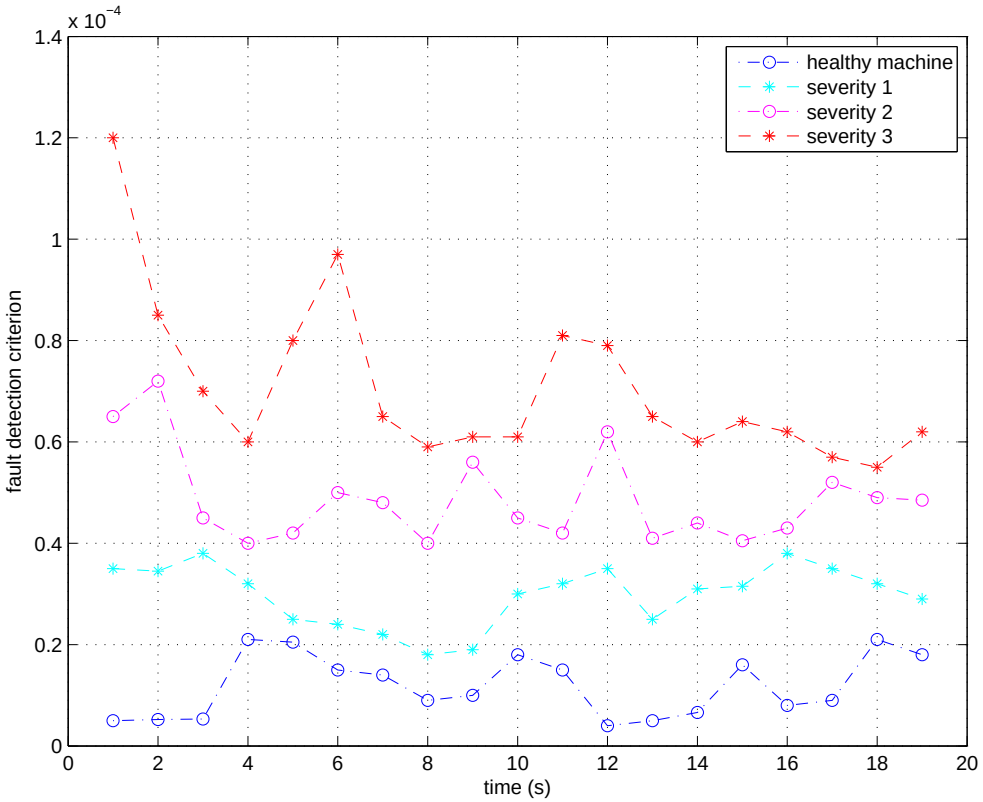

Figure 6.21: Variations du critère pour la détection du défaut de roulement en utilisant l'approche par EMV non-stationnaire.

L'algorithme non-stationnaire a également été testé afin de visualiser d'éventuelles variations du critère de détection en fonction du temps. Les résultats de simulation sont données sur la Fig. 6.21.

On peut déduire de cette figure que le critère de détection de défauts n'est pas nul lorsque la machine est saine. De plus, le critère de détection du défaut varie en fonction du temps mais reste toujours proportionnel à la sévérité du défaut. Ces résultats expérimentaux confirment les résultats sur les signaux de simulation présentés dans le la section précédente.

6.6.3 Détection des défauts de roulements par la méthode MD MUSIC

Le technique MD MUSIC est testée sur des signaux expérimentaux. L'algorithme MD MUSIC est utilisé afin d'estimer la DSP, puis le EMV est utilisé pour estimer les amplitudes des composantes fréquentielles. Ces amplitudes permettent de calculer le

Table 6.2: MD MUSIC : résultats expérimentaux.

État de la machine	$\widehat{f}_s$ (Hz)	$\widehat{f}_c$ (Hz)	$\widehat{L}$	$\widehat{a}_k$ (A)	$\mathcal{C}$ ($\times 10^{-5}$)
Machine saine	49.92	24.918	2	$a_{-2} = 0.0014$ $a_{-1} = 0.0012$ $a_0 = 2.1648$ $a_1 = 0.0016$ $a_2 = 0.0032$	0.33736
Défaut de roulement (sévérité 1)	49.99	8.4020	1	$a_{-2} = 0$ $a_{-1} = 0.0081$ $a_0 = 2.1371$ $a_1 = 0.006$ $a_2 = 0$	2.2116
Défaut de roulement (sévérité 2)	50.07	24.8294	2	$a_{-2} = 0.0066$ $a_{-1} = 0.0105$ $a_0 = 1.9856$ $a_1 = 0.0069$ $a_2 = 0.0039$	5.5043
défaut de roulement (sévérité 3)	50.05	24.8401	2	$a_{-2} = 0.0094$ $a_{-1} = 0.0110$ $a_0 = 2.0837$ $a_1 = 0.0079$ $a_2 = 0.0058$	7.037

critère de détection du défaut.

Les résultats expérimentaux sont résumés sur la Table 6.2 pour des défauts de roulements avec une sévérité croissante. Cette table donne la fréquence fondamentale, la fréquence caractéristique du défaut et les amplitudes des bandes latérales dans le cas sain et le cas défaillant. En outre, cette table présente la valeur du critère de détection du défaut dans les deux cas sain et défaillant. Ce tableau met en évidence la présence des bandes latérales même dans le cas sain. Cependant, l'amplitude de ces bandes

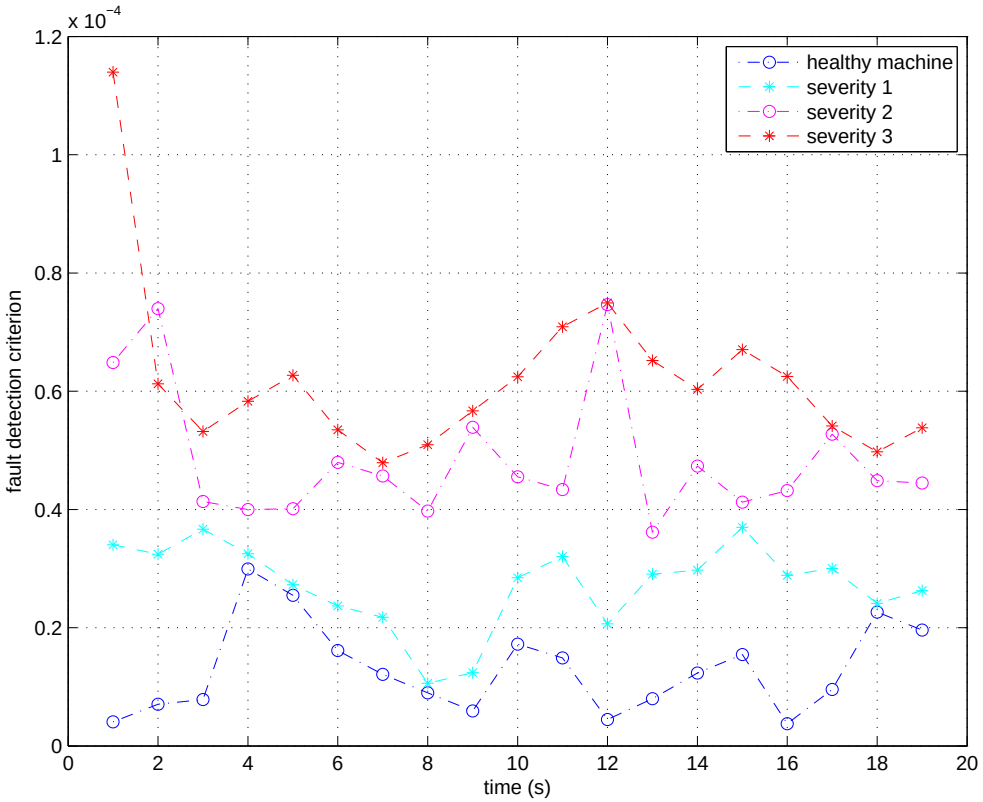

Figure 6.22: MD MUSIC : variations du critère de détection du défaut en fonction du temps.

latérales est inférieure dans le cas sain par rapport au cas défectueux. De plus, ce critère est plus important dans la cas d'un défaut d'une sévérité importante. Ainsi, on peut dire que le MD MUSIC donne des résultats similaires à ceux du EMV.

Afin d'étudier les variations du critère en fonction du temps, les signaux expérimentaux ont été échantillonnés pendant 20 s. Ensuite, la procédure dans le cas non-stationnaire a été effectuée sur des sous-vecteurs d'une seconde. La figure 6.22 donne la variation du critère de détection du défaut en fonction du temps pour des degrés de sévérité différentes.

On peut déduire de cette figure que le critère basé sur le MD MUSIC est sensible au défaut mais varie en fonction du temps. De plus, le critère de détection du défaut reste élevé dans le cas défectueux comparé au cas sain.

6.7 Conclusions et perspectives

La maintenance prédictive dans les entraînements électriques présente un intérêt considérable pour les ingénieurs et les chercheurs. En effet, celle-ci permet de pallier aux désavantages de la maintenance corrective et de la maintenance préventive. Par exemple, la maintenance préventive est d'un grand intérêt pour les systèmes installés dans un environnement hostile et difficilement d'accessible durant le fonctionnement (éoliennes, hydroliennes). La surveillance et le diagnostic des entraînements électriques et des composants mécaniques associées est un des éléments clé d'une maintenance préventive. Cela nécessite une stratégie de détection de défaut précise, efficace, robuste aux variations de charge et d'inertie et capable de détecter tout type de défauts à un stade précoce. Une grande majorité des recherches ont été orientées vers le diagnostic des machines asynchrones dans un environnement stationnaire (sans les variations de vitesse ou de couple) tel que rapporté par les références figurant au chapitre 1. Il ressort de cette bibliographie, que les sujets de recherche récents ont dépassé les méthodes basées sur des modèles traditionnels de diagnostic des défauts. En effet, l'accent a été mise sur l'utilisation des techniques de traitement du signal et des techniques de l'intelligence artificielles.

Ce projet de thèse propose une approche statistique pour la détection des défauts de la machine asynchrone. Les approches proposées sont composées de deux étapes : a) L'estimation de la DSP avec des techniques paramétriques et b) Le calcul d'un critère de détection de défaut permettant de rendre compte de l'état de fonctionnement de la machine asynchrone.

Pour l'estimation de la DSP, nous avons proposé trois techniques : l'EMV, L'EMV approché et le MD MUSIC. Concernant la première approche, l'estimation de la DSP a été réalisée en utilisant l'estimateur du maximum de vraisemblance. Contrairement aux techniques non paramétriques, la technique proposée exploite les signatures fréquentielles des défauts afin d'améliorer les performances du critère de détection du défaut. Par conséquent, l'estimateur proposé présente une meilleure résolution et précision fréquentielles que d'autres techniques telles que le périodogramme. Lorsque le nombre d'échantillons tend vers l'infini, il a également été démontré que l'estimateur DSP proposé peut être mis en œuvre efficacement en utilisant la transformée de Fourier discrète (TFD). Cependant, cette méthode approchée ne fonctionne pas aussi bien que la méthode exacte pour les signaux de courte durée. La troisième approche est basée sur le MD MUSIC associé au EMV des amplitudes du contenu fréquentiel. Concernant le critère de détection de défauts, nous avons proposé un critère basé sur l'amplitude des

fréquences liées au défaut. Ce critère est théoriquement nul pour une machine saine et augmente en fonction de la sévérité du défaut.

Les approches proposées ont été testées en simulation avec des défauts d'excentricité et de rupture de barres rotoriques. Ensuite, elles étaient validées en expérimentation sur des signaux issus d'une machine asynchrone affectée avec des défauts de roulements. Les résultats de simulation et en expérimentation ont corroboré l'efficacité du EMV et du MD MUSIC quelque soit le type de défaut, contrairement à l'approche basée sur la TFD.

Les approches proposées doivent être implémenter en utilisant des techniques d'optimisation classiques telles que le méthode du gradient, la méthode de Newton, etc. Par ailleurs, d'un point de vue traitement du signal, le calcul des bornes de Cramer-Rao pour ce problème d'estimation semble d'un grand intérêt. En effet, cela permettra de quantifier l'intérêt de l'utilisation des signatures fréquentielles dans l'élaboration d'algorithme de détection de défaut dans les machines asynchrones.

Des études supplémentaires sont nécessaires pour démontrer la faisabilité des techniques de traitement de signal en régime transitoire dans le cas d'une implémentation temps réel. Également, une généralisation des techniques d'estimation paramétrique est nécessaire. Ces techniques doivent être adaptées au régime transitoire et au fonctionnement en mode générateur des machines électriques. Cette généralisation impliquera forcément un modèle avec un nombre de paramètres plus élevés et demandera des techniques d'optimisation plus rapides et plus précises.

La plupart des études s'intéressent aux raies autour de la fondamentale (les bandes latérales) pour détecter et caractériser les défauts. Cependant, les autres raies qui sont soient dues au découpage (MLI) au niveau des convertisseurs statiques associés aux machines ou les harmoniques d'espaces qui sont dues à la structure même de la machine (saillance) peuvent être porteurs d'informations. Ils doivent aussi être exploités pour voir ce qu'on peut en extraire comme signatures du défaut étudié.

D'autres techniques doivent également être proposées pour réaliser le diagnostic non seulement de la machine mais également des éléments mécaniques autour; les multiplicateurs, la charge et des éléments électriques : les convertisseurs statiques et la partie contrôle/commande.

Nous pensons également que la commande peut avoir une influence sur l'impact de la défaillance sur les grandeurs électriques ou magnétiques (flux) grâce à son effet correcteur. Cette influence ne doit pas être négligée dans le cadre des prochaines études. La plupart des études que nous avons eu l'occasion d'analyser utilisent les entraînements électriques en boucle ouverte. Dans les applications industrielles et principalement

dans le cas de notre application éoliennes/hydroliennes, les systèmes sont couplés à des contrôleurs pour une meilleure extraction de l'énergie des vents/courants marins. Il est donc judicieux de se poser la question portant sur l'influence de la commande sur le diagnostic en se basant sur les courants statoriques ou rotoriques.

Appendix

A Stator currents samples

The signal model is given by the equation below:

$$x[n] = \sum_{k=-L}^{L} a_k \cos\left(2\pi f_k(\Omega) \times \left(\frac{n}{F_s}\right) + \phi_k\right) + b[n] \tag{A.1}$$

Thus:

$$x[0] = \sum_{k=-L}^{L} a_k \cos\phi_k + b[0] \tag{A.2}$$

$$x[1] = \sum_{k=-L}^{L} a_k \cos 2\pi f_k(\Omega) \times \left(\frac{1}{F_s}\right) + \phi_k) + b[1] \tag{A.3}$$

$$\vdots$$

$$x[N-1] = \sum_{k=-L}^{L} a_k \cos 2\pi f_k(\Omega) \times \left(\frac{N-1}{F_s}\right) + \phi_k) + b[N-1] \tag{A.4}$$

Let's note:

$$\begin{cases} \mathbf{x} = \begin{bmatrix} x[0] & x[1] & \cdots & x[N-1] \end{bmatrix}^T \\ \mathbf{b} = \begin{bmatrix} b[0] & b[1] & \cdots & b[N-1] \end{bmatrix}^T \\ \mathbf{v} = \begin{bmatrix} a_{-L}\cos(\phi_{-L}) & \ldots & a_L\cos(\phi_L), & -a_{-L}\sin(\phi_{-L}) & \ldots & -a_L\sin(\phi_L) \end{bmatrix}^T \end{cases} \tag{A.5}$$

Which gives:

$$\mathbf{x} = \mathbf{A}(\Omega)\mathbf{v} + \mathbf{b} \tag{A.6}$$

where:

$$\mathbf{A}(\Omega) = [\mathbf{A}_1(\Omega) \;\; \mathbf{A}_2(\Omega)] \tag{A.7}$$

$\mathbf{A}_1(\Omega)$ and $\mathbf{A}_2(\Omega)$ are given by (A.8).

$$\mathbf{A}_1(\Omega) = \begin{bmatrix} 1 & \cdots & 1 \\ \cos\left(2\pi f_{-L}(\Omega) \times \left(\frac{1}{F_s}\right)\right) & \vdots & \cos\left(2\pi f_L(\Omega) \times \left(\frac{1}{F_s}\right)\right) \\ \vdots & \vdots & \vdots \\ \cos\left(2\pi f_L(\Omega) \times \left(\frac{N-1}{F_s}\right)\right) & \cdots & \cos\left(2\pi f_L(\Omega) \times \left(\frac{N-1}{F_s}\right)\right) \end{bmatrix}$$

$$\mathbf{A}_2(\Omega) = \begin{bmatrix} 0 & \cdots & 0 \\ \sin\left(2\pi f_{-L}(\Omega) \times \left(\frac{1}{F_s}\right)\right) & \vdots & \sin\left(2\pi f_L(\Omega) \times \left(\frac{N-1}{F_s}\right)\right) \\ \vdots & \vdots & \vdots \\ \sin\left(2\pi f_{-L}(\Omega) \times \left(\frac{N-1}{F_s}\right)\right) & \cdots & \sin\left(2\pi f_L(\Omega) \times \left(\frac{N-1}{F_s}\right)\right) \end{bmatrix} \tag{A.8}$$

Appendix

B Link with discrete Fourier transform

$$\mathcal{J}_a(\Omega) = \frac{2}{N}\mathbf{x}^T\mathbf{A}(\Omega)\mathbf{A}^T(\Omega)\mathbf{x} \tag{B.1}$$

$$= \frac{2}{N}\|\mathbf{A}^T\mathbf{x}\|_F \tag{B.2}$$

$$= \frac{2}{N}\left\|\left[\mathbf{z}_{-L}\dots\mathbf{z}_L,\mathbf{y}_{-L}\dots\mathbf{y}_L\right]^T\begin{bmatrix}x[0] & x[1] & \dots & x[N-1]\end{bmatrix}^T\right\|_F \tag{B.3}$$

$$= \frac{2}{N}\left\|\begin{bmatrix}\sum_{n=0}^{N-1}x[n]\cos(2\pi f_{-L}(\Omega)\times\frac{n}{F_s}) \\ \vdots \\ \sum_{n=0}^{N-1}x[n]\cos(2\pi f_{L}(\Omega)\times\frac{n}{F_s}) \\ \sum_{n=0}^{N-1}x[n]\sin(2\pi f_{-L}(\Omega)\times\frac{n}{F_s}) \\ \vdots \\ \sum_{n=0}^{N-1}x[n]\sin(2\pi f_{L}(\Omega)\times\frac{n}{F_s})\end{bmatrix}\right\|_F \tag{B.4}$$

$$= \frac{2}{N}\sum_{k=-L}^{L}\left[\sum_{n=0}^{N-1}x[n]cos(2\pi f_k(\Omega)\frac{n}{F_s})\right]^2 + \left[\sum_{n=0}^{N-1}x[n]sin(2\pi f_k(\Omega)\frac{n}{F_s})\right]^2 \tag{B.5}$$

$$= \frac{2}{N}\sum_{k=-L}^{L}\left|\sum_{n=0}^{N-1}x[n]e^{-j2\pi f_k(\Omega)\frac{n}{F_s}}\right|^2 \tag{B.6}$$

$$= 2\sum_{k=-L}^{L}\widehat{P}_x\left(\frac{f_k(\Omega)}{F_s}\right) \tag{B.7}$$

Appendix

C

Synchronous demodulator demonstration

Using Euler formula, it can be shown that:

$$\cos(a)\cos(a+b) = \frac{1}{2}\left(\cos(2a+b)+\cos(b)\right) \tag{C.1}$$

$$\sin(a)\cos(a+b) = \frac{1}{2}\left(\sin(2a+b)-\sin(b)\right) \tag{C.2}$$

Using these equalities, one can show that:

$$a(n)\cos(2\pi f_0 n/Fe+\phi(n))\cos(2\pi f_0 n/Fe) = \frac{a(n)}{2}\left[\cos(4\pi f_0 n/Fe+\phi(n))+\cos(\phi(n))\right]$$

$$a(n)\cos(2\pi f_0 n/Fe+\phi(n))\sin(2\pi f_0 n/Fe) = \frac{a(n)}{2}\left[\sin(4\pi f_0 n/Fe+\phi(n))-\sin(\phi(n))\right]$$

Hence, the direct and quadrature components can be extracted by multiplying the original signal by the same carrier frequency f_0 and then low pass filtering the signal with cutoff frequency equal to f_0. Finally the direct and quadrature components are given by

$$x_1^s[n] = 2\times h[n]*x[n]\cos(2\pi f_0 n/F_e) = a[n]\cos(\phi[n]) \tag{C.3}$$

$$x_2^s[n] = -2\times h[n]*x[n]\sin(2\pi f_0 n/F_e) = a[n]\sin(\phi[n]) \tag{C.4}$$

This demodulation technique is known as a Synchronous demodulator. It is called so because it is widely used in the telecommunication field where we assume the transmitter and the receiver carrier signals are in phase.

References

[1] (2014, January) Technology transfer. [Online]. Available: http://www.techtransfer.com/resources/wiki/entry/3726/ xix, 7

[2] A. H. Bonnett and C. Yung, "Increased efficiency versus increased reliability," *IEEE Industry Applications Magazine*, vol. 14, no. 1, pp. 29–36, January/February 2008. xix, 7, 8, 9, 128, 160, 197

[3] J. Ribrant, "Reliability performance and maintenance - a survey of failure in wind power systems," Master's thesis, KTH School of Electrical Engineering, 2006. xix, 9, 10

[4] A. Siddique, G. Yadava, and B. Singh, "A review of stator fault monitoring techniques of induction motors," *IEEE Transactions on Energy conversion*, vol. 20, no. 1, pp. 106–114, 2005. xix, 11

[5] M. Rausand and A. Hoyland, *System Reliability Theory.* Hoboken: John Wiley & Sons, ISBN 0-471-47133-X, 2004. xix, 13

[6] R. Isermann, "Model-based fault-detection and diagnosis–status and applications," *Annual Reviews in control*, vol. 29, no. 1, pp. 71–85, 2005. xix, 16, 17

[7] P. Stoica and R. Moses, *Introduction to Spectral Analysis.* Prentice Hall, 1997. xx, xxiii, 24, 34, 56, 57, 71, 161, 175, 182

[8] C. M. Fonseca, P. J. Fleming *et al.*, "Genetic algorithms for multiobjective optimization: Formulationdiscussion and generalization." in *ICGA*, vol. 93, 1993, pp. 416–423. xx, 90

[9] F. Chan, H. Lau, and C. Ko, "Outage planning of electrical power system networks using genetic algorithm," *Journal of Quality in Maintenance Engineering*, vol. 6, no. 4, pp. 241–260, 2000. xx, 90

[10] G. Houdouin, "Contribution à la modélisation de la machine asynchrone en présence de défauts rotoriques," Ph.D. dissertation, Université du Havre, Le Havre, 2004. xxi, 104, 108

[11] E. H. El Bouchikhi, V. Choqueuse, and M. E. H. Benbouzid, "Current frequency spectral subtraction and its contribution to induction machines' bearings condition monitoring," *IEEE Trans. on Energy Conversion*, vol. 28, no. 1, pp. 135–144, March 2013. xxi, 103, 129

[12] M. E. H. Benbouzid, "A review of induction motors signature analysis as a medium for faults detection," *IEEE Trans. Industrial Electronics*, vol. 47, no. 5, pp. 984–993, October 2000. xxv, 6, 8, 16, 17, 18, 23, 28, 161

[13] A. Bellini, F. Filippetti, C. Tassoni, and G. A. Capolino, "Advances in diagnostic techniques for induction machines," *IEEE Transactions on Industrial Electronics*, vol. 55, no. 12, pp. 4109–4126, December 2008. xxv, 8, 16, 18, 23, 28, 161

[14] A. Bellini, F. Filippetti, G. Franceschini, C. Tassoni, and G. B. Kliman, "Quantitative evaluation of induction motor broken bars by means of electrical signature analysis," *IEEE Trans. Industrial Applications*, vol. 37, no. 5, pp. 1248–1255, Sept./Oct. 2001. xxv, 19, 23

[15] I. M. Culbert and W. Rhodes, "Using current signature analysis technology to reliably detect cage winding defects in squirrel-cage induction motors," *IEEE Transactions on Industrial Applications*, vol. 43, no. 2, pp. 422–428, Mar./Apr. 2007. 7

[16] B. Ayhan, M. Y. Chow, and M. H. Song, "Multiple discriminant analysis and neural-network-based monolith and partition fault-detection schemes for broken rotor bar in induction motors," *IEEE Transactions on Ind. Electron.*, vol. 53, no. 4, pp. 1298–1308, 2006. 7, 19

[17] W. T. Thomson and M. Fenger, "Case histories of current signature analysis to detect faults in induction motor drives," in *Proc. IEEE IEMDC'03*, vol. 3, Dundee, UK, Jun. 2003, pp. 1459–1465. 7

[18] G. Joksimovic, M. Durovic, J. Penman, and N. Arthur, "Dynamic simulation of dynamic eccentricity in induction machines-winding function approach," *IEEE Trans. Energy Conversion*, vol. 15, no. 2, pp. 143–148, June 2000. 8, 107, 109, 190

[19] W. T. Thomson, D. Rankin, and D. G. Dorrell, "On-line current monitoring to diagnose airgap eccentricity in large three-phase induction motors-industrial case histories verify the predictions," *IEEE Trans. Energy Convers.*, vol. 14, no. 4, pp. 1372–1378, 2006. 8

[20] P. Zhang, Y. Du, T. Habetler, and B. Lu, "A survey of condition monitoring and protection methods for medium-voltage induction motors," *IEEE Transactions on Industry Applications*, vol. 47, no. 1, pp. 34–46, January/February 2011. 8

[21] "List of offshore parcs," The Wind Power, Tech. Rep., 2010, http://www.thewindpower.net/29-parcs-offshore.php. 9

[22] S. Faulstich, B. Hahn, and P. Tavner, "Wind turbine downtime and its importance for offshore deployment," *Wind Energy*, vol. 14, no. 3, pp. 327–337, 2011. 9

[23] J. Ribrant and L. Bertling, "Survey of failures in wind power systems with focus on swedish wind power plant during 1997-2005," *IEEE Trans. Energy Conversion*, vol. 22, no. 1, pp. 167–173, 2007. 9, 14

[24] P. Tavner, J. Xiang, and F. Spinato, "Reliability analysis for wind turbines," *Journal of Wind Energy*, vol. 10, no. 1, pp. 1–18, 2006. 9

[25] P. Tavner and G. van Bussel, "Machine and converter reliabilities in wind turbines," in *IET PEMD'06*, Dublin, Ireland, 2006. 9

[26] M. Khan, M. Iqbal, and F. Khan, "Reliability and condition monitoring of a wind turbine," in *IEEE CCECE'05*, Saskatoon, Canada, 2005. 9

[27] J. Nilsson and L. Bertling, "Maintenance management of wind power systems using condition monitoring systems-life cycle cost analysis for two case studies," *IEEE Trans. Energy Conversion*, vol. 22, no. 1, pp. 223–229, 2007. 9

[28] S. Grubic, J. M. Aller, B. Lu, and T. G. Habetler, "A survey on testing and monitoring methods for stator insulation systems of low-voltage induction machines focusing on turn insulation problems," *IEEE Transactions on Industrial Electronics*, vol. 55, no. 12, pp. 4127–4136, 2008. 10

[29] S. Nandi, H. A. Toliyat, and X. Li, "Condition monitoring and fault diagnosis of electrical motors - a review," *IEEE Trans. Energy Conversion*, vol. 20, no. 4, pp. 719–729, December 2005. 14, 23, 160

[30] A. Garcia-Perez, R. de Jesus Romero-Troncoso, E. Cabal-Yepez, and R. Osornio-Rios, "The application of high-resolution spectral analysis for identifying multiple combined faults in induction motors," *IEEE Transactions on Industrial Electronics*, vol. 58, no. 5, pp. 2002–2010, May 2011. 14, 33, 160, 162

[31] S. Kia, H. Henao, and G. Capolino, "Torsional vibration assessment using induction machine electromagnetic torque estimation," *IEEE Transactions on Industrial Electronics*, vol. 57, no. 1, pp. 209–219, 2010. 14, 44

[32] H. Ocak and K. Loparo, "A new bearing fault detection and diagnosis schema based on hidden markov modeling of vibration signals," in *IEEE ICASSP*, Salt Lake City, USA, 2001, pp. 3141–3144. 14

[33] W. Yang, P. Tavner, C. Crabtreee, and M. Wilkinson, "Cost-effective condition monitoring for wind turbines," *IEEE Transactions on Industrial Electronics*, vol. 57, no. 1, pp. 263–271, Jan. 2010. 14, 46

[34] M. Blödt, "Fault signature detection for rolling element bearings in electric machines," Ph.D. dissertation, Georgia Institute of Technology, Nov. 2002. 14

[35] M. Blodt, J. Regnier, and J. Faucher, "Distinguishing load torque oscillations and eccentricity faults in induction motors using stator current Wigner distributions," *IEEE Trans. Industry Applications*, vol. 45, no. 6, pp. 1991–2000, November/December 2009. 14, 18, 20, 33, 47, 162

[36] W. Yang, P. Tavner, and M. Wilkinson, "Wind turbine condition monitoring and fault diagnosis using both mechanical and electrical signatures," in *Proceedings of the 2008 IEEE International Conference on Advanced Intelligent Mechatronics*, Sch. of Mech., Northwestern Polytech. Univ., Xian, Jul. 2008, pp. 1296–1301. 14

[37] I. S. for petroleum and C. Industry, "Severe duty totally enclosed fan-cooled (iefc) squirrel cage induction motors - up to and including 370 kw," IEEE Std 841-2001, Tech. Rep., 2001. 14

[38] B. Maru and P. A. Zotos, "Anti-friction bearing temperature rise for nema frame motors," *IEEE Trans. Industry Applications*, vol. 25, no. 5, pp. 883–888, Sep./Oct. 1989. 15

[39] Q. Wang, Z. Zhu, J. Duanmu, and X. Ge, "Oil filter debris analysis of aeroengine," in *Proc. 9th International Conference on Reliability, Maintainability and Safety*, Jun. 2011, pp. 276–278. 15

[40] M. W. Hawman and W. S. Galinaitis, "Acoustic emission monitoring of rolling element bearings," in *IEEE Proceedings of Ultrasonics Symposium*, Oct. 1988, pp. 885–889. 15

[41] H. Henao, C.Demian, and G. Capolino, "A frequency-domain detection of stator windings faults in induction machines using an external flux sensor," *IEEE Transactions on Industrial Applications*, vol. 39, no. 5, pp. 1272–1279, Sept./Oct. 2003. 15

[42] E. H. El Bouchikhi, V. Choqueuse, M. E. H. Benbouzid, and J. Charpentier, "Induction machine bearing failures detection using stator current frequency spectral subtraction," in *Proceedings of the 2012 IEEE ISIE*, Hangzhou (China), May 2012, pp. 1228–1233. 15

[43] E. H. El Bouchikhi, V. Choqueuse, M. E. H. Benbouzid, J. Charpentier, and G. Barakat, "A comparative study of time-frequency representations for fault detection in wind turbine," in *Proceedings of the 2011 IEEE IECON*, Melbourne (Australia), November 2011, pp. 3584–3589. 15, 123, 161, 192

[44] Y. Amirat, V. Choqueuse, M. E. H. Benbouzid, and S. Turri, "Hilbert transform-based bearing failure detection in DFIG-based wind turbines," *International Review of Electrical Engineering*, vol. 6, no. 3, pp. 1249–1256, June 2011. 15, 24

[45] V. Choqueuse, M. E. H. Benbouzid, Y. Amirat, and S. Turri, "Diagnosis of three-phase electrical machines using multidimensional demodulation techniques," *IEEE Transactions on Industrial Electronics*, vol. 59, no. 4, pp. 2014–2023, April 2011. 15, 24, 39, 41, 136, 160, 168

[46] S. Watson, B. Xiang, W. Yang, P. Tavner, and C. Crabtree, "Condition monitoring of the power output of wind turbine generators using wavelets," *IEEE Trans. Energy Conversion*, vol. 25, no. 3, pp. 715–721, Sept. 2010. 15

[47] J.Cusido, L. Romeral, J. Ortega, J. Rosero, and A. Espinosa, "Fault detection in induction machines using power spectral density in wavelet decomposition," *IEEE Transactions on Industrial Electronics*, vol. 55, no. 2, pp. 633–643, 2008. 15, 44

[48] M. Seera, C. P. Lim, D. Ishak, and H. Singh, "Fault detection and diagnosis of induction motors using motor current signature analysis and a hybrid fmm-cart model," *IEEE Transactions on Neural Networks and Learning Systems*, vol. 23, no. 1, pp. 97–108, January 2012. 15, 160

[49] R. R. Obaid and T. G. Habetler, "Current-based algorithm for mechanical fault detection in induction motors with arbitrary load conditions," in *Proceedings of the 2003 IEEE IAS Annual Meeting*, Salt Lake City, UT, Oct. 2003, pp. 1347–1351. 15, 160

[50] M. E. H. Benbouzid and G. Kliman, "What stator current processing based technique to use for induction motor rotor faults diagnosis?" *IEEE Trans. Energy Conversion*, vol. 18, no. 2, pp. 238–244, June 2003. 15, 160

[51] P. P. Harihara, K. Kim, and A. G. Parlos, "Signal-based versus model-based fault diagnosis-a trade-off in complexity and performance," in *Diagnostics for Electric Machines, Power Electronics and Drives, 2003. SDEMPED 2003. 4th IEEE International Symposium on.* IEEE, 2003, pp. 277–282. 16

[52] R. Isermann and P. Balle, "Trends in the application of model-based fault detection and diagnosis of technical processes," *Control engineering practice*, vol. 5, no. 5, pp. 709–719, 1997. 16

[53] V. Venkatasubramanian, R. Rengaswamy, K. Yin, and S. N. Kavuri, "A review of process fault detection and diagnosis: Part i: Quantitative model-based methods," *Computers & chemical engineering*, vol. 27, no. 3, pp. 293–311, 2003. 16

[54] M. Blödt, "Condition monitoring of mechanical faults in variable speed induction motor drives, applications of stator current time-frequency analysis and parameter estimation," Ph.D. dissertation, INPT, Toulouse, 2006. 18, 20, 22, 112

[55] A. DaSilva, R. Povinelli, and N. Demerdash, "Induction machine broken bar and stator short-circuit fault diagnostics based on three-phase stator current envelopes," *IEEE Transactions on Industrial Electronics*, vol. 55, no. 3, pp. 1310–1318, 2008. 19

[56] G. Didier, E. Ternisien, O. Caspary, and H. Razik, "Fault detection of broken rotor bars in induction motor using a global fault index," *IEEE Transactions on Industry Applications*, vol. 42, no. 1, pp. 79–88, Jan./Feb. 2006. 19, 28, 29, 161

[57] A. Knight and S. Bertani, "Mechanical fault detection in a medium-sized induction motor using stator current monitoring," *IEEE Trans. Energy Conversion*, vol. 29, no. 4, pp. 753–760, December 2005. 19

[58] R. Schoen, T. Habetler, F. Kamran, and R. Bartheld, "Motor bearing damage detection using stator current monitoring," *IEEE Trans. Industry Applications*, vol. 31, no. 6, pp. 1274–1279, November/December 1995. 19, 20, 22, 198

[59] M. Blodt, P. Granjon, B. Raison, and G. Rostaing, "Models for bearing damage detection in induction motors using stator monitoring," *IEEE Trans. Industrial Electronics*, vol. 55, no. 4, pp. 1813–1822, Avril 2008. 20, 22, 138, 144

[60] J. R. Stack, T. G. Habetler, and R. G. Harley, "Fault-signature modeling and detection of inner-race bearing faults," *IEEE Trans. on Industry Applications*, vol. 42, no. 1, pp. 61–68, Jan./Feb. 2006. 20

[61] J. R. Stack, R. G. Harley, and T. G. Habetler, "An amplitude modulation detector for fault diagnosis in rolling element bearings," *IEEE Transactions on Industrial Electronics*, vol. 51, no. 5, pp. 1097–1102, 2004. 20

[62] J. Faiz, B. M. Ebrahimi, B. Akin, , and H. A. Toliyat, "Finite-element transient analysis of induction motors under mixed eccentricity fault," *IEEE Trans. Magn.*, vol. 44, no. 1, pp. 66–74, Jan. 2008. 20

[63] G. M. Joksimovic, "Dynamic simulation of cage induction machine with air gap eccentricity," in *Proc. Inst. Elect. Eng. Elect. Power Appl.*, vol. 152, no. 4, Cargèse, France, Jul. 2005, pp. 803–811. 20

[64] M. Blodt, M. Chabert, J. Regnier, and J. Faucher, "Mechanical load fault detection in induction motors by stator current time-frequency analysis," *IEEE Trans. Industry Applications*, vol. 42, no. 6, pp. 1454–1463, 2006. 20, 47

[65] M. Blodt, J. Faucher, B. Dagues, and M. Chabert, "Mechanical load fault detection in induction motors by stator current time-frequency analysis," *IEEE Trans. Industry Applications*, vol. 55, no. 2, pp. 522–533, 2008. 20

[66] B. Heller and V. Hamata, *Harmonic Field Effects in Induction Machine.* Elsevier Scientific Publishing Company, 1977. 20

[67] M. Blodt, D. Bonacci, J. Regnier, M. Chabert, and J. Faucher, "On-line monitoring of mechanical faults in variable-speed induction motor drives using the Wigner distribution," *IEEE Trans.Industrial Electronics*, vol. 55, no. 2, pp. 522–533, 2008. 21, 33, 47, 162, 198

[68] P. Vas, *Parameter Estimation, Condition Monitoring and diagnosis of Electrical Machines.* Oxford, U.K.: Clarendon, 1993. 23

[69] P. Tavner and J. Penman, *Condition Monitoring of Electrical Machines.* Letchworth, U.K.: res. Stud. Press, 1987. 23

[70] A. Mohanty and C. Kar, "Fault detection in a multistage gearbox by demodulation of motor current waveform," *IEEE Transactions on Industrial Electronics*, vol. 53, no. 4, pp. 1285–1297, 2006. 24, 36, 165

[71] B. Trajin, M. Chabert, J. Regnier, and J. Faucher, "Hilbert versus concordia transform for three phase machine stator current time-frequency monitoring," *Mechanical systems & signal processing*, vol. 23, no. 8, pp. 2648–2657, 2009. 24, 39, 167

[72] A. Espinosa, J. Rosero, J. Cusido, L. Romeral, and J. Ortega, "Fault detection by means of Hilbert-Huang transform of the stator current in a PMSM with demagnetization," *IEEE Transactions on Energy Conversion*, vol. 25, no. 2, pp. 312–318, 2010. 24, 37, 50, 166

[73] D. Yu, J. Cheng, and Y. Yang, "Application of emd method and Hilbert spectrum to the fault diagnosis of roller bearings," *Mech. Syst. Signal Process.*, vol. 19, no. 2, pp. 259–270, 2005. 24

[74] N. Huang, Z. Shen, S. Long, M. Wu, H. Shih, Q. Zheng, N. Yen, C. Tung, and H. Liu, "The empirical mode decomposition and Hilbert spectrum for nonlinear and nonstationary time series analysis," *Proc. Roy. Soc. London*, vol. 454, pp. 903–995, 1998. 24, 48, 139, 171

[75] N. Q. Hu, L. R. Xia, F. S. Gu, and G. J. Qin, "A novel transform demodulation algorithm for motor incipient fault detection," *IEEE Transactions on Instrumentation and measurement*, vol. 60, no. 2, pp. 480–487, Feb. 2011. 24

[76] F. Zidani, M. Benbouzid, D. Diallo, and M. Nait-Said, "Induction motor stator faults diagnosis by a current concordia pattern-based fuzzy decision system," *IEEE Transactions on Energy Conversion*, vol. 18, pp. 469–475, 2003. 24, 26

[77] M. A. Awadallah and M. M. Morcos, "Application of ai tools in fault diagnosis of electrical machines and drives-an overview," *IEEE Transactions on Energy Conversion*, vol. 18, no. 2, pp. 245–251, Jun. 2003. 24

[78] F. Filippetti, G. Franceschini, C. Tassoni, and P. Vas, "Ai techniques in induction machines diagnosis including the speed ripple effect," *IEEE Transactions on Ind. Appl.*, vol. 34, no. 1, pp. 98–108, Jan./Feb. 1998. 24

[79] C. M. Bishop, *Neural Networks for Pattern Recognition.* Oxford University Press, 1995. 24

[80] S. Yang, W. Li, and C. Wang, "The intelligent fault diagnosis of wind turbine gearbox on artificial neuralnetwork," in *Proceedings International Conference on Condition Monitoring and Diagnosis*, Beijing, China, April 2008. 24, 25

[81] G. Salles, F. Filippetti, C. Tassoni, G. Grellet, and G. Franceschini, "Monitoring of induction motor load by neural network," *IEEE Transactions on Power Electronics*, vol. 15, no. 4, pp. 762–768, Jul. 2000. 24, 25

[82] M. Delgado, A. Garcia, J. A. Ortega, J. J. Cardenas, , and L. Romeral, "Multidimensional intelligent diagnosis system based on support vector machine classifier," in *Proceedings of the 2011 IEEE ISIE*, Gdansk, Poland, Jun. 2011, pp. 2127–2131. 24, 25

[83] B. Samanta, "Gear fault detection using artificial neural networks and support vector machines with genetic algorithms," *Mechanical Systems and Signal Processing*, vol. 18, no. 3, pp. 625–644, May 2004. 24, 25

[84] F. Zidani, D. Diallo, M. Benbouzid, and R. Nait-said, "A fuzzy-based approach for the diagnosis of fault modes in a voltage-fed pwm inverter induction motor drive," *IEEE Transactions on Ind. Electronics*, vol. 55, no. 2, pp. 586–593, Feb. 2008. 24, 26

[85] H. Razik, M. Beltrao, and E. Roberto, "A novel monitoring of load level and broken bar fault severity applied to squirrel-cage induction motors using a genetic algorithm," *IEEE Transactions on Industrial Electronics*, vol. 56, no. 11, pp. 4615–4626, 2009. 24

[86] N. K. Bose and P. Liang, *Neural Network Fundamentals with Graphs, Algorithms and Applications.* McGraw-Hill, 1996. 24

[87] S. Theodoridis and K. Koutroumbas, *Pattern recognition.* Elsevier Academic Press, 2003. 24, 25

[88] M. Barakata, D. Lefebvre, M. Khalil, O. Mustapha, and F. Druaux, "Bsp-bdt classification technique: Application to rolling elements bearing," in *Proceedings of the 2010 IEEE SYSTOL*, Nice (France), Oct. 2010, pp. 654–659. 25

[89] S. Altug, M.-Y. Chen, and H. J. Trussell, "Fuzzy inference systems implemented on neural architectures for motor fault detection and diagnosis," *IEEE Transactions on Industrial Electronics*, vol. 46, no. 6, pp. 1069–1079, 1999. 26

[90] M. S. Ballal, Z. J. Khan, H. M. Suryawanshi, and R. L. Sonolikar, "Adaptive neural fuzzy inference system for the detection of inter-turn insulation and bearing wear faults in induction motor," *IEEE Transactions on Industrial Electronics*, vol. 54, no. 1, pp. 250–258, 2007. 26

[91] H. Wang and P. Chen, "Fuzzy diagnosis method for rotating machinery in variable rotating speed," *IEEE Sensors Journal*, vol. 11, no. 1, pp. 23–34, 2011. 26

[92] M. S. Ballal, Z. J. Khan, H. M. Suryawanshi, and R. L. Sonolikar, "Adaptive neural fuzzy inference system for the detection of inter-turn insulation and bearing wear faults in induction motor," *IEEE Trans. Industrial Electronics*, vol. 54, no. 1, pp. 586–593, Feb. 2007. 26

[93] S. Kay, *Modern Spectral Estimation: Theory and Application.* Prentice Hall, Englewood Cliffs, New Jersey, 1998. 27, 32, 54, 59

[94] S. Kay and S. Marple, "Spectrum analysis - a modern perspective," *Proceedings of the IEEE*, vol. 69, no. 11, pp. 1380–1419, November 1981. 27, 32

[95] P. Stoica and R. L. Moses, *Introduction to Spectral Analysis.* Prentice-Hall,New Jersey, 1997. 28, 29, 30, 32, 61, 177

[96] M. E. H. Benbouzid, M. Vieira, and C. Theys, "Induction motors' faults detection and localization using stator current advanced signal processing techniques," *IEEE Transactions on Power Electronics*, vol. 14, no. 1, pp. 14–22, January 1999. 28

[97] A. Bellini, A. Yazidi, F. Filippetti, C. Rossi, and G. Capolino, "High frequency resolution techniques for rotor fault detection of induction machines," *IEEE Trans. Industrial Electronics*, vol. 55, no. 12, pp. 4200–4209, December 2008. 28, 161

[98] A. Yazidi, H. Henao, G. A. Capolino, M. Artioli, and F. Filippetti, "Improvement of frequency resolution for three-phase induction machine fault diagnosis," in *Proceedings of the 2005 IEEE IAS Annual Meeting*, Hong Kong (China), October 2005, pp. 20–25. 28, 161

[99] Z. Leonowicz, T. Lobos, and J. Rezmer, "Advanced spectrum estimation methods for signal analysis in power electronics," *IEEE Transactions on Industrial Electronics*, vol. 50, no. 3, pp. 514–519, June 2003. 29, 162

[100] J. R. Stack, T. G. Habetler, and R. G. Harley, "Bearing fault detection via autoregressive stator current modeling," *IEEE Transactions on Industry Applications*, vol. 40, no. 3, pp. 740–747, May/June 2004. 29, 162

[101] P. Stoica and A. Nehorai, "MUSIC, Maximum Likelihood, and Cramer-Rao Bound," *IEEE Transactions on Acoustics. Speech. and Signal Processing*, vol. 37, no. 5, pp. 720–741, 1989. 30, 69

[102] O. Besson, F. Castanié, A. Ferrari, E. L. Charpentier, C. Mailhes, S. Marcos, and N. Martin, *Traitement de signal et de l'image - Analyse spectrale.* Lavoisier, 2003. 31

[103] P. Stoica and Y. Selen, "A review of information criterion rules," *IEEE Signal Processing Magazine*, vol. 21, no. 4, pp. 36–47, July 2004. 32, 66, 84, 173, 177, 186

[104] F. Cupertino, E. de Vanna, L. Salvatore, and S. Stasi, "Analysis techniques for detection of im broken rotor bars after supply disconnection," *IEEE Transactions on Industry Applications*, vol. 40, no. 2, pp. 526–533, March/April 2004. 33, 162

[105] A. Bracale, G. Carpinelli, L. Piegari, and P. Tricoli, "A high resolution method for on line diagnosis of induction motors faults," in *Proceedings of IEEE Power Tech.*, Lausanne, Suisse, July 2007, pp. 994–998. 33, 162

[106] S. H. Kia, H. Henao, and G. A. Capolino, "A high-resolution frequency estimation method for three-phase induction machine fault detection," *IEEE Transactions on Industrial Electronics*, vol. 54, no. 4, pp. 2305–2314, August 2007. 33, 162

[107] B. Xu, L. Sun, L. Xu, and G. Xu, "Improvement of the Hilbert method via ESPRIT for detecting rotor fault in induction motors at low slip," *IEEE Transactions on Energy Conversion*, vol. 28, no. 1, pp. 225–233, March 2013. 33, 39, 167

[108] Y. Kim, Y.and Youn, Hwang, D. Sun, and D. J.; Kang, "High-resolution parameter estimation method to identify broken rotor bar faults in induction motors," *IEEE Transactions on Industrial Electronics*, vol. :pp, no. 99, November2012. 33

[109] M. Nemec, K. Drobnic, D. Nedeljkovic, R. Fiser, and V. Ambrozic, "Detection of broken bars in induction motor through the analysis of supply voltage modulation," *IEEE Transactions Industrial Electronics*, vol. 57, no. 8, pp. 2879–2888, Aug. 2010. 33, 162

[110] S. Kia, H. Henao, and G. Capolino, "Analytical and experimental study of gearbox mechanical effect on the induction machine stator current signature," *IEEE Transactions on Industry Applications*, vol. 45, no. 4, pp. 1405–1415, 2009. 33, 162

[111] D. Vakman, "On the analytic signal, the teager-kaiser energy algorithm, and other methods for defining amplitude and frequency," *Signal Processing, IEEE Transactions on*, vol. 44, no. 4, pp. 791–797, April 1996. 35, 165

[112] S. L. Hahn, *Hilbert Transforms in Signal Processing.* Norwell, MA: Artech House, 1996. 36, 68

[113] M. Schwartz, W. R. Bennett, and S. Stein, *Communication Systems and Techniques.* New York, 1995, 1995. 37

[114] B. Picinbono, "On instantaneous amplitude and phase of signals," *IEEE Trans. Signal Processing*, vol. 45, no. 3, pp. 552–560, 1997. 37, 166

[115] B. Boashash, *Time-Frequency signal analysis, in advances in Spectrum Estimation, S. Haykin, Ed.* Engewood Cliffs, NJ: Prentice-Hall, 1991. 37, 166

[116] L. Marple Jr, "Computing the discrete-time "analytic" signal via fft," *Signal Processing, IEEE Transactions on*, vol. 47, no. 9, pp. 2600–2603, 1999. 37, 166

[117] J. Pons-Llinares, J. Roger-Folch, and M. Pineda-Sanchez, "Diagnosis of eccentricity based on the Hilbert transform of the startup transient current," in *Procedings of SDEMPED'09*, Cargese, France, Aug./Sept. 2009, pp. 1–6. 37, 166

[118] M. Pineda-Sanchez, M. Riera-Guasp, J. Roger-Folch, J. Antonino-Daviu, and J. Perez-Cruz, "Diagnosis of rotor bar breakages based on the Hilbert transform of the current during the startup transient," in *Procedings of IEMDC '09*, Miami, FL, USA, May 2009, pp. 1434–1440. 37, 166

[119] P. Maragos, J. Kaiser, and T. Quartieri, "On amplitude and frequency demodulation using energy operators," *IEEE Transactions on Signal Processing*, vol. 41, no. 4, 1993. 38, 166

[120] P. Maragos, J. Kaiser, and T. Quatieri, "Energy separation in signal modulations with application to speech analysis," *IEEE Transactions on Signal Processing*, vol. 10, no. 41, pp. 3024–3051, 1993. 38, 166

[121] H. Li, L. Fu, and Y. Zhang, "Bearing fault diagnosis based on teager energy operator demodulation technique," in *International Conference on Measuring Technology and Mechatronics Automation*, Zhangjiajie, China, 2009, pp. 594–597. 38, 167

[122] M. Pineda-Sanchez, R. Puche-Panadero, M. Riera-Guasp, J. Perez-Cruz, J. Roger-Folch, J. Pons-Llinares, V. Climente-Alarcon, and J. A. Antonino-Daviu, "Application of the teager–kaiser energy operator to the fault diagnosis of induction motors," *IEEE Trans. Signal Processing*, vol. pp, no. 99, pp. 1–9, 16 Sept. 2013. 38

[123] I. Onel and M. Benbouzid, "Induction motor bearing failure detection and diagnosis: Park and concordia transform approaches comparative study," *IEEE/ASME Transactions on Mechatronics*, vol. 13, no. 2, pp. 257–262, 2008. 39

[124] M. Benbouzid, "Induction motor bearing failure detection and diagnosis: Park and concordia transform approaches comparative study," *IEEE Transactions on Industrial Electronics*, vol. 47, no. 5, pp. 984–993, 2000. 39

[125] J. M. Aller, A. Bueno, and T. Pagá, "Power system analysis using space-vector transformation," *Power Systems, IEEE Transactions on*, vol. 17, no. 4, pp. 957–965, 2002. 39, 167

[126] V. Pires, J. Martin, and A. Pires, "Eigenvector/eignevalue analysis of a 3d current referential fault detection and diagnosis of an induction motor," *Energy Conversion and Management*, pp. 901–907, 2010. 41, 168

[127] J. Martins, V. F. Pires, and A. Pires, "Unsupervised neural-networks-based algorithm for on-line diagnosis of three-phase induction motor stator fault," *IEEE Transactions on Industrial Electronics*, vol. 54, no. 1, pp. 259–264, 2007. 41, 168

[128] P. Flandrin, *Time-frequency/time-scale analysis*. Academic Press, 1998. 42, 43, 170

[129] S. Rajagopalan, J. A. Restrepo, J. Aller, T. Habetler, and R. Harley, "Nonstationary motor fault detection using recent quadratic time-frequency representations," *IEEE Transactions on Industry Applications*, vol. 44, no. 3, 2008. 42, 47

[130] F. Auger, P. Flandrin, P. Goncalves, and O. Lemoine, "Time-frequency toolbox, for use with matlab," CNRS, GDR ISIS, Tech. Rep., 1997. 42, 139

[131] G. Rilling, P. Flandrin, and P. Gonçalves, "On empirical mode decomposition and its algorithms," in *IEEE-EURASIP Workshop on Nonlinear Signal and Image Processing*, Grado, Italia, 2003. 42, 48, 139, 171

[132] S. Mallat, *A Wavelet Tour of Signal Processing: The Sparse Way*, 3rd ed. Academic Press, 2008. 43, 44, 46

[133] B. Yazici and G. Kliman, "An adaptive statistical time-frequency method for detection of broken bars and bearing faults in motors using stator current," *IEEE Trans. Industry Applications*, vol. 35, no. 2, pp. 442–452, March/April 1999. 43, 50, 162

[134] S. Rajagopalan, J. Aller, J. A. Restrepo, T. Habetler, and R. Harley, "Detection of rotor faults in brushless dc motors operating under nonstationary conditions," *IEEE Transactions on Industry Applications*, vol. 42, no. 6, pp. 1464 – 1477, Nov./dec. 2006. 44, 47

[135] ——, "Analytical-wavelet-ridge-based detection of dynamic eccentricity in brushless direct current (bldc) motors functioning under dynamic operating conditions," *IEEE Transactions on Industrial Electronics*, vol. 54, no. 3, 2007. 46

[136] J.Pons-Llinares, J. Antonino-Daviu, M. Riera-Guasp, M. Pineda-Sanchez, and V. Climente-Alarcon, "Induction motor diagnosis based on a transient current analytic wavelet transform via frequency b-splines," *IEEE Trans. Industrial Electronics*, vol. 58, no. 5, pp. 1530–1544, May 2011. 46

[137] L. Cohen, "Time-frequency distributions: A review," *Proceedings of the IEEE*, vol. 77, no. 7, pp. 941–981, 1989. 46, 170, 171

[138] F. Auger and P. Flandrin, "Improving the readability of time-frequency and time-scale representations by the reassignment method," *IEEE Transactions on Signal Processing*, vol. 43, no. 5, pp. 1068–1089, 1995. 46

[139] J. Rosero, L. Romeral, J. Ortega, and E. Rosero, "Short-circuit detection by means of empirical mode decomposition and Wigner-Ville distribution for PMSM running under dynamic condition," *IEEE Transactions on Industrial Electronics*, vol. 56, no. 11, pp. 4534–4547, 2009. 47, 50

[140] J. Antonino-Daviu, M. Riera-Guasp, M. Pineda-Sanchez, and R. Pérez, "A critical comparison between DWT and Hilbert-Huang-based methods for the diagnosis of rotor bar failures in induction machines," *IEEE Transactions on Industry Applications*, vol. 45, no. 5, pp. 1794–1803, 2009. 50

[141] C. Kral, T. G. Habetler, and R. G. Harley, "Detection of mechanical imbalances of induction machines without spectral analysis of time-domain signals," *IEEE Trans. Ind. Appl.*, vol. 40, no. 4, pp. 1101–1106, Jul./Aug. 2004. 50

[142] C. Crabtree, S. Djurovic, P. Tavner, and A. Smith, "Fault frequency tracking during transient operation of wind turbine generators," in *International conference on electrical machines - ICEM 2010*, Rome, Italy, 2010, pp. 1–5. 50

[143] A. Bellini, G. Franceschini, and C. Tassoni, "Monitoring of induction machines by maximum covariance method for frequency tracking," *IEEE Transactions on Industry Applications*, vol. 42, no. 1, pp. 69–78, Jan./Feb. 2006. 50, 162

[144] A. Papoulis and S. U. Pillai, *Probability, random variables, and stochastic processes*. Tata McGraw-Hill Education, 2002. 56

[145] M. Rosenblatt, "A central limit theorem and a strong mixing condition," *Proceedings of the National Academy of Sciences of the United States of America*, vol. 42, no. 1, p. 43, 1956. 56

[146] P. Stoica and O. Besson, "Training sequence design for frequency offset and frequency-selective channel estimation," *Communications, IEEE Transactions on*, vol. 51, no. 11, pp. 1910–1917, 2003. 56

[147] P. Stoica and P. Babu, "The gaussian data assumption leads to the largest cramér-rao bound [lecture notes]," *Signal Processing Magazine, IEEE*, vol. 28, no. 3, pp. 132–133, 2011. 56

[148] S. Kay, *Fundamentals of Statistical Signal Processing: Estimation Theory*. Prentice-Hall signal processing series, 1993, 17th Printing. 56, 61, 63, 172, 178

[149] K. B. Petersen and M. S. Pedersen, "The matrix cookbook," November 2008. 60

[150] M.Wax and T. Kailath, "Detection of signals by information theoretic criteria," *IEEE Trans. Acoust. Speech, Signal Processingl*, vol. 33, no. 2, pp. 387–392, 1985. 66, 177

[151] R. R. Bouckaert, *Probabilistic network construction using the minimum description length principle.* Springer, 1993. 66

[152] M. G. Christensen, S. H. Jensen, S. V. Andersen, and A. Jakobsson, "Subspace-based fundamental frequency estimation," in *Proc. European Signal Processing Conf*, 2004, pp. 637–640. 74, 182

[153] M. G. Christensen, A. Jakobsson, and S. H. Jensen, "Joint high-resolution fundamental frequency and order estimation," *IEEE Trans. Audio, Speech, and Language Processing*, vol. 15, no. 5, pp. 1635–1644, July 2007. 74, 75, 182

[154] D. D. Sabin, D. L. Brooks, and A. Sundaram, "Indices for assessing harmonic distortion from power quality measurements: definitions and benchmark data," *Power Delivery, IEEE Transactions on*, vol. 14, no. 2, pp. 489–496, 1999. 77

[155] M. G. Christensen and A. Jakobsson, *Multi-pitch Estimation.* vol. 5 of Synthesis Lectures on Speech & Audio Processing, Morgan & Claypool Publishers, 2009. 83, 185

[156] T. Bäck, *Evolutionary algorithms in theory and practice: evolution strategies, evolutionary programming, genetic algorithms.* Oxford University Press, New York, 1996, vol. 996. 89

[157] H.-P. Schwefel and G. Rudolph, *Contemporary evolution strategies.* Springer, 1995. 89

[158] H. Toliyat and T. Lipo, "Transient analysis of cage induction machines under stator, rotor bar and end ring faults," *IEEE Trans. Energy Conversion*, vol. 10, no. 2, pp. 241–247, June 1995. 102, 104

[159] H. Toliyat, M. Arefeen, and A. Parlos, "A method for dynamic simulation of air-gap eccentricity in induction machines," *IEEE Trans. Industry Applications*, vol. 32, no. 4, pp. 910–918, July/August 1996. 102

[160] D. Dupont and A. Gautriaud, "Failure modeling in wind and tidal turbine generators: development of simulation tool," University of Brest, Tech. Rep., November 2011. 102, 114

[161] G. Houdouin, G. Barakat, B. Dakyo, E. Destobbeleer, and C. Nichita, "A coupled magnetic circuit based global method for the simulation of squirrel cage induction machines under rotor and stator faults," in *Proceedings of ELECTRIMACS'02*, Montreal (Canada), August 2002, pp. 18–21. 103, 190

[162] A. Ceban, R. Pusca, and R. Romary, "Study of rotor faults in induction motors using external magnetic field analysis," *IEEE Transactions on Industrial Electronics*, vol. 59, no. 5, pp. 2082–2096, May 2012. 104

[163] S. Nandi, R. M. Bharadwaj, and H. A. Toliyat, "Performance analysis of a three-phase induction motor under mixed eccentricity condition," *Energy Conversion, IEEE Transactions on*, vol. 17, no. 3, pp. 392–399, 2002. 113

[164] M. Lajoie-Mazenc, H. Hector, and R. Carlson, "Procédé d'analyse des champs électrostatiques et magnétostatiques dans les structures planes et de révolution: programme difimedi," *in the Proceedings of Compumag, Grenoble, France*, 1978. 114

[165] Z. Obeid, S. Poignant, J. Regnier, and P. Maussion, "Stator current based indicators for bearing fault detection in synchronous machine by statistical frequency selection," in *Proceedings of the 2011 IEEE IECON 2011*, Melbourne, Australia, Nov. 2011, pp. 2036–2041. 129, 198

[166] P. Stoica and A. Eriksson, "MUSIC estimation of real-valued sine-wave frequencies," *Signal processing*, vol. 42, no. 2, pp. 139–146, 1995. 132

[167] S. Das, P. Purkait, and S. Chakravorti, "Space-vector characterization of induction motor operating conditions," in *Fifteen National Power System Conference*, Bombay, India, 2008, pp. 512–517. 137

[168] D. Diallo, M. Benbouzid, D. Hamad, and X. Pierre, "Fault detection and diagnosis in an induction machine drive: A pattern recognition approach based on concordia stator mean current vector," *IEEE Transactions on Energy Conversion*, vol. 20, no. 3, pp. 512–519, September 2005. 137

[169] S. M. Kay, "Fundamentals of statistical signal processing: detection theory," 1998. 148

[170] (2013, July) Machinery fault simulator. [Online]. Available: http://spectraquest.com/ 150

[171] M. Benbouzid, H. Nejjari, R. Beguenane, and M. Vieira, "Induction motor asymmetrical faults detection using advanced signal processing techniques," *IEEE Trans. Energy Conversion*, vol. 14, no. 2, pp. 147–152, June 1999. 161

[172] N. Thirion-Moreau and P. Y. Arquès, "Analyse temps fréquence linéaires et quadratiques," *Techniques de l'Ingénieur, Traité Télécoms*, Novembre 2002. 168

[173] L. Cohen, *Time-Frequency Analysis*. Englewood Cliffs, NJ: Prentice-Hall, 1995. 169

[174] W. Mecklenbräuker and F. Hlawatsch, "The Wigner distribution- theory and applications in signal processing," *Amsderdam, The Netherlands: Elsevier*, 1997. 170

[175] P. F. P. O. Rioul, "Time-scale energy distributions: a general class extending wavelet transforms," *IEEE Trans. On Signal Processing*, vol. 40, no. 7, July 1992. 171

[176] J. C. Cexus, "Analyse des signaux non-stationnaires par transformation de huang, opérateur de teager-kaiser, et transformation de huang-teager (tht)," Ph.D. dissertation, Thèse de Doctorat de l'Université de Rennes 1, Décembre 2005. 172

[177] M. G. Christensen, J. H. Jensen, A. Jakobsson, and S. H. Jensen, "On optimal filter designs for fundamental frequency estimation," *IEEE Signal Processing Letters*, vol. 15, pp. 745–748, 2008. 172

[178] H. Li, P. Stoica, and J. Li, "Computationally efficient parameter estimation for harmonic sinusoidal signals," *Signal Processing*, vol. 80, pp. 1937–1944, September 2000. 172

[179] Y. Bresler, "Exact maximum likelihood parameter estimation superimposed exponential signals in noise," *IEEE Transactions on Acoustics, Speech, and Signal Processing*, vol. 1, no. 5, pp. 1081–1089, October 1986. 172

[180] M. Blodt, M. Chabert, J. Regnier, and J. Faucher, "Current based mechanical fault detection in induction motors through maximum likelihood estimation," in *Proceedings of the 2006 Conference IEEE IECON*, Paris, France, Nov. 2006, pp. 4999–5004. 173

RESUME

Sur l'estimation spectrale paramétrique pour la détection des défauts dans les machines asynchrones en environnements stationnaire et non stationnaire

Ce travail de thèse traite de la détection et du diagnostic des défaillances par analyse du courant statorique dans les entraînements mécaniques à base de machine asynchrone. En se basant sur des travaux ultérieurs un modèle du signal en présence de défaut est présenté. Pour estimer les paramètres du modèle, nous proposons une technique statistique basée sur le Maximum de Vraisemblance et une approche basée sur les sous-espaces signal/bruit. Ces techniques ont été développées pour analyser des courants statoriques dans le cas stationnaire et non-stationnaire. Ces techniques permettent de révéler la présence d'une défaillance et de mesurer sa sévérité. Les résultats de simulation sur des signaux issus d'un modèle de la machine asynchrone, basé sur les circuits électriques magnétiquement couplés, permettent de valider les méthodes de détection proposées et démontre l'intérêt des techniques afin d'extraire de façon automatique un indicateur de défaut. L'étude est complétée par une validation expérimentale sur des signaux issus d'un banc expérimental pour la détection des défauts de roulement.

ABSTRACT

On parametric spectral estimation for induction machine faults detection in stationary and non-stationary environments

In this thesis, a signal processing-based approach for induction machine faults detection through stator currents has been proposed. A parametric spectral estimation approach has been adopted to extract sensitive index to induction machine faults. The proposed approach can perform induction machine condition monitoring in stationary and non-stationary environment. Moreover, it allows to propose a reliable diagnosis scheme for electrical and mechanical faults that may occur induction machines. Moreover, A Matlab-simulink®-based tool for faulty induction machines has been developed to generate faults database and therefore to allow the performance of the proposed approach assessment. The coupled magnetic circuits approach combined with the arbitrary reference frames theory has been used for induction machines modeling.

The proposed technique has been validated using experiments on conventional induction machine test bed for bearing faults detection and diagnosis. The obtained results were satisfactory and very promising.